



**HAL**  
open science

# Deposition and characterization of single and multilayered boron carbide and boron carbonitride thin films by different sputtering configurations

Tolga Tavsanoglu

► **To cite this version:**

Tolga Tavsanoglu. Deposition and characterization of single and multilayered boron carbide and boron carbonitride thin films by different sputtering configurations. Engineering Sciences [physics]. École Nationale Supérieure des Mines de Paris, 2009. English. NNT : 2009ENMP1641 . pastel-00005772

**HAL Id: pastel-00005772**

**<https://pastel.hal.science/pastel-00005772>**

Submitted on 1 Feb 2010

**HAL** is a multi-disciplinary open access archive for the deposit and dissemination of scientific research documents, whether they are published or not. The documents may come from teaching and research institutions in France or abroad, or from public or private research centers.

L'archive ouverte pluridisciplinaire **HAL**, est destinée au dépôt et à la diffusion de documents scientifiques de niveau recherche, publiés ou non, émanant des établissements d'enseignement et de recherche français ou étrangers, des laboratoires publics ou privés.



Collège Doctoral



Institute of Science  
and Technology

ED n° 432 : Science des Métiers de l'Ingénieur

*N° attribué par la bibliothèque*

□□□□□□□□□□

## THESE EN COTUTELLE

pour obtenir le grade de  
**Docteur de l'Ecole des Mines de Paris**  
Spécialité "Science et Génie des Matériaux"  
et  
**Docteur de l'Université Technique d'Istanbul**  
Spécialité "Matériaux"

présentée et soutenue publiquement par  
**Tolga TAVSANOGLU**

le 14 Mai 2009

**DEPOSITION AND CHARACTERIZATION OF SINGLE AND  
MULTILAYERED BORON CARBIDE AND BORON CARBONITRIDE  
THIN FILMS BY DIFFERENT SPUTTERING CONFIGURATIONS**

*Directeurs de thèse : Michel JEANDIN  
Okan ADDEMIR*

Jury

|                      |  |                    |
|----------------------|--|--------------------|
| M. Ali A. KAYA       | Université de Mugla                    | Rapporteur         |
| Mme Caroline RICHARD | Université de Technologie de Compiègne | Rapporteur         |
| M. E. Sabri KAYALI   | Université Technique d'Istanbul        | Examineur          |
| M. Sid LABDI         | Université d'Evry-Val-d'Essonne        | Examineur          |
| M. Onuralp YUCEL     | Université Technique d'Istanbul        | Examineur          |
| M. Okan ADDEMIR      | Université Technique d'Istanbul        | Directeur de thèse |
| M. Michel JEANDIN    | Ecole des Mines de Paris               | Directeur de thèse |



## FOREWORD

Finally, after a long long way, I found myself writing the first and the most difficult part of this dissertation. I have started my PhD study in 2001 at Istanbul Technical University which became a cotutelle (international joint supervised) thesis in 2005 with Ecole des Mines de Paris/France as a result of a convention signed between two institutions. All of the results that will be presented in the following pages are outcomes of this cooperative study. Naturally, after all these years, there will be a heavy list to acknowledge from two countries.

First, I would like to express my deepest gratitude and appreciation to the directors of two institutions; Dr. Benoit Legait, director of Ecole des Mines de Paris and Prof. Dr. H. Faruk Karadoğan, former rector of Istanbul Technical University. Without their approval, this cooperation would not have been realized.

I will always stay indebted to Prof. Dr. Adnan Tekin who passed away unexpectedly in 2000. He was the founder of the research center where I continue my researches. I am always proud of working with him before and during the installation of the center in 1999. With his great vision, enthusiasm and leader characteristics, he will be my role model during whole my research life.

I am deeply grateful to Jean-Pierre Trottier, former director of the Centre des Matériaux P.M. Fourt, Ecole des Mines de Paris, for his interest in my cooperation request and for making possible the realization of this cotutelle thesis. I am also grateful to Daniel Broussaud, Conseiller Scientifique of the Centre des Matériaux, as being my first contact at Ecole des Mines de Paris.

I wish to express my sincere thanks to Prof. Dr. Okan Addemir, not only for being my thesis supervisor but also for everything in the past more than 10 years that we have worked together.

I would like to express my deepest thanks to Michel Jeandin, for having made feasible this joint thesis, by accepting to supervise French side of the study and for all his efforts and patience, as well as for valuable discussions and advices.

I wish to express my sincere gratitude to all the members of the jury for accepting to devote their valuable time to evaluate my thesis study. Especially French members of the jury, Caroline Richard, Sid Labdi and Michel Jeandin, for having traveled from France to Turkey for the viva. Prof. Dr. E. Sabri Kayalı, for accepting to be the chairman of the jury. Dr. Caroline Richard and Prof. Dr. Ali Aslan Kaya for their careful investigation of the dissertation as “rapporteur”.

I would like to thank Prof. Dr. Onuralp Yücel, current director of Prof. Dr. Adnan Tekin Applied Research Center of Materials Science, for not only being participated to the jury but also, for his understanding during my PhD study and the warm

working environment. Equally, I express my gratitude to Prof. Esteban Busso, current director of Centre des Matériaux for the high quality international research environment he created.

I wish to express special thanks to Marie-Hélène Berger, for her great skills on Transmission electron microscopy and for all the observations, we did together.

I also want to acknowledge Olek Maciejak, Pascal Aubert, and especially Sid Labdi from Laboratoire d'Etudes des Milieux Nanométriques, Université d'Evry Val-d'Essone, for their cooperation in nanomechanical characterization as well as for RF sputtering of boron carbide thin films.

I wish to express my sincere thanks to Assoc. Prof. Dr. Gültekin Göller for letting me use his facilities, especially high-resolution SEM and FTIR. I am also grateful to Hüseyin Sezer for SEM observations, for his competence and help during all the study. I would also like to thank Hasan Dinçer, especially for EPMA analyses but also for his constant help for years. I wish to thank Nicole De Dave-Fabrègue for SEM observations on the wear tracks and for her assistance in “pin-on-disc” tests.

Special thanks to my colleagues, lab and office mates in two countries, Dr. Şeref Sönmez, especially for his expertise in thesis format, M. Erkin Cura, François Borit, Dimitris Christoulis, Mélissa Delqué, Sophie Barradas, Serge Guetta, Nicolas Revuz, and Melis Aslan, for all their help, support and friendship.

I am grateful to BMBT Inc. for industrially producing boron carbide powders and hot pressing of the target used in this study for the first time in Turkey and Hat Teknik Inc. for careful substrate preparations.

Financial supports of French Embassy in Turkey and TUBITAK during my visits to France are much appreciated.

I would like to express special thanks to my family, my father Taylan Tavşanoğlu especially for his financial support at critical times, my mother Buket Alsaman and my brother Tuna Tavşanoğlu for their moral motivation throughout the study.

Finally, I would like to express my deepest love to my wife, Şeyda Ürgen Tavşanoğlu. Nothing would be possible without her constant support and her true confidence against me in any circumstances.

January 2009

Tolga TAVŞANOĞLU

## TABLE OF CONTENTS

|   | <u>Page</u> |
|---|-------------|
| <b>FOREWORD</b> .....   | iii         |
| <b>TABLE OF CONTENTS</b> .....                                  | v           |
| <b>ABBREVIATIONS</b> .....                                      | ix          |
| <b>LIST OF TABLES</b> .....                                     | xi          |
| <b>LIST OF FIGURES</b> .....                                    | xiii        |
| <b>LIST OF SYMBOLS</b> .....                                    | xix         |
| <b>SUMMARY</b> .....  | xxi         |
| <b>RÉSUMÉ</b> .....   | xxiii       |
| <b>ÖZET</b> .....   | xxv         |
| <b>1. INTRODUCTION</b> .....                                    | <b>3</b>    |
| <b>1.1 Résumé du Chapitre</b> .....                             | <b>6</b>    |
| <b>2. THEORETICAL BACKGROUND</b> .....                          | <b>9</b>    |
| <b>2.1 Sputtering Phenomena</b> .....                           | <b>9</b>    |
| 2.1.1 An historical overview .....                              | 9           |
| 2.1.2 Sputtering theory .....                                   | 17          |
| 2.1.3 Sputtering mechanisms .....                               | 18          |
| 2.1.4 Sputtering rate .....                                     | 22          |
| 2.1.5 The nature of sputtered species .....                     | 24          |
| 2.1.6 Energy and direction of sputtered atoms.....              | 26          |
| <b>2.2 Sputtering Configurations</b> .....                      | <b>27</b>   |
| 2.2.1 Planar diode and DC glow discharge configuration .....    | 28          |
| 2.2.2 Magnetron sputtering .....                                | 29          |
| 2.2.3 RF sputtering.....  | 31          |
| 2.2.4 Bias sputtering – ion plating .....                       | 32          |
| 2.2.5 Reactive Sputtering .....                                 | 34          |
| <b>2.3 Film Growth and Microstructural Evolution</b> .....      | <b>35</b>   |
| 2.3.1 Nucleation mechanisms in thin film growth .....           | 36          |
| 2.3.2 Microstructure evolution and structure-zone diagrams..... | 38          |
| 2.3.3 Ion bombardment effects during film growth .....          | 44          |
| <b>2.4 Boron Carbide Thin Films</b> .....                       | <b>49</b>   |
| 2.4.1 Phase diagram and structure.....                          | 52          |
| 2.4.2 Sputtering yield of boron carbide.....                    | 56          |
| 2.4.3 Mechanical properties .....                               | 57          |
| 2.4.4 Wear properties .....                                     | 60          |
| 2.4.5 Microstructure .....                                      | 65          |
| 2.4.6 Electrical properties .....                               | 65          |
| <b>2.5 Boron Carbonitride (BCN) Thin Films</b> .....            | <b>66</b>   |
| <b>2.6 Functionally Graded Thin Films</b> .....                 | <b>70</b>   |
| <b>2.7 Résumé du Chapitre</b> .....                             | <b>72</b>   |

|            |  |            |
|------------|--|------------|
| <b>3.</b>  | <b>EXPERIMENTAL STUDIES .....</b>                                  | <b>77</b>  |
| <b>3.1</b> | <b>Film Deposition.....</b>  | <b>77</b>  |
| 3.1.1      | Sputtering systems .....   | 77         |
| 3.1.1.1    | Plasma enhanced DC magnetron sputtering system .....               | 77         |
| 3.1.1.2    | RF sputtering system.....  | 80         |
| 3.1.2      | Substrates .....   | 80         |
| 3.1.3      | Target material .....  | 80         |
| 3.1.3.1    | Boron carbide powder production.....                               | 81         |
| 3.1.3.2    | Hot pressing of boron carbide powders .....                        | 82         |
| 3.1.4      | Processes parameters for thin films.....                           | 84         |
| 3.1.4.1    | Conventional DC magnetron sputtered B <sub>4</sub> C films.....    | 84         |
| 3.1.4.2    | Plasma-enhanced DC magnetron sputtered B <sub>4</sub> C films..... | 85         |
| 3.1.4.3    | RF sputtered B <sub>4</sub> C films .....                          | 85         |
| 3.1.4.4    | BCN films .....  | 86         |
| 3.1.4.5    | Functionally graded films .....                                    | 86         |
| <b>3.2</b> | <b>Characterization Techniques .....</b>                           | <b>87</b>  |
| 3.2.1      | Scanning electron microscopy .....                                 | 87         |
| 3.2.2      | Electron probe micro analysis.....                                 | 88         |
| 3.2.3      | Transmission electron microscopy.....                              | 89         |
| 3.2.3.1    | Sample preparation for TEM analyses.....                           | 91         |
| 3.2.4      | Secondary ion mass spectrometry.....                               | 93         |
| 3.2.5      | Nanoindentation .....  | 95         |
| 3.2.6      | FTIR technique .....   | 100        |
| 3.2.7      | Tribological studies.....  | 101        |
| 3.2.7.1    | Friction measurement.....  | 103        |
| 3.2.7.2    | Wear rate measurement.....   | 104        |
| <b>3.3</b> | <b>Résumé du Chapitre .....</b>                                    | <b>106</b> |
| <b>4.</b>  | <b>RESULTS AND DISCUSSION .....</b>                                | <b>111</b> |
| <b>4.1</b> | <b>DC Sputtered B<sub>4</sub>C Films.....</b>                      | <b>111</b> |
| 4.1.1      | Early studies and the optimization of deposition parameters.....   | 111        |
| 4.1.2      | Conventional DC magnetron sputtered B <sub>4</sub> C films.....    | 115        |
| 4.1.2.1    | Microstructural studies.....                                       | 115        |
| 4.1.2.2    | Chemical composition.....  | 118        |
| 4.1.2.3    | Nanostructural analyses .....                                      | 119        |
| 4.1.2.4    | Nanomechanical properties.....                                     | 123        |
| 4.1.2.5    | Bonding properties .....   | 126        |
| 4.1.2.6    | Tribological properties.....                                       | 126        |
| 4.1.2.7    | SIMS elemental depth profiles.....                                 | 128        |
| 4.1.3      | Plasma-enhanced DC magnetron sputtered B <sub>4</sub> C films..... | 130        |
| 4.1.3.1    | Microstructural studies.....                                       | 130        |
| 4.1.3.2    | Chemical compositions .....  | 133        |
| 4.1.3.3    | Nanomechanical properties.....                                     | 133        |
| 4.1.3.4    | Nanostructural analyses .....                                      | 141        |
| 4.1.3.5    | Bonding properties.....  | 147        |
| 4.1.3.6    | Tribological studies.....  | 148        |
| 4.1.3.7    | SIMS elemental depth profiles.....                                 | 161        |
| 4.1.4      | Conclusion .....   | 163        |

|            |  |            |
|------------|--|------------|
| <b>4.2</b> | <b>RF Sputtered B<sub>4</sub>C Thin Films</b> .....                | <b>164</b> |
| 4.2.1      | Microstructural studies.....                                       | 165        |
| 4.2.2      | Chemical compositions.....   | 166        |
| 4.2.3      | Nanomechanical properties.....                                     | 166        |
| 4.2.4      | Bonding properties.....  | 169        |
| 4.2.5      | Tribological studies.....  | 169        |
| 4.2.6      | SIMS elemental depth profiles.....                                 | 171        |
| 4.2.7      | Conclusion.....  | 172        |
| <b>4.3</b> | <b>BCN Thin Films</b> .....  | <b>173</b> |
| 4.3.1      | Microstructural studies.....                                       | 173        |
| 4.3.2      | Chemical compositions.....   | 175        |
| 4.3.3      | Nanomechanical properties.....                                     | 175        |
| 4.3.4      | Bonding properties.....  | 176        |
| 4.3.5      | Tribological studies.....  | 178        |
| 4.3.6      | SIMS elemental depth profiles.....                                 | 180        |
| 4.3.7      | Conclusion.....  | 181        |
| <b>4.4</b> | <b>Functionally Graded B<sub>4</sub>C and BCN Thin Films</b> ..... | <b>182</b> |
| 4.4.1      | Microstructural studies.....                                       | 182        |
| 4.4.2      | Elemental depth profile analyses.....                              | 185        |
| 4.4.3      | Nanomechanical properties.....                                     | 187        |
| 4.4.4      | Conclusion.....  | 187        |
| <b>4.5</b> | <b>Résumé du Chapitre</b> .....                                    | <b>188</b> |
| <b>5.</b>  | <b>GENERAL CONCLUSIONS AND RECOMMENDATIONS</b> .....               | <b>195</b> |
| 5.1        | Résumé du Chapitre.....  | 202        |
|            | <b>REFERENCES</b> .....  | <b>203</b> |
|            | <b>CURRICULUM VITAE</b> .....                                      | <b>219</b> |



## ABBREVIATIONS

|              |  |
|--------------|--|
| <b>BCN</b>   | : Boron Carbonitride                               |
| <b>FGM</b>   | : Functionally Graded Materials                    |
| <b>DLC</b>   | : Diamond Like Carbon                              |
| <b>SI</b>    | : Systèmes Internationales d'Unités                |
| <b>PVD</b>   | : Physical Vapor Deposition                        |
| <b>CVD</b>   | : Chemical Vapor Deposition                        |
| <b>DC</b>    | : Direct Current                                   |
| <b>RF</b>    | : Radio Frequency                                  |
| <b>IBED</b>  | : Ion Beam Enhanced Deposition                     |
| <b>IBAD</b>  | : Ion Beam Assisted Deposition                     |
| <b>iPVD</b>  | : Ionized Physical Vapor Deposition                |
| <b>PEMS</b>  | : Plasma Enhanced Magnetron Sputtering             |
| <b>PACVD</b> | : Plasma Assisted Chemical Vapor Deposition        |
| <b>PECVD</b> | : Plasma Enhanced Chemical Vapor Deposition        |
| <b>MSIBD</b> | : Mass Selected Ion Beam Deposition                |
| <b>PLD</b>   | : Pulsed Laser Deposition                          |
| <b>ML</b>    | : Mono Layer                                       |
| <b>3D</b>    | : Three Dimensional                                |
| <b>2D</b>    | : Two Dimensional                                  |
| <b>MC</b>    | : Monte Carlo                                      |
| <b>MD</b>    | : Molecular Dynamic/Movchan and Demchishin         |
| <b>SZM</b>   | : Structure Zone Model                             |
| <b>SEM</b>   | : Scanning Electron Microscopy                     |
| <b>TEM</b>   | : Transmission Electron Microscopy                 |
| <b>STEM</b>  | : Scanning Transmission Electron Microscopy        |
| <b>EFTEM</b> | : Energy Filtered Transmission Electron Microscopy |
| <b>EELS</b>  | : Electron Energy Loss Spectroscopy                |
| <b>FFT</b>   | : Fast Fourier Transform                           |
| <b>SE</b>    | : Secondary Electron                               |
| <b>BSE</b>   | : Back Scattered Electron                          |
| <b>FIM</b>   | : Field Ion Microscopy                             |
| <b>IR</b>    | : Infrared   |
| <b>XRD</b>   | : X-Ray Diffraction                                |
| <b>XPS</b>   | : X-Ray Photoelectron Spectroscopy                 |
| <b>EPMA</b>  | : Electron Probe Micro Analysis                    |
| <b>SIMS</b>  | : Secondary Ion Mass Spectrometry                  |
| <b>FTIR</b>  | : Fourier Transform Infrared Spectrometry          |
| <b>EDS</b>   | : Energy Dispersive X-Ray Spectrometry             |
| <b>EDX</b>   | : Energy Dispersive X-Ray Spectrometry             |
| <b>AFM</b>   | : Atomic Force Microscopy                          |
| <b>UHV</b>   | : Ultra High Vacuum                                |



## LIST OF TABLES

|   | <u>Page</u> |
|---|-------------|
| <b>Table 2.1</b> : General properties of boron carbide.....   | 50          |
| <b>Table 2.2</b> : Mechanical properties of boron carbide coatings. ....  | 58          |
| <b>Table 3.1</b> : Chemical compositions of steel substrates.....   | 80          |
| <b>Table 3.2</b> : Deposition parameters for magnetron sputtered B <sub>4</sub> C films. ....                                   | 84          |
| <b>Table 3.3</b> : Deposition parameters of plasma enhanced magnetron<br>sputtered B <sub>4</sub> C films. ....                 | 85          |
| <b>Table 3.4</b> : Deposition parameters for RF sputtered B <sub>4</sub> C films. ....  | 86          |
| <b>Table 3.5</b> : Deposition parameters for BCN thin films. ....   | 86          |
| <b>Table 3.6</b> : Deposition parameters for functionally graded films. ....  | 87          |
| <b>Table 4.1</b> : Elemental composition of the boron carbide coatings deposited<br>without auxiliary plasma. ....              | 119         |
| <b>Table 4.2</b> : Elemental composition of boron carbide coatings deposited by<br>plasma enhanced DC magnetron sputtering..... | 133         |
| <b>Table 4.3</b> : Profilometer measurement of the wear track after 25 m.....   | 150         |
| <b>Table 4.4</b> : Profilometer measurement of the wear track after 125 m.....  | 151         |
| <b>Table 4.5</b> : Profilometer measurement of the wear track after 225 m.....  | 154         |
| <b>Table 4.6</b> : Elemental composition of boron carbide coatings deposited<br>by RF sputtering.....                           | 166         |
| <b>Table 4.7</b> : Elemental composition of boron carbonitride coatings deposited<br>by reactive DC magnetron sputtering. ....  | 175         |
| <b>Table 4.8</b> : Profilometer measurement of wear track on BC67 after 300 m. ....   | 179         |



## LIST OF FIGURES

|  | <u>Page</u> |
|--|-------------|
| <b>Figure 2.1</b> : Grove’s sputtering apparatus (1852).....   | 11          |
| <b>Figure 2.2</b> : (a) Geissler tube made from uranium glass (b) Activated Geissler tube (c) Crookes tube (d) Activated Crookes tube showing different regions of a glow discharge (e) Schematic of a glow-discharge tube showing various named regions .....                           | 14          |
| <b>Figure 2.3</b> : Wright deposition apparatus based on the description given in his paper .....  | 15          |
| <b>Figure 2.4</b> : T. A. Edison’s sputtering apparatus .....  | 16          |
| <b>Figure 2.5</b> : Schematic representation of diode sputtering assembly .....  | 17          |
| <b>Figure 2.6</b> : Synopsis of the interaction events occurring at and near the target surface during the sputtering process.....   | 18          |
| <b>Figure 2.7</b> : Computer simulation of a portion of a collision sequence initiated by a single ion-bombardment event in a solid lattice.....   | 19          |
| <b>Figure 2.8</b> : Schematic diagram showing momentum exchange processes that occur during sputtering .....   | 21          |
| <b>Figure 2.9</b> : Sputtering yield versus energy of the incident ion.....  | 23          |
| <b>Figure 2.10</b> : Variation of the sputtering yield of several materials as a function of Ar <sup>+</sup> ion energy at normal angle of incidence .....   | 23          |
| <b>Figure 2.11</b> : Schematic diagram showing variation of the sputtering yield with ion angle of incidence for constant ion energy .....   | 24          |
| <b>Figure 2.12</b> : (a) Comparison of velocity distributions of sputtered and evaporated Cu atoms (b) Energy distribution of sputtered Cu atoms at various energies .....   | 26          |
| <b>Figure 2.13</b> : Angular emission distribution for sputtered atoms .....   | 27          |
| <b>Figure 2.14</b> : Schematic representation of a planar diode sputtering system with various named regions .....   | 28          |
| <b>Figure 2.15</b> : (a) Magnet design effect on electron’s motion in a sputtering system (b) 3D graphic showing magnetic field lines for a circular magnet design behind a circular target material (c) Erosion effect of the target material due to the circular magnetron design..... | 30          |
| <b>Figure 2.16</b> : Schematic illustration of the development of a negative bias in a RF system.....  | 31          |
| <b>Figure 2.17</b> : Steps involved in the condensation of a vapor during film growth. ...   | 35          |
| <b>Figure 2.18</b> : Schematic representation of three film growth modes where $\theta$ is the overlayer coverage in monolayers (ML).....  | 36          |
| <b>Figure 2.19</b> : Schematic representation of the island density $n$ as a function of the coverage $\theta$ during three-dimensional growth .....   | 37          |
| <b>Figure 2.20</b> : Nucleation, growth and coalescence of Ag films on (111) NaCl substrates .....   | 37          |
| <b>Figure 2.21</b> : Movchan and Demchishin (MD) structure-zone diagram .....  | 39          |

|                      |   |    |
|----------------------|---|----|
| <b>Figure 2.22 :</b> | Structure-zone diagram showing schematic microstructures of films deposited by cylindrical magnetron sputtering as a function of growth temperature and Ar pressure.....                                      | 40 |
| <b>Figure 2.23 :</b> | SEM cross-sections of metallic coatings showing different microstructures (a) zone 1 (b) zone T (c) zone 2 .....  | 40 |
| <b>Figure 2.24 :</b> | Structure-zone diagram showing the effects of both bombardment and thermal induced mobility .....   | 42 |
| <b>Figure 2.25 :</b> | Monte Carlo computer simulations of amorphous films deposited with incident flux angles (a) 90° (b) 45° (c) 60° (d) 75° .....   | 42 |
| <b>Figure 2.26 :</b> | Computer simulated microstructures of Ni films during deposition at different times (t) for substrate temperatures of (a) 350 K (b) 420 K and (c) 450 K.....  | 43 |
| <b>Figure 2.27 :</b> | Molecular dynamic simulation of a collision sequence induced by a 100 eV Ar ion which hits the porous Ni film at different times (a)-(d) preventing the formation of a void .....                             | 46 |
| <b>Figure 2.28 :</b> | Molecular dynamic simulation of a collision sequence induced by 100 eV Ar ion which hits the porous Ni film at different times (a)-(d) showing the rearrangement of atoms in order to fill a closed void..... | 47 |
| <b>Figure 2.29 :</b> | Molecular dynamic simulation of microstructures obtained (a) without ion bombardment (b) with 10 eV Ar ion bombardment (c) with 75 eV Ar ion bombardment.....   | 48 |
| <b>Figure 2.30 :</b> | Boron-carbon phase diagram .....  | 52 |
| <b>Figure 2.31 :</b> | Rhombohedral unit cell of boron carbide .....   | 53 |
| <b>Figure 2.32 :</b> | Rhombohedral crystal structure of boron carbide (a) each icosahedron is bonded to six other icosahedra through direct bonds (b) three atom intericosahedral chains that connect icosahedra. ....              | 53 |
| <b>Figure 2.33 :</b> | Sputtering yield versus energy of incident Ar <sup>+</sup> ions for boron carbide.....  | 56 |
| <b>Figure 2.34 :</b> | List of hard and superhard materials and B-C-N ternary diagram.....   | 67 |
| <b>Figure 3.1 :</b>  | (a) DC Magnetron sputtering system used in this study (b) schematic of the deposition chamber. ....   | 78 |
| <b>Figure 3.2 :</b>  | Inside view of the deposition reactor (a) Conventional magnetron sputtering mode during film growth (without auxiliary plasma) (b) PEMS mode during film growth (in presence of the auxiliary plasma).....    | 79 |
| <b>Figure 3.3 :</b>  | SEM images of boron carbide powders.....  | 81 |
| <b>Figure 3.4 :</b>  | XRD spectra of boron carbide powders.....   | 82 |
| <b>Figure 3.5 :</b>  | Hot-pressed boron carbide target microstructure.....  | 82 |
| <b>Figure 3.6 :</b>  | Hot-pressed boron carbide target (a) front view of the target showing its diameter (b) section view showing the thickness of the target. ....   | 83 |
| <b>Figure 3.7 :</b>  | TECNAI F 20 ST TEM used in the study.....   | 91 |
| <b>Figure 3.8 :</b>  | Sample preparation steps of the sandwich technique for cross-sectional TEM observations. ....   | 92 |
| <b>Figure 3.9 :</b>  | Specimen prepared for cross-sectional TEM observations (a) view on the copper ring (b) demonstration of the probable analyses areas.....  | 92 |
| <b>Figure 3.10 :</b> | Cameca ims 6f secondary ion mass spectrometer used in this study.....   | 94 |

|                      |  |     |
|----------------------|--|-----|
| <b>Figure 3.11 :</b> | (a) Schematic of the Berkovich indenter (b) SEM image of the Berkovich indenter (c) Schematic indent impression .....  | 96  |
| <b>Figure 3.12 :</b> | Schematic representation of the nanoindentation process .....  | 97  |
| <b>Figure 3.13 :</b> | Schematic of a load–displacement curve .....   | 97  |
| <b>Figure 3.14 :</b> | Nanomechanical test system (a) AFM instrument (b) nanoindenter head that is placed in the place of the AFM head for nanomechanical measurements.....   | 99  |
| <b>Figure 3.15 :</b> | Schematic of FTIR spectrometry .....   | 100 |
| <b>Figure 3.16 :</b> | “pin-on-disc” tribometer. ....   | 102 |
| <b>Figure 3.17 :</b> | Schematic of the “pin-on-disc” testing principle .....   | 102 |
| <b>Figure 3.18 :</b> | Representative profile of the wear track obtained by profilometer. ....  | 104 |
| <b>Figure 4.1 :</b>  | Cross-sectional SEM micrograph of the first boron carbide film deposited in this study showing (a) the columnar microstructure of the film (b) cauliflower-like surface morphology .....   | 112 |
| <b>Figure 4.2 :</b>  | (a) Delaminated boron carbide coating on AISI M2 substrate (b) well adherent boron carbide coating on AISI 430 substrate (c) delaminated boron carbide coating on AISI 430 substrate (d) well adherent boron carbide coating on AISI 430 substrate. .... | 114 |
| <b>Figure 4.3 :</b>  | Cross-sectional SEM observation of the specimen BC47 (a) columnar structure of the B <sub>4</sub> C thin film (b) corresponding morphology on Thornton diagram (c) corresponding morphology on Messier’s SZD .....                                       | 116 |
| <b>Figure 4.4 :</b>  | Cross-sectional SEM image of the specimen BC48 .....   | 117 |
| <b>Figure 4.5 :</b>  | Cross-sectional SEM observation of the specimen BC49 .....   | 118 |
| <b>Figure 4.6 :</b>  | Cross-sectional TEM observations of the specimen BC47 (a) general view of the columnar structure (b) column boundaries in detail (c) HRTEM observation of one single column and Fast Fourier Transform (FFT) diffraction pattern.....                    | 120 |
| <b>Figure 4.7 :</b>  | EFTEM analysis on the specimen BC47 (a) the area of observation (b) boron distribution in the same area.....   | 121 |
| <b>Figure 4.8 :</b>  | Elemental distribution by EFTEM analyses, (a) low-resolution TEM image of boron carbide coating indicating the observed zone (b) zero loss image of the observed zone (b) boron distribution (c) oxygen distribution (d) carbon distribution .....       | 122 |
| <b>Figure 4.9 :</b>  | Load-displacement curves for BC47 on Si and AISI 430 substrates. ....  | 123 |
| <b>Figure 4.10 :</b> | (a) Hardness vs. indentation depth diagram of the specimen BC 47 (b) Young’s modulus vs. indentation depth diagram of the same specimen. ....  | 124 |
| <b>Figure 4.11 :</b> | The effect of the bias voltage on the nanomechanical properties of B <sub>4</sub> C films deposited without auxiliary plasma configuration.....  | 125 |
| <b>Figure 4.12 :</b> | Representative FTIR spectra of boron carbide films deposited by conventional DC magnetron sputtering .....   | 126 |
| <b>Figure 4.13 :</b> | Representative friction coefficient vs. distance diagram of conventional DC magnetron sputtered B <sub>4</sub> C thin film against alumina ball.....   | 127 |
| <b>Figure 4.14 :</b> | Representative wear track measurement of B <sub>4</sub> C coating against Al <sub>2</sub> O <sub>3</sub> pin. ....   | 128 |
| <b>Figure 4.15 :</b> | SIMS elemental depth profile of boron carbide coatings deposited by conventional DC magnetron sputtering. ....   | 129 |

|  |     |
|--|-----|
| <b>Figure 4.16 :</b> Cross-sectional micrograph of the specimens (a) BC92 and (b) BC87.....  | 131 |
| <b>Figure 4.17 :</b> Cross-sectional SEM observations of the same coating BC90 on three different substrates (a) AISI 430 (b) AISI M2 (c) Si (100).....  | 132 |
| <b>Figure 4.18 :</b> Load-displacement curves for BC87 on AISI M2 and AISI 430 substrates.....   | 134 |
| <b>Figure 4.19 :</b> Hardness and Young's modulus vs. load and corresponding indentation depths curves of (a) BC87 on AISI M2 (b) BC87 on AISI 430 substrates.....   | 135 |
| <b>Figure 4.20 :</b> Hardness and Young's modulus versus load and indentation depth curves of BC86 (a) on AISI M2 (b) on Si (100).....   | 137 |
| <b>Figure 4.21 :</b> The effect of bias voltages and temperatures on the (a) hardness and (b) Young's modulus of the B <sub>4</sub> C thin films deposited by plasma-enhanced DC magnetron sputtering..... | 138 |
| <b>Figure 4.22 :</b> Load-displacement curves of (a) BC 96 (b) BC90.....   | 140 |
| <b>Figure 4.23 :</b> Representative indent profiles obtained by AFM on the specimen BC90 (a) 2D view of the indent (b) 3D visualization of the same area.....  | 141 |
| <b>Figure 4.24 :</b> Cross-sectional TEM micrographs of the specimen BC92 (a) low-magnification (b) high-resolution TEM of the selected area.....  | 142 |
| <b>Figure 4.25 :</b> High-resolution TEM observation of the specimen BC94.....   | 143 |
| <b>Figure 4.26 :</b> Cross-sectional TEM micrographs of the specimen BC90 (a) low-magnification (b) high-resolution TEM of the selected area.....  | 144 |
| <b>Figure 4.27 :</b> High resolution TEM micrograph of the specimen demonstrating the coating-substrate interface and the cristallinity of the substrate and coating with inset FFT patterns.....          | 145 |
| <b>Figure 4.28 :</b> Typical EELS spectrum taken from boron carbide coatings.....  | 146 |
| <b>Figure 4.29 :</b> FTIR spectra of boron carbide film deposited without external heating and at floating potential.....  | 147 |
| <b>Figure 4.30 :</b> FTIR spectra of the boron carbide films deposited at 250 °C with different bias voltages.....   | 148 |
| <b>Figure 4.31 :</b> Representative friction coefficient vs. distance diagram of (a) AISI M2 steel without coating against alumina ball (b) B <sub>4</sub> C coated AISI M2 against alumina ball.....      | 149 |
| <b>Figure 4.32 :</b> SEM investigation of wear track after 25 m sliding.....   | 150 |
| <b>Figure 4.33 :</b> Friction coefficient during early stage of the wear test.....   | 150 |
| <b>Figure 4.34 :</b> SEM investigation of wear track after 125 m sliding.....  | 151 |
| <b>Figure 4.35 :</b> (a) Backscattered electron image of the worn track after 125 m (b) line scan on the zone shown by the square.....   | 152 |
| <b>Figure 4.36 :</b> SIMS elemental ion imaging of the worn surfaces (a) B distribution (b) Al distribution (c) Fe distribution (d) representative SEM image of the wear track.....                        | 153 |
| <b>Figure 4.37 :</b> Friction coefficient vs. distance diagram for 125 m sliding distance.....   | 153 |
| <b>Figure 4.38 :</b> SEM investigations of the worn surfaces after 225 m.....  | 154 |
| <b>Figure 4.39 :</b> SEM investigations of the worn surfaces after 225 m.....  | 155 |

|                      |   |     |
|----------------------|---|-----|
| <b>Figure 4.40 :</b> | Friction coefficient vs. distance diagram for 225 m sliding distance.....   | 155 |
| <b>Figure 4.41 :</b> | (a) Optical observation of the debris present at the sides of the wear track (b) SEM image of same debris (c) Optical observation of the debris on the Al <sub>2</sub> O <sub>3</sub> counterface (d) SEM image of same debris..... | 156 |
| <b>Figure 4.42 :</b> | Wear track measurements of B <sub>4</sub> C coating against (a) WC (b) B <sub>4</sub> C (c) Al <sub>2</sub> O <sub>3</sub> pins.....  | 157 |
| <b>Figure 4.43 :</b> | Wear rates of boron carbide coatings deposited with different temperatures and bias voltages by plasma-enhanced DC magnetron sputtering.....  | 158 |
| <b>Figure 4.44 :</b> | Representative SEM investigations of the wear track, the magnification increases from (a) to (c) for the same wear track .....  | 159 |
| <b>Figure 4.45 :</b> | EDS line scan analysis of the wear track (a) BSE image of the analyzed area (b) boron (c) carbon (d) aluminum (e) iron and (f) oxygen elemental distributions .....   | 160 |
| <b>Figure 4.46 :</b> | Representative depth profile of boron carbide films deposited by plasma-enhanced DC magnetron sputtering by using O <sub>2</sub> <sup>+</sup> primary ion beam .....  | 162 |
| <b>Figure 4.47 :</b> | Representative depth profile of boron carbide films deposited by plasma-enhanced DC magnetron sputtering by using Cs <sup>+</sup> primary ion beam.....   | 162 |
| <b>Figure 4.48 :</b> | Cross-section SEM micrographs of (a) BC27 (b) BC28 (c) BC29 (d) BSE image of BC29.....  | 165 |
| <b>Figure 4.49 :</b> | The effect of sputtering power on the nanomechanical properties of boron carbide films deposited by RF sputtering.....  | 167 |
| <b>Figure 4.50 :</b> | Representative load-displacement curve for boron carbide coatings deposited by RF sputtering.....   | 167 |
| <b>Figure 4.51 :</b> | Representative indent profile obtained by AFM on the RF sputtered boron carbide coatings (a) 2D view of the indent (b) 3D visualization of the same area.....   | 168 |
| <b>Figure 4.52 :</b> | Representative FTIR spectra of RF sputtered boron carbide film. ..  | 169 |
| <b>Figure 4.53 :</b> | Friction coefficient evaluations of (a) BC27 (b) BC28 (c) BC29....  | 170 |
| <b>Figure 4.54 :</b> | Representative depth profile of boron carbide films deposited by RF sputtering by using O <sub>2</sub> <sup>+</sup> primary ion beam.....   | 171 |
| <b>Figure 4.55 :</b> | Cross-sectional SEM micrograph of the specimen BC67.....  | 173 |
| <b>Figure 4.56 :</b> | Cross-sectional SEM micrograph of the specimen BC68.....  | 174 |
| <b>Figure 4.57 :</b> | Cross-sectional SEM micrograph of the specimen BC69.....  | 174 |
| <b>Figure 4.58 :</b> | Hardness and modulus vs. N <sub>2</sub> in the processing gas and N incorporated in BCN films.....  | 176 |
| <b>Figure 4.59 :</b> | FTIR spectrum of BCN coatings deposited with different N <sub>2</sub> contents. ....  | 177 |
| <b>Figure 4.60 :</b> | Friction coefficient versus distance diagram of the specimen BC67. ....   | 178 |
| <b>Figure 4.61 :</b> | Wear track measurements of BCN coating after 300 m sliding. ....  | 179 |
| <b>Figure 4.62 :</b> | SIMS elemental depth profile of BCN film deposited at 5% N <sub>2</sub> in the processing gas. ....   | 180 |
| <b>Figure 4.63 :</b> | Cross-sectional SEM micrographs of (a) secondary electron image (b) back scattered image of boron carbide thin film on boronized steel substrate. ....  | 183 |

|  |     |
|--|-----|
| <b>Figure 4.64 :</b> Cross-sectional SEM micrographs of (a) secondary electron image (b) back scattered image of Ti/TiC/B <sub>4</sub> C graded film on Si substrate. .... | 184 |
| <b>Figure 4.65 :</b> Cross-section SEM micrographs of (a) secondary electron image (b) back scattered image of Ti/TiN/BCN graded film on Si substrate. ....                | 185 |
| <b>Figure 4.66 :</b> SIMS depth profiles of (a) Ti/TiC/B <sub>4</sub> C (b) Ti/TiN/BCN (c) Boride layer/B <sub>4</sub> C functionally graded structures.....               | 186 |
| <b>Figure 4.67 :</b> Hardness, Young's modulus and elemental compositions of the substrates and layers .....   | 187 |

## LIST OF SYMBOLS

|                     |   |
|---------------------|---|
| $M_i$               | : Mass of incident particle                                   |
| $M_t$               | : Mass of target particle                                     |
| $V_i$               | : Velocity of incident particle                               |
| $\epsilon$          | : Energy transfer coefficient/Indenter geometry constant      |
| $S$                 | : Sputtering yield  |
| $E$                 | : Kinetic energy  |
| $U$                 | : Heat of sublimation   |
| $U_{sb}$            | : Surface binding energy                                      |
| $f$                 | : Fraction of initial kinetic energy                          |
| $\Delta N/\Delta E$ | : Differential flux of sputtered particles                    |
| $B$                 | : Bulk modulus  |
| $N_c$               | : Average coordination number                                 |
| $d$                 | : Bond length/Density   |
| $\lambda$           | : Ionicity of chemical bonds                                  |
| $d_L$               | : Density of the liquid                                       |
| $W_A$               | : Weight of the material                                      |
| $W_B$               | : Apparent immersed weight in liquid                          |
| $P$                 | : Indentation load  |
| $P_{max}$           | : Peak load   |
| $h$                 | : Elastic displacement of the indenter                        |
| $h_{max}$           | : Depth at peak load  |
| $h_f$               | : Final depth of contact impression after unloading           |
| $h_c$               | : Contact depth   |
| $A$                 | : Projected contact area of the hardness impression/Wear area |
| $S$                 | : Stiffness   |
| $\beta$             | : Indenter constant ( $\beta=1.034$ for the Berkovich)        |
| $H$                 | : Hardness  |
| $E$                 | : Young's modulus   |
| $E_i$               | : Young's modulus of the Berkovich indenter                   |
| $E_r$               | : Indentation or reduced modulus                              |
| $\nu$               | : Poisson's ratio   |
| $\nu_i$             | : Poisson's ratio of the indenter                             |
| $\mu$               | : Friction coefficient  |
| $F$                 | : Tangential force  |
| $N$                 | : Applied load  |
| $k$                 | : Wear rate   |
| $V$                 | : Volume loss   |
| $l$                 | : Sliding distance  |
| $r$                 | : Wear track diameter   |
| $n$                 | : Sliding tour number   |



# **DEPOSITION AND CHARACTERIZATION OF SINGLE AND MULTILAYERED BORON CARBIDE AND BORON CARBONITRIDE THIN FILMS BY DIFFERENT SPUTTERING CONFIGURATIONS**

## **SUMMARY**

Over the last 30 years there has been a great deal of interest in the research of hard and wear resistant coatings. There exist ceramic thin films for industrial applications such as cutting tools, automobile and machine part including TiN, TiAlN, TiC, SiC, WC and diamond-like carbon (DLC) as examples. However, increasing technological and industrial demands request thin films with more complicated properties. For this purpose, B-C-N ternary system with its superhard phases is of great interest during last ten years. Boron carbide ( $B_4C$ ) with its high hardness and modulus besides other relevant properties is one of the most prominent candidates. Furthermore, boron carbonitride (BCN) thin films are attracting due to the combination of different properties as a result of that of different phases such as diamond, cubic boron nitride (c-BN) and hexagonal boron nitride (h-BN). A thorough literature study shows that these two materials have not been yet investigated in details in thin film form. Boron carbide is one of the least studied materials by atomistic deposition techniques such as sputtering and the least studied compound in the B-C-N ternary diagram. On the other hand, almost all the efforts were given by different researchers to deposit cubic boron nitride. Very limited studies could be found focusing on the effect of nitrogen incorporation into boron carbide structure and on the different phases that could be obtained.

The aim of this thesis study is first to investigate the effect of different sputter deposition parameters on the properties of boron carbide thin films and to establish a relation between deposition parameters, growth morphologies of boron carbide films and mechanical and wear properties. Second, to study the effect of nitrogen incorporation into boron carbide structure and to grow optimized hard and tough BCN thin films with an improved wear resistance.

In this work, single and multilayered boron carbide and boron carbonitride thin films were deposited by several sputtering configurations. Three types of well adherent and homogenous boron carbide films were deposited by conventional direct current (DC) magnetron sputtering, plasma-enhanced DC magnetron sputtering, and radio frequency (RF) sputtering. Boron carbonitride thin films deposited by reactive DC magnetron sputtering with addition of nitrogen to the processing gas were also studied. Functionally-graded multilayered designs were used to grow thicker boron carbide and boron carbonitride films. An “in-house” produced, direct current compatible, hot-pressed boron carbide target and a commercial boron carbide target were used for the deposition of thin films. The effect of deposition parameters on film properties were studied by using various characterization techniques. Elemental composition of the films was measured by electron probe microanalysis (EPMA). Field-emission gun scanning electron microscope (FE-SEM) was used to investigate

the microstructure and the morphology of the films. Elemental depth profiles of the coatings were obtained using a secondary ion mass spectrometer (SIMS). Nanomechanical properties were determined by nanoindentation. Tribological properties of the coatings were studied using “pin-on-disc” testing. Chemical bonding was investigated by Fourier transform infrared spectroscopy (FTIR). Nanostructure and crystallinity of the films were evaluated by transmission electron microscopy (TEM) observations.

Results demonstrated that boron carbide films are promising candidates for wear resistance and hardness related applications. With a controlled change of process parameters, different microstructures, thus films with different properties were obtained. With N incorporation into boron carbide structure, optimized hard and better wear-resistant films were achieved. This showed that application ranges may be further expanded. Additionally, it was found that functionally-graded multilayered approach is an adequate solution to prevent film delamination and intrinsic stress related problems of hard and wear-resistant films. Thicker boron carbide and boron carbonitride films for several industrial applications could therefore be deposited easily with a proper design for the different underlayers.

**Keywords:** Boron carbide, BCN, thin films, sputtering, ion plating, nanomechanics, SIMS depth profile, microstructure, nanostructure, tribology

# **ELABORATION PAR DIFFERENTS PROCEDES DE PULVERISATION ET CARACTERISATION DE MONO ET MULTI-COUCHES MINCES DE CARBURE DE BORE ET DE CARBONITRURE DE BORE**

## **RÉSUMÉ**

Au cours des 30 dernières années l'intérêt fut très marqué pour la recherche dans le domaine des couches minces dures et résistant à l'usure. Des matériaux ont été développés sous forme de couches minces céramiques pour des applications industrielles telles que des outils de coupe, des pièces d'automobile et différents composants de machine. Les matériaux en jeu étaient, TiN, TiAlN, TiC, SiC, WC et carbone adamantin (DLC) par exemple. Cependant, les besoins technologiques et industriels d'aujourd'hui nécessitent l'utilisation des couches minces avec des propriétés plus évoluées. Pour cela, le système ternaire de B-C-N avec ses phases ultra-dures a attiré beaucoup l'attention ces dernières années. Le carbure de bore ( $B_4C$ ) en particulier, avec sa haute dureté et son module d'Young élevé en plus de ses autres propriétés intéressantes, est l'un des matériaux les plus prometteurs. Une autre possibilité repose sur le carbonitride de bore (BCN) qui présente des propriétés différentes en raison de la combinaison possible de plusieurs phases telles que le diamant, la nitrure de bore cubique (c-BN) et la nitrure de bore hexagonale (h-BN). Une recherche bibliographique détaillée indique le fait que ces deux matériaux n'ont pas été suffisamment étudiés quand sous forme de couches minces. Le carbure de bore est l'un des matériaux les moins étudiés dans le cas de techniques de dépôt en phase vapeur telles que la pulvérisation cathodique. C'est également le composé le moins étudié dans le diagramme ternaire B-C-N. D'autre part, dans la bibliographie, presque tout l'effort a porté sur le dépôt du nitrure de bore cubique. Il existe très peu d'études centrées sur l'effet de l'incorporation d'azote dans la structure de carbure de bore et les différentes phases qui pourraient être obtenues.

Le but de ce travail est d'étudier, en premier, l'effet de différents paramètres de pulvérisation sur les propriétés des couches minces de carbure de bore et d'établir des relations entre les paramètres de dépôt, croissance des couches de carbure de bore et propriétés mécaniques et d'usure-frottement. Le deuxième objectif est d'étudier l'effet de l'incorporation d'azote dans la structure de carbure de bore pour établir une couche de carbonitride de bore avec une dureté et une ténacité optimales ainsi qu'une résistance à l'usure élevée.

Trois types de couches de carbure de bore bien adhérentes et homogènes ont été déposées par pulvérisation cathodique magnétron classique à courant continu (DC), pulvérisation cathodique magnétron DC assisté par plasma et pulvérisation cathodique radiofréquence (RF). Les couches minces de carbonitride de bore déposées par pulvérisation cathodique magnétron à courant continu en mode réactif avec addition d'azote dans la composition du gaz plasmagène ont été également étudiées. La conception de multicouches fonctionnelles a permis de déposer des couches de carbure et carbonitride de bore plus épaisses et adhérentes. Une cible de

carbure de bore conductrice, produite par pressage à chaud de poudres de carbure de bore et une cible de carbure de bore commerciale ont été utilisées pour les dépôts par décharge à courant continu et RF respectivement. L'effet des paramètres de dépôt sur les différentes propriétés des couches a été évalué par plusieurs techniques de caractérisation. La composition élémentaire des dépôts a été déterminée par microsonde électronique de Castaing (EPMA). La microscopie à balayage électronique haute résolution avec un canon à émission de champ (FE-SEM) a servi à examiner la microstructure et la topographie des couches. Les profils de profondeur élémentaires des dépôts ont été obtenus par spectrométrie de masse d'ions secondaires (SIMS). Les propriétés nanomécaniques ont mesurées par nanoindentation. Le comportement tribologique des dépôts a été étudié en utilisant un tribomètre « pion-disque ». Les liaisons chimiques ont été identifiées par la spectroscopie infrarouge à transformée de Fourier (FTIR). La nanostructure et la cristallinité des couches ont été caractérisées grâce à des observations par microscopie électronique en transmission (TEM).

Les résultats ont démontré que les couches de carbure de bore constituent de bons revêtements à dureté élevée pour résister à l'usure. Grâce au contrôle des paramètres de pulvérisation, différentes microstructures correspondants à différentes propriétés ont pu être obtenues. Grâce à l'incorporation de l'azote dans la structure de carbure de bore, des couches présentant une dureté optimale et une résistance à l'usure élevée ont été développées, donnant ainsi la possibilité d'élargir la gamme d'applications pour ces dépôts. On a aussi constaté que la conception en multicouche fonctionnelle était une façon d'empêcher le décollement des couches et éviter des problèmes liés aux contraintes résiduelles pour les dépôts durs et résistants à l'usure. Des couches plus épaisses de carbure de bore et de carbonitride de bore pour plusieurs applications industrielles, peuvent donc efficacement être déposées grâce à une conception appropriée des différentes sous-couches.

**Mots-clés:** Carbure de bore, BCN, couches minces, pulvérisation cathodique, dépôt ionique, nanomécanique, SIMS, microstructure, nanostructure, tribologie

## TEK VE ÇOK KATMANLI BOR KARBÜR VE BOR KARBONİTRÜR İNCE FİLMLEİN FARKLI SIÇRATMA TEKNİKLERİYLE BİRİKTİRİLMESİ VE KARAKTERİZASYONU

### ÖZET

Son 30 yılda sert ve aşınmaya dayanıklı kaplama çalışmalarında önemli bir artış görülmektedir. Endüstriyel uygulamalara yönelik özellikle, otomotiv endüstrisinde kullanılan çeşitli parçalar, takım uçları ve makine parçaları gibi uygulamalarda kullanılan ve detaylı olarak çalışılmış seramik ince filmlere, TiN, TiAlN, TiC, SiC, WC ve elmas benzeri karbon (DLC) örnek olarak verilebilir. Ancak, son yıllarda gelişen teknolojik ve endüstriyel uygulamalar birden fazla özelliği bir arada barındıran ince film türlerini gerektirmektedir. Bu sebeple bünyesinde bulundurduğu çok sert fazlar göz önüne alındığında B-C-N üçlü sistemi son on yılda ilgi çekici hale gelmiştir. Özellikle bor karbür ince filmler yüksek sertlikleri ve elastik modülleri ile en önemli adaylardan biri olarak ortaya çıkmaktadır. Bir diğer alternatif yapısında bulundurduğu farklı fazlarla birçok özelliği bünyesinde toplayan bor karbonitrür ince filmlerdir. Geniş kapsamlı bir literatür çalışması, bu iki tip malzemenin ince film formunda detaylı olarak çalışılmadığını göz önüne sermiştir. Bor karbür, sıçratma gibi atomal düzeyde biriktirmenin gerçekleştirildiği ince film kaplama yöntemleri ile en az çalışılmış malzemelerden biridir. Aynı zamanda B-C-N üçlü sistemi içerisinde en az çalışılmış olan bileşiktir. Öte yandan, literatürde B-C-N sistemi içerisinde en fazla çalışmanın kübik bor nitrür biriktirmek amacıyla gerçekleştirildiği görülmektedir. Bor karbür yapısına azot ilavesi ve sonucunda oluşabilecek fazlar ve özellikleri üzerine gerçekleştirilmiş çok sınırlı sayıda çalışma bulunmaktadır.

Bu çalışmanın amacı, ilk olarak, biriktirme parametrelerinin elde edilen bor karbür kaplamaların özelliklerine olan etkilerini incelemek ve biriktirme şartları, bor karbür ince filmlerin büyüme morfolojileri ile mekanik ve aşınma özellikleri arasında bir ilişki kurmaktır. İkinci olarak ise, bor karbür yapısına azot ilavesinin etkilerini incelemek ve optimum sertlik ve tokluğa sahip aşınma dirençleri daha yüksek bor karbonitrür ince filmler elde etmektir.

Bu çalışmada, farklı sıçratma teknikleriyle biriktirilmiş tek ve çok katmanlı bor karbür ve bor karbonitrür ince filmler incelenmiştir. Homojen ve taban malzemeye iyi yapışan bor karbür kaplamalar, sırasıyla, konvansiyonel doğru akım manyetik alanda sıçratma, plazma destekli doğru akım (DC) manyetik alanda sıçratma ve radyo frekans (RF) sıçratma teknikleriyle üretilmiştir. Proses gazına azot ilavesiyle, gerçekleştirilen reaktif doğru akım manyetik alanda sıçratma tekniğiyle bor karbonitrür ince filmler kaplanmıştır. Kalın bor karbür ve bor karbonitrür kaplamalar elde etmek için fonksiyonel gradyanlı çok katmanlı sistemler biriktirilmiş ve sonuçlar tartışılmıştır.

Bor karbür, bor karbonitrür ve fonksiyonel gradyanlı kaplamaların biriktirilmesinde, bu çalışma bünyesinde bor karbür tozlarının sıcak preslenmesiyle elde edilmiş, bor karbür hedef malzeme kullanılmıştır. Ticari kalitede bir bor karbür hedef malzeme radyo frekans sıçratma tekniğiyle biriktirilen bor karbür ince filmlerin üretiminde kullanılmıştır. Biriktirme parametrelerinin kaplama özelliklerine etkileri çeşitli karakterizasyon tekniklerinden faydalanılarak ortaya konulmuştur. Biriktirilen filmlerin elementel bileşimleri elektron prob mikro analizörü (EPMA) kullanılarak tespit edilmiştir. Filmlerin mikroyapı ve yüzey morfolojileri field-emission taramalı elektron mikroskobu (FE-SEM) kullanılarak incelenmiştir. Elementel derinlik profilleri ikincil iyon kütle spektrometresi (SIMS) kullanılarak çıkartılmıştır. Kaplamaların tribolojik özellikleri disk üzerinde pin testi kullanılarak tespit edilmiştir. Kimyasal bağ yapılarının özellikleri Fourier kızılötesi spektroskopisi (FTIR) kullanılarak incelenmiştir. Filmlerin nanoyapıları ve kristal yapı özellikleri geçirimli elektron mikroskobu (TEM) çalışmaları ile ortaya konmuştur.

Çalışma neticesinde elde edilen sonuçlara dayanarak, bor karbür ince filmlerin sertlik ve aşınma direnci gerektiren uygulamalar için önemli bir alternatif olduğu düşünülmektedir. Üretim parametrelerinin değiştirilmesi ile farklı mikroyapılarda, dolayısıyla farklı özelliklere sahip bor karbür kaplamalar elde edilmiştir. Yapıya azot ilavesi ile optimum sertlik ve daha iyi aşınma dirençlerine sahip kaplamalar elde edilmiş ve söz konusu kaplamaların uygulama alanlarının daha da genişletilebileceği ortaya konmuştur. Fonksiyonel gradyanlı çok katmanlı kaplama tasarımlarının, içsel gerilmelerden kaynaklanan problemleri ve film yapışması gibi özellikle sert ve aşınmaya dayanıklı filmlerde çok karşılaşılan sorunları ortadan kaldırmakta kullanılabileceği tespit edilmiştir. Elde edilen sonuçlara göre, çeşitli endüstriyel uygulamalara yönelik, kalın bor karbür ve bor karbonitrür kaplamalar, uygun alt katmanların seçimiyle başarıyla biriktirilebilir.

**Anahtar kelimeler:** Bor karbür, BCN, ince film, sıçratma, iyon destekli kaplama, nanomekanik, SIMS derinlik profili, mikroyapı, nanoyapı, triboloji

---

# **CHAPTER 1: INTRODUCTION**

---



## 1. INTRODUCTION

“God made the bulk; the surface was invented by the devil”, an aphorism quoted from the eminent physicist Wolfgang Pauli describes well the importance of the materials surface properties. He explained the diabolical characteristic of surfaces by a simple fact that a solid surface shares its border with the external world, while inside the solid; each atom is surrounded by other similar atoms. Therefore, surface properties of a solid are quite different from that of the bulk material.

Humankind has tried to change the surface properties of the materials since antique ages. For example, gold beating and leafing to microscopically thinner form dates back to ancient Egypt and had used for protection and decorative purposes. An axe dating back to 900 B.C., possessing a Brinell hardness value of 444 at the edge, demonstrates that it had been carburized, which is a still used technique to increase surface hardness of materials.

Today, surface coatings are used in the entire cross-section of applications ranging from microelectronics, display devices, corrosion, tribology and wear-resistance including cutting tools and different machine parts, high temperature oxidation, solar cells, thermal insulation and decorative coatings to improve the performance, extending the life, and enhancing the appearance of materials. First observations on thin film deposition dates back more than 150 years, but has advanced drastically during the past 30 years as a result of the technological achievements in deposition systems, plasma based techniques and atomistic deposition processes.

A large variety of materials is used to produce these coatings. They are metals, alloys, refractory compounds (e.g., oxides, nitrides, and carbides), intermetallic compounds and polymers in single or multiple layers. The thickness of the coatings ranges from a few atom layers to millions of atom layers.

Hard and wear resistant coatings constitute an important part of surface engineering applications and thin film researches. There are well-studied ceramic thin films for

industrial applications especially for cutting tools and other wear-resistance applications including TiN, TiAlN, TiC, SiC, WC, and DLC as examples. However, increasing technological and industrial demands request thin films with more complicated properties. For this purpose, B-C-N ternary system with its superhard phases is of great interest during last ten years. Especially boron carbide ( $B_4C$ ) with its high hardness and modulus besides other relevant properties is one of the most prominent candidates for wear resistance applications. Furthermore, boron carbonitride (BCN) thin films are attracting from the wear resistance point of view, due to the combination of different properties as a result of that of different phases such as ultra-hard diamond and cubic boron nitride (c-BN), as well as hexagonal boron nitride (h-BN).

A thorough literature study shows that these two materials have not been yet investigated in details in the thin film form. First, there are very limited researches on boron carbide, which is a well-known man made technological ceramics with very large technological interest and application areas in bulk form. It is one of the least studied materials by atomistic deposition techniques such as sputtering and also the least studied compound in the B-C-N ternary diagram. Especially the effect of deposition parameters on film growth morphologies, on the micro and nanostructure of the coatings and consequently on different properties such as wear resistance, mechanical, optical and electronical properties have not been well established. On the other hand, almost all the efforts were given by different researchers to deposit cubic boron nitride. Very limited studies could be found focusing on the effect of nitrogen incorporation into boron carbide structure and on the different phases that could be obtained.

Historically, sputtering is one of the oldest thin film deposition techniques and it occupies an important place between different physical vapor deposition (PVD) methods. In addition to its several advantages such as, high deposition rates, low temperature deposition, improved adhesion; with sensitive control of deposition parameters and different possible configurations, thin films with controlled microstructures thus well controlled properties can be obtained by sputtering.

The aim of this study is to investigate at first, the effect of different sputter deposition parameters on the properties of boron carbide thin films and to establish a

relation between the deposition parameters, growth of boron carbide films and mechanical and wear properties. At the second, to study the effect of nitrogen incorporation into boron carbide structure and to establish optimum hard and lubricant boron carbonitride thin films.

The dissertation is organized in the following way; first, a theoretical background on the deposition techniques and thin film system will be given in Chapter 2. In Chapter 3, experimental details, the system used for the deposition of thin films including the deposition parameters, the properties of the target and substrate materials used in this study will be discussed followed by the presentation of the various characterization techniques used to elucidate different properties of thin films deposited. All the results obtained from different characterization techniques will be presented and discussed in Chapter 4. The dissertation will be closed with general conclusions and recommendations given in Chapter 5.

## 1.1 Résumé du Chapitre

Les premières observations sur les couches minces remontent plus de 150 ans, mais l'utilisation et les applications se sont multipliées pendant les 30 dernières années en raison des avancées technologiques dans des systèmes de dépôt. Aujourd'hui, les couches minces ont des domaines d'applications très variés telle que la microélectronique, la corrosion, la résistance à l'usure avec les outils de coupe et différentes pièces de machine, l'oxydation à hautes températures, les piles solaires, l'isolation thermique et les couches décoratives.

Les couches minces sont fréquemment utilisées pour améliorer les performances, prolonger la durée de vie, et améliorer l'aspect des matériaux. Parmi ces applications, les couches dures et résistantes à l'usure constituent une part importante d'un point de vue technologique, industriel et de recherche. Il existe des matériaux bien étudiés sous forme de couches minces céramique pour des applications industrielles telles que des outils de coupe, des pièces d'automobile et différentes pièces de machine, comprenant TiN, TiAlN, TiC, SiC, WC et DLC (Diamond like carbon – carbone adamantine) comme exemples. Cependant, les besoins technologiques et industriels d'aujourd'hui nécessitent l'utilisation de couches minces avec des propriétés plus évaluées. Pour cela, le système ternaire de B-C-N avec ses phases ultra dures a retenu beaucoup l'attention pendant ces dernières années. Particulièrement le carbure de bore ( $B_4C$ ), avec sa haute dureté et son module d'Young élevé en plus d'autres propriétés intéressantes, est l'un des matériaux les plus prometteurs. Une autre solution envisageable est le carbonitride de bore (BCN) qui combine différentes propriétés en raison de la combinaison possible de plusieurs phases telles que le diamant, le nitrure de bore cubique (c-BN) et le nitrure de bore hexagonal (h-BN).

Le but de ce travail est d'étudier, en premier lieu, l'effet de différents paramètres de pulvérisation sur les propriétés des couches minces de carbure de bore et d'établir une relation entre les paramètres de dépôt, la croissance des couches de carbure de bore et les propriétés mécaniques dont principalement la résistance à l'usure. Le 2<sup>ème</sup> objectif est d'étudier l'effet de l'incorporation d'azote dans la structure de carbure de bore pour établir une couche de carbonitride de bore à dureté et ténacité optimales combinées à une résistance à l'usure élevée.

---

**CHAPTER 2:**  
**THEORETICAL**  
**BACKGROUND**

---



## **2. THEORETICAL BACKGROUND**

In this chapter, the basis of the deposition techniques and thin film system investigated in this study will be given. The chapter will be started with sputtering phenomena, with an overview of the historical aspects, followed by detailed basics of the technique, different sputtering configurations used in this study and will be concluded with the nucleation and growth mechanisms of atomistically deposited thin films.

In the second part, a literature survey on boron carbide, its structural, mechanical, chemical, electrical, and tribological properties, and its application areas will be presented. N incorporation into boron carbide structure, B-C-N ternary system will also be discussed in a separate section. Finally, the concept of multilayered functionally graded design and its usage in thin film applications will be given.

### **2.1 Sputtering Phenomena**

Historically, sputtering is one of the oldest thin film deposition techniques. Today, it is the most widely used technique in industry and academia to deposit thin films in a very large spectrum and for many purposes. It is generally believed that sputtering is the simplest thin film deposition technique from both operational and theoretical point of view, which is relatively and/or partially true. However, it is ironically the most incompletely and incorrectly known thin film deposition technique. Therefore, a detailed explanation of the technique, starting from historical timeline, including the mechanism and different configurations is a prerequisite to interpret clearly the results obtained during this study.

#### **2.1.1 An historical overview**

If a surface is subjected to bombardment by energetic ions, it is eroded and surface atoms are ejected. This phenomenon is named "Sputtering" in English, "Sıçratma" in

Turkish, "Pulvérisation (Cathodique)" in French, "(Kathoden) Zerstäubung" in German and "(Katodnoe) Raspylenie" (Распыление) in Russian.

The phenomenon was first reported by Sir William Robert Grove who is also known as being the inventor of the first fuel cell, in his historical article in 1852 [1]. Grove realized his experiments in a glass discharge tube and used a von Guericke type vacuum pump to get a pressure of about half to three-quarters of an inch of mercury with his own words, which equals to  $\sim 12.7 - 19.0$  Torr or to  $\sim 1700 - 2500$  Pa when converted to current SI units. He used a steel needle as the cathode and a polished silver plate as the anode at the beginning of his series of 16 experiments. The cathode–anode distance was fixed at 2.54 mm (0.1 inch). The details of the apparatus he used can be seen in Figure 2.1. This figure is scanned from the original offprint of the historical article signed by him. He observed hollow (sputtered) deposits which he called oxidation on the polished silver surface when it was made the anode and drawn them as can be seen in the figure (1-10). He inverted the anode and the cathode and observed the same phenomenon, which he called reduction. He used different materials instead of steel needle such as wires of copper, silver, platinum and changed the silver plate to bismuth, lead, tin, zinc, copper, iron, and platinum. He also realized his experiments in different gas atmospheres, such as oxygen, hydrogen, protoxide of nitrogen, carbonic acid, and carbonic oxide. Even the cathode–anode distance was changed in his experiments. Considering his systematical experiments, the general introduction of many books and papers on sputter deposition which cites only an observation of a deposit on the glass walls (this was an observation from one of his additional experiments and the glass in question was not the discharge tube but an additional glass which the wire (cathode) was sealed in) which implies a coincidence, is quite incomplete.

Summarize the history of the sputtering phenomena is an hard but fascinating work as the subject is strictly connected to the most important scientific achievements of the 18<sup>th</sup> and 19<sup>th</sup> centuries. Great experimentalist of that time worked on sputtering directly or occasionally. The most satisfactory and detailed review on the subject has been realized by D. Mattox in “The Foundations of Vacuum Coating Technology” [2] and is used as a guide throughout of this historical part.

[ 87 ]

*From the Author*

VII. *On the Electro-Chemical Polarity of Gases.*  
By W. R. Grove, Esq., M.A., F.R.S.

Received January 7.—Read April 1, 1852.

THE different effect of electricity upon gases and liquids has long been a subject of interest to physical inquirers. There are, as far as I am aware, no experiments which show any analogy in the electrization of gases to those effects now commonly comprehended under the term electrolysis. Whether gases at all conduct electricity, properly speaking, or whether its transmission is not always by the disruptive discharge, the discharge by convection, or something closely analogous, is perhaps a doubtful question; but I feel strongly convinced that gases do not conduct in any similar manner to metals or electrolytes.

In a paper published in the year 1849\*, I have shown that hydrogen or atmospheric air intensely heated, showed no sign of conduction for voltaic electricity even when a battery of very high intensity was employed.

In the Eleventh, Twelfth and Thirteenth Series of FARADAY'S Experimental Researches, the line of demarcation between induction across a dielectric and electrolytic discharge is repeatedly adverted to; induction is regarded as an action of contiguous particles, and as a state of polarization anterior to discharge, whether disruptive, as in the case of dielectrics, or electrolytic, as in electrolytes. See §§ 1164—1298—1345—1368, &c.

MR. GASSIOT, in a paper published in the year 1844†, has shown that the static effects, or effects of tension, produced by a voltaic battery, are in some direct ratio with the chemical energies of the substances of which the battery is composed; in other words, that in a voltaic series, whatever increases the decomposing power of the battery when the terminals are united by an electrolyte, also increases the effects of tension produced by it, when its terminals are separated by a dielectric.

In none of the above papers, and in no researches on electricity of which I am aware, is there any experimental evidence that the polarization of the dielectric is or may be chemical in its nature, that, assuming a dielectric to consist of two substances having antagonist chemical relations, as for instance, oxygen and hydrogen, the particles of the oxygen would be determined in one direction, and those of the hydrogen in the other; the only experimental result bearing on this point with which I am acquainted, is the curious fact which was observed by Mr. Gassiot and

\* Philosophical Transactions, 1849, p. 55.      † Philosophical Transactions, 1844, p. 29.

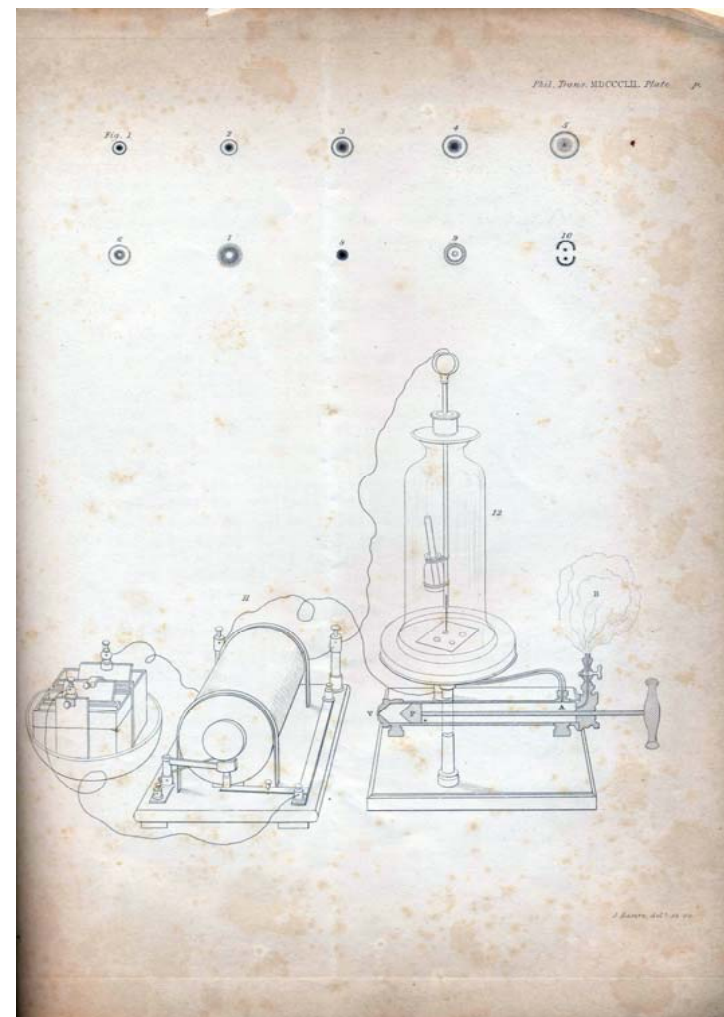


Figure 2.1: Grove's sputtering apparatus (1852) [1].

The history of the components of a sputtering system could easily be dated to the 16<sup>th</sup> century, about 1640, to the discovery of the first piston-type vacuum pump by Otto von Guericke [2]. Michael Faraday was the first person who used a vacuum tube to create a glow discharge (plasma) in 1838, and the first who described the dark space lately known with his name in a glow discharge (See Figure 2.2 (d)). He also reported film deposition in a glow discharge tube in 1854 [2]. Heinrich Geissler, who was a German glassblower, invented sealed-off glow discharge tubes which are known as Geissler tubes in 1857 and by means of the mercury vacuum pump he invented in 1855, the tubes were evacuated more effectively to a relatively high vacuum [3]. The tube in question is an evacuated glass cylinder with an electrode at each end, which contains rarified gases such as neon, argon, air or conductive liquids or minerals. When a high voltage is applied to the electrodes, an electrical current goes through the tube, ionization of the gas occurs, hence different lighting effects are created. This was the first widespread recognition of glow-discharge plasmas. Some of the tubes were like Victorian style pieces of art and used for enjoyment (the basis of the neon lights of advertising) but others, especially the ones made for Julius Plücker who was a German mathematician and physician and his pupil Johan Wilhelm Hittorf working on the glow-discharges had given rise to the first important observations on the cathode rays<sup>1</sup>. Plücker is the first researcher who reported the formation of a (platinum) film inside of a discharge tube, creating a “beautiful metallic mirror” in 1858 [4]. This was the first report on the observation of a sputter deposited film over a relatively large area.

It was by the work of William Crookes who modified the Geissler tubes and further improved the vacuum that the phosphorescent effects were further explored. The term cathode rays is often pronounced with his name and he is credited to be the first person proposed the fourth state of matter<sup>2</sup> (plasma as it is known today) in 1879 [5].

---

<sup>1</sup> The term “cathode rays” was introduced to the literature by Eugen Goldstein in 1876, a German physician who had undertaken his own investigations of the discharge tubes. He is also the discoverer of anode rays (canal rays), and in some sources is credited with the discovery of proton.

<sup>2</sup> Plasma is an expression coined by I. Langmuir in 1928 [I. Langmuir, “Oscillations in ionized gases”, Proceedings of the National Academy of Sciences 14 (1928) 628]

First, he used the term “radiant matter”<sup>3</sup> for this new state of material. In 1891, W. Crookes published an article on sputter deposition, which he called “electrical evaporation” [6]. He systematically analyzed the amount of sputtered materials (volatilized with his own words) for different metals and alloys by measuring the weight losses under similar discharge conditions. This was the first step in measuring the relative sputtering rates of materials and that article was probably the first popular publication on sputtering. Examples of activated Geissler and Crookes tubes can be seen in Figure 2.2. These tubes and observations made on cathode rays not only led the development of today’s sputtering applications but also caused the discovery of x-rays by Röntgen in 1895 and the electron<sup>4</sup> by J.J. Thompson in 1897, both working with a Crookes tube, and constituted the basis for the development of fluorescent lights, television and computer monitors, many decades later.

In 1877, A.W. Wright (Professor of Yale University) published a paper on the use of an electrical deposition apparatus to form mirrors and study their properties [7], which even today raise a question between scientists working on the history of vacuum deposition, whether he was using sputtering or cathode arcing. According to D. Mattox, Wright was sputtering because he was using an arrangement very similar to that of Grove, based on the description given in his paper, with one major difference; he used a swinging balance-pan fixture that allowed him to deposit a film over a relatively large area [2]. The apparatus drawn “a posteriori”, based on the description given in the Wright’s article can be seen in Figure 2.3. According to R. L. Boxmann, the question is, whether the discharge was a glow or an arc [8]. His opinion is that, as the inductor current given in Wright’s article was sufficiently great and the cathode diameter sufficiently small, the discharge operated in the arc mode [9].

---

<sup>3</sup> The term “radiant matter” is attributed to Crookes in many sources, however in his lecture titled “on radiant matter” delivered at Sheffield University in 1879 before the publication of his article he stated that the expression was first proposed by Faraday, when delivering a series of lecture in 1816 at the early period of his career.

<sup>4</sup> Stoney used the term “electron” for the first time in 1894 as a unit of the elementary electrical quantity [G.J. Stoney, “Of the "Electron," or Atom of Electricity”, *Philosophical Magazine*, 38:5 (1894) 418]

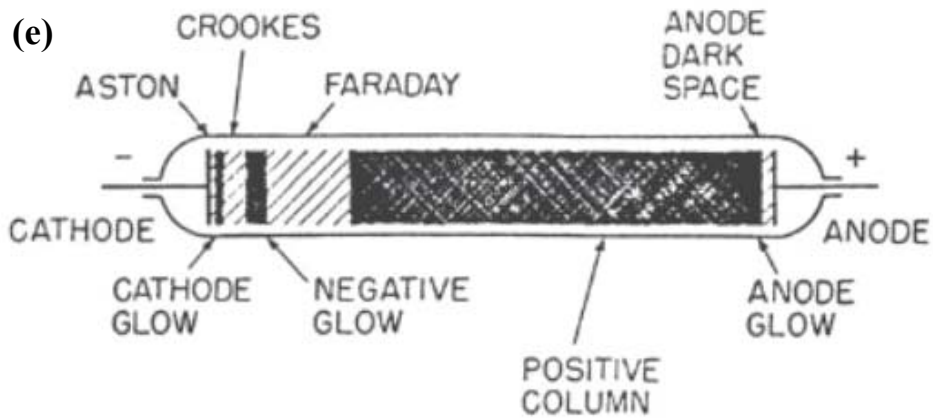
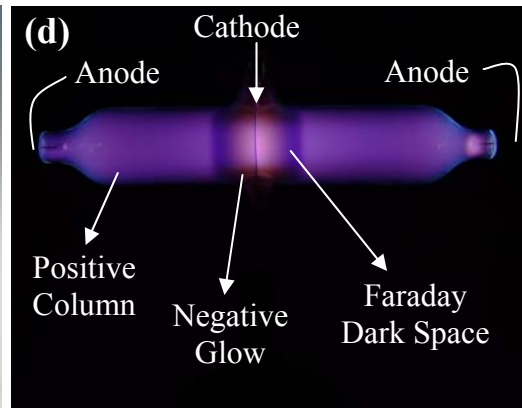


**Figure 2.2:** (a) Geissler tube made from uranium glass [10] (b) Activated Geissler tube [10] (c) Crookes tube [11] (d) Activated Crookes tube showing different regions of a glow discharge [11] (e) Schematic of a glow-discharge tube showing various named regions [2].

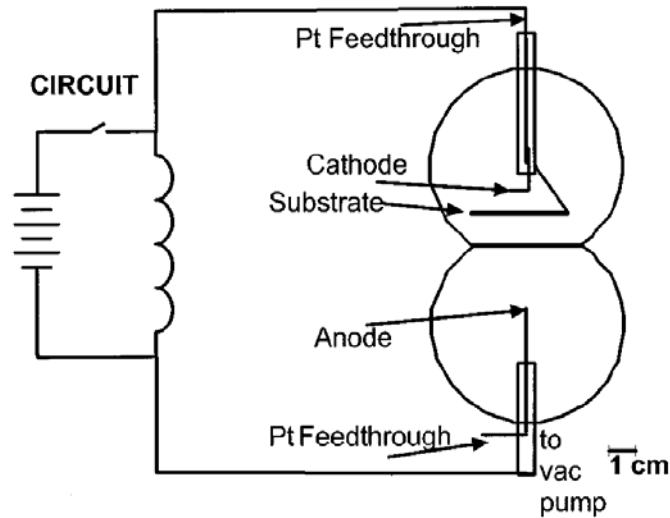


**Figure 2.3:** Wright deposition apparatus based on the description given in his paper [9].

Another evidence of the uncertainty on the Wright's description of the deposition process he used, is the decision of U.S. Patent Office when challenging Thomas Edison's 1884 patent application on arc-based "vacuous deposition" [12]. The patent examiners pointed out the work of Wright, which Edison was apparently unaware [2]. Edison modified his application by describing Wright's work as a laboratory curiosity and a too slow process to be commercially useful and by maintaining that Wright used a pulsed arc whereas his was a continuous arc. The patent office used Wright's work as "prior art" and finally the patent issued in 1894 [2,9]. By using whether sputtering or cathodic arc, Wright should be credited with being the first to characterize vacuum-deposited films for their specific properties such as visual appearance of the films by reflected and transmitted light, chemical stability and adhesion. Crookes, in his article on sputtering, referred to Wright's work on producing mirrors [6]. In 1892, Edison used a vacuous deposit to seed coat his wax cylinder phonograph masters for subsequent electroplating [12,13]. In his 1902 patent on the subject [14] he indicated that the deposition process (arc deposition) described in his previous patent [12] wasn't suitable because of uniformity and heating problems, and in the figure in this patent (Figure 2.4) he showed a sputtering cathode for depositing the metal. Therefore, Edison should be credited with the first commercial use of sputter deposition. Later on, he interested in making filaments in form of freestanding foils for his light bulbs using sputter deposition [2].

T. A. EDISON.  
PROCESS OF COATING PHONOGRAPH RECORDS.

(Application filed June 16, 1900.)

(No Model.)

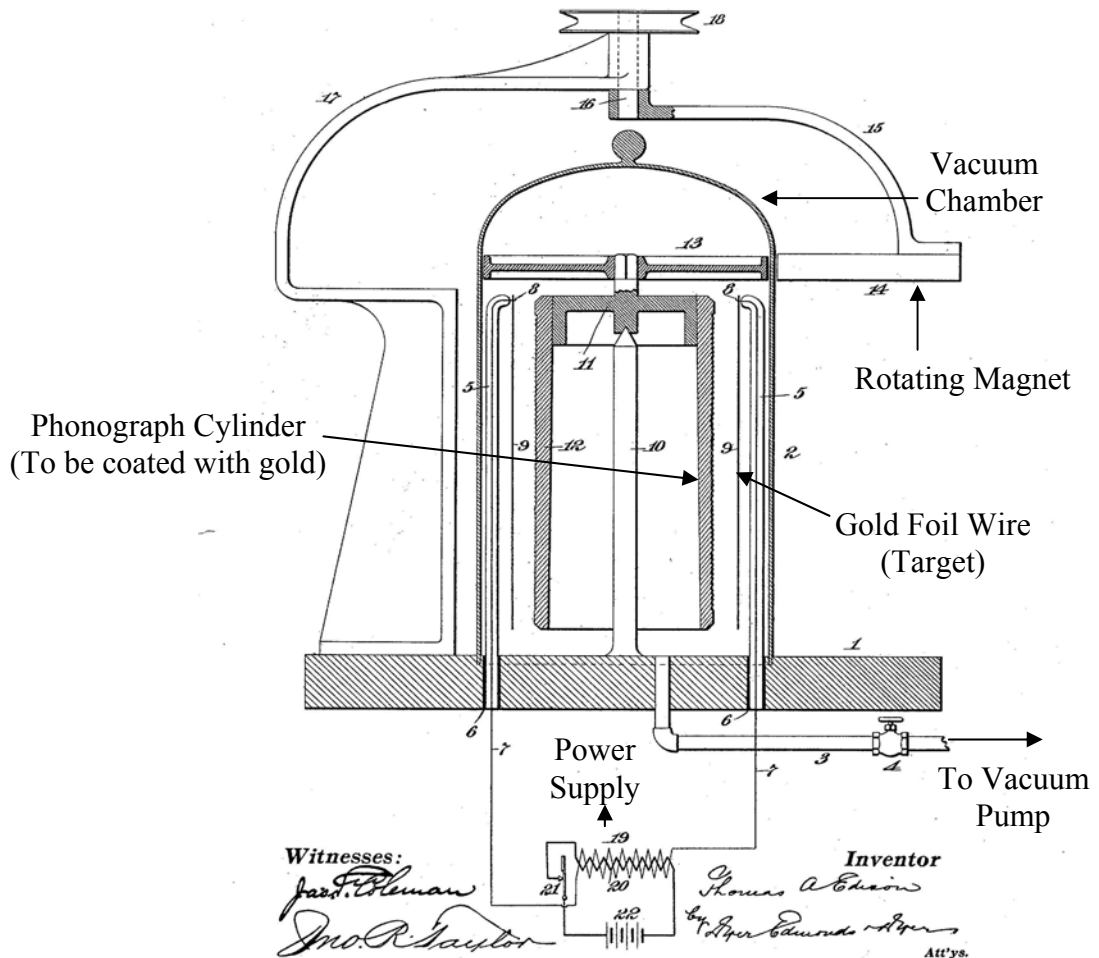


**Figure 2.4:** T. A. Edison's sputtering apparatus [14].

After the late 1800s, sputter deposition was used occasionally to make mirrors [15]. With the advance of the technology and process modifications such as magnetron sputtering, RF sputtering for non-conductive materials, reactive sputter deposition for compounds, and the use of controlled concurrent ion bombardment, sputter deposition rapidly developed after the mid-1970s. Today's applications are numerous, ranging from microelectronics, display devices, corrosion, tribology and wear-resistance including cutting tools and different machine parts, high temperature oxidation, solar cells, thermal insulation and decorative coatings.

The term "sputtering" was probably created to distinguish the source of vaporization; between thermal evaporation and non-thermal (momentum transfer) process [2]. At the beginning, the term "spluttering" was used. However, there is no convincing

information in the literature on who and when coined the term sputtering. A literature search by G.K. Wehner [16] shows that J.J. Thomson was using the word sputtering in 1913 [17] and this does not seem as the first usage of the term. Probably first elimination of the “l” was made by I. Langmuir and K.H. Kingdon in 1923, which was the first use of the term “sputtering”. Both of the verbs to “splutter” and to “sputter” originate from Latin “sputare” which means, “to emit saliva with noise”. Other expressions proposed to describe the phenomena were, “impact evaporation” by Kay and Guenterschulze [16], “cathodic bombardment” [15] and “cathode disintegration” [18] to refer the destructive and unwanted effect when the first observations were made on the phenomena.

### 2.1.2 Sputtering theory

Sputter deposition is a Physical Vapor Deposition (PVD) process. To deposit a coating, the source of coating material, termed the “target” is mounted opposite to the substrates in a vacuum chamber. The chamber is then evacuated to a base pressure in the ranges of  $10^{-6}$  to  $10^{-10}$  Torr ( $10^{-4}$  to  $10^{-8}$  Pa), depending upon the process. A sputtering apparatus, in which the target and substrate are opposing parallel plates, is shown schematically in Figure 2.5 [19].

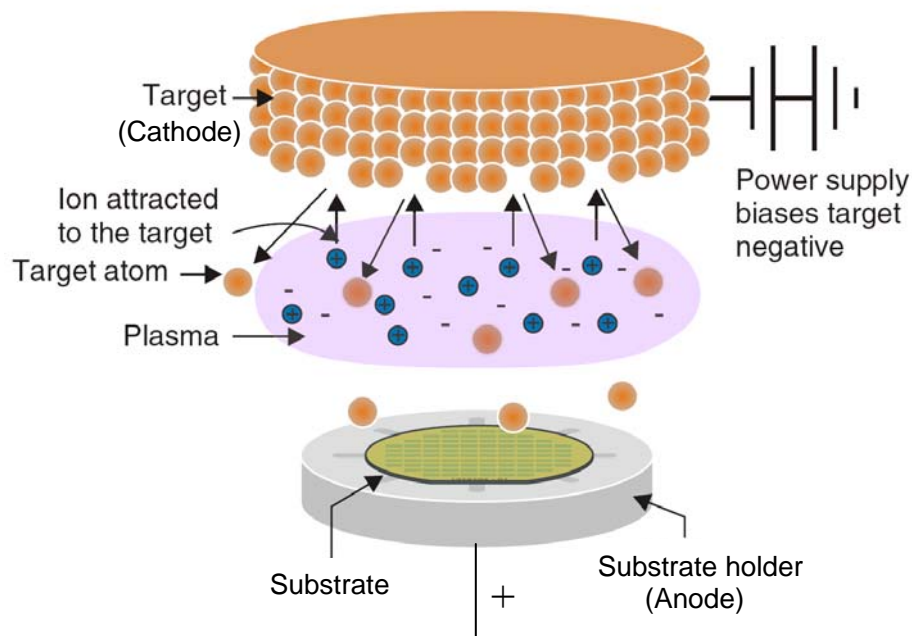


**Figure 2.5:** Schematic representation of diode sputtering assembly [20].

A precursor gas, Argon in most applications because of its mass compatibility with materials of engineering interest and its low cost, is then inserted into the deposition chamber to a pressure from 1 to 100 mTorr (0.1 to 1 Pa) [19]. When the target is powered negatively, typically between 0.5 and 5 kV, ionized Argon atoms provides the ion bombardment of the target. The process is then, the ejection of the target atoms as a result of the argon ion bombardment, their transfer to the substrate with a kinetic energy and the nucleation and growth of the thin film on the substrate surfaces.

### 2.1.3 Sputtering mechanisms

When an ion strikes the cathode, many interactions can occur on its surface as illustrated in Figure 2.6. These interactions include liberation of neutral atoms, ionized atoms, backscattering, x-ray emission, photon generation, secondary electron emission, and desorption of gas atoms from the target surface. Several other processes can occur also in the target, including the generation of collisional cascades, the creation of point defects, local heating, amorphization, implantation, and compound formation [21].

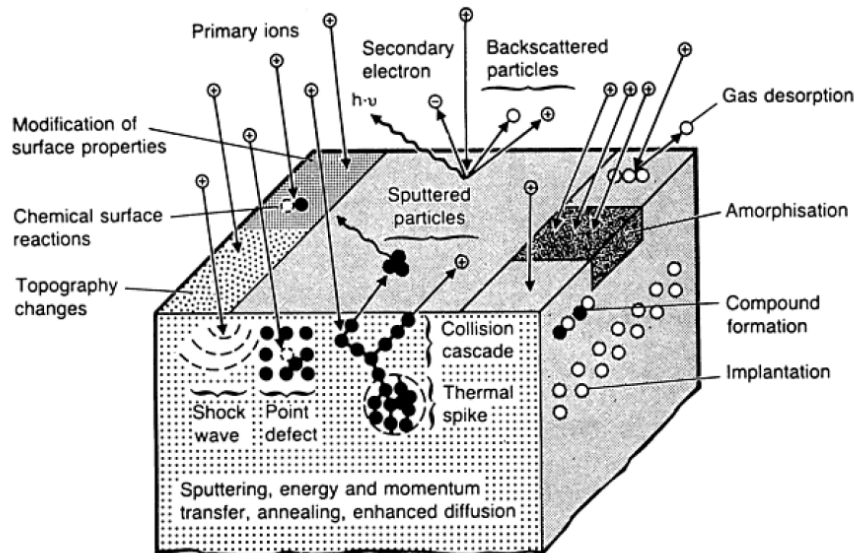


**Figure 2.6:** Synopsis of the interaction events occurring at and near the target surface during the sputtering process [21].

In the sputtering process shown in Figure 2.6, if the incident particle impacts the surface of the solid with sufficient energy, it breaks bonds and dislodges atoms. The atoms thus removed from the solid are considered as sputtered atoms [22].

Sputtering can be described in four general energy ranges, from energies at near the binding energy to many MeV [22]. Very low energies: Although recent approaches demonstrated that, at incident ion energies of a few eV up to 30–50 eV, there is very little sputtering and the minimum ion energy for sputtering is the binding energy of the most-weakly-bound surface atom [22], there is still a general consensus on the presence of a sputter threshold below which no sputtering occurs as presented in early works (1960’s) [19]. Very low energy sputter yield measurements are difficult to make accurately and there is almost no mention of them in the literature [22].

Single Knock-on energy regime: At low energies  $<1$  keV, the interaction is referred to as knock on regime [22,23]. In this regime, the incoming particle has more than enough energy to dislodge tens to hundreds of atoms. When collision takes place, the incident and the impacted particles move into the material causing more collisions [22]. Knock-on sputtering has been modeled by computer calculations, which follow the trajectories of a large number of incident and impacted particles [22]. Figure 2.7 shows a computer simulation of such a process resulting from a single bombardment event. It is clear that sputtering cannot result from a single binary collision since the momentum vector of the target atom must be altered by more than  $90^\circ$ .

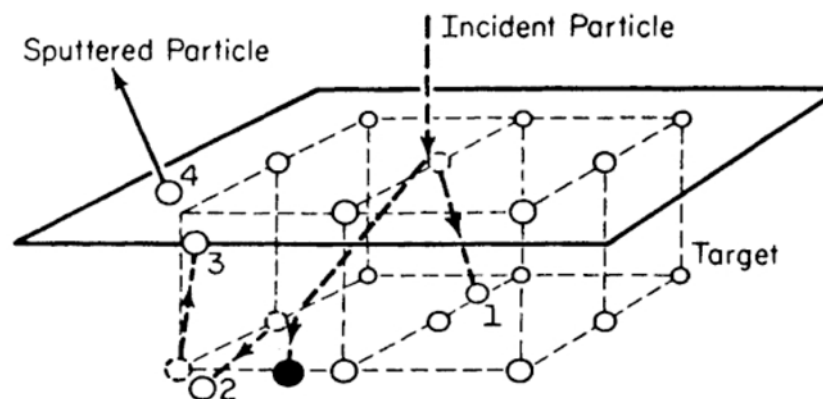


**Figure 2.7:** Computer simulation of a portion of a collision sequence initiated by a single ion-bombardment event in a solid lattice [19].

In the simulated collision sequence of Figure 2.7, the incoming projectile strikes target atom 1 and moves it deeper into the lattice. The collision with atom 2 causes the projectile to hit atom 3, which is displaced and collides with surface atom 4. Thus, sufficient momentum is transferred to atom 4 to overcome the surface energy barrier and be ejected [19]. Knock-on sputtering characterizes the practical energy range used for most sputtering applications [19].

Collision-cascade sputtering: At ion energies between 1 keV and 50 keV, the incident particle has sufficient energy to break all the bonds between atoms in a spherical region around the impact point [22]. As the incident ion hit the surface it creates a series of collisions with atoms in the solid. In many of these collisions, sufficient energy is transferred to displace the atoms. The displaced atoms may displace other atoms and so on, thus creating a cascade of atomic collisions [23]. While this regime has generally higher yields than the knock-on regime, the higher energies (and voltages) make it impractical to use for most industrial scale sputter deposition applications [22]. This regime is mostly used for analytical characterization of surfaces by techniques such as Rutherford Backscattering Spectroscopy and Secondary Ion Mass Spectroscopy, which will be explained in details in Section 3.2.4.

High-energy implantation: At ion energies above 50 keV, the incident particle can travel well into the bulk of the solid before depositing all its energy. While this can create significant damage a micron or so below the surface, little or no sputtering occurs as the energy is deposited so far away from the surface. In addition, the incident particle is often trapped or implanted within the sample [22]. This regime is used especially in semiconductor device fabrication. The introduction of dopants in a semiconductor is the most common application of ion implantation. Dopant ions such as boron, phosphorus or arsenic are generally created from a gas source then implanted with high energies, modifying the conductivity of the semiconductor in its vicinity.

The momentum-transfer theory for physical sputtering was proposed early-on but was supplanted by the “hot-spot” theory involving thermal vaporization [16]. It has only been in recent years that the true nature of the physical sputtering process has been defined and modeled [24]. Much of that knowledge came from the work of Guntherschulze in the 1920’s and 30’s and Wehner and his co-workers in the 1950’s and 60’s [24]. To explain the momentum transfer theory, a particle of mass  $M_i$  with a velocity  $V_i$  which impacts on a line of centers with a target particle of mass  $M_t$  will be considered, as shown in Figure 2.8.

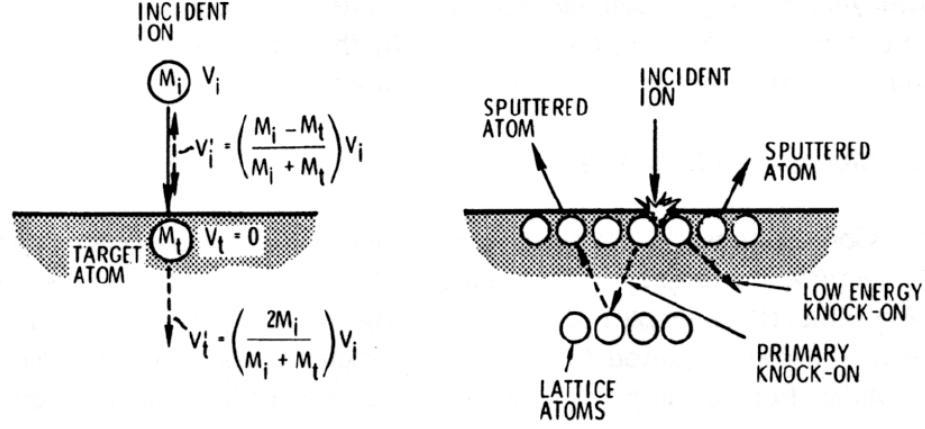


**Figure 2.8:** Schematic diagram showing momentum exchange processes that occur during sputtering [19].

Three simple observations can be made. First, the momentum delivered to the target particle drives it into the lattice. Secondly, from a simple line-of-centers atomic collision calculation, a fraction of the kinetic energy of the incident particle is transferred to the target particle [19].

$$\varepsilon = \frac{4M_i M_t}{(M_i + M_t)^2} \quad (2.1)$$

An expression for the yield, which can be written in the form shown in Eq. (2.2) has been derived below [19].

$$S = (const) \varepsilon \frac{E}{U} \alpha(M_t/M_i) \quad (2.2)$$

The relationship is useful for illustrating the functional dependences of the important parameters and provides reasonably good agreement with measurements for medium mass (Ar, Kr) bombardment of a wide variety of materials. The yield is seen to depend directly on the energy transfer coefficient  $\varepsilon$ . The term  $\alpha(M_t/M_i)$  is a near-linear function of  $M_t/M_i$ ,  $E$  is the kinetic energy of the incident ion, and  $U$  is the heat of sublimation for the target material. The mass dependence of  $\varepsilon\alpha$  does not vary greatly from one material to another. The primary material-sensitive factor is the heat of sublimation, and this is only a first power dependence. This is in contrast to chemical and thermal processes that depend exponentially on activation energy. It is this relative insensitivity to the properties of the target material that gives sputtering the universality [19].

When the ion mass is lower than that of the target atom, it may be reflected backward in a single collision with a kinetic energy that is still a significant fraction of its initial energy. For a 180° reflection, this fraction is  $f = \frac{M_i - M_t}{M_i + M_t}$ . If  $M_i > M_t$ , reflection requires more than one collision and the reflection coefficient is low [19].

$$f = \frac{(M_i - M_t)^2}{(M_i + M_t)^2} \quad (2.3)$$

Since the ions have a high probability of being neutralized prior to impact, they are reflected as energetic neutrals, which are therefore not influenced by the electric field over the target surface. The flux of reflected species contributes to substrate heating, particularly in devices operating at low pressures where the reflected neutralized ions may reach the substrates with little loss of kinetic energy by gas-phase collisions. Consequently, the reflected species bombard, and can become entrapped in the growing film [19].

#### 2.1.4 Sputtering rate

The sputtering process is quantified in terms of the sputtering yield, which is defined as the number of target atoms ejected per incident particle. The yield depends on the target species and the nature, energy, and angle of incidence of the bombarding species [19]. The sputtering yield tends to be greatest when the mass of the bombarding particle is in the same order or larger than that of the target atoms. It is relatively insensitive to the target temperature [16]. The yield is also independent of whether or not the bombarding species is ionized [19].

Sputtering yields are determined experimentally. The dependence of sputtering yield on incident ion energy shows a characteristic appearance as shown in Figure 2.9. As explained before, below the threshold energy no sputtering occurs. The surface binding energy,  $U_{sb}$ , (2–10 eV) of the atoms must be exceeded for the atom in order to escape from the solid by sputtering [23].

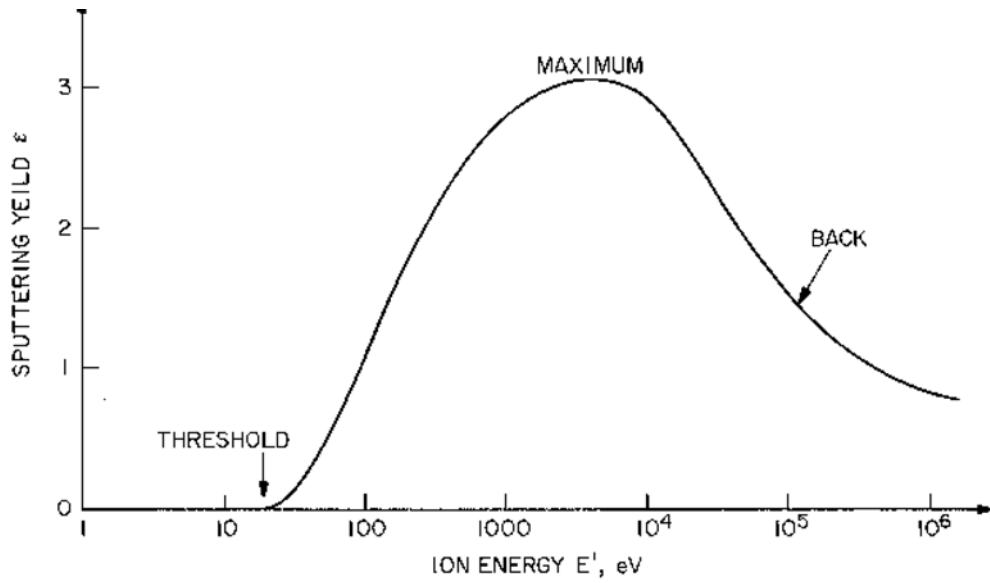


**Figure 2.9:** Sputtering yield versus energy of the incident ion [25].

Above the threshold energy, the sputtering yield increases initially in a quadratic manner and then increases linearly and attains a maximum. At higher energies, the sputtering yields decrease quite rapidly as the ions penetrate far inside the solid. In the energy range of 100–1000 eV, the sputtering yield is approximately linear in ion energies and independent of incident ion species [23].

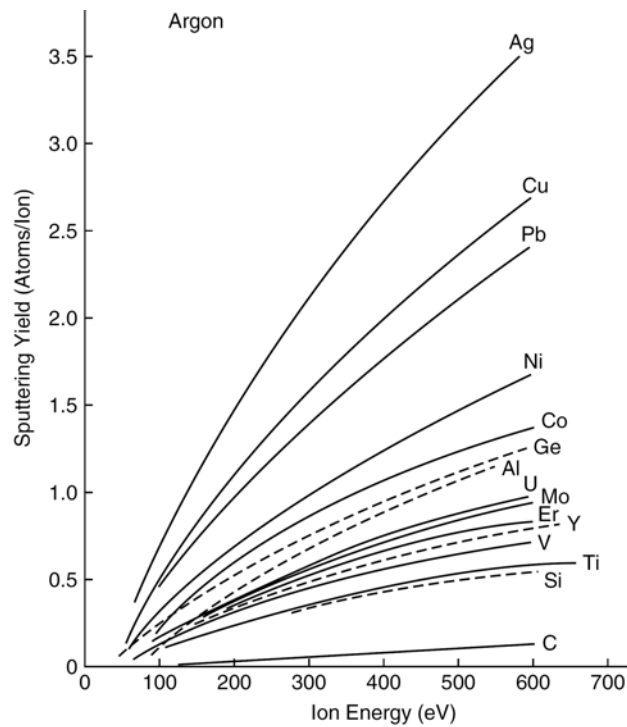


**Figure 2.10:** Variation of the sputtering yield of several materials as a function of  $\text{Ar}^+$  ion energy at normal angle of incidence [23].

At typical ion acceleration energies, sputtering yields of most metals are very close to one another. The values of sputtering yield lie between 0.5 and 20 in the keV energy range for medium mass ions [23]. Figure 2.10 shows sputtering yield versus ion-energy data for several materials under normal ion incidence.

The general dependence of the sputtering yield on the ion angle of incidence is indicated in Figure 2.11. In glow-discharge sputtering devices, the ions generally approach the target in a direction normal to the target surface. Thus, the relationship shown in the figure is of particular significance when the target surface is highly irregular or for ion-beam sputtering where the ion-incidence angle can be controlled [19].

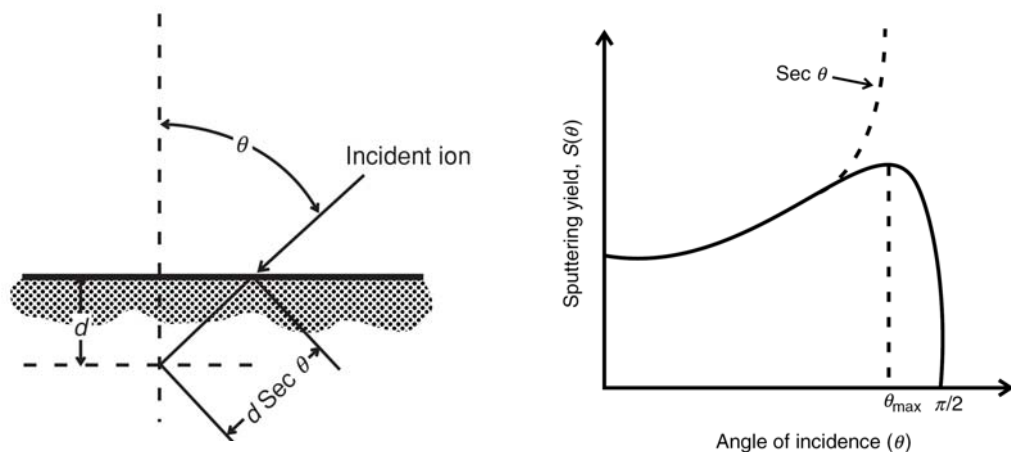


**Figure 2.11:** Schematic diagram showing variation of the sputtering yield with ion angle of incidence for constant ion energy [24].

For off-normal bombardment, the sputtering yield initially increases to a maximum then decreases rapidly as the bombarding particles are reflected from the surface [22] and this effect is called the “angle-of-incidence effect” as shown in Figure 2.11. The maximum sputtering yield for argon generally occurs at about 70 degrees off normal but this varies with the relative masses of the bombarding and target species. The increase of sputtering yield from normal incidence to the maximum can be as much as an increase of 2 to 3 times [24].

### 2.1.5 The nature of sputtered species

Under typical conventional sputtering configurations, most sputtered material is ejected in the neutral atomic state. The fraction of charged particles sputtered from

target surface is on the order of  $10^{-4}$ , becoming larger for surfaces contaminated with strongly electropositive or electronegative species [19]. Plasma characterization such as the ionization degree and the nature of species present in the flux is difficult and necessitates in-situ special arrangements such as Langmuir probes or mass spectrometers attached to the deposition systems. Therefore, the data on said properties of glow discharge plasmas is limited. A literature review realized by Thornton and Greene in [19] will be quoted here. They stated that relatively little experimental data is available on the probability of material being sputtered as molecules or clusters. Investigation by Oechsner and Gerhard [26] using mass spectrometric analyses of post-ionized sputtered neutral particles has shown that with 1 keV  $\text{Ar}^+$  bombardment, the maximum fraction of sputtered dimers is 0.1 for Ag, Au, and Cu and about 0.03 for other metals. The fraction of trimers is about 0.001. The mechanism for the sputtering of molecular species is not well established. Statistical models have been proposed in which sputtered neutral atoms resulting from nearly-simultaneous ejection events agglomerate above the surface if their ejection is properly correlated and their relative kinetic energy is less than the dissociation energy of the molecule formed [27,28].

In the case of compounds, most of the information available on molecular sputtering is for alkali halides and oxides where clusters can account for a significant percent of the total sputtered flux. Coburn et al. showed that the relative fraction molecules/neutrals of sputtered species from  $\text{M}_x\text{O}_y$  metal oxide targets increased with increasing M-O bond energy [29].

Using 140 eV  $\text{Ar}^+$  bombardment, comparable to the average impact energy in many glow discharge deposition experiments, Comas and Cooper found from post-ionized mass spectroscopy measurements that molecular species ( $\text{GaAs}$ ,  $\text{Ga}_2$ ,  $\text{As}_2$ ) amounted to less than 1% of the total sputtered flux [30]. However, for 6 keV  $\text{Ar}^+$  ion sputtering, Szymonski and Bhattacharya observed that at room temperature, sputtered  $\text{GaAs}$  and  $\text{As}_2$  molecules accounted for  $\sim 14\%$  and  $11\%$  respectively of the flux [31]. The fraction of sputtered  $\text{GaAs}$  molecules was found to increase rapidly for target temperatures above  $250^\circ\text{C}$ . This latter effect was explained as being due to enhanced sputtering from collisional spikes.

As a conclusion, if a special configuration such as ionized PVD or ion plating is not mentioned, the transferred flux is formed of mostly single neutral atoms ejected from the target material in conventional (magnetron) sputtering. Above mentioned special configurations will be explained in details in Section 2.2.4.

### 2.1.6 Energy and direction of sputtered atoms

An important distinction between sputtering and other vapor phase deposition techniques is that sputtered atoms can have quite high kinetic energies. For example, the average ejection energy of Ge atoms under 1.2 keV  $\text{Ar}^+$  bombardment is  $\sim 15$  eV compared to only  $\sim 0.1$  eV for evaporated Ge. In sputter deposition systems for which the target-substrate separation is less than a few mean free paths, the energy distribution of sputtered species impinging on the substrate will be approximately the same as the ejected species energy distribution [19].

The most probable ejection energy is typically half of the surface binding energy, but because of the extended high-energy tail the average ejection energy is considerably higher (Figure 2.12) and, in general, is found to increase with the atomic number of the target [19].

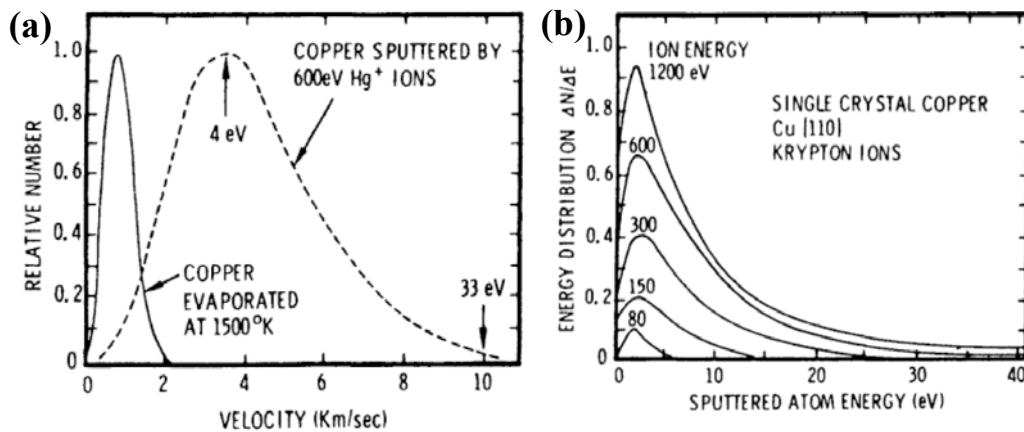


**Figure 2.12:** (a) Comparison of velocity distributions of sputtered and evaporated Cu atoms (b) Energy distribution of sputtered Cu atoms at various energies [19].

The angular emission distribution for sputtered atoms is often described as a cosine distribution. This means that the relative amount of material sputtered at any particular angle can be compared to the amount sputtered at normal incidence times the cosine of the angle from normal incidence.

This is shown schematically in Figure 2.13. The overall distribution is often drawn as a circle, which is the relative amount emitted at any particular angle. In three dimensions, this would appear as a sphere centered on the impact point [22].

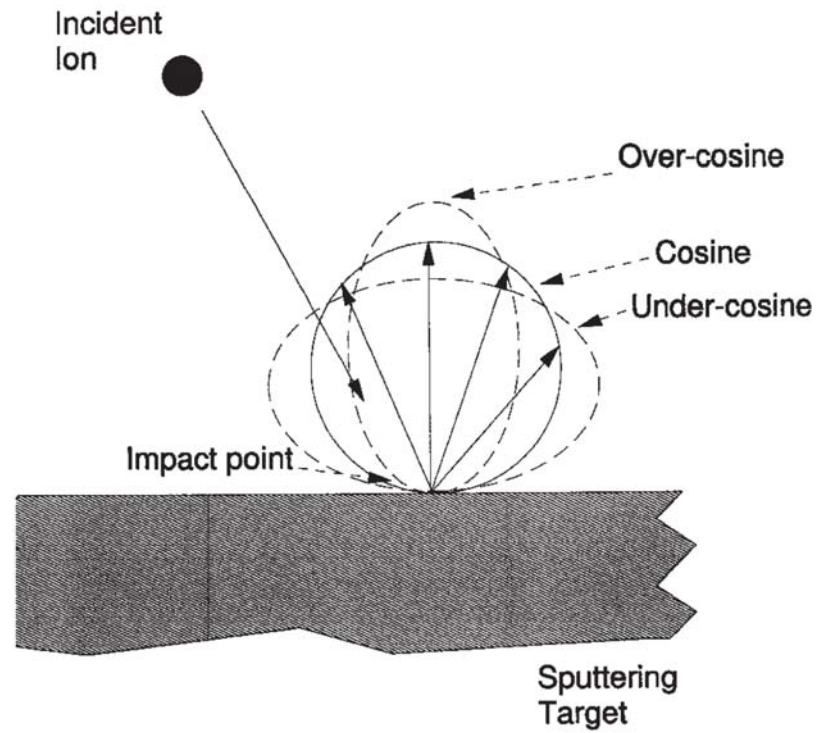


**Figure 2.13:** Angular emission distribution for sputtered atoms [22].

## 2.2 Sputtering Configurations

The technological advances in the power supplies, vacuum pumps and other components have caused different sputtering configurations to be developed during last 40 years for the following attempts:

1. Increase the sputtering rate
2. Increase the available deposition area
3. Reduce plasma heating of the substrates
4. Operate at lower working-gas pressures
5. Facilitate the coating of complex substrate shapes.
6. Increase the ionization
7. Deposit non-conductive or compound thin films

There is a wide range of sputtering configurations, therefore in the following discussion, only the configurations used in this study will be reviewed.

### 2.2.1 Planar diode and DC glow discharge configuration

The planar diode shown schematically in Figure 2.14 is the simplest and the most widely used sputtering configuration [19]. The target, in the form of a plate, consists of the material that will eventually result in a thin film. A DC power supply capable of supplying several kilovolts (0.5–5 kV) is used to energize the electrodes. The substrate is placed as to face the target [23]. Cathode diameters are typically 5 to 30 cm and the cathode to anode spacing is generally 3 to 10 cm [19]. Arrangement for cooling or heating the substrate can be used. The substrate can be electrically grounded, biased or floating [23].

The chamber is evacuated to a base pressure that typically ranges from  $10^{-6}$  to  $10^{-10}$  Torr ( $10^{-4}$  to  $10^{-8}$  Pa) depending on the specific needs. The base pressure obtained prior to sputtering should give an outgassing flux that is significantly less than the total sputtering flux in the process. The chamber is backfilled with argon up to a pressure of 1 to 100 mTorr (0.1 to 1 Pa) [23].

When the electrodes receive power, a glow discharge type of plasma is created [32]. Because of the relatively low mobility of the ions compared to the electrons, most of the electrical potential that is applied between the anode and cathode is consumed in the cathode dark space, or sheath region [19].

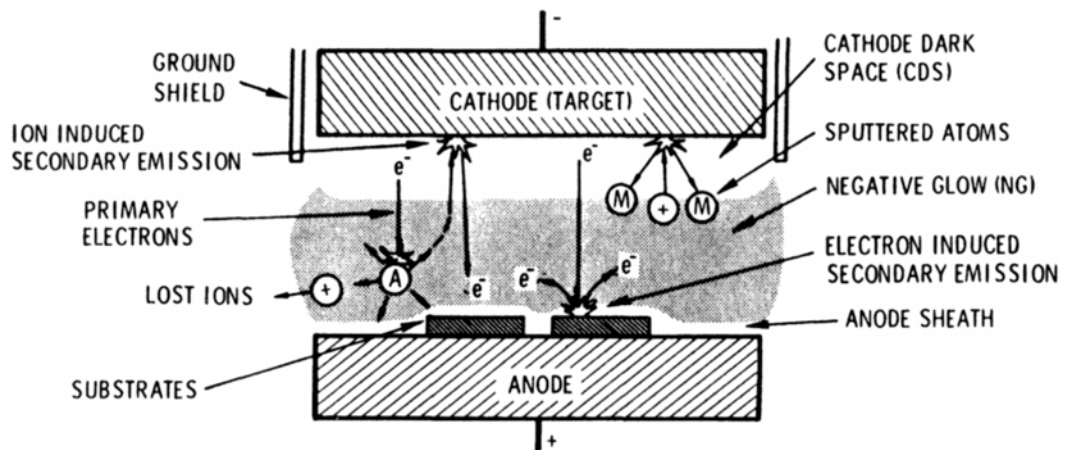


**Figure 2.14:** Schematic representation of a planar diode sputtering system with various named regions [19].

Only 1% of the energy is used to produce the ejection of sputtered particles, and about 75% goes into heating the target, remaining 26% is dissipated by secondary electrons when they bombard the substrate [23].

Dark space thicknesses are typically 1 to 4 cm, depending on the pressure and current density. Strong electric fields are formed in the dark space, and ions passing from the plasma volume to the cathode are accelerated by these fields to impact the cathode. These ions not only sputter target atoms, but also cause a small number of secondary electrons to be emitted from the target surface (approximately one for every ten ions in the case of Ar ions impacting on a metal cathode). These electrons are accelerated in the cathode dark space and enter the plasma volume (negative glow) where they collide with gas atoms causing the ionization of the gas and sustain the discharge [19]. The atoms ejected from the target with a momentum as a result of the ion bombardment, are transferred to the substrate where they condensate and nucleate to form a thin film.

Planar diodes are widely used despite substrate heating and low deposition rates. The reason is their simplicity and their ease of fabrication from a wide range of materials. It has also to be noted that such planar diode systems are suitable to operate with both DC and RF power supplies [19,23].

### **2.2.2 Magnetron sputtering**

The use of magnetron design was first introduced by Penning in 1936 [18] by using “crossed field” (electric and magnetic) electron trap to enhance plasmas in sputtering from cylindrical hollow magnetrons, and from cylindrical post magnetrons by Penning and Mobius in 1940 [33]. The development of high performance magnetron sputtering sources allowed sputtering to be performed at higher deposition rates, larger deposition areas, lower voltages and lower substrate temperatures than with non-magnetic DC sputtering [2,19]. Hence, almost a century after the first discovery of the phenomenon by Grove, sputtering became a suitable technique for industrial application of thin films [2].

Magnetron sputtering sources are diode devices in which magnetic fields are so configured that the  $E \times B$  electron drift currents close upon themselves, thus form traps for electrons to stay near the target surface [19]. An appropriate arrangement of the magnets allows a closed path for the electrons on the target surface, moving normal to the magnetic field then a “circulating current” is established on the surface.

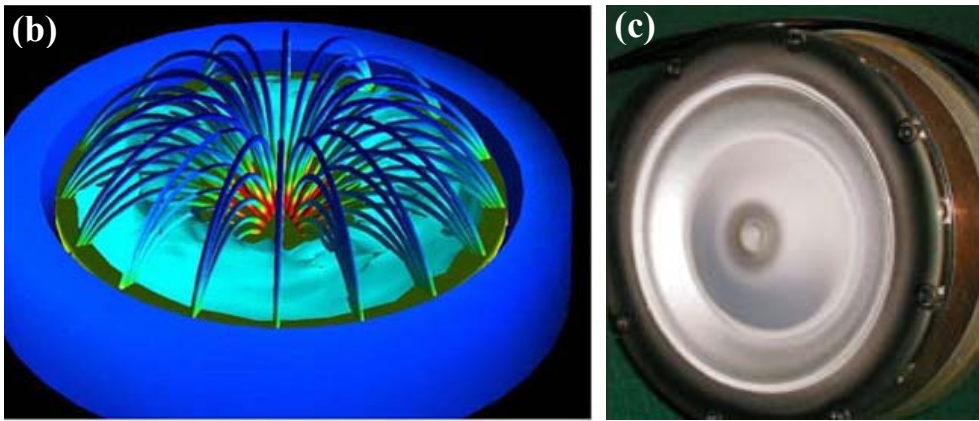
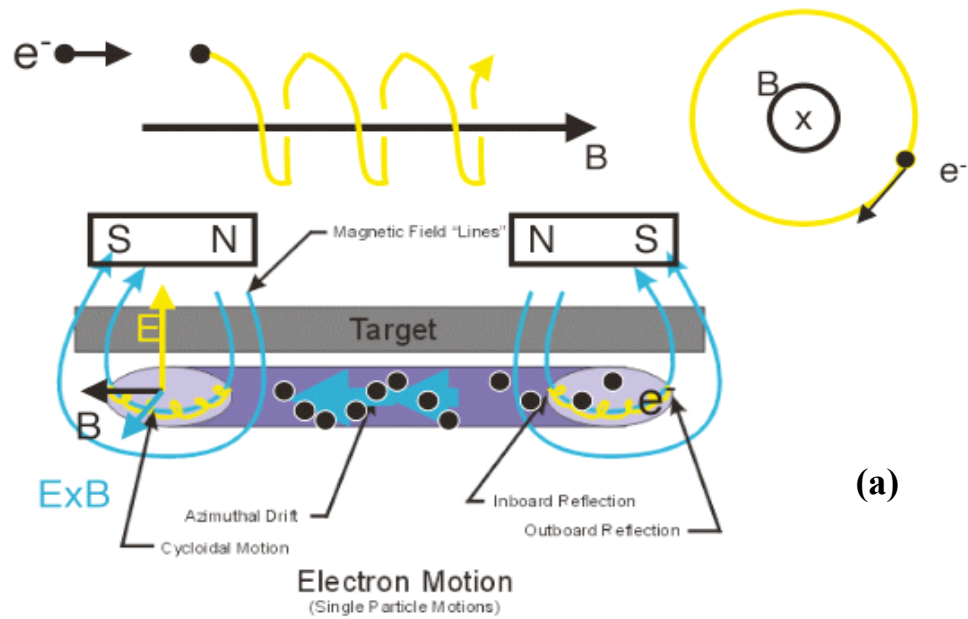


**Figure 2.15:** (a) Magnet design effect on electron's motion in a sputtering system[34] (b) 3D graphic showing magnetic field lines for a circular magnet design behind a circular target material [35] (c) Erosion effect of the target material due to the circular magnetron design [34].

This circulating current may be several times the current measured in the external electrical circuit [24]. As can be seen from Figure 2.15, the electron trajectory became sinusoidal which increases the path and consequently the probability of the collisions with Ar atoms. Therefore, the high flux of electrons creates high-density plasma near the target surface hence increase the deposition rates. Several magnetron configurations can be found in the literature including planar magnetron shown in the figure, the S-Gun type, and the cylindrical type [19].

### 2.2.3 RF sputtering

The technique was first introduced to the literature by Anderson, Mayer, and Wehner in 1962. They reported on the RF sputtering of a film that had been deposited on the inside of a glass window [36,37]. This was based on a suggestion by Wehner in 1955 [38].

DC methods cannot be used to sputter non-conducting targets because of charge accumulation at the target surface. The use of RF methods for sputtering non-conducting materials is based upon the fact that a self-bias voltage, negative with respect to the plasma potential, develops on any surface that is capacitively coupled to a glow discharge [19]. The basis for this potential, which forms as a consequence of the difference in mobility between electrons and ions, is illustrated schematically in Figure 2.16.

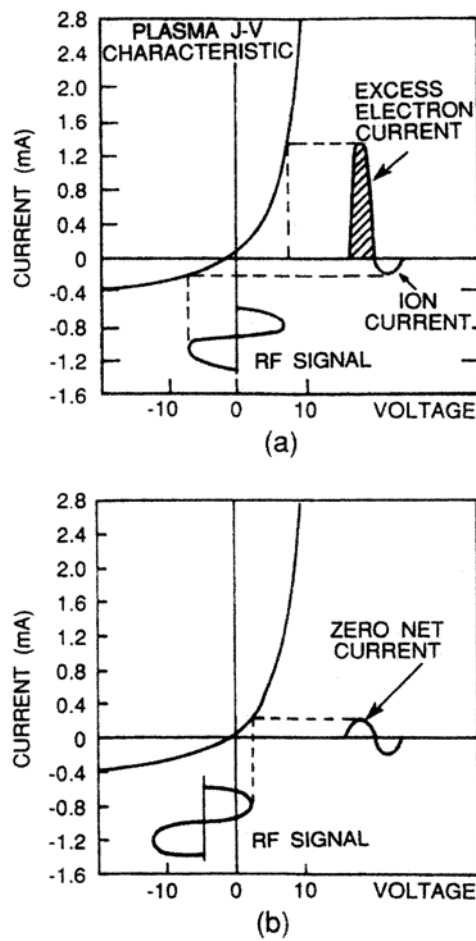


**Figure 2.16:** Schematic illustration of the development of a negative bias in a RF system [19].

The current-voltage characteristic for an electrode immersed in plasma is given in Figure 2.16 (a). The voltage is negative relative to the plasma potential by an amount that depends upon the gas species and electron energy distribution, but is typically -20 to -50 V and therefore too low to produce significant sputtering of most materials [19,24]. When an alternating voltage is applied to an electrode, a positive/negative potential appears on the surface as can be seen in Figure 2.16 (b). During part of each half-cycle, the potential is such that ions are accelerated to the surface with enough energy to cause sputtering while on alternate half-cycles, electrons reach the surface to prevent any charge buildup [24].

RF frequencies used for sputter deposition can be in the range of 0.5–30 MHz. Most systems are operated at a frequency of 13.56 MHz, since this has been allocated by the Federal Communications Commission (USA) for industrial-scientific-medical purposes [19]. Although the deposition rates are relatively low compared to DC magnetron sputtering, its ability to sputter insulator cathodes has adapted this technique to wide variety of applications [39]. All types of magnetron designs are successfully used in rf sputtering configurations [19].

#### **2.2.4 Bias sputtering – ion plating**

Bias sputtering or ion plating are the generic terms used to describe that substrate surface and the growing film are subjected to a flux of energetic particles which influence the film formation process and the properties of the deposited films [24,40].

In 1962 Wehner patented the process of deliberate concurrent bombardment before and during sputter deposition using a “bias sputter deposition” arrangement and mercury ions to improve the epitaxial growth of silicon films on germanium substrates and to lower the epitaxial temperature [41]. Separately, in 1964 Mattox introduced the term “ion plating” [42] and patented the process in 1966 [43]. By definition, the term ion plating does not specify the source of the depositing film particles, the bombarding particles, nor the environment in which the deposition takes place. The idea is to change the film properties by particle bombardment during its growth. Bias sputtering, hence, can be considered one form of ion plating.

As explained in previous sections, during conventional sputter deposition and especially in magnetron designs, the plasma is held near the cathode. For an effective bias sputtering however, plasma must be sustained near the substrate surfaces [40]. This may be done by having an auxiliary plasma generating technique such as, hot filament, hollow cathode triode configuration, or unbalanced magnetron sputtering. In this kind of configurations, the substrate is negatively biased and is in contact with plasma. Bombarded positive ions from the plasma are accelerated by the negative voltage applied to the substrates and arrive at the surface with a spectrum of energies [24].

The advantages of bias sputtering can be listed as follows:

1. The substrate surfaces can be cleaned in the deposition chamber (bias etching) which means a final surface finishing before deposition to remove any contaminants from the surface in an atomic matter and also surfaces would be activated by this operation.
2. Bombardment during the nucleation stage of film deposition can increase the nucleation density.
3. Bombardment during interface formation adds thermal energy to the surface and introduces lattice defects into the surface region which promotes diffusion and reaction.
4. Bombardment during film growth results with the increase of the film density. It causes recoil displacement of near surface atoms (atomic peening), causes sputtering and redeposition, bombardment aids chemical reactions on the surface and the presence of plasma activates reactive species. The bombardment can also preferentially remove unreacted species [24].

There are different terms for different configurations used to bombard the growing film; bias sputtering, bias sputter deposition, ion plating, ion vapor deposition, ion beam enhanced deposition (IBED), ion beam assisted deposition (IBAD), ionized physical vapor deposition (iPVD), plasma enhanced magnetron sputtering (PEMS) are some of them found in the literature. It has to be noted that at the beginning, the aim of auxiliary plasma configurations was only the effective bombardment of the

growing film by ions of the sputtering gas while sustaining the plasma onto the substrates. However, recent advances in the sputtering technique and power supplies led also post-ionization of the neutrals ejected from the target materials. Especially the term i-PVD coined at the beginning of 2000's refers the case that the deposition flux consists of more ions than neutrals. Hence, the ions of the film forming material named "film ions" are guided more precisely towards the complex shaped substrates. Inner sides of the materials can also be coated by this way. The growing film is bombarded by mostly its own ions (film ions) and even self-sputtering applications without a precursor gas, thus without impurity incorporation is possible. However, it is not the subject of the present study and extensive review on the ionized PVD can be found in [44,45].

### **2.2.5 Reactive Sputtering**

Reactive sputtering is a process in which a fraction of at least one of the coating species enters the deposition system in the gas phase [19]. The first observation on the deposition of compounds by sputtering in a reactive gas for use as optical coating was reported by Overbeck in 1933 [46]. The term "reactive sputtering" was introduced by Veszi in 1953 [2].

With the incorporation of reactive gas, a wide variety of compounds including oxides, nitrides, carbides, sulfides may be deposited from a metallic or a compound target. A brief list of most common reactively sputtered compounds can be given as follows;

1. Oxides (oxygen) –  $\text{Al}_2\text{O}_3$ ,  $\text{In}_2\text{O}_3$ ,  $\text{SnO}_2$ ,  $\text{SiO}_2$ ,  $\text{ZnO}$ ,
2. Nitrides (nitrogen, ammonia) –  $\text{TiN}$ ,  $\text{AlN}$ ,  $\text{Si}_3\text{N}_4$ ,  $\text{TaN}$
3. Carbides (acetylene, methane, propane) –  $\text{TiC}$ ,  $\text{SiC}$ ,  $\text{WC}$ ,  $\text{B}_4\text{C}$
4. Sulfides ( $\text{H}_2\text{S}$ ) –  $\text{CdS}$ ,  $\text{CuS}$ ,  $\text{ZnS}$
5. Oxycarbides and oxynitrides of  $\text{Ti}$ ,  $\text{Ta}$ ,  $\text{Al}$ ,  $\text{Si}$  [39]

Desired gas composition and flow for reactive sputtering can be established by monitoring the partial pressure of the reactive gas as a function of gas flow in the deposition reactor [24]. Chemical reactions to form compound thin films can occur at

the target surface, at the substrate or at high working pressures, in the gas phases [19]. The most important problem in reactive sputtering is to prevent the poisoning of the sputtering target by the formation of a compound layer on its surface. This layer greatly reduces the sputtering rate and efficiency, and could even stop the process by forming a non-conductive layer while using DC power supplies [24]. The advantages of reactive sputtering can be listed as follows; compounds can be formed by using relatively easy to fabricate metallic targets, insulating compounds can be deposited by DC power supplies with a special care to target poisoning, films with graded compositions can be formed by step by step adjustment of the reactive gas flow [19].

### 2.3 Film Growth and Microstructural Evolution

The growth of vacuum deposited films proceeds in three general steps as indicated schematically in Figure 2.17. The first step involves the transport of the coating species to the substrate. The second step involves the adsorption of these species onto the substrate surface or growing coating, their diffusion over this surface, and their incorporation into the coating or their removal from the surface by evaporation or sputtering. The third step involves movement of the coating atoms to their final position within the coating by processes such as bulk diffusion [47].

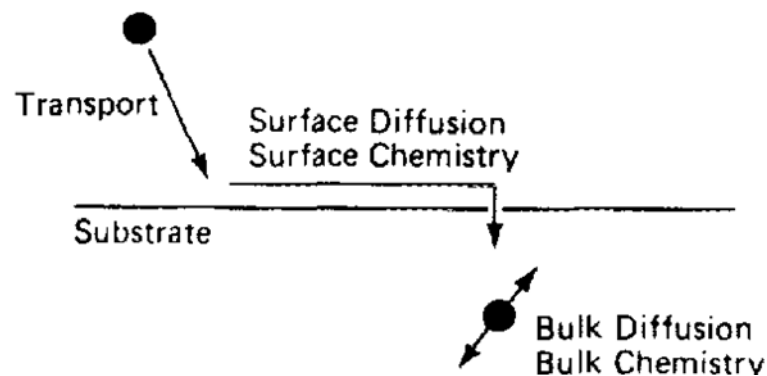


**Figure 2.17:** Steps involved in the condensation of a vapor during film growth [47].

In the case of sputtering, the primary deposition variables which determine the nucleation, growth kinetics and microstructural properties of films are; the film material, the incident film flux, the kinetic energy  $E$  of species incident at the film growth surface, the film growth temperature  $T_s$ , the flux of contaminants, and the substrate material surface cleanliness, crystallinity and orientation [48].

### 2.3.1 Nucleation mechanisms in thin film growth

For atomistically deposited films using vapor phase deposition techniques, there are three primary modes of film growth on substrates as illustrated schematically in Figure 2.18.

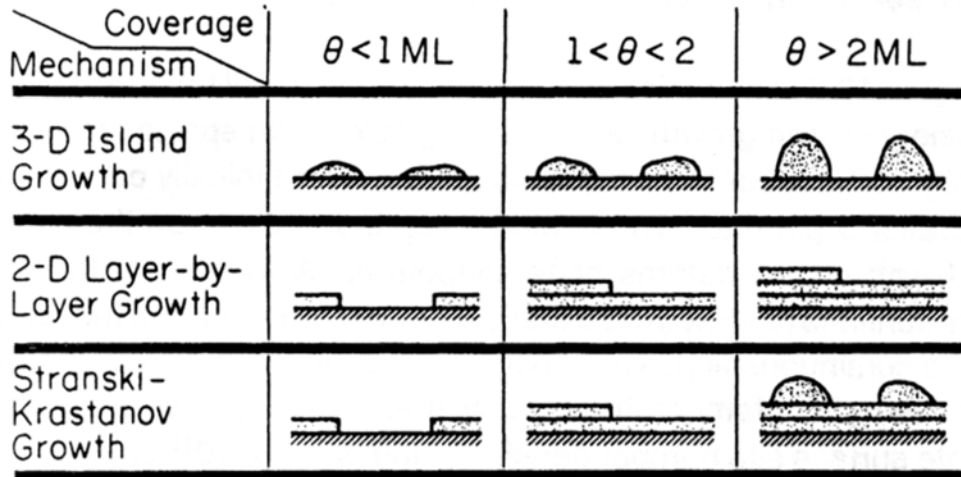


**Figure 2.18:** Schematic representation of three film growth modes where  $\theta$  is the overlayer coverage in monolayers (ML) [49].

Three-dimensional (3-D) island, or Volmer-Weber growth, in this growth mode, the adatoms (adsorbed atoms that are mobile on a surface) diffuse on the surface and interact with other adatoms or reevaporate. A fraction of the adatoms nucleates directly on the substrate surface as small clusters. The clusters then grow into islands which in turn coalesce to form a continuous film as shown schematically in Figure 2.19 and by TEM observations in Figure 2.20 respectively [20,39,49]. This type of growth occurs when the film atoms are more strongly bound to each other than to the substrate [48]. 3D nucleation can initiate at active surface sites, atomic steps and impurities. However, even if there are no active nucleation sites on the surface, 3D nuclei can still form at random surface locations by the spontaneous accumulation of mobile adatoms. Thus formed stable nuclei, which are bigger than a critical size, overcome the nucleation barrier and form clusters [39]. The columnar growth of physical vapor deposited films is the most well known example of 3D growth and will be explained in details in the next section.

In 3D growth, at sufficiently high deposition rates and/or low deposition temperatures, resultant films are amorphous since the adatoms do not have enough time to diffuse across the surface, consequently they cannot find low energy sites

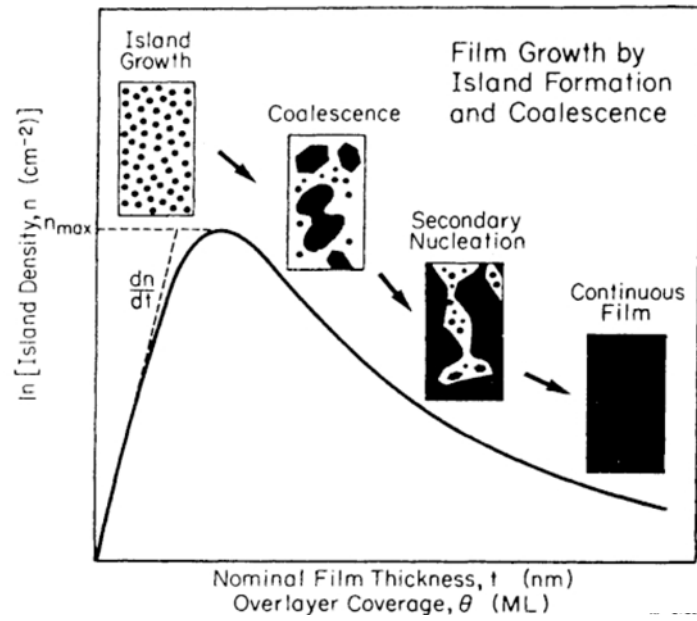


**Figure 2.19:** Schematic representation of the island density  $n$  as a function of the coverage  $\theta$  during three-dimensional growth [48].

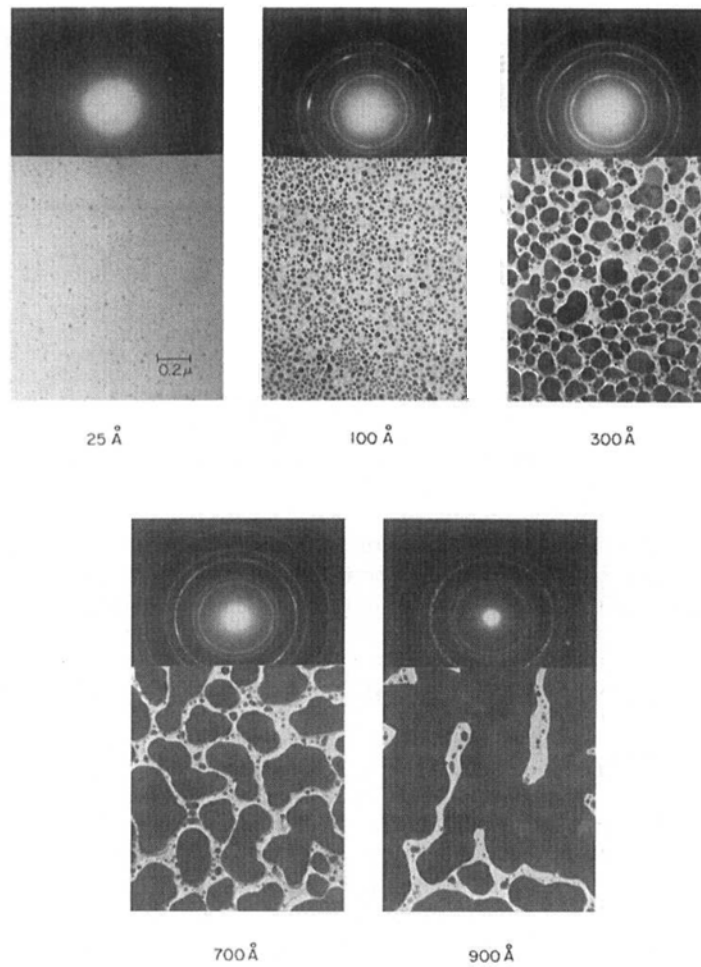


**Figure 2.20:** Nucleation, growth and coalescence of Ag films on (111) NaCl substrates [39].

before they are buried by subsequently deposited adatoms [49]. Covalently and ionically bonded materials have low packing densities and strong bonding directionality, thus easily deposited in the amorphous state [49]. Metals exhibit much higher diffusivities and are considerably more difficult to obtain in the amorphous state [49].

Two-dimensional (2-D) layer-by-layer, or Frank-van der Merwe, growth occurs when the binding between film atoms is equal to or less than that between the film atoms and the substrate [20]. In 2D growth, there is no nucleation barrier, hence the adsorbing atoms do not accumulate into 3D islands but, instead, spread out on the surface in a partial monolayer as shown in Figure 2.18 [19,39]. The most important examples of this growth mode are the homoepitaxial growth of Si on Si or heteroepitaxial growth of semiconductor AlAs films on GaAs. There are other examples of 2-D growth in metal-metal systems such as Cd on W growth [39,49].

Stranski-Krastanov growth is a combination of the first two. In this case, after first forming one or more monolayers, further layer growth becomes unfavorable and 3-D islands form. The transition from 2-D to 3-D growth is not completely understood but can be driven in some cases by the release of elastic energy stored in the film due to film/substrate lattice mismatch. This growth mode occurs much more frequently in metal-metal and metal-semiconductor system [49].

### **2.3.2 Microstructure evolution and structure-zone diagrams**

After a growth mode has been established, the film morphology can be described by a Structure-Zone Diagram (SZD). Movchan and Demchishin [50] were the first to categorize microstructures observed in vapor-deposited films using a SZD in which the general features were schematically illustrated as a function of the normalized growth temperature,  $T/T_m$  as shown in Figure 2.21. Where  $T$  is the substrate temperature and  $T_m$  is the melting point of the coating material. Based primarily upon optical metallographic studies, they concluded that their evaporated thick coatings (0.3 to 2 mm) of Ti, Ni, W,  $ZrO_2$ , and  $Al_2O_3$  could be represented as a function of  $T/T_m$  in terms of three zones, each with its own characteristic microstructure and physical properties.

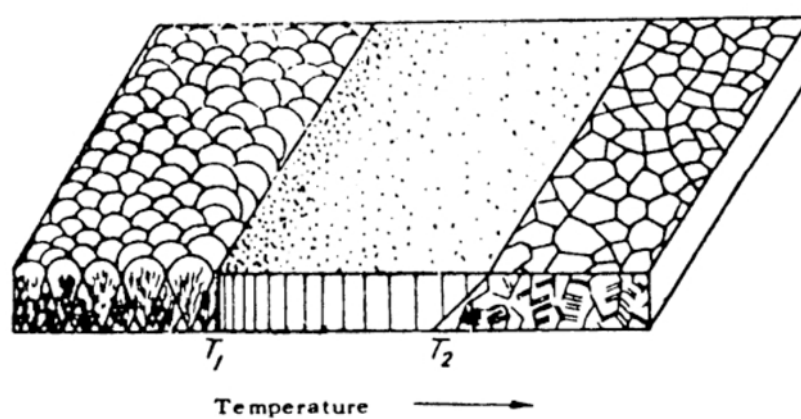


**Figure 2.21:** Movchan and Demchishin (MD) structure-zone diagram [50].

The low temperature ( $T/T_m < 0.2 - 0.3$ ) zone 1 structure was columnar, consisting of tapered units defined by voided growth boundaries. The zone 2 structure ( $0.3 < T/T_m < 0.5$ ) consisted of columnar grains which were defined by metallurgical grain boundaries. The high temperature zone 3 ( $0.5 < T/T_m < 1$ ) structure consisted of equiaxed grains. The simplicity of the Movchan and Demchisin SZD insured its popularity and many researchers showed that the general features represented in the diagram also applied to films with thickness in the order of micrometers rather than millimeters, and also to films deposited by other techniques such as sputtering, and to polycrystalline as well as amorphous materials [49].

Thornton, in 1974, extended the Movchan and Demchishin (MD) SZD by adding an additional axis for the pressure of the sputtering gas during cylindrical-post magnetron sputter deposition of relatively thinner (compared to MD), 25–250  $\mu\text{m}$  Ti, Cr, Fe, Cu, Mo, and Al coatings [51]. In Thornton's SZD which is shown in Figure 2.22, the sputtering gas pressure  $P$  is not a fundamental parameter. Rather, the pressure affects the film microstructure through several indirect mechanisms. Increasing the pressure to values such that the mean-free path for elastic collisions between sputtered (or evaporated) species and the gas becomes of the order of the target-substrate distance increases the oblique component of the deposition flux resulting in a more open zone-1 type structure. In addition, the energy of sputtered atoms and therefore, adatom mobilities on the substrate surface are decreased as a result of collisions in the plasma. Finally, decreasing the pressure during sputter deposition results in increased energetic particle (neutral) bombardment, and hence densification, of the growing film [53].

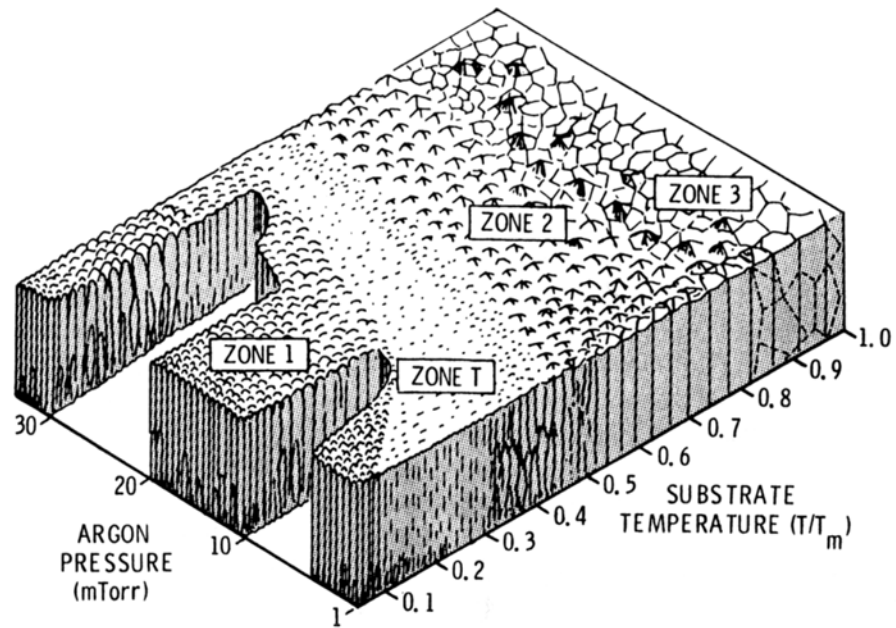


**Figure 2.22:** Structure-zone diagram showing schematic microstructures of films deposited by cylindrical magnetron sputtering as a function of growth temperature and Ar pressure [51].

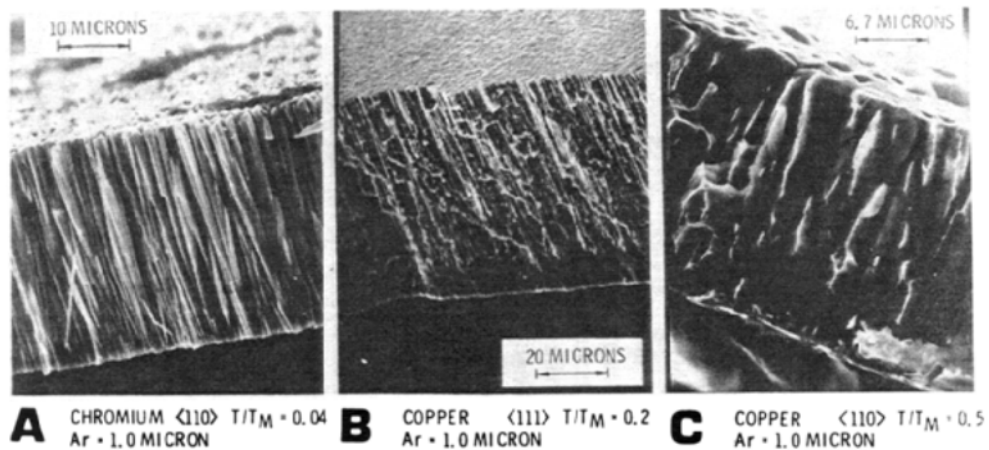


**Figure 2.23:** SEM cross-sections of metallic coatings showing different microstructures (a) zone 1 (b) zone T (c) zone 2 [51].

Thornton in his revised SZD, directly related the three zones in the MD SZD to the steps of vapor deposited film condensation given in Figure 2.17 as zone 1, atomic shadowing during transport, zone 2, surface diffusion and zone 3, bulk diffusion. He also added an additional region, labeled zone T that can be seen in Figure 2.22, which consists of a “dense array of poorly defined fibrous grains” and represents the transition between zones 1 and 2 according to his observations made by SEM. Examples of fracture cross-sections of metal coatings exhibiting zones 1, T, and 2 structures from Thornton’s study are shown in Figure 2.23.

After the SZD of Thornton, many researchers reported that the cross-sections of both polycrystalline as well as amorphous films deposited from vapor phase at low temperatures are typically composed of columnar structures with extended voids along the column boundaries [49]. Especially in the zone 1 regime, the columns are generally not single grains but are composed of smaller equiaxed grains, or can be completely amorphous [52].

This columnar structure is formed due to preliminarily clustering effects and atomic self-shadowing which occur in the very low adatom mobility. Shadowing induces open boundaries because high points on the growing surface receive more flux than valleys, particularly when a significant oblique component is present in the flux. Substrate surface roughness plays an important role on the production of columnar type structures by creating oblique deposition angles [47]. Limited surface diffusion of adatoms at low temperatures is also a very important factor for this type of structure [52]. Increasing adatom surface diffusion at higher growth temperatures (Zones T and 2) give rise to denser although still columnar structures while grain growth (recrystallization during deposition) occurs at deposition temperatures above  $0,5 T_m$  [49].

A revised version of Thornton SZD has proposed by Messier et al. in 1986 and is shown in Figure 2.24 [53].  $T/T_m$  is still preserved as being the most important parameter. However, argon pressure axis was converted to the bombardment energy in their study. As can be seen from the figure, at lower bombardment energies (or bias voltages) zone T is small and may even not exist. When the bombardment energy increases the width of the zone T increases although the study is limited to 100 eV bombarding energies.

The structure zone diagrams started from macro characterization for thick films with optical microscopy by MD, improved with microstructural SEM observations for thin films by Thornton and reached nanostructured thin films by Messier et al. who realized extensive studies on both relatively thick and very thin films (30 to 0.01  $\mu\text{m}$ ) by SEM, TEM and Field ion microscopy (FIM). As a function of film thickness they observed five characteristic column sizes which are: 1-3, 5-20, 20-40, 50-200 and 200-400 nm. The columns ranged from 1-3 nm for the thinnest films (15 nm) to 300 nm for the thickest films (10  $\mu\text{m}$ ) [53].

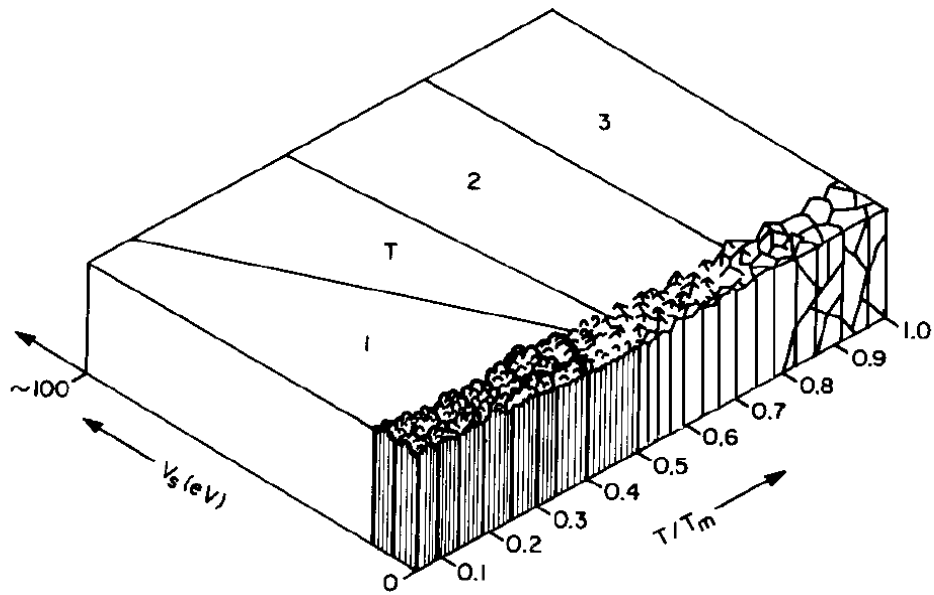


**Figure 2.24:** Structure-zone diagram showing the effects of both bombardment and thermal induced mobility [53].

Computer simulations of film growth and microstructural evolution have been shown to qualitatively explain many of the features observed experimentally. In addition, the simulations provide a very useful tool for visualizing atomistic model of film growth. Figure 2.25 shows a Monte Carlo simulation of film growth realized by Dirks and Leamy using hard-sphere atoms which are incident at randomly chosen surface positions [54].

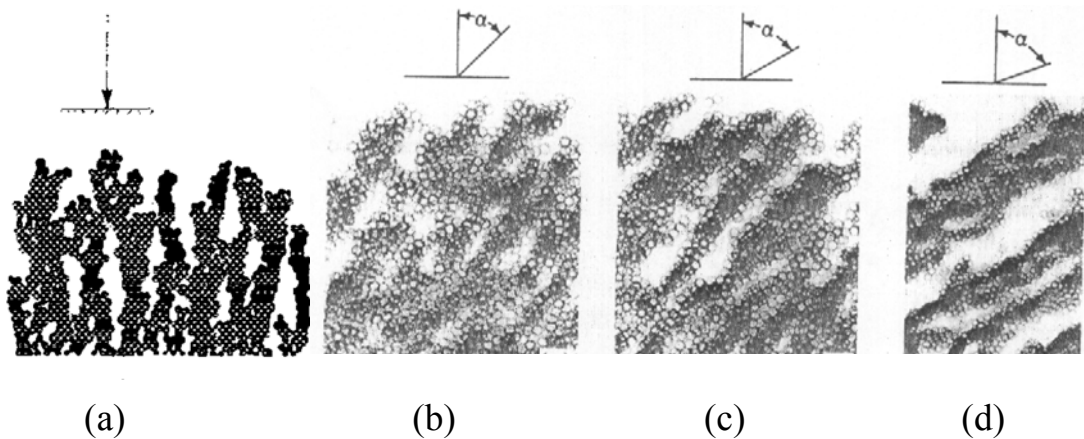


**Figure 2.25:** Monte Carlo computer simulations of amorphous films deposited with incident flux angles (a) 90° (b) 45° (c) 60° (d) 75° [54].

The adatoms are not allowed to diffuse over the surface but only to relax into the nearest lying cradle formed by at least two deposited atoms. Consequently, extended microvoid formation leading to columnar microstructures occurs due to atomic

self-shadowing by projecting clusters and small edges. From Figure 2.25, it can be clearly seen that, the columnar structure becomes increasing more noticeable with larger angles of incidence  $\alpha$ , measured with respect to the substrate surface normal.

The effect of temperature was studied by Müller who included adatom migration effects in microstructure evolution growth simulations. He allowed thermally adatoms to jump to empty neighboring sites of maximum coordination number. He found that above a critical temperature range, the porous columnar microstructure changes to a configuration of maximum packing density [55]. The lower three atom layers in Figure 2.26 correspond to the substrate. The typical open columnar structure characterizing low adatom mobility growth was obtained at  $T_s=350$  K. Increasing the deposition temperature to 420 K resulted in a film with higher density, although still columnar. At  $T_s=450$  K, a fully dense film with local defects was obtained [55].

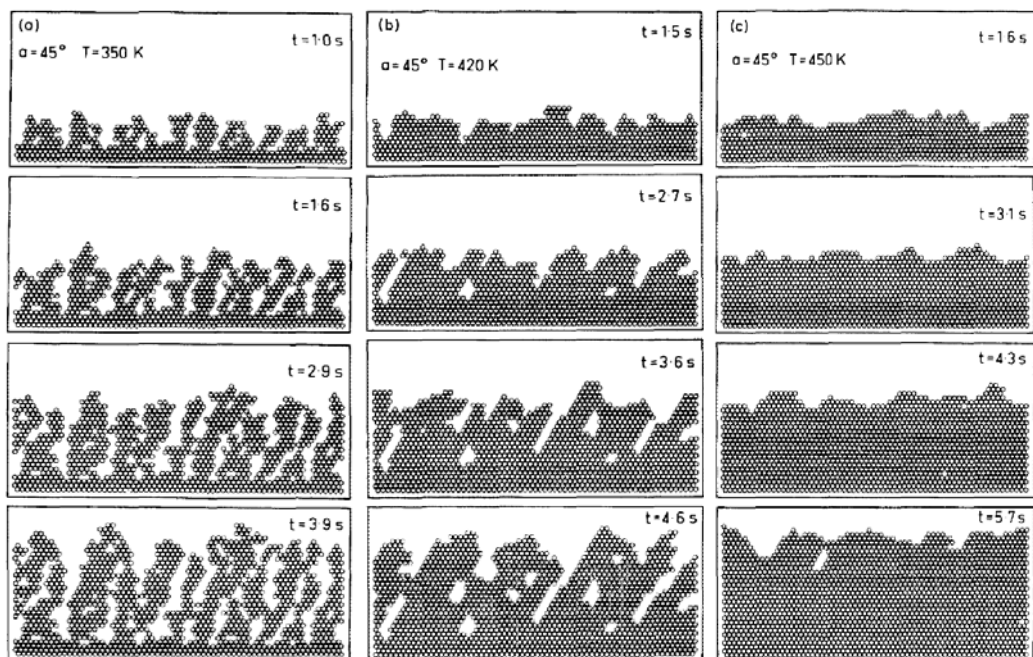


**Figure 2.26:** Computer simulated microstructures of Ni films during deposition at different times ( $t$ ) for substrate temperatures of (a) 350 K (b) 420 K and (c) 450 K [55].

As a result of the microstructural investigations coupled with computer simulations, it is evident that the columnar structure observed in atomistically deposited films with open boundaries characteristic of zone 1 in the Thornton diagram, is formed due to atomic self-shadowing and clustering effects which occur at low  $T/T_m$ , at very

low adatom mobility and in presence of oblique flux independently of whether resultant films are crystalline or amorphous. Increasing adatom surface diffusion by increasing growth temperatures result with denser columnar films. Crystallization of amorphous films or recrystallization and grain growth of already crystalline films occur probably above  $0.8 T_m$ .

It should also be noted that, although there are researches on the manipulation of growth kinetics, these are quite limited with more idealized growths such as 2D or layer by layer growth of the thin films and especially homoepitaxially growth [56]. When the deposited material and the substrate are very dissimilar, as in many cases of hard tribological coatings deposited by sputtering, the growth becomes rapidly 3D, that is, the deposited material does not wet the surface [56]. For a given coating material and substrate couple, if these are not similar, a modification of nucleated clusters and 3D growth of the film by process parameters, such as deposition temperature, pressure, and ion irradiation (which will be explained in the next section) should be discussed for the changes in the microstructure, rather than a change in the film growth modes.

### **2.3.3 Ion bombardment effects during film growth**

Low energy ( $< 1$  keV) ion irradiation during vapor phase film growth can be used for the modification of film microstructure, densification and increase of the oxidation resistance, minimization or elimination of columnar microstructure, altering the state of stress, average grain size, and preferred orientation, increase film/substrate adhesion, enhance conformal coverage, and control magnetic anisotropy by a variety of techniques such as bias sputter deposition and ion plating (see Section 2.2.4) [19,49].

By bombarding the substrate with energetic ions before deposition, bias etching, in other words cleaning of the substrate in atomistic matter can be realized as a final surface preparation. In addition to sputter cleaning, ion bombardment can lead to fundamental changes in nucleation and growth, especially during the first stage of the film deposition. Examples of irradiation-induced effects which have been proposed and discussed in the literature include the production of defects in the substrate surface which can act as preferred adsorption sites, trapping or subsurface implanting of incident species in the near-surface region, the dissociation of small clusters

during the early stages of growth, localized high temperatures, enhanced adatom diffusion, and local electric field effects due to charging. Bombarding related effects are complex and all of these effects play a role under certain circumstances. There is no single mechanism that can explain all observed results. The effects, which dominate in a given case, depend upon the film/substrate materials combination, the energy  $E_i$ , flux  $J_i$ , and mass  $m_i$ , of the incident particles and the growth temperature  $T$  [49].

In areas such as optical and wear protective films, the application of ion irradiation to densify and increase the internal strength of the layers as well as to increase film/substrate adhesion is already a prerequisite to commercial success. However, ion irradiation during film growth can also be disadvantageous. There are numerous examples in the literature reporting the generation of very high compressive stress levels in the films, which lead to adhesion problems and premature delamination [48].

It is well known from the work of Thornton that, during growth at low substrate temperatures the films are generally underdense with a voided columnar microstructure. Numerous researches have shown that the number density of voids and pores decreases dramatically with increasing ion energy and/or ion flux. Mattox and Kominiak were among the first to demonstrate this effect. They found, in the case of sputter-deposited Ta films, the microstructure changed from a columnar morphology to a more equiaxed structure and that the film density increased from  $14.5$  to  $16.3 \text{ g cm}^{-3}$  (bulk density =  $16.6 \text{ g/cm}^3$ ) as the negative substrate bias was increased from  $0$  to  $500 \text{ V}$  [57].

Monte Carlo (MC) and molecular dynamic (MD) simulations realized by Müller visualized the basic interaction mechanisms between ions and film species occurring during ion bombardment and their effects on film growth. He used 2D MD calculations including up to 800 particles to simulate Ar ion assisted growth of Ni films on Ni substrates at  $T_s = 0 \text{ K}$  [58]. First, he simulated the case of a single ion that hits the surface of a porous film. Figure 2.27 and Figure 2.28 show structure rearrangements occurring at different times ( $t$ ) when an Ar ion of  $100 \text{ eV}$  strikes the surface.

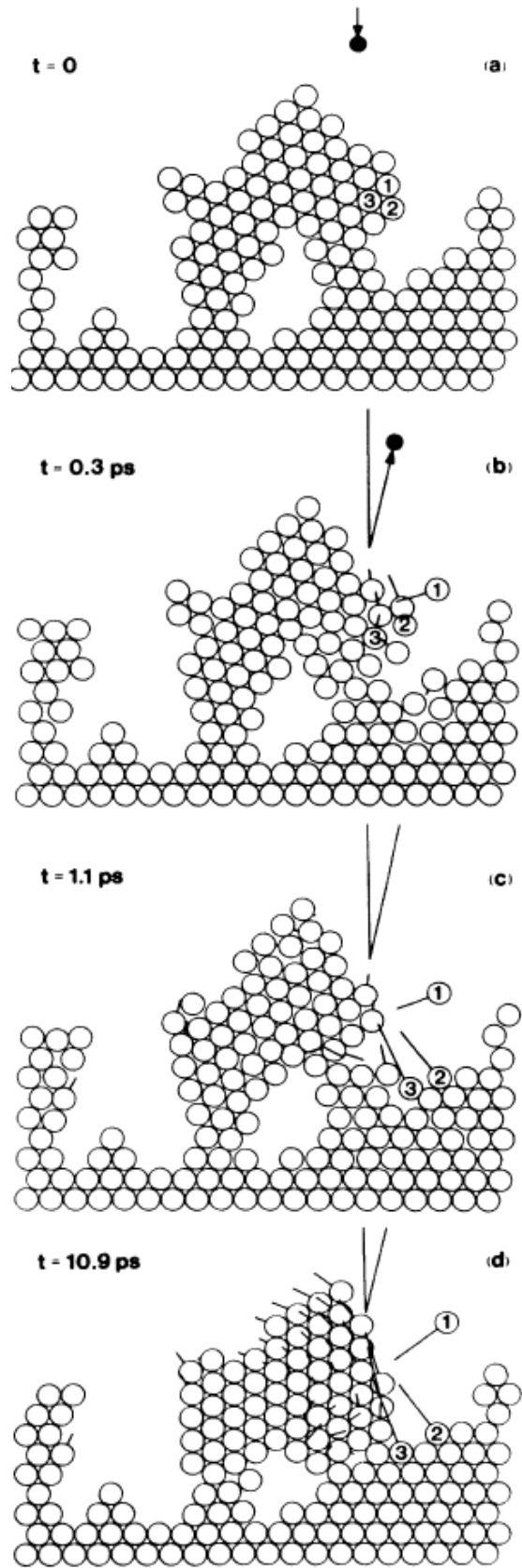


**Figure 2.27:** Molecular dynamic simulation of a collision sequence induced by a 100 eV Ar ion which hits the porous Ni film at different times (a)-(d) preventing the formation of a void [58].

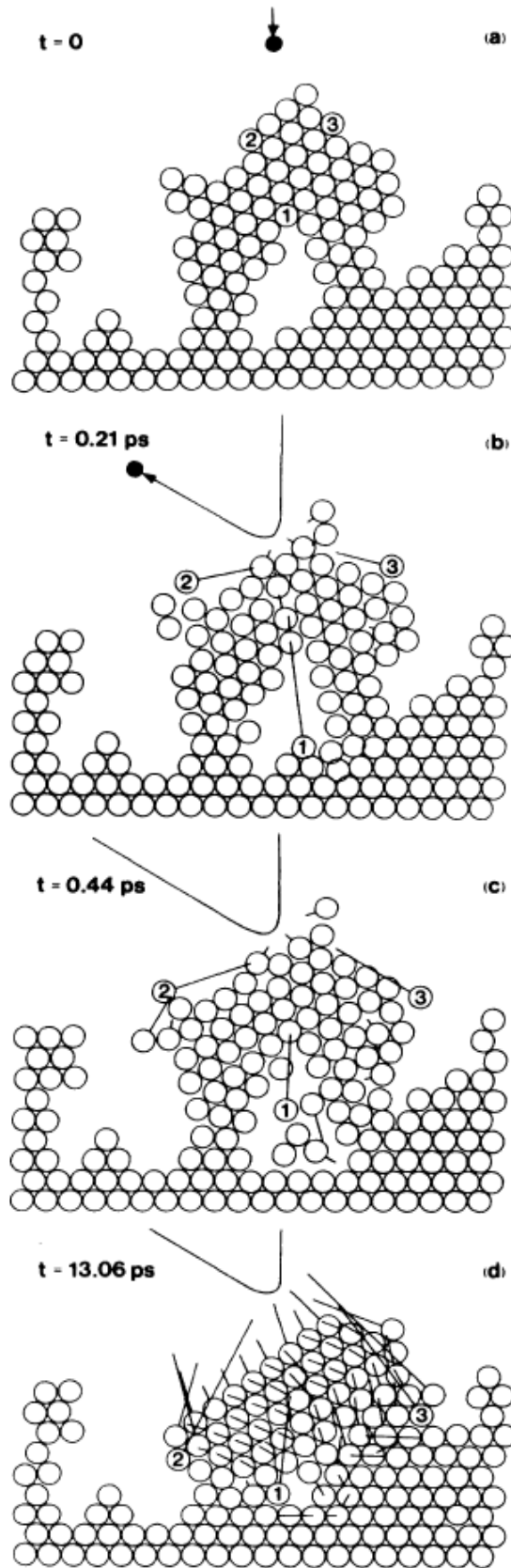


**Figure 2.28:** Molecular dynamic simulation of a collision sequence induced by 100 eV Ar ion which hits the porous Ni film at different times (a)-(d) showing the rearrangement of atoms in order to fill a closed void [58].

In both cases, the striking ion transfers a part of its kinetic energy to a few surface atoms, which transfer their kinetic energies to other film atoms resulting with a collision sequence. In Figure 2.27, the bombardment during growth removes overhanging atoms by forward sputtering and thus the void remains open until filled by new depositing atoms, preventing the formation of voids and columnar structure. Figure 2.28 visualizes how the striking ion causes the filling of a closed void by surface diffusion and local heating dominated atomic rearrangements [58].

After visualizing the microstructural changes caused by the cascade collisions from a strike of a single ion, Müller simulated also the microstructures obtained when large number of ions bombards the film during growth for more realistic results. In Figure 2.29, the substrate consists of 5 layers of 40 atoms in a row and a total of 500 atoms approach sequentially the surface of growing film [58].

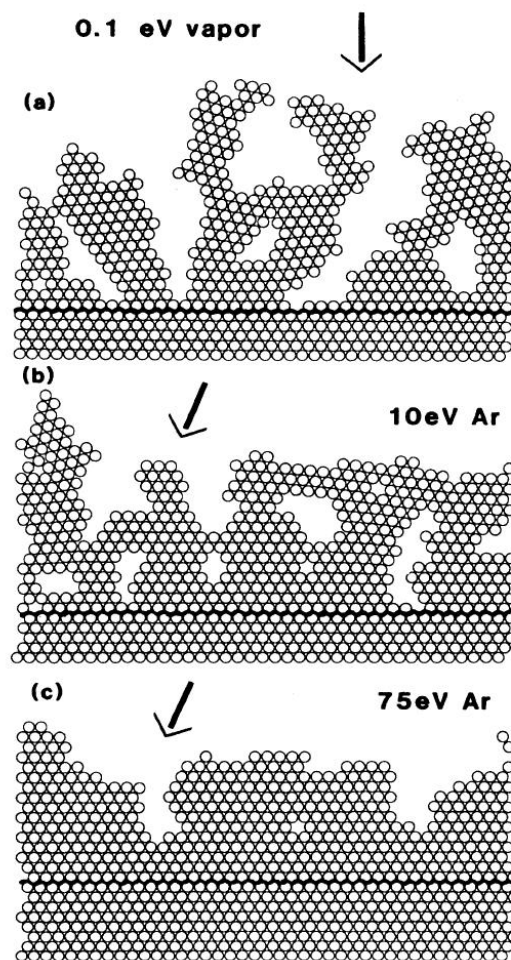


**Figure 2.29:** Molecular dynamic simulation of microstructures obtained (a) without ion bombardment (b) with 10 eV Ar ion bombardment (c) with 75 eV Ar ion bombardment [58].

As can be seen from the figure (a) the microstructure obtained by Müller by MD simulations, corresponds well the Monte Carlo simulation given in Figure 2.25 realized by Dirks and Leamy at normal angle of incidence. Both simulations at low adatom mobility resulted with voided columnar microstructures. In (b) with 10 eV Ar bombardment, the densification effect can be clearly seen although the structure has still large voids. Finally in (c) at 75 eV Ar bombardment a nearly fully dense microstructure with local defects can be observed

Although simulations such as these are not intended to correspond to a particular physical reality, they do provide a means for visualizing the general effects of ion irradiation on the atomic level.

The calculations also predicted that there should be an optimum ion energy  $E_i^*$  for densification; at  $E_i < E_i^*$  the number of recoil events is small and there is a linear increase in the density with the increase of ion-to-vapor flux ratio while at  $E_i > E_i^*$  an increasing fraction of the ion energy is lost deeper in the lattice, hence a decrease in the density for the ion energies above the critical value is predicted. A good example of the comparison of both experimental and calculated data can be found in [59] for CeO<sub>2</sub> films. Müller found a linear increase in the density with the increase in the ion energy until 200 eV which is the optimum ion energy from both experimental and calculated results and then a linear decrease with further increase in the ion energies. This fact is proved by many researchers experimentally, not only by the density measurements but also with the rise and fall behavior of the hardness of various thin films obtained with different bias voltages hence, different ion energies.

## 2.4 Boron Carbide Thin Films

Boron carbide occupies an important place in the group of most important non-metallic hard materials. A boron carbide compound was first discovered in 1858, then Joly in 1883 and Moissan in 1894 prepared and identified the compounds B<sub>3</sub>C and B<sub>6</sub>C respectively [60]. The stoichiometric formula B<sub>4</sub>C was assigned in 1934 [60].

Boron carbide (B<sub>4</sub>C) is the third hardest material at room temperature, surpassing even diamond and cubic boron nitride at temperatures over 1100 °C, it has many

other attractive properties such as good wear resistance, low specific weight, high modulus, high thermal stability. It is chemically inert and not attacked by cold chemical agents. It has very high neutron absorption cross-section. [60,61,62,63,64,65]. Boron carbide is p-type semiconductor material even at very high temperatures [65]. In bulk form, it is currently used in grinding wheels for sharpening cutting tools, as abrasives in polishing, lapping and grinding media, in sand-blasting nozzles due to its high wear resistance, fibers for reinforced ceramic composites, lightweight armors, and high-temperature thermoelectric conversion [60,66]. Due to its high neutron absorption capability it is also used as a neutron shielding material, as a poison in fuel elements and in nuclear control rods [60,65]. General properties of boron carbide can be seen in Table 2.1.

**Table 2.1:** General properties of boron carbide [60,65,100].

| Properties of boron carbide                           |  |
|---|--|
| Molecular weight (g/mol)                              | 55.26  |
| Density (g/cm <sup>3</sup> )                          | 2.52 – 2.465 for B <sub>4</sub> C-B10.4C                           |
| Melting point (°C)                                    | ~ 2400 (does not decompose)  |
| Specific heat (Cal/mol K at 300 K)                    | 12.7   |
| Heat of formation (-ΔH) (kJ/mol K at 298.15 K)        | 57.8 ± 11.3  |
| Thermal conductivity (W/cm K)                         | 0.35-0.16 (25-800 °C)  |
| Thermal expansion (1/K)                               | 4-8 E <sup>-6</sup> (25-800 °C)                                    |
| Electrical resistivity (Ω cm)                         | B <sub>13</sub> C <sub>2</sub> : 2, B <sub>4</sub> C: 5 (at 298 K) |
| Electrical conductivity(1/ Ω cm)                      | ~ 10 <sup>3</sup>  |
| Band gap (eV)   | 0.77-1.80  |
| Dielectric constant                                   | 5  |
| Seebeck coefficient (μV/K)                            | 200-300  |
| Vickers hardness (GPa)                                | 27.4-40  |
| Young's modulus (GPa)                                 | 290-460  |
| Shear modulus (GPa)                                   | 158-200  |
| Bulk modulus (GPa)                                    | 190-250  |
| Tensile strength (N/mm <sup>2</sup> )                 | 155 (980 °C) 162 (1425 °C)   |
| Toughness (K <sub>Ic</sub> ) (M Pa m <sup>1/2</sup> ) | 1.3-3.7  |
| Poisson's Ratio                                       | 0.14-0.18  |
| Flexural strength (MPa)                               | 323-430  |
| Velocity of sound (m/s)                               | 14400  |
| Lattice constant (nm)                                 | c = 1.207 a = 0.561  |
| Oxidation resistance                                  | In air up to 600°C.  |
| Chemical resistance                                   | Generally excellent. Reacts with halogens at high temperature.     |
| Absorption Cross Sec. for Thermal Neutrons (barn)     | 755  |

In thin film form, it is considered a promising candidate as hard and protective coatings for cutting tools, automobile parts, hard disk drives and other wear-resistance and corrosion-resistance applications [62,64,67]. It is reported that boron carbide properties suggest applications in tribological systems under high load and/or elevated temperatures [68,69]. It has also been reported that B<sub>4</sub>C coating is used by General Motors to protect sun gears from fatigue pitting in transmissions that are used in the Volvo S80 Turbo [68]. B<sub>4</sub>C finds an important application area as first wall protective coating material in fusion devices, in thick film form [65]. Thin film boron carbide is also a candidate material for the electronic devices that can be operated at elevated temperatures and an excellent thermoelectric material especially at elevated temperatures due to its high temperature stability [70]. It is considered to be a good candidate material for semiconductor devices in harsh environments as heterojunction diodes with silicon [71]. Its usage in high intensity electron emitting devices is also reported [72].

Interestingly, as it is mentioned by several authors as well, despite of its significant properties, boron carbide thin films have not been investigated extensively, especially regarding the effect of deposition parameters on the coating properties [63,73,74]. However, it has to be noted that, this lack of knowledge did not prevent the industrial applications of B<sub>4</sub>C thin films. Between 1982 and 1987, Bodycote Inc. (Conover, NC, USA) patented the sputter deposition of boron-carbon containing coatings, including boron carbide and a large variety of multilayer design [75,76,77,78,79]. Although their patents are full of interesting information such as lubricity of boron carbide (see Section 2.4.4), the formation of columnar structure with the increase in applied bias voltages (see Section 2.3.3) or the decrease of internal stresses with the increase in bias voltages (see Section 2.3.3), the company has commercialized boron carbide coatings with the trademark DiamondBLACK<sup>TM</sup>. It is also known that IonBond Inc. (Olten, Switzerland) commercializes boron carbide coatings after the merger of two companies in 2004.

Several techniques have been used to synthesize boron carbide thin films, including chemical vapor deposition (CVD) [65,80,81], plasma-enhanced chemical vapor deposition [82,83], supersonic plasma jet CVD [84,85], laser CVD [67,86], cathodic arc [87], ion-beam evaporation [88], mass selected ion beam deposition (MSIBD) [89], pulsed laser deposition [72,90,91], atmospheric plasma spraying [92], vacuum

plasma spraying [93], electromagnetically accelerated plasma spraying [94], ion beam sputtering [95], RF magnetron sputtering [61,62,63] and DC magnetron sputtering [74,96,97,98]. Among these, magnetron sputtering techniques have been successfully commercialized in a large scale because of their high film-deposition rate and low-temperature features [99].

#### 2.4.1 Phase diagram and structure

Many controversial phase diagrams have been proposed for B-C in the period of 1955-1960 [60]. The most widely accepted standard diagram for this binary system was introduced by Elliott in 1961 [60] and is shown in Figure 2.30.

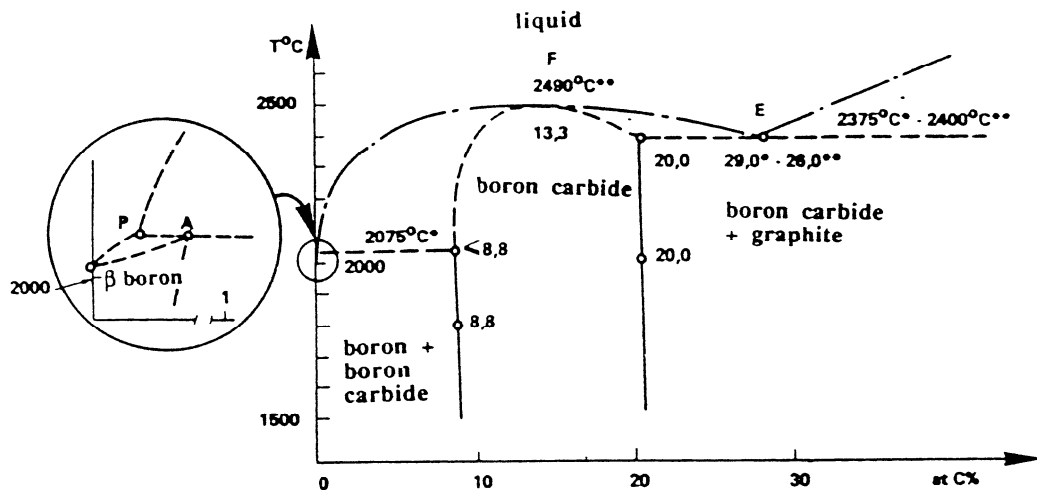
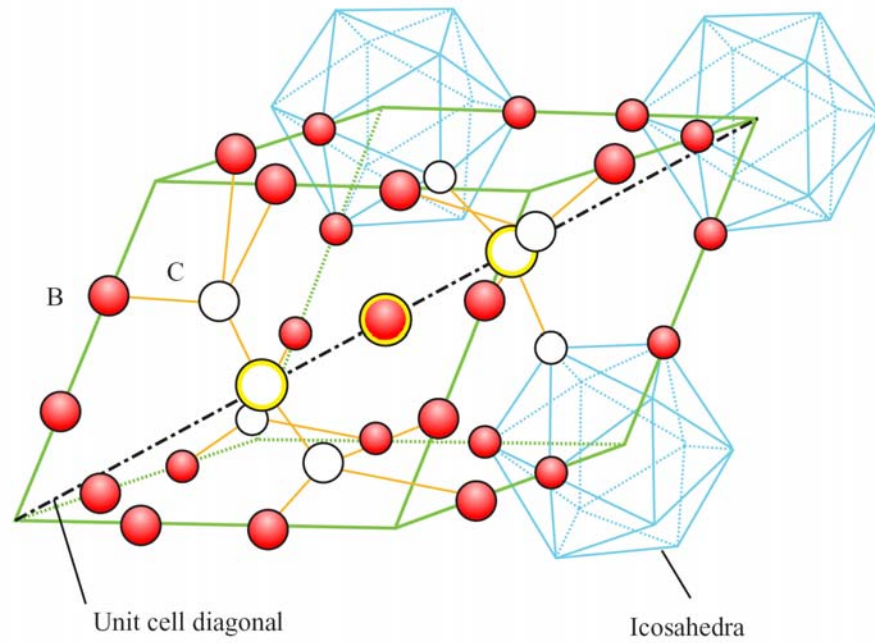


Figure 2.30: Boron-carbon phase diagram [60].

According to the phase diagram, boron carbide has a wide phase homogeneity range between 9-20 at.% C (with a relative accuracy of 3-5%). An eutectic between  $B_4C$  and C at 26 at.% C at 2400 °C can also be seen from the binary phase diagram given in the figure. As a result of this wide homogeneity range, the term boron carbide and its chemical formula “ $B_4C$ ” is used generically to describe stoichiometric as well as various non-stoichiometric phases in the literature.

The crystal structure of boron carbide is rather unique and ideally described by a rhombohedral unit cell with icosahedral arrangement of 12 atoms, in addition to a three-atom chain along the crystallographic c-axis that interconnect the icosahedra [60,100]. Figure 2.31 and Figure 2.32 show rhombohedral unit cell and crystal structure of boron carbide respectively.



**Figure 2.31:** Rhombohedral unit cell of boron carbide [60,101].

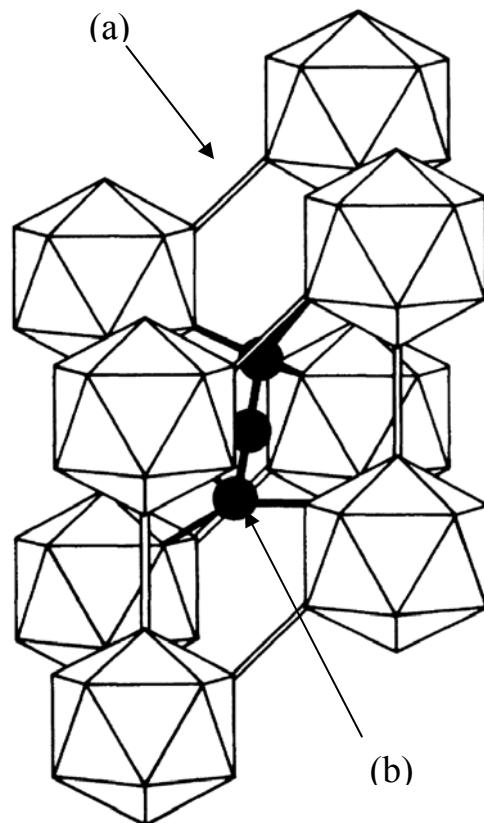


**Figure 2.32:** Rhombohedral crystal structure of boron carbide (a) each icosahedron is bonded to six other icosahedra through direct bonds (b) three atom intericosahedral chains that connect icosahedra [65].

The 12 atoms of the icosahedra and 3 atoms of the intericosahedral chain form a 15-atom unit cell. Four sites are available for 15 B and C atoms in the crystal arrangement. Thus, B and C atoms can easily substitute for each other within both the icosahedra and the intericosahedral chains. This fact is the main reason for the large homogeneity range of boron carbide [60,65]. The most widely accepted structural model for  $B_4C$  with 20 at.% C has  $B_{11}C$  icosahedra with C-B-C intericosahedral chains ( $B_{12}C_3$ ) [60,65].

Recent studies on boron carbide bonding properties by IR, Raman spectroscopy and XRD demonstrated that with the decrease of C content in the boron carbide structure, the intericosahedral C-B-C chains are replaced with C-B-B ( $B_{13}C_2$ ) chains until they are nearly depleted. Further decreases in the carbon content result in the replacement of  $B_{11}C$  icosahedra with  $B_{12}$  icosahedra. Several metastable boron carbide phases prepared by CVD have also been reported, such as  $B_{51}C$ ,  $B_{50}C$ ,  $B_{25}C$ ,  $B_{49}C_3$ ,  $B_{48}C_3$  (all tetragonal) and  $B_8C$  (orthorhombic). However, these phases are more difficult to prepare than the rhombohedral phase, their physical properties are not well known and usually not considered in metallurgical phase diagrams. Therefore, it can be stated that the most stable boron carbide structure is rhombohedral with a stoichiometry of  $B_{13}C_2$ ,  $B_{12}C_3$  or  $B_4C$ , and some other phases close to  $B_{12}C_3$  [60,65].

In thin film forms however, with a few exceptions, all reported sputter deposited boron carbide films in the literature are amorphous. It has to be noted that, for amorphous boron carbide structures, it is believed that the structure is still based on a random icosahedral network at a carbon content less than 50 at.% [95]. Chiang et al. have obtained crystalline boron carbide films at temperatures above 950 °C by RF sputtering [102]. Han et al. have suggested that with the increase of the temperature to about 450 °C boron carbide films deposited by DC magnetron sputtering shows a tendency of crystallization [103]. In a recent study, Kulikovskiy et al. demonstrated the possibility to deposit crystalline  $B_4C$  phase at temperatures above 900 °C by DC magnetron sputtering [104]. Chen et al. have demonstrated that by using ion beam sputtering, the boron carbide films crystallized at about 350 °C [105]. Lee et al. have deposited boron carbide films by reactive sputtering of a boron target in presence of methane gas as carbon source and suggested that the films were partially crystallized at 100 °C [106].

A few techniques other than sputtering were reported with resultant polycrystalline boron carbide films. Chemical vapor deposited boron carbide films were grown in polycrystalline form as a result of elevated deposition temperatures needed for film forming in this technique [65,84]. It is reported that in a conventional CVD when depositing boron carbide, the reactions take place at temperatures in the range of 1000–1600 °C [86]. For the modified CVD processes such as supersonic plasma jet [84] or plasma-enhanced CVD [82] crystalline boron carbide films can be deposited at relatively lower temperatures in order of 500–600 °C, but no film deposition is possible below this temperature range [84]. The use of hazardous gases such as BCl<sub>3</sub> and boranes (e.g. B<sub>2</sub>H<sub>6</sub>) in case of boron carbide, the lack of thickness homogeneity and significantly elevated temperatures which are destructive for most substrates limit the industrial scale usage of CVD.

Suematsu et al. have showed the possibility to deposit crystalline boron carbide thin films at room temperature without external heating, by pulsed ion-beam evaporation [88]. However, this is a laboratory scale technique and is not yet suitable for large-scale industrial applications mainly due to the substrate dimension limitations.

O.R. Monteiro et al. have prepared partially crystallized boron carbide films by cathode arcing [87]. However, the technique needs the use of high conductivity targets and hence, does not effectively suitable for mostly semiconductor boron carbide targets. The authors surpassed this handicap by increasing the temperature of the cathode while increasing also the amount of droplets incorporated into resultant boron carbide coating surface.

As a result, it is clear from the literature that sputtering is the most used and convenient technique for boron carbide and derived thin films deposition, especially for its ease of operation, universality, relatively high deposition rates and integration to industrial scale usage. Sputter deposited boron carbide films are mostly amorphous and they tend to crystallize at elevated temperatures which are above the practical limits for most PVD systems. However, as will be seen in the next section, although they are amorphous, sputter deposited boron carbide films have mechanical properties comparable and even superior to that of crystalline bulk boron carbide

## 2.4.2 Sputtering yield of boron carbide

As presented in Section 2.1.4, sputtering rates were measured especially for pure metals and some alloys. For boron carbide, a lack in sputtering data in the literature exists. It can be found only a computational measurement study using Monte Carlo simulation, realized by Ono et al. [107]. The motivation for their study was not sputter deposition applications of boron carbide, instead they realized these measurements for different ion irradiation such as  $H^+$ ,  $D^+$ ,  $T^+$ ,  $He^+$ ,  $Be^+$ ,  $C^+$ ,  $Ne^+$ ,  $Ar^+$  and  $Kr^+$  to investigate the erosion of thick boron carbide films used in nuclear industry, especially as plasma facing materials in fusion devices. As mentioned by the authors, there are no experimentally comparable data for  $Ar^+$  ion irradiation of boron carbide. However, the simulations and experimental results fit well for H, D, T, He, C and Ne ions. Thus in Figure 2.33 the simulated data is given for the sputter yield of boron carbide.

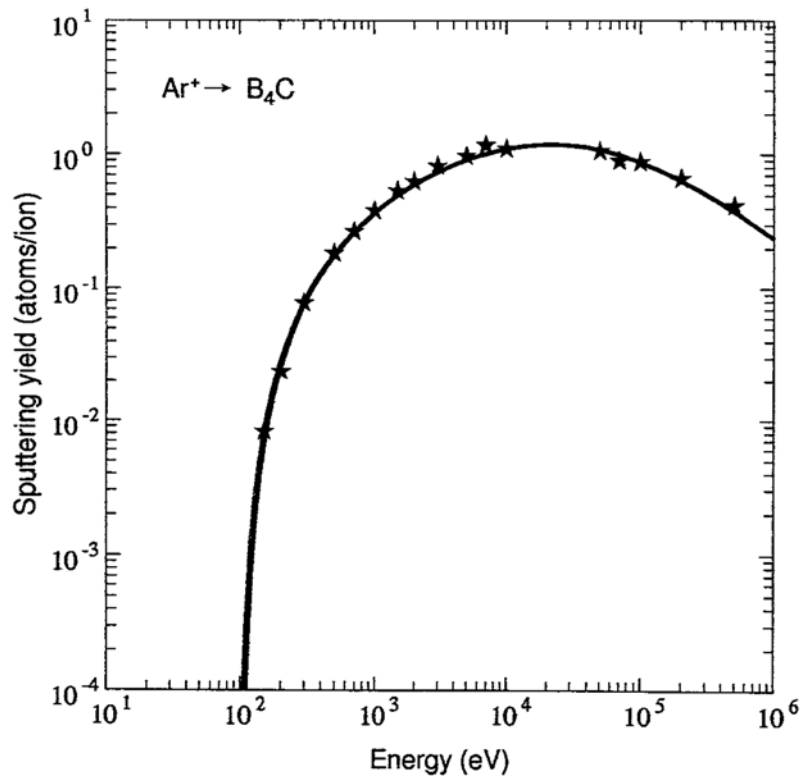


**Figure 2.33:** Sputtering yield versus energy of incident  $Ar^+$  ions for boron carbide [107].

The surface binding energy of carbon and boron are 6 eV and 5.6 eV respectively [108]. At a bombardment energy of 1 keV, the sputter yields for boron and carbon amount to 0.54 and 0.135 respectively. With  $B_4C$  stoichiometry taken into account,

no preferential sputtering effect is expected [114]. When compared to the sputtering yield of most metals given in Section 2.1.4, it can be seen from the figure that the sputtering yield of boron carbide is very low. Thus, a low deposition rate could be expected for boron carbide thin films.

### 2.4.3 Mechanical properties

The general definition of the hardness will be given in Section 3.2.5. However, an empirical formula developed by Cohen (Eq.2.5) which relates the hardness of a material to its bulk modulus,  $B$ , is more generically used for covalently bonded hard and super-hard materials [109,110].

$$B = \frac{\langle N_c \rangle}{4} \frac{1971 - 220 \times \lambda}{d^{3.5}} \quad (2.4)$$

Where,

$B$  is the bulk modulus in GPa,  $N_c$  is the average coordination number,  $d$  is the bond length in  $\text{\AA}$  and  $\lambda$  is a parameter describing the ionicity of the chemical bonding. According to this equation, the bulk modulus of an ideal crystal depends on bond length  $d$ , the nature of the chemical bonding and the crystal structure. Solids with small covalent bonds exhibit the highest bulk modulus. It can be concluded from the equation that the lower the bond length of the material, the higher the bulk modulus thus the hardness. Diamond has the lowest known bond length of 1.54  $\text{\AA}$  and the highest bulk modulus of 435 GPa [111]. Liu and Cohen supposed that the hypothetical material  $\beta\text{-C}_3\text{N}_4$  is expected to be harder than diamond [111]. Although many groups tried to deposit this material, no really convincing evidence could be found up to now [112]. The ionicity  $\lambda$  depends on the electron wave functions and therefore on the electron densities. Typical  $\lambda$  values are 0 for diamond or silicon, 0.5 for  $\text{B}_4\text{C}$ , 1 for cubic boron-nitride (c-BN) and 2 for heteropolar compounds of Group II to VI elements [113].

This approach is believed to be valid also for amorphous boron carbide thin films as the amorphous structure is still based on a random icosahedral network and explains well the high hardness values obtained from boron carbide and other thin films in the ternary B-C-N system obtained with N incorporation into boron carbide structure.

For boron carbide thin films, the literature data on the hardness and Young's modulus are scattered. The hardest boron carbide film was reported by S. Ulrich et al. with 72 GPa [114]. The films were deposited by rf sputtering of a B<sub>4</sub>C target by applying bias voltages [113,114]. However, no details of the analyses procedures could be found in their article. The softer boron carbide films were reported by H.Y. Chen et al. with 13 GPa for the films deposited without external heating [105] and by H.S. Ahn et al. with 18 GPa [99]. A list of the literature survey on the mechanical properties of boron carbide films is shown in Table 2.2.

Boron carbide films shown in the table which are softer than 13 GPa were deposited with modifications in the processing gas, by adding different amount of acetylene or methane. Although the authors tend to name the coatings B<sub>4</sub>C, the actual stoichiometry of their coatings is far away from the large stoichiometry range of boron carbide. In many cases the B/C ratios of 1 was found as a result of processing gas modifications [96,99].

**Table 2.2:** Mechanical properties of boron carbide coatings.

| Hardness (GPa) | Young's Modulus (GPa) | Technique       | Reference                  |
|----------------|-----------------------|-----------------|----------------------------|
| 30-72          | Not reported          | Microhardness   | S. Ulrich et al. [114]     |
| 20-40          | 180-280               | Nanoindentation | T. Eckardt et al. [69]     |
| 8-18           | 90-140                | Nanoindentation | H.S. Ahn et al. [99]       |
| 15.4           | 138.5                 | Nanoindentation | P.D. Cuong et al. [115]    |
| 13-43          | Not reported          | Microhardness   | H.Y. Chen et al. [105]     |
| 42.5-50.4      | 300-420               | Nanoindentation | Z. Han et al. [103]        |
| 30             | 250                   | Nanoindentation | Y. Chen et al. [64]        |
| 36-40          | Not reported          | Nanoindentation | M.U. Guruz et al. [74]     |
| 10-35          | 145-275               | Nanoindentation | T. Hu et al. [96]          |
| 14-32          | 175-313               | Nanoindentation | F. Kokai et al. [90]       |
| 17-27          | 210-245               | Nanoindentation | L.G. Jacobsohn [97]        |
| 19,5-25        | 250-300               | Nanoindentation | E. Pascual et al. [73]     |
| 25-30          | 290-350               | Nanoindentation | A. Lousa et al. [63]       |
| 16             | 200                   | Nanoindentation | K.E. Lee et al. [106]      |
| 30-32          | Not reported          | Nanoindentation | O.B. Postel et al. [85]    |
| 24-33          | Not reported          | Nanoindentation | M.J. Zhou et al. [95]      |
| 20-35          | Not reported          | Microhardness   | O. Knotek et al. [116]     |
| 23-39          | 252-348               | Nanoindentation | J. Sun et al. [91]         |
| 15.6-26        | 16-210                | Nanoindentation | O.R. Monteiro et al. [87]  |
| 20.8-60        | 255-518               | Nanoindentation | V. Kulikovskiy et al [104] |

From the literature data, it is concluded that, the main interest was given to increase the deposition temperature in order to crystallize boron carbide coatings. Although no report of the totally crystallized pure boron carbide coating (without a combination of a crystalline and amorphous phases and free carbon) by sputtering has been reported as far as the author is aware, the increases in the hardness given in the table are mainly correlated with the increase of the deposition temperature. Few works have investigated the effect of ion bombardment during film growth. Ulrich et al. have investigated the effect of bias voltages between 0 and 175 V, on the hardness of amorphous boron carbide films deposited by rf sputtering. They found a drastic increase of the hardness (from 30 GPa to about 72 GPa) and compressive stress (from 4 GPa to 7 GPa) with the increase in bias voltages from floating to 75 V, then a decrease after a threshold of 75 V until 175 V [114]. Lousa et al. have found an increase from 24 to 30 GPa with increasing negative bias voltage applied to the substrates and a threshold value (10 V) above which the hardness started to decrease. The intrinsic stresses increased linearly from about 4 to 5.5 GPa with increasing bias voltages in their study [63]. Kulikovskiy et al. found a decrease from 28 GPa to 20 GPa for rf sputtered boron carbide films with increasing applied bias voltages from floating to 165 V. In their study, the hardness values were increased with the increase of the deposition temperature, from 27 GPa for the films deposited without external heating to about 40 GPa at 970 °C. For some points they measured hardness values of about 60 GPa. They concluded that crystallized films resulted with such increase in the hardness, however the inhomogeneities present in the crystal film structure and the presence of free carbon may explain the scattered nature of the hardness values in their study [104].

A few studies have investigated the coupled effect of the deposition temperature and ion bombardment. Knotek et al. have realized experiments at 100 °C and 300 °C by applying bias voltages between 0 and 100 V. They found an increase in the hardness from about 20 to 35 GPa for the films deposited at 100 °C and 20 to 30 GPa at 300 °C. Hence, interestingly in their study, boron carbide films deposited by applying 100 V bias voltages at 100 °C were harder than the ones deposited with the same bias but at 300 °C. They concluded that both the heating and applied bias voltages increase the hardness. However, bias voltage has more dominant effect on the increase of the hardness [117].

It is clear from Table 2.2 that, depending on the deposition conditions and because of the large homogeneity range of boron carbide, different values of hardness and modulus for boron carbide coatings has been reported previously. It can also be said that, the reported hardness and modulus values for boron carbide thin films are comparable and even superior to that of bulk boron carbide given in Table 2.1. Nevertheless, they are more localized about 25-30 GPa and Young's modulus values measured from nanoindentation measurements about 200-250 GPa. It has also to be noted that, for all the studies investigating the mechanical properties versus the increase of the deposition temperature, the authors observed an increase of the hardness and modulus of the coatings no matter the resultant coating crystallized or not. However, for the bias voltages, while some investigators reported a continuous increase of the hardness with the increase of the negative bias voltages applied [96,117], others have observed a rise and fall behavior with the increase of the bias voltages with a maximum value at intermediate voltages [63,114], and others have reported a continuous decrease of the hardness while increasing bias voltages [104,118]. The deposition configurations are various (conventional or ion plating) and there is a lack of detailed structural and morphological investigation of the coatings deposited, therefore it is difficult to give a general dependence of the applied bias voltages on the mechanical properties of boron carbide thin films.

#### **2.4.4 Wear properties**

For the friction and wear properties of boron carbide thin films, the data reported by different researchers in the literature are again scattered like mechanical properties. Knotek et al. investigated the tribological properties of dc and rf magnetron sputtered boron carbide coatings by using a "pin-on-disc" tribometer against a 100Cr6 counterface. The tests were carried out in air at 15 °C, with a relative humidity of 60%, under unlubricated conditions, with a sliding velocity of 0.5 m/s and with 10 N applied load. They found friction coefficient values of about 0.7-0.8 for DC sputtered boron carbide films and 0.2 for rf sputtered boron carbide films [117].

Eckardt et al. have investigated the frictional properties of boron carbide coatings against 100Cr6 ball with 4.67 mm diameter using a load of 1 N and a disk speed of 0.04 m.s<sup>-1</sup> at constant temperature and humidity which were 21 °C and 45-50% respectively. They found that boron carbide thin films have friction coefficient of

about 0.9. With acetylene ( $C_2H_2$ ) addition of 4-5 sccm into processing gas, they observed a decrease to about 0.2-0.3 [69]. The same approach was used by Ahn et al. who incorporated methane ( $CH_4$ ) to the processing gas. They found a decrease in the friction coefficient from 0.4 for pure boron carbide coating to 0.1 with addition of 1.2 vol.%  $CH_4$ . They used a micro-oscillating friction and wear tester, a 3 mm diameter steel ball (the type of steel is not indicated) as counterface and a sliding speed of 4.43 mm/s. The relative humidity was between 40-45% and the tests were realized at ambient temperatures according to their paper [99].

The same group was also studied the effect of relative humidity on the wear properties of boron carbide coating deposited with addition of 1.2 vol.%  $CH_4$ , by using the same wear test parameters [115]. They found a decrease of the friction coefficient from about 0.5 at 5% relative humidity to 0.1 at 85% relative humidity. An XPS study within the wear track obtained at 45% relative humidity and after 5000 cycle revealed the presence of boric acid/boron oxide. They suggested that boron carbide oxidized and boron oxide was formed on boron carbide surface which than reacted with the moisture in air to form boric acid as a low friction layer.

This result is also in accordance with the findings of Erdemir et al. who studied the tribological properties of post-annealed bulk boron carbide and boron carbide thin films. They reported very low friction coefficient of about 0.03 by the formation of boron oxide film on the boron carbide during the annealing process as a result of the oxidization of boron carbide and top boric acid layers with the spontaneous reaction of boron oxide with moisture in air [66,119]. The tests were realized in a “pin-on-disc” tribometer, zirconia pins were used as counterfaces at room temperature in open air of 40-50% relative humidity. The normal force applied was 5 N. The wear rates of zirconia pins were measured in their study. Against un-treated  $B_4C$  they measured wear rates of about  $2.0 \times 10^{-5} \text{ mm}^3/\text{Nm}$ , however against annealed  $B_4C$  wear rates decreased to  $5.7 \times 10^{-8} \text{ mm}^3/\text{Nm}$ . The suggestion of the formation of double layer, boron oxide-boric acid films was based on the difference between the Raman spectra of untreated and annealed boron carbide in their study.

The lubricity of the boron carbide at elevated temperatures was known since the work of Rabinowicz and Imai who investigated the frictional properties of  $B_4C$  at various temperatures and found that  $B_2O_3$  layers become lubricious above 650 °C,

therefore provide a friction coefficient as low as 0.1 [120]. However, it was by the work of Erdemir et al. that the low friction mechanism was further revealed.

The formation of a solid lubricant boric acid layer was also confirmed by Larsson et al. on sintered bulk boron carbide [120]. Their sliding tests were carried out with a “pin-on-disc” tribometer. They used B<sub>4</sub>C pins of 5 mm in diameter with 5, 15, 30 and 45 N applied load. The experiments were realized in air at room temperature under atmospheric pressure. Different tests were carried out with 20%, 35%, 45%, 60%, 80% and 100% relative humidity values. They obtained friction coefficient values between 0.9-0.07. The low friction coefficient values were obtained with increasing the relative humidity. Depending on the test conditions, wear rates between  $3 \times 10^{-3}$  and  $2 \times 10^{-5}$  mm<sup>3</sup>/Nm were obtained for the B<sub>4</sub>C pins in their study. The formation of B<sub>2</sub>O<sub>3</sub> and H<sub>3</sub>BO<sub>3</sub> together with hydrocarbons was revealed by XRD measurements realized on the wear debris.

Guruz et al. have investigated the friction and wear properties of boron carbide coatings by using a block-on-ring apparatus for the tests and M2 steel as counterface. The analyses were carried out in air using poly-alpha-olefin (PAO) as lubricant. The sliding speed was 0.139 m/s with a load of 1.96 N. In this lubricated conditions, they found friction coefficient values of about 0.06 for the M2 steel-boron carbide pair and  $7.3 \pm 5 \times 10^{-9}$  mm<sup>3</sup>/Nm wear rates [74].

Martinez et al. have studied the nanowear properties of boron carbide coatings. In their study, the friction coefficient was measured by microscratch test with a diamond tip and was found about 0.12. They also presented their results on wear rates. However the analyses were carried out by scanning a preselected 3 μm<sup>2</sup> area with the diamond tip and the wear rates were given in nm/cycle. Hence their results were relative and could not be used for comparison purpose. Accordingly, they explain in their article that friction and wear seem to be different at atomic scale. [121]. Reigada et al. have also reported the nanowear properties of boron carbide coatings deposited by DC magnetron sputtering. They mainly studied the effect of applied bias voltages on the wear properties and found that with the increase in negative bias voltages both friction and wear decreased at nanoscale [122]

Kustas et al. have investigated the wear rates of metal doped (Mo, W, Ni-Cr) boron carbide coatings deposited by rf sputtering. Wear testing was performed by reciprocating sliding of a 5 mm WC-Co ball against the boron carbide coated substrates for a total number of 50 cycles. 5 and 15 N loads were used for the tests. No details of other test conditions, such as temperature or relative humidity were found in their article. Depending on the dopant material, bias voltage and applied loads during the tests, wear rates between  $9.1 \times 10^{-4}$  and  $4.7 \times 10^{-5}$  mm<sup>3</sup>/Nm were obtained during their study. They explained the improvement of the wear properties for the coatings deposited with bias voltages, by a process of densification of the coatings [123].

Harris et al. studied the wear of boron carbide coatings against 52100 steel balls with a “pin-on-disc” system. In their study, the wear tests were conducted at room temperature and at relative humidity of  $35 \pm 15\%$  [68]. The load was varied between 0.05 and 11 N. They studied the polishing of the counterface during sliding wear by boron carbide coatings, after a suggestion by Erdemir that hard coatings could increase the fatigue resistance of a coated part by polishing mating surfaces during sliding contact [124]. Harris et al. have introduced a term, “coating abrasiveness”, to characterize the ability of the coatings to polish their counterfaces. The abrasiveness is defined in their article as the volume of material removed from a counter surface per distance traveled (mm<sup>3</sup>/m). They observed two main aspects; the abrasive removal of steel from the ball by boron carbide and the counter-polishing of the boron carbide by the steel ball. They found that the average abrasion rate of the steel balls decreased with the increase of the sliding distance following a power law scaling relationship. As an example, at 0.05 N normal load, the amount of material removal during the first 1000 cycles was about  $3.6 \times 10^{-3}$  l mm<sup>3</sup> (for  $l=2\pi r$ , with  $r$ =wear track diameter), while the amount of material removed during the first 10000 cycles was about  $4 \times 10^{-3}$  l mm<sup>3</sup>. That indicates that only 10% as much material was removed after the first 1000 cycles as was removed during the first 1000 cycles [68]. Thus, they suggested that boron carbide could be used as a run-in purpose finite-life coating with only tens of nanometer thickness, surviving a short period of time to polish its mating surface in typical machine components [125]. This fact explains also the usage of boron carbide coating on gears; the coating increase the overall fatigue resistance of the coated part during sliding contact through a polishing action

that it provides to the counterpart surface [126]. The same group investigated the effects of the contact conditions on the abrasiveness of boron carbide coatings in their follow-up paper. By running experiments using different contact conditions such as, ball-on-disc, con-on-disc, “pin-on-disc” and spiral track wear experiments at the 0.1 N fixed normal loads, they found that the decrease of the coating abrasiveness was independent of the macro-scale contact conditions [126]. According to their findings, the boron carbide-steel system is an example of chemical-mechanical polishing in which the steel is mechanically abraded by boron carbide, while boron carbide is chemically polished by steel. However, the mechanism by which the polishing occurs and by which such smooth surfaces are generated is not well understood and need complementary studies [68].

Several conclusions can be drawn from the above literature survey; first of all it is clear that for boron carbide thin films which are not modified by processing gas or by post-annealing, and tested at low to moderate humidity conditions, the friction coefficients of between 0.4-0.9 were reported by different investigators. Thus, the introduction of several articles which cites low friction coefficients and high lubricity among different properties of boron carbide thin films, repeat only the cliché “low friction – high wear resistance” which is not the case for boron carbide coatings. The reason of the remarkable wear resistance of boron carbide thin films especially against erosive and abrasive wear lie on their high hardness and high strength. As it is mentioned by Erdemir [66], despite its excellent wear resistance, B<sub>4</sub>C does not provide low friction to sliding surfaces, especially at low to moderately high temperatures.

Although there are interesting researches on the tribological properties of boron carbide films such as the polishing of the counterpart, the formation of low friction boric acid layer by post-annealing treatments, the main interest was given to the tribological properties of steel-boron carbide pair. No effort was made to connect the microstructural changes of boron carbide thin films by deposition parameters to their tribological properties. No report could also be found for example for alumina which is a frequently used counterpart, especially to investigate the tribological properties of ceramic bulk materials and thin films.

### 2.4.5 Microstructure

Despite its significant properties and all potential technological applications, boron carbide films were not investigated extensively in regard to their microstructures. As mentioned early by several authors, no investigation of relations between deposition parameters, microstructure and mechanical, tribological or other properties exist in the literature [118,127].

Although there are no extensive investigations, examples of microstructures can be found. Two types of microstructures reported by different authors, columnar structure by DC magnetron sputtering [68,69], reactive sputtering [106], pulsed ion-beam evaporation [88] and non-columnar, featureless grown films by DC magnetron sputtering [118], plasma jet CVD [84] and by PLD [90]. Hu et al. have studied the effect of bias voltages on the microstructure and found that boron carbide coatings deposited at floating potential had coarse columnar microstructure, at 200 V bias voltages it transformed to a denser Zone T type microstructure [96]. Knotek et al. have studied the effect of argon pressure on the microstructure of boron carbide coatings and found that the columnar structure for the films deposited at 4 Pa changed to no structure growth at 1 Pa [116].

Chen et al. [64], Han et al. [103] and Zhou et al. [95] have demonstrated the amorphous nature of boron carbide films by high resolution TEM investigations.

### 2.4.6 Electrical properties

Boron carbide is a p-type semiconductor with a band gap of 1.2-1.8 eV [83]. With its high melting point, B<sub>4</sub>C phase is very stable even at high temperatures [60]. With the combination of these properties, B<sub>4</sub>C is known as a candidate material for the electronic devices that can be operated at elevated temperatures and an excellent thermoelectric material especially at high temperature [70]. Suematsu et al. have studied the electrical properties of crystalline boron carbide films deposited by ion-beam evaporation. For increased thermoelectric conversion efficiency, deposited film should have high conductivity. They found that the carbon content of the films have important influence on the electrical properties. The electrical conductivity measured with a four point probe decreased from about  $10^5 \Omega^{-1}\text{cm}^{-1}$  to  $10^4 \Omega^{-1}\text{cm}^{-1}$  as a result of an increase of the carbon content from 14% to 20% in boron carbide

coating structure. The Seebeck coefficient (measured for thermoelectric properties) also decreased from about  $300 \mu\text{VK}^{-1}$  to  $150 \mu\text{VK}^{-1}$  with an increase of the carbon content from 14% to 20%. [70]. The same group was also studied the electrical conductivity and Seebeck coefficients at different temperatures and concluded that boron rich thin films are promising candidate to be used as thermoelectric device to convert heat energy into electrical energy [128].

Ahmad et al. have investigated boron carbide coatings as candidates to be used in semiconductor devices in harsh environments. Their work details the rf magnetron sputter deposition of high resistivity boron carbides and the fabrication of boron carbide/silicon heterojunction diodes [129]. To be used as junction with silicon deposited boron carbide films should have high resistivity. They mentioned in their article that boron carbide films deposited via sputtering have low resistivity values  $\rho < 10 \Omega\text{cm}$  and thus, do not form rectifying junctions with silicon. They developed an interesting way which includes the saturation of boron carbide target before deposition, in methane/argon plasma for several hours. They then used the saturated target to produce  $\text{B}_5\text{C}$  films with a constant B/C ratio. Thus produced films result with resistivities greater than  $10^7 \Omega\text{cm}$ . The same group has also evaluated the optical properties of boron carbide films deposited by PECVD on glass substrates, using both spectroscopic ellipsometry and spectrophotometry [130]. They concluded that boron carbide films with about 0.75 eV indirect band gap and about 1.5 eV direct band gap, exhibited heterojunction diode characteristics.

## **2.5 Boron Carbonitride (BCN) Thin Films**

In the last few years, thin films with composition within the ternary system B–C–N have attracted much attention. Films of superhard materials can be found in the system B-C-N such as diamond, cubic boron nitride, tetragonal amorphous carbon and boron carbide [113,131]. A list of hard and superhard materials as well as B-C-N phase diagram can be seen in Figure 2.34. Moreover, materials in this system are characterized by short bond lengths and expected to combine some specific properties of diamond, cubic boron nitride (c–BN), hexagonal boron nitride (h–BN) and boron carbide ( $\text{B}_4\text{C}$ ), such as, high hardness, low friction coefficients, lubricity and good wear resistance and therefore are considered to be promising candidate as hard and protective coatings for cutting tools and other wear–resistance applications. [121,131,132].

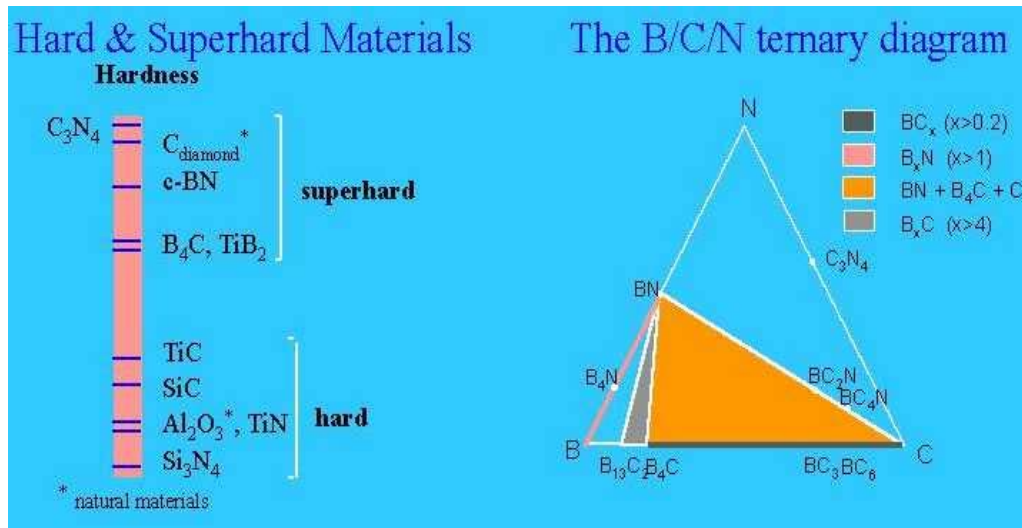


**Figure 2.34:** List of hard and superhard materials and B-C-N ternary diagram [113].

The system includes also materials with interesting optical and electrical properties such as high refractive index or a large band gap (diamond and cubic boron nitride) [133,134]. In addition to the above mentioned examples which consist of only one or two elements, there are possibilities to form ternary materials within the system which can combine the advantages of less complex materials and/or to form more relaxed ternary phases which would still preserve the structure and properties of those localized on the sides and vertices of the triangle, like diamond, c-BN and boron carbide (See Figure 2.34) [131,134]. Different attempts have been made to merge materials with extremely different properties, for example superhard diamond and soft h-BN, hard and wear resistant  $B_4C$  and soft and lubricating h-BN, semimetallic graphite and insulating h-BN, or the cubic phases of diamond and c-BN ( $BC_2N$  heterodiamond) [134].

Many different techniques were used to synthesize phases in the B-C-N ternary system including chemical vapor deposition, PACVD, sputtering, or pulsed laser deposition [134]. Only sputter deposition attempts will be presented here. They can be actually divided in two parts, the use of h-BN target in a plasma that contains methane or acetylene as reactive gases, by RF sputtering obligatory due to the high electrical resistivity of h-BN and the use of  $B_4C$  target with  $N_2$  introduction into processing plasma atmosphere, by RF and as well as DC sputtering. There are several attempts in the literature, which focalizes only on the deposition of c-BN phase by sputtering or other techniques.

A few works, which have studied the effect of nitrogen incorporation into boron carbide structure, will be discussed as background of the present study. Phase composition of N incorporated boron carbide coatings were studied by several authors. IR spectrometry was used in almost all the studies to distinguish the h-BN and c-BN phases and to quantitatively estimate the ratio of these two phases in the deposited coating structures. Some of them were deposited a mixture of h-BN and amorphous C [135] and h-BN [131], while other investigators, by the assistance of ion bombarding of growing film, were able to obtain a cubic phase dominated structure [133,136,137]. It exists a general consensus on the necessity of extensive ion bombardment to nucleate and growth of cubic boron nitride films. However, thus deposited films contain very high compressive stress and premature delamination of the films thicker than a few hundred nanometers occurs especially after their exposition to the ambient air [133,137,138,139]. As an example, Kouptsidis et al. have deposited nearly single-phase c-BN from a B<sub>4</sub>C target by an unbalanced DC magnetron sputtering design at bias voltages between 220 to 320 V [136]. Tsai et al. deposited cubic boron nitride phase as high as about 82% by a pulsed DC magnetron sputtering system at 250 V bias voltages [133]. The same group has also investigated the coupled effect of the bias voltages and temperature on the formation of cubic phase. They found that, in their case, the maximum c-BN content of 82% was reached at 250 °C and 250 V bias voltages. They also suggested that by a multi-step biasing process, by applying different bias voltages at the nucleation and grown of thin films, 95% c-BN content could be reached with a better crystallinity [137]. Yamamoto et al. have proposed a multilayered design of B<sub>4</sub>C as the first underlayer and B-C-N as gradient layer, thus were able to deposit a c-BN top layer of 2.65 μm thick [140]. Linss et al. studied the bonding properties of N incorporated boron carbide thin films in the range of 0 to 100% N<sub>2</sub> in the working gas by FTIR spectrometry. The structure was hexagonal boron nitride, with the presence of large absorption peak for B-N bonding. In addition they observed C-C stretching bonds, and C-N and N-H bonds especially for films deposited with ≥ 25% N<sub>2</sub> in the processing gas [141].

Film compositions were measured by either XPS or EPMA. A strong influence of the N<sub>2</sub> incorporation was found by all the investigators. Without N<sub>2</sub> incorporation B<sub>4</sub>C coatings are generally near stoichiometric.

With the increase of N<sub>2</sub>, for example in [135], at 10% N<sub>2</sub>, the structure composed of about 50% B, 40% N, 10% C (relative %). In [134], the incorporation of N in the coating increased linearly till 25% N<sub>2</sub> in the gas, from 0 at.% to 45 at.% N and stabilized at this point. Further increase of N<sub>2</sub> in the processing gas led a slight increase of the N incorporated in the coating structure about 50 at.% N at 100% N<sub>2</sub>. The composition of the coatings changed from 72 at.% B, 20 at.% C, 8 at.% O without N<sub>2</sub> in the processing gas, to 44 at.% B, 38 at.% N, 17 at.% C, 1 at.% O with 25% N<sub>2</sub> incorporation to the processing gas in [131]. Kouptsidis et al. reached B/C ratio of nearly 1 with about 46% B, 42% N and 10% C at 20% N<sub>2</sub> in the processing gas [136]. With 20% N<sub>2</sub> in the processing gas, a composition of 50 at.% B, 38 at.% N, 12 at.% C was obtained by Tsai et al. [133].

Growth rates of the coatings were increased with addition of N<sub>2</sub> into processing gas. From 6.6 nm/min at 0% N<sub>2</sub> to 18.3 nm/min at 10% N<sub>2</sub> [135]. From 1.3 nm/min at 0% N<sub>2</sub> to 2 nm/min at 25% N<sub>2</sub> and then decreased to 1.2 nm/min in [131].

With the incorporation of nitrogen into boron carbide structure, the hardness and modulus of the coatings obtained decreased gradually by increasing the N<sub>2</sub> flow rate or partial pressure in the processing gas, from for example 27 GPa at 0% N<sub>2</sub> to 13 GPa at 40% N<sub>2</sub>. The same trend was also observed for modulus of the coatings from 280 GPa to about 180 GPa in [121]. From 25 GPa at 0% N<sub>2</sub> to 8 GPa at 40% N<sub>2</sub> [134]. An extreme hardness value of about 80 GPa obtained in [136] at 20% N<sub>2</sub> as a result of the formation of nearly single cubic phase.

The stress values of the films were also decreased by the incorporation of N<sub>2</sub> with the exception of the studies in which a dominating c-BN phase in the coating structure was obtained. For example, from 5 GPa at 0% N<sub>2</sub> to 2 GPa at 40 % N<sub>2</sub> in [121].

Friction coefficient values were also affected by the nitrogen incorporation. It decreased from about 0.12 to 0.05 in [121]. However, interestingly the wear rate of the coatings measured by nanowear tests was increased in the same study. The authors concluded that at the atomic scale the wear rates are much dependent to hardness rather than the friction coefficient or adhesion to the substrate [121]. Friction coefficient values measured by nanowear testing decreased from 0.25 to about 0.1 in [131]. “pin-on-disc” tests were carried out in [134] against 100Cr6 balls

in air with a humidity between 40 and 50%. Friction coefficient values of between 0.05 and 0.5 were obtained on coatings with different roughness and at different normal loads between 0.5 and 1.5 N.

Surface roughness of the coatings measured by a profilometer or AFM was decreased with the increase of the nitrogen incorporation. From about 0.9 nm for B<sub>4</sub>C coating at 0% N<sub>2</sub> to 0.2 nm at 25% N<sub>2</sub> for BCN films in [131].

As a result of the above literature survey; with the incorporation of N into boron carbide structure and by appropriate changes of process parameters such as bias voltages and N<sub>2</sub> partial pressure, it is possible to deposit several phases in the B-C-N ternary system. By means of this versatility, resultant thin film properties may be easily tailored for specific applications.

## **2.6 Functionally Graded Thin Films**

The concept of functionally graded materials (FGM) was proposed in 1984 by material scientists in Japan [142]. By definition, a functionally graded material is a material, in which the composition and microstructure gradually change resulting in a corresponding change in the properties [142,143].

Advanced high-performance components for structural, electrical, chemical, optical and biological applications demand materials with more than one superior value among the set of available properties. Such materials are difficult to obtain from either monolithic, multilayer, or composite systems. This has prompted the development of a new category of material known as functionally graded materials that possess various functions simultaneously [144]. The FGM concept is applicable to many fields. In engineering applications such as cutting tools, machine parts, and engine components, incompatible functions such as heat, wear, corrosion resistance, toughness, machinability are incorporated into one single part [142]. By the end of 1980s, FGM concepts have triggered world-wide research activities and are applied to metals, ceramics and organics, composite bulk materials as well as thin films to generate improved components with superior physical properties [145]

In thin film form, FGM concept is defined as a compositionally graded multilayer coating where two successive layers have at least one common element [144]. These

graded interfaces ensure no abrupt change in composition, and therefore the mismatch in elastic modulus, thermal expansion coefficient and hardness between two materials which could lead to excessive residual stresses and consequent delamination or cracking of the coating, will be altered by the functionally graded design [144,146]. Therefore, much improved coating-substrate adhesion, less intrinsic stresses, thus, thicker hard and wear resistant coatings could be obtained by the proper configuration of gradient layers.

The functionally graded approach has been largely used for wear resistant Me-DLC systems [144,147] or TiN and its derivatives (e.g. TiAlN) [148], however very few works can be found in the literature for BCN and especially c-BN films although the internal stress and adhesion problems are well known for these coatings as explained in the previous section. There are attempts to use gradually increased bias voltages and low/high circle of bias voltages to obtain gradual underlayers to deposit thick BCN and c-BN coatings respectively [74,139]. There is no FGM approach to B<sub>4</sub>C reported in the literature as far as the author is aware. Only, metallic Ti bondcoat layer was used in [69] and Cr bondcoat layer by Bodycote Inc. on its commercially available Diamondblack coating [149].

## 2.7 Résumé du Chapitre

La pulvérisation cathodique consiste à bombarder, sous vide partiel, un solide (cible) au moyen d'ions d'énergie suffisante, afin d'en extraire des atomes qui vont se transformer pour se déposer sur le substrat. Historiquement, la pulvérisation cathodique est l'une des techniques les plus anciennes d'élaboration de couches minces découverte par Sir William Robert Grove en 1852. Elle occupe une place importante entre différentes méthodes de dépôt physique en phase vapeur (PVD). Aujourd'hui, c'est la technique de dépôt par voie atomique la plus employée dans l'industrie et dans le milieu universitaire pour l'élaboration de couches minces. Elle couvre une très large gamme de matériaux et pour différents applications comme, par exemple, des dépôts anti-usures sur outils de coupe et pièces de machine, des dépôts semi-conducteurs pour dispositifs microélectroniques, des dépôts sur vitres pour raisons d'économie d'énergie ou encore pour applications décoratives. En plus de ses nombreux avantages comme, un taux de dépôt élevé, la réalisation possible de dépôts à basse température, une adhérence améliorée, plusieurs types et configurations sont couramment utilisées principalement la pulvérisation magnétron, la pulvérisation réactive, la pulvérisation radio fréquence, la pulvérisation assisté par plasma (dépôt ionique), et la pulvérisation triode. Grâce à une large palette de paramètres de pulvérisation et de configurations possibles, des couches minces avec les microstructures aux propriétés bien ajustées peuvent être obtenues par la pulvérisation cathodique.

Le système ternaire de B-C-N a retenu beaucoup l'attention ces dernières années surtout sans, cependant, se limiter aux applications anti-usure avec des phases ultra dures comme le carbure de bore et le carbonitride de bore plus particulièrement. Une recherche bibliographique détaillée indique que le carbure de bore est un matériau bien connu, sous sa forme massive, à haute dureté et module d'Young élevé en plus d'autres propriétés intéressantes comme une faible masse volumique, une grande résistance aux milieux chimiques agressifs et une absorption neutronique élevée. En revanche, sous forme de dépôt, obtenu par exemple par pulvérisation cathodique, il reste extrêmement peu connu. C'est également le composé le moins étudié dans le diagramme ternaire B-C-N. D'autre part, presque tout l'effort a porté sur le dépôt du nitrure de bore cubique dans la bibliographie. Il existe très peu d'études qui se

focalisent sur l'effet de l'incorporation d'azote dans la structure de carbure de bore et les différentes phases qui pourraient en être issues.

Selon la bibliographie, l'effet des paramètres de dépôt sur des morphologies de croissance des couches, sur le micro et la nanostructure et, par conséquent, sur différentes propriétés des couches telles que la résistance à l'usure, les propriétés mécaniques, optiques et électroniques n'est pas encore bien établi.



---

**CHAPTER 3:**  
**EXPERIMENTAL STUDIES**

---



### **3. EXPERIMENTAL STUDIES**

In this chapter, the systems used for thin film deposition, production and properties of the target material, types of substrates used, parameters used to deposit different types of films, and characterization techniques used to elucidate different properties of the films obtained will be presented in details.

#### **3.1 Film Deposition**

In this section, details of the film deposition related studies, such as, deposition systems, target materials, different substrates used in the study and deposition conditions for different types of films will be given.

##### **3.1.1 Sputtering systems**

Two sputtering system were used to deposit thin films investigated in this study. Conventional DC magnetron sputtered boron carbide films, plasma-enhanced magnetron sputtered boron carbide films, BCN films, functionally graded B<sub>4</sub>C and BCN films were deposited by (plasma enhanced) DC magnetron sputtering system of Prof. Dr. Adnan Tekin Applied Research Center of Materials Science & Production Technologies of Istanbul Technical University/Turkey, RF sputtering system of the Laboratoire des Milieux Nanometrique (LMN) of Université d'Evry-Val-D'Essone/France was used to deposit RF sputtered boron carbide films.

##### **3.1.1.1 Plasma enhanced DC magnetron sputtering system**

TSD 350 PCVD model hybrid coating machine (HEF-France) was used to deposit B<sub>4</sub>C, BCN and functionally graded films. The deposition system as well as the schematic of the deposition chamber is shown in Figure 3.1. Detailed description of the technique is given in Section 2.2. With its magnetron source powered by an 2500 W DC power supply (Huttering Inc./Germany) and an auxiliary plasma source (plasma booster), the machine is capable to work both in PVD (magnetron sputtering) and plasma enhanced magnetron sputtering modes (a type of ion plating configuration explained in Section 2.2.4).

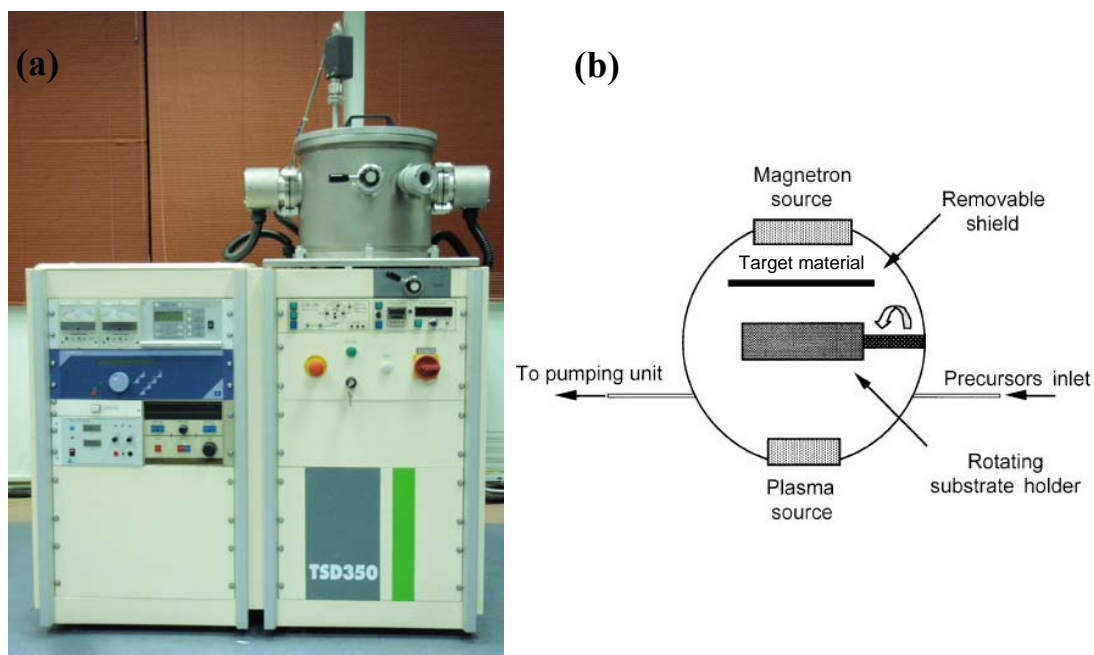


**Figure 3.1:** (a) DC Magnetron sputtering system used in this study (b) schematic of the deposition chamber.

PECVD (Plasma enhanced chemical vapor deposited) thin films can also be deposited with the same system. In the patented plasma-enhanced magnetron sputtering design [150], the auxiliary plasma source is powered positively, thus, fast electrons produced by the ion bombardment of the target are trapped near the target by means of the magnetron design, whereas slow electrons are accelerated towards the positively powered plasma source. They collide with Argon atoms and create high-density plasma over the substrate holder. Figure 3.2 demonstrates inside of the deposition reactor during film growth for two deposition modes. In Figure 3.2 (a) at the left hand side, the brilliant part is the plasma generated by boron carbide target. Different shaped substrates can be seen in front of the target on a rotational substrate holder. In the figure (b), in addition to the plasma created near boron carbide target by means of the magnetron configuration, high-density plasma created by means of the auxiliary source can be seen at the right of the picture, distinguishable with its pink color. The substrates that are in rotation are passing through this high-density plasma. In operation, the plasma generated by auxiliary plasma covers more homogeneously the substrate holder than it is seen in the figure (due to the image resolution limitations), although the density is higher at the zone close to the source. In this configuration, the collision energy of the ions to the substrate was controlled through negative DC bias applied to the sample holder (an isolated holder attached to

a 1000 W DC power supply), whereas the ion flow was controlled by the applied plasma booster current. Thus, during film growth by the negative magnetron source, the substrates were bombarded with energetic ions generated by the assistance of positive plasma source.

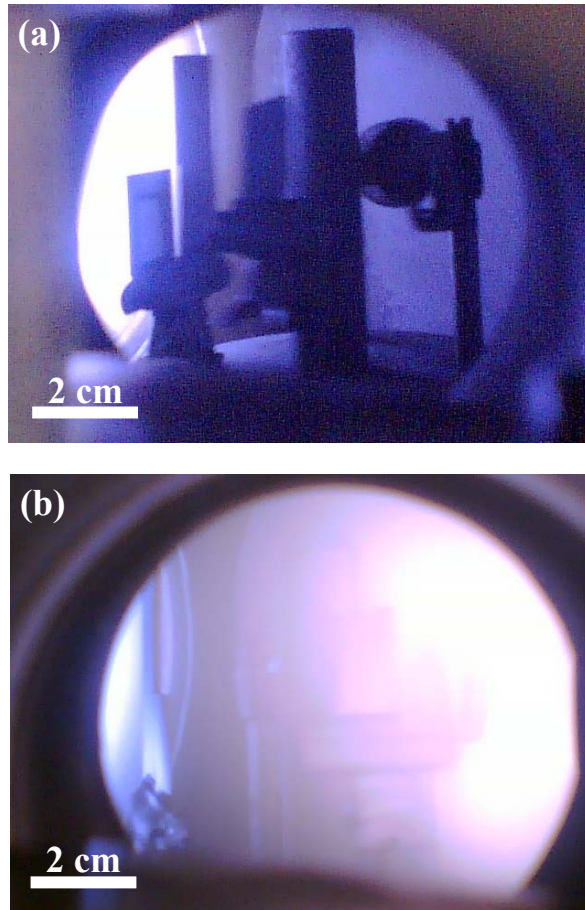


**Figure 3.2:** Inside view of the deposition reactor (a) Conventional magnetron sputtering mode during film growth (without auxiliary plasma) (b) PEMS mode during film growth (in presence of the auxiliary plasma).

The base pressure of  $5 \times 10^{-5}$  Pa was obtained by a combination of a rotary and turbomolecular pump system. Vacuum levels were measured by the combination of a thermocouple Pirani gage up to  $10^{-1}$  Pa and with a cold cathode Penning gage up to  $10^{-5}$  Pa. The system can be heated up to  $300^{\circ}\text{C}$  by a radiant heater and the temperature was controlled by a thermocouple. By means of the removable shield in front of the target and with the auxiliary plasma source, the substrates were bias-etched before deposition to remove the surface oxide layer and to clean any remaining contamination on the target and the substrates surfaces.

### 3.1.1.2 RF sputtering system

A non-magnetron ultra high vacuum (UHV) RF deposition system with a 13.56 MHz RF power supply was used to deposit B<sub>4</sub>C thin films. Detailed description of the RF deposition technique is given in Section 2.2.3. A base pressure of  $1.33 \times 10^{-6}$  Pa was obtained by a combination of rotary and turbomolecular pumps. By means of the load-lock chamber, specimens were loaded into the deposition chamber without breaking the vacuum. Hence, the deposition of the films can be realized at ultra high vacuum conditions with this system.

### 3.1.2 Substrates

Three types of substrates, AISI M2 grade high speed steel, 2 cm in diameter, 0.5 mm in thickness, AISI 430 steel, 5x2 cm<sup>2</sup>, with 0.5 mm thickness and one side polished Si (100) wafers were used in the experiments. Table 3.1 demonstrates the chemical compositions of two different steel substrates. All steel substrates were mirror polished to Ra values of approximately 0.03  $\mu$ m. Before being introduced into the deposition chamber, all the substrates were pre-cleaned in ultrasonic bath, in acetylene and in ethanol respectively and were then blown dry with dry nitrogen gas.

**Table 3.1:** Chemical compositions of steel substrates.

|          | C%   | Cr%  | Mo%  | V%   | W%   | Fe%     |
|----------|------|------|------|------|------|---------|
| AISI M2  | 0.9  | 4.10 | 5.00 | 1.90 | 6.40 | balance |
| AISI 430 | 0.08 | 17   | -    | -    | -    | balance |

### 3.1.3 Target material

An “in-house” produced boron carbide target material was used for the deposition of thin films in this study except a commercially available B<sub>4</sub>C target (99.5% purity) which was used for RF sputtering. The advantage of the target production is to control over the composition and different properties of the target material. As explained in Section 2.4, one reason of the insufficient researches on the boron carbide in thin film form may be the properties of the target material. For example, the electrical resistivity of the boron carbide depends strongly on its chemical composition and on its relative density, which is the result of sintering conditions. That is the reason that some of the commercially purchased targets are not compatible with DC configurations. In this study, boron carbide target was hot pressed from own produced boron carbide source powders.

### 3.1.3.1 Boron carbide powder production

Boron carbide powders were obtained from the carbothermal reduction of boric acid in a graphite resistance furnace at 2000°C. As the powder production is not the subject of this study and as the process is already commercialized, the details of the powder production will not be presented here. Extensive literature can be found on the subject, one example is already given in the Section 2.4 [60]. The powders obtained were then crushed and milled to fine boron carbide powders with average grain size  $d(0.5)$ : 3.702  $\mu\text{m}$  (measured with a laser particle size analyzer) for hot pressing. Figure 3.3 shows SEM image of boron carbide powders.

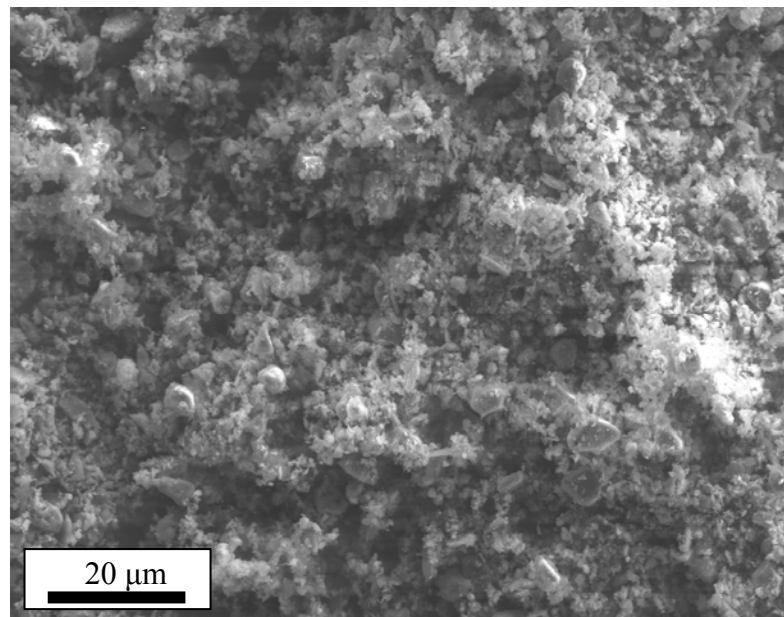


**Figure 3.3:** SEM images of boron carbide powders.

Elemental composition of the powders was revealed by EPMA. Boron carbide powders had an elemental composition of (at.%) 78% boron, 21.5% carbon, with 0.2% oxygen and 0.3% silicon as impurities. Thus, in this study, the relative ratio of B/C for boron carbide powder was 3.62. Figure 3.4 shows the phase distribution of boron carbide powders obtained by XRD analysis. As it can be seen from XRD results, the initial powder contained small amounts of free carbon and boric acid in addition to boron carbide phase.

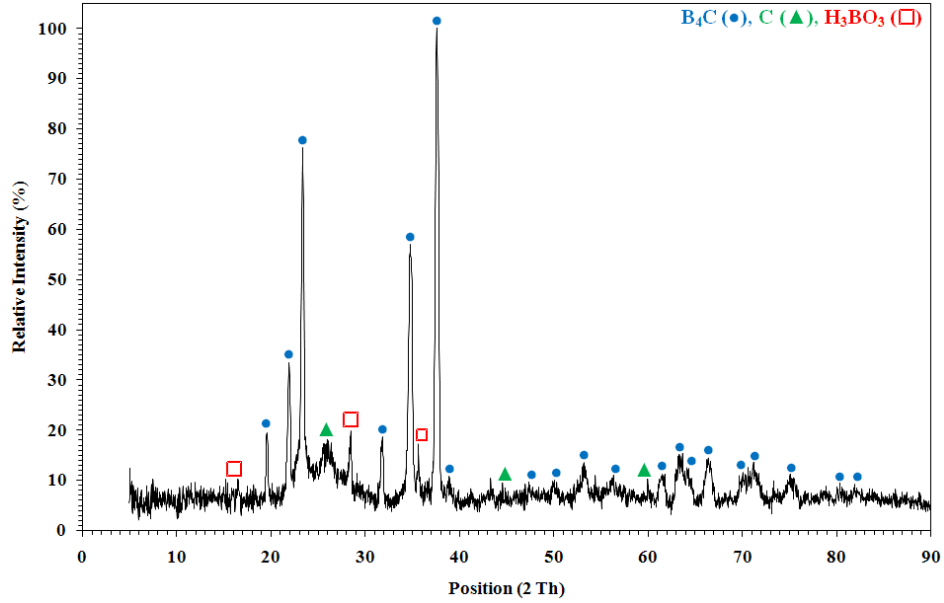


**Figure 3.4:** XRD spectra of boron carbide powders.

### 3.1.3.2 Hot pressing of boron carbide powders

Boron carbide powders were hot pressed in pure nitrogen atmosphere with 100 MPa applied force at 2100 °C for 15 minutes to obtain boron carbide target used in this study. Microstructure of hot-pressed boron carbide target is shown in Figure 3.5.

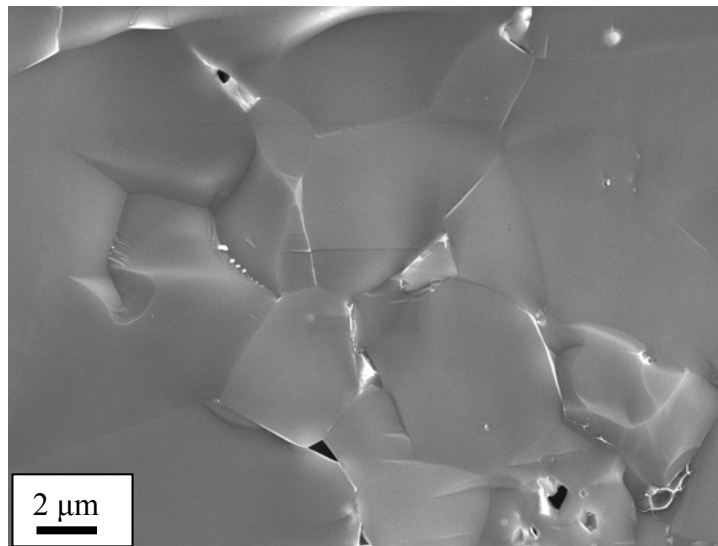


**Figure 3.5:** Hot-pressed boron carbide target microstructure.

Dense structure of sintered boron carbide can be seen from SEM observation given in the figure, realized by fractured cross-sections. Hot-pressed sputtering target was 15 cm in diameter and 7 mm in thickness as can be seen in Figure 3.6 (a) and (b) respectively. The picture of the target was taken after the preliminary experiments.

The eroded area shown in the figure (a) is the zone that most of sputtering occurs due to the circular magnet design of the source.

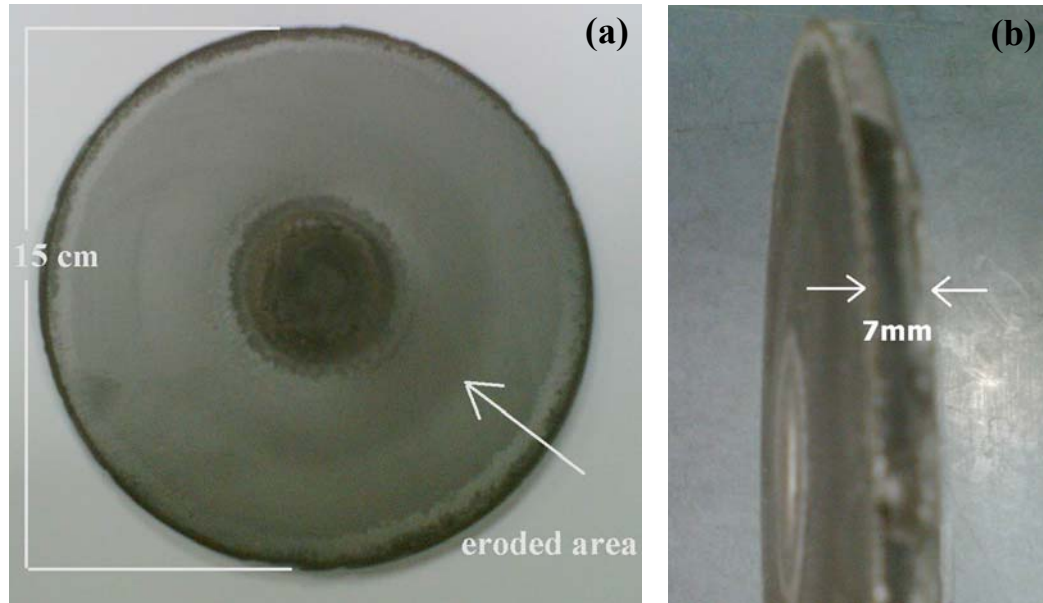


**Figure 3.6:** Hot-pressed boron carbide target (a) front view of the target showing its diameter (b) section view showing the thickness of the target.

Chemical analysis of the sintered boron carbide was realized with EPMA and nearly the same composition as source powders was found. Density measurement of the sintered target was carried out by Archimedes's method, referring to the industry standard of commonwealth Germany 'DIN51056' [151]. According to Archimedes's principle, any object, wholly or partially immersed in a fluid, is buoyed up by a force equal to the weight of the fluid displaced by the object. Thus, the density of the immersed object relative to the density of the fluid can easily be calculated without measuring any volumes according to the following equation;

$$d = \frac{W_A}{(W_A - W_B)} \times d_L \quad (3.1)$$

Where,  $d$  is the density of the material,  $W_A$  is the weight of the material,  $W_B$ , is apparent immersed weight of the same material in liquid and  $d_L$  is the density of the liquid (water in our case). It was found that, theoretical density of 99% was achieved for boron carbide target with the sintering conditions used.

### 3.1.4 Processes parameters for thin films

In this section, process parameters used to deposit different films will be given in separate sections. First standard configuration of the system before deposition will be described, than different parameters used for different films will be listed.

#### 3.1.4.1 Conventional DC magnetron sputtered B<sub>4</sub>C films

All pre-cleaned substrates (3 types of substrates for each deposition) were placed in the special designed substrate holder and were then introduced to the deposition reactor. The base pressure of about  $10^{-5}$  Pa was attained before each deposition. Argon was introduced into the chamber as precursor with a 20 sccm flow rate to ignite the plasma by applying a negative voltage to the cathode. Before deposition of each film, the boron carbide target was presputtered in argon atmosphere for 30 minutes, and meanwhile with the help of the removable shield in front of the target and the auxiliary plasma source, the substrates were bias-etched with a gradually applied voltage (50 V for 5 minutes, 100 V for 5 minutes, 200 V for 10 minutes, and 250 V for 10 minutes) to remove the surface oxide layer and to clean any remaining contamination on the target and the substrates surfaces. After the bias etching of the substrates, the auxiliary plasma source was shut down, the removable shield in front of the target was removed, and variable parameters, bias voltages in the case of conventional magnetron sputtered B<sub>4</sub>C films, was set to desired values. Deposition time was 75 minutes for all the experiments. No external heating was used during experiments, however, because of the ion-target material interactions and kinetic energy transfers of the atoms to the substrate during film growth, the temperature reached  $\sim 50^{\circ}\text{C}$  in all the experiments. Details of the deposition parameters for magnetron sputtered B<sub>4</sub>C films is given in the Table 3.2.

**Table 3.2:** Deposition parameters for magnetron sputtered B<sub>4</sub>C films.

| Exp. Number                        | BC47      | BC48      | BC49      |
|------------------------------------|-----------|-----------|-----------|
| Exp. Duration (min)                | 75        | 75        | 75        |
| Base Pressure (Pa)                 | $10^{-5}$ | $10^{-5}$ | $10^{-5}$ |
| Work. Pressure (Pa)                | 0.3       | 0.3       | 0.3       |
| Ar (sccm)                          | 20        | 20        | 20        |
| Power (W)                          | 500       | 500       | 500       |
| Voltage (V)                        | 701       | 701       | 701       |
| Current (A)                        | 0.71      | 0.71      | 0.71      |
| Bias (-V)                          | 0         | 50        | 250       |
| Temperature ( $^{\circ}\text{C}$ ) | 44        | 45        | 46        |

### 3.1.4.2 Plasma-enhanced DC magnetron sputtered B<sub>4</sub>C films

For plasma enhanced magnetron sputtered B<sub>4</sub>C films exactly the same procedure described in the previous section was used until the end of the bias etching process only, when the external heating was used, the heating of the system was started once the base pressure of 10<sup>-3</sup> Pa had been reached. After the bias etching of the substrates, the removable shield in front of the target was removed and the auxiliary plasma source was leaved on. Variable parameters, bias voltage, and temperature were set to desired values. Details of the deposition parameters for plasma enhanced magnetron sputtered B<sub>4</sub>C films are given in the Table 3.3.

**Table 3.3:** Deposition parameters of plasma enhanced magnetron sputtered B<sub>4</sub>C films.

| Exp Number | Exp. Duration (min) | Working Pressure (Pa) | Base Pressure (Pa) | Ar (sccm) | Power (W) | Voltage (V) | Current (A) | Bias (V) | Booster current (A) | Booster voltage (V) | Temp. (°C) |
|------------|---------------------|-----------------------|--------------------|-----------|-----------|-------------|-------------|----------|---------------------|---------------------|------------|
| BC82       | 75                  | 0.3                   | 10 <sup>-5</sup>   | 20        | 520       | 689         | 0.76        | 100      | 1                   | 30                  | 52         |
| BC83       | 75                  | 0.3                   | 10 <sup>-5</sup>   | 20        | 520       | 689         | 0.76        | 50       | 1                   | 30                  | 50         |
| BC84       | 75                  | 0.3                   | 1x10 <sup>-5</sup> | 20        | 520       | 689         | 0.76        | 150      | 1                   | 29                  | 51         |
| BC85       | 75                  | 0.3                   | 2x10 <sup>-5</sup> | 20        | 520       | 689         | 0.76        | 250      | 1                   | 29                  | 53         |
| BC86       | 75                  | 0.3                   | 10 <sup>-5</sup>   | 20        | 520       | 689         | 0.76        | 250      | 1                   | 29.5                | 150        |
| BC87       | 75                  | 0.3                   | 6x10 <sup>-4</sup> | 20        | 520       | 689         | 0.76        | 250      | 1                   | 28.5                | 250        |
| BC88       | 75                  | 0.3                   | 8x10 <sup>-4</sup> | 20        | 520       | 689         | 0.76        | 150      | 1                   | 28.5                | 250        |
| BC89       | 75                  | 0.3                   | 5x10 <sup>-4</sup> | 20        | 520       | 689         | 0.76        | 50       | 1                   | 28.7                | 150        |
| BC90       | 75                  | 0.3                   | 10 <sup>-4</sup>   | 20        | 520       | 689         | 0.76        | 100      | 1                   | 28                  | 250        |
| BC91       | 75                  | 0.3                   | 2x10 <sup>-5</sup> | 20        | 520       | 689         | 0.76        | 150      | 1                   | 28.8                | 150        |
| BC92       | 75                  | 0.3                   | 1x10 <sup>-5</sup> | 20        | 520       | 689         | 0.76        | 0        | 1                   | 29.8                | 51         |
| BC93       | 75                  | 0.3                   | 5x10 <sup>-5</sup> | 20        | 520       | 689         | 0.76        | 100      | 1                   | 27.5                | 150        |
| BC94       | 75                  | 0.3                   | 6x10 <sup>-4</sup> | 20        | 520       | 689         | 0.76        | 0        | 1                   | 29.2                | 250        |
| BC95       | 75                  | 0.3                   | 6x10 <sup>-4</sup> | 20        | 520       | 689         | 0.76        | 50       | 1                   | 29.7                | 250        |
| BC96       | 75                  | 0.3                   | 10 <sup>-5</sup>   | 20        | 520       | 689         | 0.76        | 0        | 1                   | 30.4                | 150        |

### 3.1.4.3 RF sputtered B<sub>4</sub>C films

Boron carbide thin films were deposited by a non-magnetron RF sputtering (13.56 MHz) of a commercial boron carbide target with 99.5% purity. Mirror polished AISI 430 steel with average roughness (Ra) of 0.03 μm and one-side polished Si (100) wafer were used as substrates in each deposition. The distance of the insulated substrate holder from the target was 3 cm. The base pressure of 1.33 x 10<sup>-6</sup> Pa was obtained by a combination of a rotary and turbomolecular pump system. High-purity Argon was used as precursor and was introduced into the vacuum chamber through a mass flow controller to establish the desired working pressure. All depositions were realized without external heating.

However, as a result of long deposition times needed to establish desired thicknesses because of the non-magnetron design, the temperature gradually increased and reached a steady-state level around 250 °C. The processing parameters used for RF sputtered B<sub>4</sub>C films are listed in Table 3.4.

**Table 3.4:** Deposition parameters for RF sputtered B<sub>4</sub>C films.

|                       | BC27                  | BC28                  | BC29                  |
|-----------------------|-----------------------|-----------------------|-----------------------|
| Base pressure (Pa)    | 1.33x10 <sup>-6</sup> | 1.33x10 <sup>-6</sup> | 1.34x10 <sup>-6</sup> |
| Working pressure (Pa) | 0.67                  | 0.26                  | 0.4                   |
| Power (W)             | 80                    | 140                   | 100                   |
| Voltage (V)           | 500                   | 700                   | 600                   |
| Exp. Duration (h)     | 8                     | 6                     | 8                     |
| Temperature (°C)      | 250                   | 250                   | 250                   |

#### 3.1.4.4 BCN films

For BCN films, after the bias etching, high purity N<sub>2</sub> gas was introduced into the deposition chamber and the shield was removed after the stabilization of reactive plasma. Different reactive gas flows to deposit different BCN films was set for each experiment. Table 3.5 gives the parameters used to deposit BCN films with different N<sub>2</sub> partial pressure.

**Table 3.5:** Deposition parameters for BCN thin films.

|                       | BC67                | BC68                | BC69                |
|-----------------------|---------------------|---------------------|---------------------|
| Exp. Duration (min)   | 50                  | 55                  | 55                  |
| Base Pressure (Pa)    | 5x 10 <sup>-5</sup> | 5x 10 <sup>-5</sup> | 5x 10 <sup>-5</sup> |
| Work. Pressure (Pa)   | 0.3                 | 0.3                 | 0.3                 |
| Ar (sccm)             | 19                  | 15                  | 10                  |
| N <sub>2</sub> (sccm) | 1                   | 5                   | 10                  |
| Power (W)             | 510                 | 500                 | 500                 |
| Voltage (V)           | 619                 | 525                 | 509                 |
| Current (A)           | 0.82                | 0.95                | 0.99                |
| Bias (-V)             | 50                  | 50                  | 50                  |
| Booster current (A)   | 1                   | 1                   | 1                   |
| Booster voltage (V)   | 30                  | 22-32               | 15-40               |
| Temperature (°C)      | 49                  | 56                  | 53                  |

#### 3.1.4.5 Functionally graded films

The preparation of the graded films has been carried out by means of plasma enhanced DC magnetron sputtering in a two-step process. A titanium target (99,5% purity) was used to pre-deposit Ti-TiN and Ti-TiC underlayers using nitrogen and acetylene as reactive gases respectively. Pack boriding method was used to obtain boride underlayers on AISI 430 steel substrates. Samples were embedded in the powder mix (EKABORTM2) and sealed in a stainless steel container than were

placed in a resistance furnace. The process was performed under atmospheric pressure and N<sub>2</sub> gas environment at 930°C for 12 hours. Once the underlayers were deposited, boron carbide and boron carbonitride films were grown onto them by plasma enhanced DC magnetron sputtering of our hot-pressed boron carbide target. The synthesis conditions of underlayers and B<sub>4</sub>C and BCN films are summarized in Table 3.6.

**Table 3.6:** Deposition parameters for functionally graded films.

|  | Ti                  | TiC                 | TiN                 | B <sub>4</sub> C    | BCN                 |
|--|---------------------|---------------------|---------------------|---------------------|---------------------|
| Base pressure (Pa)                             | 5x 10 <sup>-5</sup> | 5x 10 <sup>-5</sup> | 5x 10 <sup>-5</sup> | 5x 10 <sup>-5</sup> | 5x 10 <sup>-5</sup> |
| Working pressure (Pa)                          | 0.3                 | 0.3                 | 0.3                 | 0.3                 | 0.3                 |
| Target power (W)                               | 1000                | 1000                | 1000                | 520                 | 520                 |
| Voltage (V)                                    | 447                 | 548                 | 560                 | 689                 | 541                 |
| Current (A)                                    | 2.26                | 1.83                | 1.8                 | 0.76                | 0.96                |
| Ar flow rate (sccm)                            | 20                  | 12                  | 12                  | 20                  | 17                  |
| N <sub>2</sub> flow rate (sccm)                | -                   | -                   | 8                   | -                   | 3                   |
| C <sub>2</sub> H <sub>2</sub> flow rate (sccm) | -                   | 8                   | -                   | -                   | -                   |
| Substrate bias (V)                             | 125                 | 125                 | 125                 | 100                 | 250                 |
| Temperature (°C)                               | 250                 | 250                 | 250                 | 250                 | 250                 |
| Deposition time (min)                          | 7-10                | 15                  | 15                  | 180                 | 120                 |

## 3.2 Characterization Techniques

In this section, characterization techniques such as SEM (Scanning Electron Microscopy), TEM (Transmission Electron Microscopy), EPMA (Electron Probe Micro Analysis), SIMS (Secondary Ion Mass Spectrometry), FTIR (Fourier Transform Infrared Spectrometry), nanoindentation and “pin-on-disc” test, used in this study will be described.

### 3.2.1 Scanning electron microscopy

Scanning electron microscopy is used for surface imaging of solids using electron beam generated secondary electrons. Upon interacting with the solid, secondary electrons are generated which are utilized to image the surface [152]. When the energy of the emitted electron is less than about 50 eV, by convention it is referred to as a secondary electron. Most of the emitted secondary electrons are produced within the first few nm of the surface [153]. Some of the primary electrons will be backscattered toward the surface with little or no loss in energy. As the atomic number of the element increases, the back-scattering coefficient increases, hence the brightness of the BSE image tends to increase.

Therefore with BSE imaging, strong topographical contrasts can be obtained depending on the position of the detector [21,152]. One of the most common analytical attachments to the SEM is the energy dispersive x-ray spectrometer (EDX or EDS). Energetic primary electrons ionize atoms in the solid producing x-rays which are characteristic of the elements that are present.

With suitable detectors, x-rays may be detected to provide qualitative, semi-quantitative and quantitative elemental analysis [152]. X-ray emission signal can also be detected with a wavelength spectrometer (EPMA will be described in the next section). Although with modern detectors and electronics, recent EDS systems can detect X-rays above beryllium ( $Z = 4$ ), if present in sufficient quantity, the EDS analyses are accurate for elements with  $Z > 9$ . Light elements could not be properly detected with EDS systems [154].

In this study, three SEM; JEOL 6320 FV field-emission gun scanning electron microscope, field-emission gun ZEISS DSM 982 (GEMINI) and LEO 450 VP were used to study mostly the microstructures and surface topographies of the films deposited, and in limited cases, to study qualitative and quantitative elemental analyses.

### **3.2.2 Electron probe micro analysis**

Electron Probe Microanalysis (EPMA) is a spatially resolved, quantitative elemental analysis technique based on the generation of characteristic X-rays by a focused beam of energetic electrons [155]. EPMA is used to measure the concentrations of elements (beryllium to the actinides) at levels as low as 100 parts per million (ppm) and to determine lateral distributions by mapping [24,155]. Hence, the quantitative analysis of light elements can be realized with this technique even for trace amounts. EPMA combines the imaging capabilities of a SEM with quantitative elemental analysis using mainly wavelength dispersive spectrometry and possibly energy dispersive spectrometry [155].

Wavelength Spectrometry (WDS) is based on the phenomenon of Bragg diffraction. The diffraction is described by the expression:

$$n\lambda = 2d \sin \theta_B \tag{3.2}$$

Where,  $\lambda$  is the wavelength equivalent of the X-ray,  $d$  is the crystal spacing for the diffracting planes, and  $\theta_B$  is the angle at which constructive interference occurs (i.e., the Bragg angle). The X-ray source, the specimen, the diffracting crystal, and the gas counter must follow a specific geometry (a Rowland circle) to detect the X-rays. Accurate positioning is ensured by incorporating an optical microscope into the electron probe. To detect a wide energy range, different crystals with various  $d$  spacing are mounted on a mechanical turret, and are selectable under computer control [155].

As thin films studied in this thesis were mainly constituted by light elements such as, B, N, C and O, their chemical compositions were determined by EPMA. Two models of the same company, CAMECA SX 50 and CAMECA SX 100 were used for quantitative elemental analyses during this study.

### **3.2.3 Transmission electron microscopy**

The transmission electron microscopy (TEM) utilizes an electron beam much like the SEM but at higher accelerating potential since in this technique, electrons that are transmitted through thinned specimens (less than 50 to 300 nm) are imaged. The accelerating potential required, depends on the sample thickness and atomic mass but is typically 100 - 400 kV [152].

TEM's strong cards are its high lateral spatial resolution, which is stated generally as better than 0.2 nm "point-to-point" in the literature [152,156] (recently a resolution of 0.07 nm is announced by Carl Zeiss on an ultra-high resolution model [157]), and its capability to provide both image and diffraction information from a single sample.

The information obtained by electron microscopy is derived from either elastic or inelastic scattering processes. Electrons that do not undergo any scattering or elastic scattering with little change in trajectory will form the transmitted beam (bright field mode). Elastically scattered electrons with a significant change in trajectory form the diffracted beam (dark field mode) [152]. A series of magnetic lenses at and below the sample position are responsible for delivering the signal to a detector. Accompanying this signal transmission is a magnification of the spatial information in the signal by as little as 50 times to as much as a factor of  $10^6$  [156].

Modern analytical electron microscopes are often equipped with a wide variety of signal detectors. In the scanning TEM mode (STEM), any of these signals (transmitted electrons, diffracted electrons, backscattered electrons, secondary electrons and characteristic x-rays) can be used to modulate the input signal to a cathode ray tube (CRT) to form an image [156]. There are numerous special analytical techniques or operation modes, which are in use with this powerful technique. Present, is a limited description in order to explain the techniques used specially to characterize thin films during this study.

In Energy Filtered TEM (EFTEM), the transmitted electrons are subjected to an additional energy selection after the angle selection. The contrast is optimised by filtering the contrast-reducing electrons from the spectrum of transmitted electrons, or by only allowing electrons containing specific information to be used for imaging. The ability to quantify chemical information at a near atomic-scale and the possibility to obtain elemental distribution images (mapping) including light elements makes EFTEM an important tool for materials characterization [158].

EELS (Electron energy loss-spectroscopy) is an analytical methodology which derives its information from the measurement of changes in the energy and angular distribution of an initially nominally monoenergetic beam of electrons that has been scattered during transmission through a thin specimen [156]. The high energy primary electrons lose energy passing through the sample due to ionization of the energy levels of atoms present. This results in loss peaks at discrete energy levels. The physics of energy loss favors strong EELS signal generation for light elements, which is complimentary to EDS analysis which is insensitive to light elements [152].

By means of EELS, local elemental concentration of each atomic species present can be derived. Additionally, by studying the detailed shape of the spectral profiles, the analyst may derive information about the electronic structure, chemical bonding, and average nearest neighbor distances for each atomic species detected [156].

A TECNAI F 20 ST model TEM shown in Figure 3.7 was used to further investigate thin films deposited in this study. High-resolution observations from in plane and cross-sections of different films were realized. EELS analyses of boron carbide structure were carried out. EFTEM analyses were also carried out on some specimens.



**Figure 3.7:** TECNAI F 20 ST TEM used in the study.

### **3.2.3.1 Sample preparation for TEM analyses**

Two techniques were used to prepare thin foils for in-plane and cross-section TEM observations. Specimens that were observed by their cross-sections were prepared with a special technique named “sandwich method” developed particularly for multilayered materials and thin film observations, but suitable as well as bulk materials. In this technique, first two platelets, which belong to the same specimen, were glued face to face with a low viscosity epoxy resin as can be seen in the Figure 3.8 (a). The main idea is to protect the material surface while achieving a cross-section. Also by means of this technique, the observable material quantity in the same sample can be multiplied. The specimen thus obtained, was cut to 1 mm thick slices with a low speed diamond wheel saw. Then it was glued on the glass insert of a tripod and the whole mounting was placed on a heating plate (150 °C) for half an hour to ensure a proper glue polymerization. The planarity of the tripod was already verified before the mounting process. The first face was directly polished up to 500  $\mu\text{m}$ , then the specimen was pulled out by heating on the plate, and the other face was mounted exactly by the same way. This face was gradually polished and thinned by means of micrometric screws of the tripod and a corner with a thickness of 500 nm was obtained as can be seen in (c).

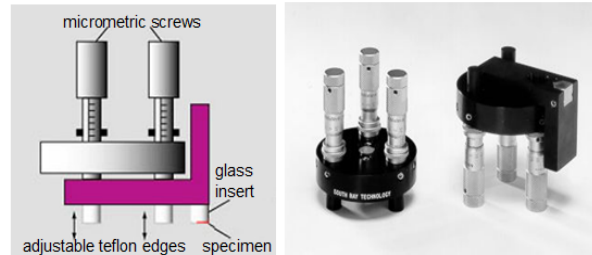
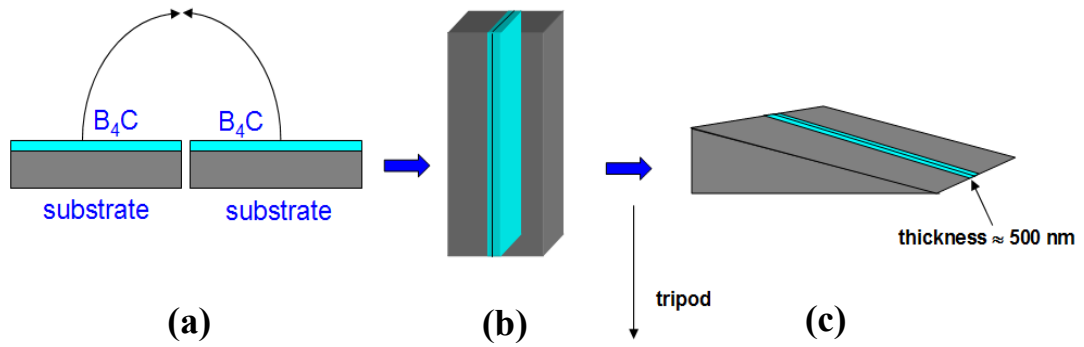


**Figure 3.8:** Sample preparation steps of the sandwich technique for cross-sectional TEM observations.

Then, the specimen was put on a copper ring and a final thinning to electron transparency was realized with a GATAN ion beam thinning machine with dual argon ion beam during 3-15 minutes, at 3 kV, with  $6^\circ$  incidence angle. In Figure 3.9, the final form of the specimen before being introduced into TEM for analyses can be seen.

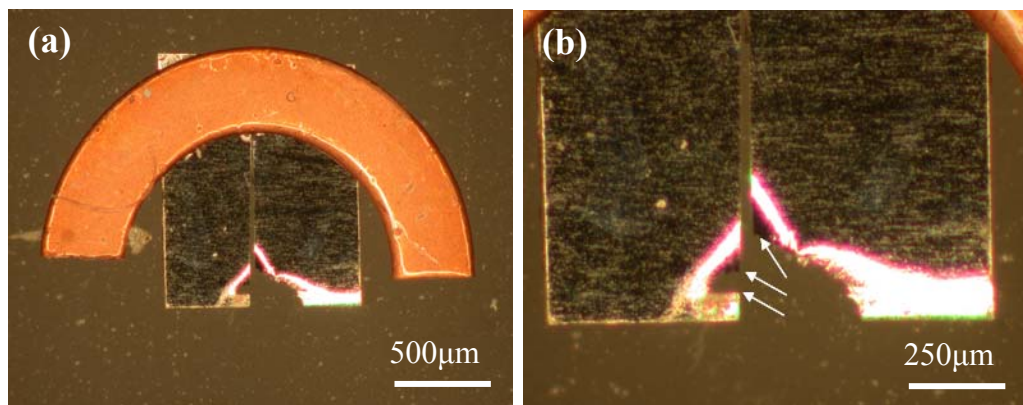


**Figure 3.9:** Specimen prepared for cross-sectional TEM observations (a) view on the copper ring (b) demonstration of the probable analysis areas.

Small arrows in Figure 3.9 (b), visualizes probable analyze areas where were thinned to electron transparency. For in-plane observations, the specimens were directly cut with a low speed diamond wheel saw and the process explained thereafter in the sandwich method was repeated exactly for these samples.

### 3.2.4 Secondary ion mass spectrometry

Secondary ion mass spectrometry (SIMS) is a sputtering based analytical technique as mentioned in the Section 2.1.3. With ion bombardment, sample surface particles are sputtered. The ionized flux (secondary ions) is then mass separated by different types of mass analyzers before to reach the convenient detector [159]. SIMS ion sources are usually designed to operate in the 1 to 20 keV energy range. As only a few percent of the atoms removed by sputtering are ionized, proper selection of the primary ion is a prerequisite to accurate analyses. Positive primary ions enhance the yield of negative secondary ions while negative primary ions enhance the yield of positive secondary ions. The favored primary ions are O and Cs for their high yield of positive and negative secondary ions, respectively [159].

SIMS is one of the most sensitive analytical techniques, with elemental detection limits in the ppm to sub-ppb range, depth resolution as good as 2 nm and lateral resolution depending upon the application and mode of operation. SIMS can be used to measure any elemental impurity, from hydrogen to uranium and any isotope of any element. The detection limit of most impurities is typically between  $10^{12}$  and  $10^{16}$  atoms/cm<sup>3</sup>, which is at least several orders of magnitude lower (better) than the detection limits of other analytical techniques capable of providing similar lateral and depth information. Therefore, SIMS is usually the analytical technique of choice when ultrahigh sensitivity with simultaneous depth or lateral information is required. Additionally, its ability to detect hydrogen is unique and not possible using most other non-mass spectrometry surface sensitive analytical techniques [160].

There are two main subtypes of SIMS named static and dynamic SIMS. In the static mode, the incident flux of primary ions is kept below  $5 \times 10^{12}$  atoms/cm<sup>2</sup>, with ion current densities of  $< 1$  nA cm<sup>-2</sup> obtained using primary beams operated at kinetic energies between 1 and 10 keV. This mode of operating is used generally to obtain chemical information of the top most surface layers of the materials and its applications is well known for polymers and biomaterials [161]. In dynamic mode, kinetic energies between 10 and 20 keV are used generally, which result with ion current densities greater than 1 nA cm<sup>-2</sup> and primary ion flux above  $5 \times 10^{12}$  atoms/cm<sup>2</sup>. Thus, statistically, a given area has a high probability of being repetitively bombarded, causing a crater to be formed in the sample.

This mode of SIMS provides depth profiles) of any element and its isotopes with excellent detection limits. [159,160,162]. Dynamic SIMS can be operated in any of four basic modes to yield a wide variety of information:

1. The depth-profiling mode, by far the most common, is used to measure the concentrations of specific preselected elements as a function of depth from the surface.
2. The bulk analysis mode is used to achieve maximum sensitivity to trace-level components, while sacrificing both depth and lateral resolution.
3. The mass scan mode is used to survey the entire mass spectrum within a certain volume of the specimen.
4. The ion-imaging mode is used to determine the lateral distribution of specific preselected elements. In certain circumstances, an imaging depth profile (3D imaging) is acquired, combining the use of both depth profiling and imaging.



**Figure 3.10:** Cameca ims 6f secondary ion mass spectrometer used in this study.

In this study, Cameca ims 6f model secondary ion mass spectrometer was used. The machine is capable to work both in static and dynamic modes. Dynamic SIMS mode has been used for the elemental depth profiling of the coatings and scanning ion imaging was realized to analyze the wear tracks obtained during tribological examinations.

### 3.2.5 Nanoindentation

The most important hardness definitions for engineers are by Vickers, Knoop, Brinell, and Rockwell. Apart from the last one, all of them define hardness as the quotient of applied load  $P$  and remaining area  $A$  of indentation [163]. According to this definition, hardness cannot be measured if there is no remaining impression as the area of the impression is normally measured by optical microscopy. While the force can be measured with good accuracy, the error in indentation area measurements can reach high values if the area is small and the end of the diagonals cannot be well-resolved [163]. By the early 1980s, the necessity to measure the mechanical properties of thin hard films and small depth ranges was rapidly increasing. Such measurements could be carried out only with smaller forces, and it became difficult to get the accurate size of the indentation area [163]. This was the main reason for the development of a new measurement technique of hardness called “depth sensing indentation” or “instrumented indentation testing”. In this technique, depth and force are recorded simultaneously over the whole indentation cycle (loading and unloading). There is no need to measure the indentation area directly because it can be derived from the known shape of the indenter at any depth. The depth can be measured automatically with nanometer resolution and it is this nanometer range resolution that gives the well known name “nanoindentation” to this indentation technique [163,167].

In nanoindentation, three-sided Berkovich pyramidal indenters instead of four-sided Vickers pyramids are mostly used because they can be produced with sharper tips and, therefore allows a better depth resolution [167]. Figure 3.11 shows the SEM image and the schematic of the Berkovich indenter demonstrating angles and its representative indent impression.

As can be seen from the figure, the Berkovich tip has a nominal angle of  $65.3^\circ$  between the (side) face and the normal and an angle of  $76.9^\circ$  between edge and normal with a radius of curvature between 50 and 150 nm. When compared with the radius of curvature of the four-sided Vickers tip, which is bigger than 500 nm, it is clear that for the thin film applications with thicknesses of several hundred nanometers, Berkovich indenter should be decided for accurate analyses.

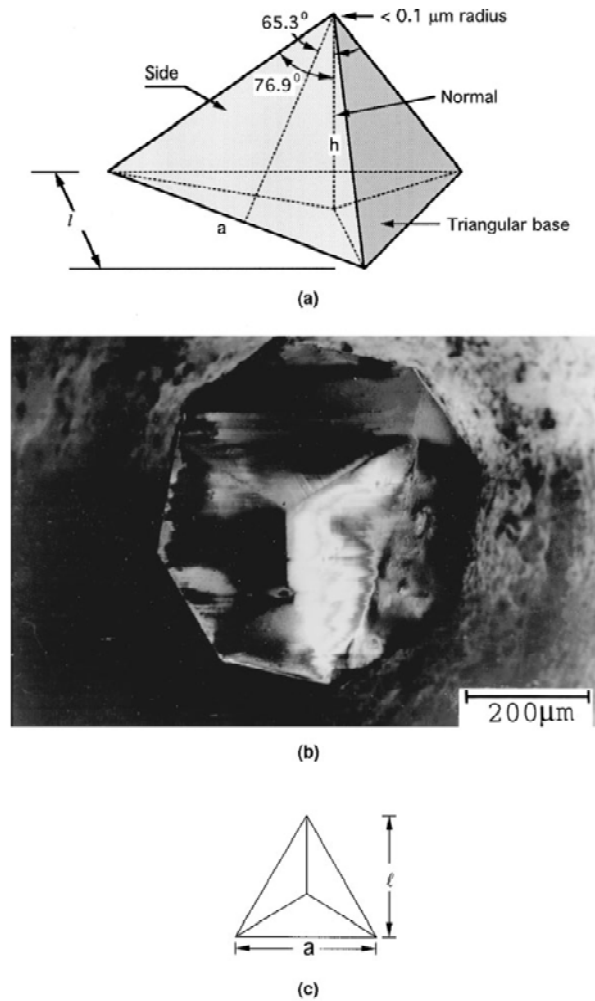


**Figure 3.11:** (a) Schematic of the Berkovich indenter (b) SEM image of the Berkovich indenter (c) Schematic indent impression [164].

The deformation pattern of a real elastic–plastic sample during and after indentation is shown schematically in Figure 3.12. In this figure, the contact depth ( $h_c$ ) is defined as the depth of indenter in contact with the sample under load. The depth measured during the indentation ( $h$ ) includes the depression of the sample around the indentation in addition to the contact depth. The depression of the sample around the indentation ( $h_s = h - h_c$ ) is caused by elastic displacements and must be subtracted from the data to obtain the actual depth of indentation or actual hardness [164]. At peak load, the load and displacement are  $P_{max}$  and  $h_{max}$ , respectively, and the radius of the contact circle is  $a$ . Upon unloading, the elastic displacements in the contact region are recovered and, when the indenter is fully withdrawn, the final depth of the residual hardness impression is  $h_f$  [164]. Schematic of a load–displacement curve obtained at the end of the nanoindentation process is shown in Figure 3.13.

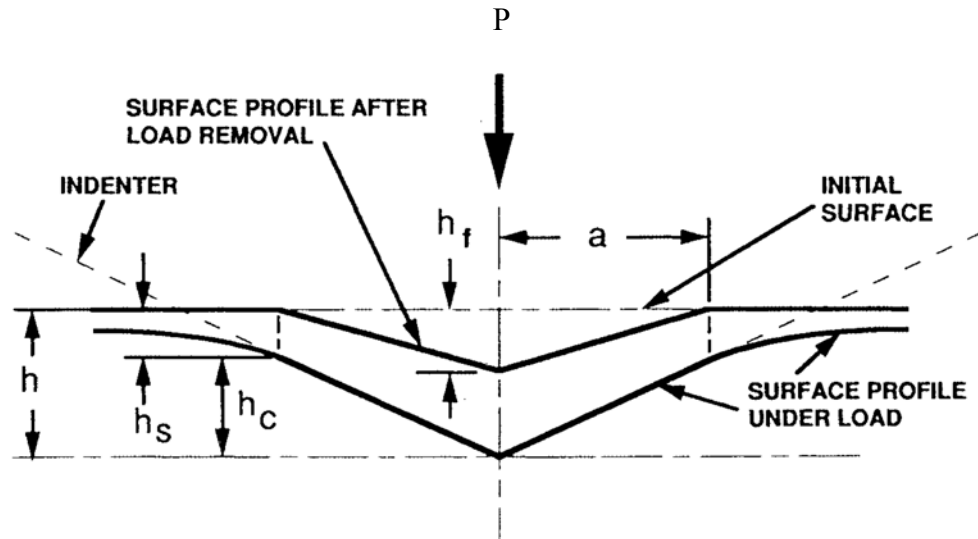


**Figure 3.12:** Schematic representation of the nanoindentation process [164].

There are several models to predict the mechanical properties, Hardness and Young's modulus as well as the elastic and creep properties of the materials by analyzing the load-displacement curve shown in Figure 3.13 [48,164]. Among them, the methods of Loubet et al. [165], Doerner and Nix [166] are well known but the most widely used today, is that of Oliver and Pharr [167] which was also the model used in this study to measure hardness and modulus of the thin films deposited.

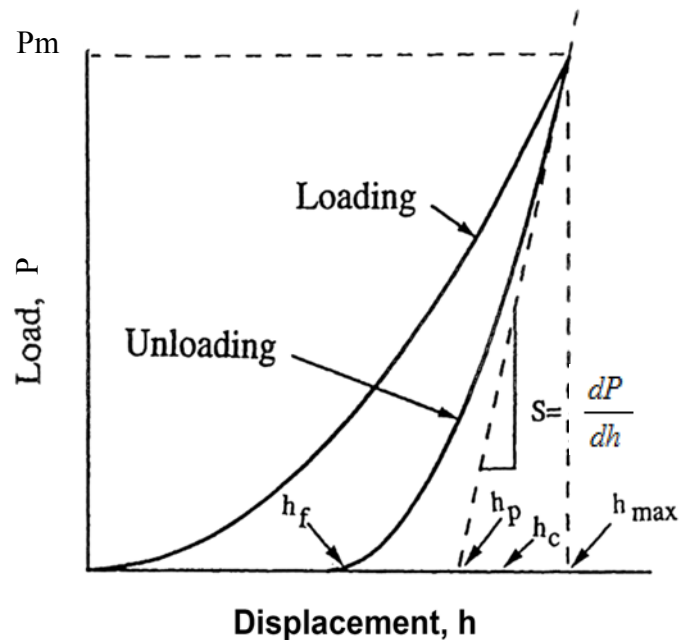


**Figure 3.13:** Schematic of a load–displacement curve [167].

The Oliver–Pharr data analysis procedure [167] begins by fitting the unloading curve to the power-law relation

$$P = B(h - h_f)^m \quad (3.3)$$

Where;  $P$  is the indentation load,  $h$  is the displacement,  $B$  and  $m$  are empirically determined fitting parameters, and  $h_f$  is the final displacement after complete unloading (also determined by curve fitting). The unloading stiffness,  $S$ , is then established by differentiating Eq. (3.3) at the maximum depth of penetration,  $h = h_{max}$ ;

$$S = \frac{dP}{dh}(h = h_{max}) = mB(h_{max} - h_f)^{m-1} \quad (3.4)$$

The contact depth is also estimated from the load-displacement data using;

$$h_c = h_{max} - \varepsilon \frac{P_{max}}{S} \quad (3.5)$$

Where;  $P_{max}$  is the peak indentation load and  $\varepsilon$  is a constant which depends on the indenter geometry [167]. Oliver and Pharr empirical studies have shown that  $\varepsilon=0.75$  for a Berkovich indenter [167]. From the basic measurements contained in the load-displacement data, the projected contact area of the hardness impression,  $A$ , is estimated by evaluating an empirically determined indenter shape function at the contact depth,  $h_c$ ; that is  $A=f(h_c)$ . The shape function,  $f(d)$ , relates the cross-sectional area of the indenter to the distance,  $d$ , from its tip. For a geometrically perfect Berkovich indenter, the shape function is given by  $f(d)=24.56d^2$ , but for real Berkovich indenters,  $f(d)$  is considerably more complex due to tip rounding. A simple experimental procedure has been developed for determining shape functions without having to image the indenter or hardness impressions made with it [167]. In the procedure, a series of indentations of various sizes are made in a material with well-known, isotropic elastic properties (usually fused quartz), and the shape function is deduced from the load-displacement data by assuming the elastic modulus of the material is independent of depth. Once the contact area is determined from the load-displacement data, the hardness,  $H$ , and reduced or indentation elastic modulus,  $E_r$ , follow from;

$$H = \frac{P_{\max}}{A} \quad (3.6)$$

and

$$E_r = \frac{1}{\beta} \frac{\sqrt{\pi}}{2} \frac{S}{\sqrt{A}} \quad (3.7)$$

where  $\beta$  is a constant which depends on the geometry of the indenter ( $\beta=1.034$  for the Berkovich) [167]. The reduced modulus, which accounts for the fact that elastic deformation occurs in both the specimen and the indenter, is given by;

$$\frac{1}{E_r} = \frac{1-\nu^2}{E} + \frac{1-\nu_i^2}{E_i} \quad (3.8)$$

Where;  $E$  and  $\nu$  are the Young's modulus and Poisson's ratio for the specimen, and  $E_i$  and  $\nu_i$  are the same quantities for the indenter [3]. For diamond,  $E_i=1141$  GPa and  $\nu_i=0.07$ . Eq. (3.6) is founded in elastic contact theory [168].

The indentation or reduced modulus obtained from the load-displacement curves as explained above can be slightly different from the Young's modulus determined by ultrasonic or other methods, because it is a weighted average of the elastic properties in a certain sample volume and the Young's modulus is directional. For isotropic materials however, there is no physical reason for this differentiation, and both values should agree if the contact area can be correctly determined [164].

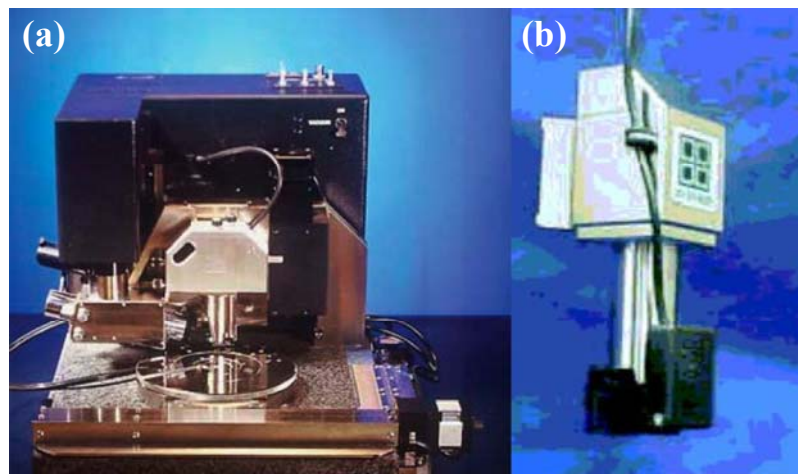


**Figure 3.14:** Nanomechanical test system (a) AFM instrument (b) nanoindenter head that is placed in the place of the AFM head for nanomechanical measurements.

In this study, Hysitron Triboscope mounted on a Veeco AFM instrument was used to measure nanomechanical properties of thin films deposited. This AFM coupled nanoindentation technique provides in-situ imaging of the surface topography of the test location and the resulting test deformation with the same tip that is used to perform the nanomechanical testing.

### 3.2.6 FTIR technique

Fourier transform infrared spectrometry (FTIR) is one of the few techniques that can provide information about the chemical bonding in a material [153]. The goal of the basic infrared experiment is to determine the changes in the intensity of a beam of infrared radiation as a function of wavelength or frequency ( $2.5\text{-}50\ \mu\text{m}$  or  $4000\text{-}200\ \text{cm}^{-1}$ , respectively) after it interacts with the sample [153]. In operation, radiation from the IR source passes through a beam splitter onto a fixed and movable mirror as shown in Figure 3.15. The IR radiation is recombined in an interference pattern which is determined by the position of the movable mirror. Infrared radiation transmitted through the sample or reflected from the surface is detected and a plot of IR absorption versus wavelength is generated [152].

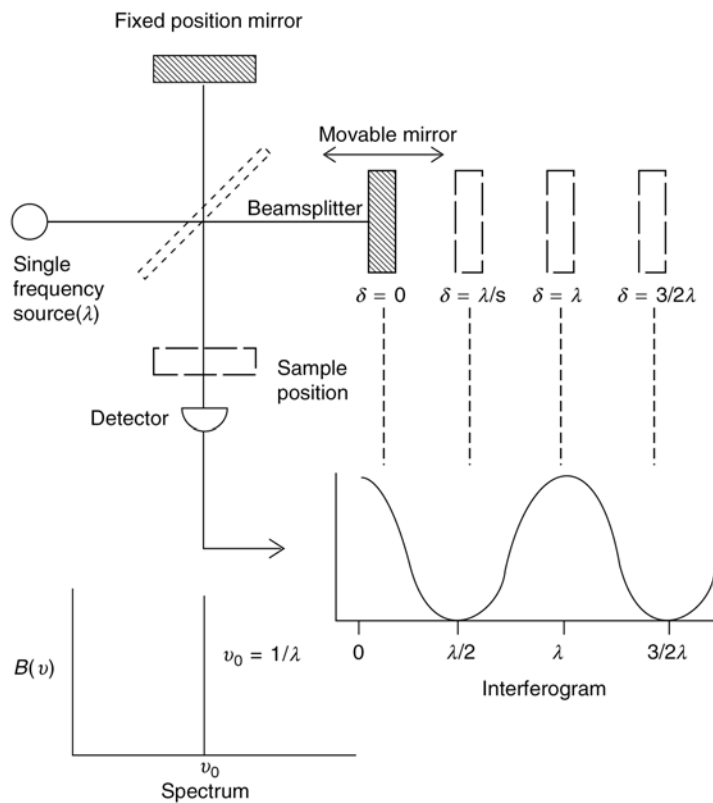


**Figure 3.15:** Schematic of FTIR spectrometry [23].

Peak position is most commonly exploited for qualitative identification, because each chemical functional group displays peaks at a unique set of characteristic frequencies. Hence, computer databases of peak positions and some relative intensity information are used to identify the chemical bonding of analyzed material [153].

In this study the chemical bonding properties of boron carbide and boron carbonitride thin films were investigated by a Parkin-Elmer Spectrum – One System Fourier transform infrared spectrometer with a variable-angle specular reflectance attachment for thin film analysis in the wavenumber range 500 – 4000  $\text{cm}^{-1}$ .

### **3.2.7 Tribological studies**

Tribology is the science and technology of two interacting surfaces in relative motion and of related subjects and practices. The popular equivalent is friction, wear, and lubrication. The word tribology coined in 1966, is derived from the Greek word tribos meaning rubbing, thus the literal translation would be the science of rubbing [169,170].

Wear is the major cause of material wastage and loss of mechanical performance and any reduction in wear can result in considerable savings. Friction is a principal cause of wear and energy dissipation. Considerable savings can be made by improved friction control. It is estimated that one-third of the world's energy resources in present use is needed to overcome friction in one form or another [170].

The introduction of a fluid between the surfaces has long been the most common way to change the tribological behavior of two surfaces moving relative to each other. Another increasingly popular possibility is to apply a thin surface layer or coating on one or both of the surfaces [171]. Hard, wear resistant coatings, especially hard carbides, nitrides and carbonitrides are used to reduce abrasive, adhesive and fretting wear. Applications of wear resistant coatings are found in every industry. In most of these applications, wear rather than friction is the critical problem. Another benefit of hard-coating technology is that a cheap substrate material can be improved by a coating of a high performance material. Most engineering items are made of steel and it is often found that some material other than steel is needed to fulfill the wear and friction requirements. Many wear resistant materials are brittle or expensive and can only be used as a coating, so improved coating technology has

extended the control of wear to many previously unprotected engineering components [170]. “pin-on-disc” testing is a commonly used laboratory technique for investigating the friction and sliding wear of a variety of bulk materials and thin films [171].

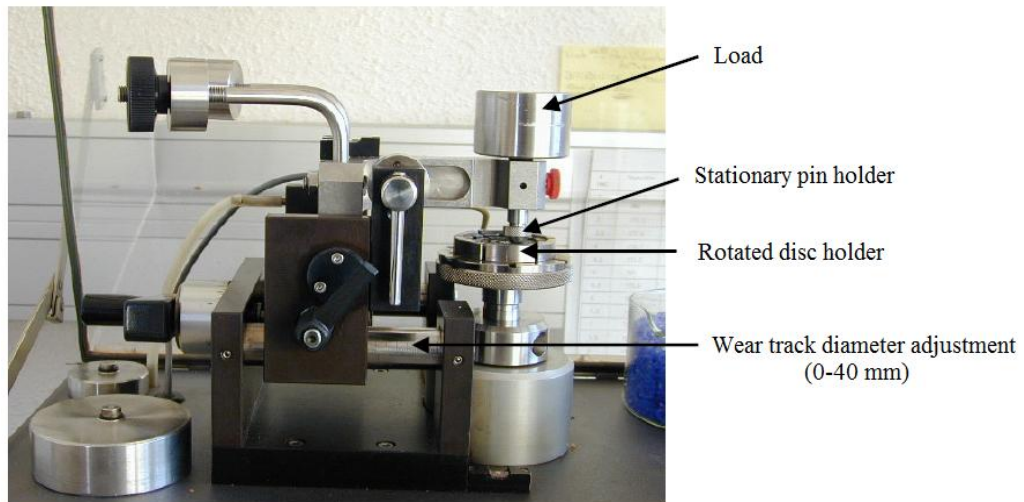


**Figure 3.16:** “pin-on-disc” tribometer.

In the present study, CSEM “pin-on-disc” tribometer shown in Figure 3.16 was used to measure tribological properties of the thin films deposited. As the name implies, such apparatus consists essentially of a stationary "pin" in contact with a rotating disc as can be seen in Figure 3.17. Either the pin or the disc can be the test piece of interest. The contact surface of the pin is generally spherical but may also be flat or any convenient geometry. The normal load, rotational speed, and the wear track diameter are all set by the user prior to the “pin-on-disc” test.

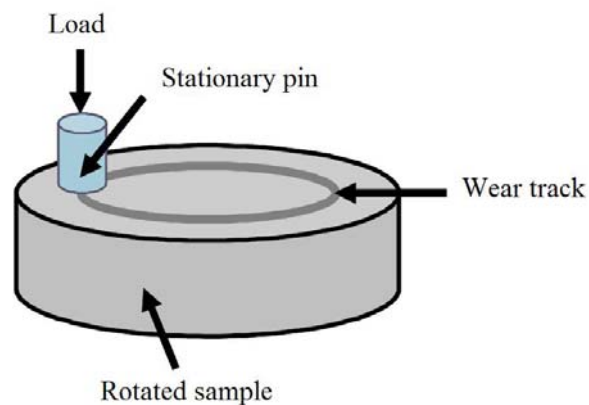


**Figure 3.17:** Schematic of the “pin-on-disc” testing principle [172].

In a typical “pin-on-disc” experiment, the coefficient of friction is continuously monitored as wear occurs and it is calculated by dividing the friction by the applied load. The material removed is determined by weighing or the volume loss is calculated by measuring the profile of the resulting wear track to investigate the wear properties of dry or lubricated surfaces. Changes in coefficient of friction are frequently indicative of a change in wear mechanism, although marked changes are often seen during the early stages of wear tests as equilibrium conditions become established. The main variables which affect friction and wear are velocity and normal load. In addition, specimen orientation can be important if retained wear debris affects the wear rate. The loads used are dependant of the material system and can be in the range of 500 mN–1000 N for most commercial “pin-on-disc” test systems.

In this study, alumina balls of 6 mm diameter were used as counterface to measure the friction and wear properties of all the coatings deposited. In some of the tests on boron carbide coatings, WC and boron carbide coated steel pins were also used. A sliding speed of 0.1 m/s was selected for all of the measurements. All friction tests were carried out in air with controlled humidity between 25% and 30% by means of the silicagel particles placed inside the tribotest environment. Before each test, the pin and specimen were cleaned in ethanol, in an ultrasonic bath for 5 minutes. Wear track diameter of 6 mm was used for all the tests, however when necessary, 7 and 8 mm diameter wear tracks were also produced on the specimens to proof the reproducibility of the results. Friction and wear measurement procedures used in this study are described in the next two sections.

### **3.2.7.1 Friction measurement**

Friction is the resistance to movement of one body over body. The word comes from the Latin verb *fricare*, which means to rub [173].

Friction is commonly represented by the friction coefficient, for which the symbols  $\mu$  or  $f$  generally are used. The friction coefficient is the ratio between the tangential force,  $F$ , and the applied load,  $N$ .

$$\mu = \frac{F}{N} \tag{3.9}$$

For the friction coefficient measurements, during testing, the tangential force,  $F$ , was measured by a set of load cells and was then monitored by a computerized data acquisition system. As the applied load,  $N$ , is known, the friction coefficient is calculated according to the Eq. (3.8) by the data acquisition software and registered as a function of number of tours or sliding distance.

### 3.2.7.2 Wear rate measurement

Wear is a direct consequence of friction and occurs at the contact zones. The wear resistance (wear rate) is estimated by calculating the volume loss of the materials according to the equation:

$$k = \frac{V}{N \times l} \quad (3.10)$$

Where;

$k$  = Wear rate ( $\text{mm}^3/\text{Nm}$ )                       $V$  = Volume loss ( $\text{mm}^3$ )

$N$  = Applied load (N)                               $l$  = Sliding distance (m)

To calculate the wear rates of the coatings, the maximum wear depth  $D$ , the wear length  $l$  and the wear area  $A$ , of the wear tracks were measured by a profilometer (Hommel Tester T500). A schematic example of the measured wear track profile can be seen in Figure 3.18. For each sample, 4 measurements on the same wear track were carried out and the averages of 4 measurements were used to obtain the wear depth, length and area.

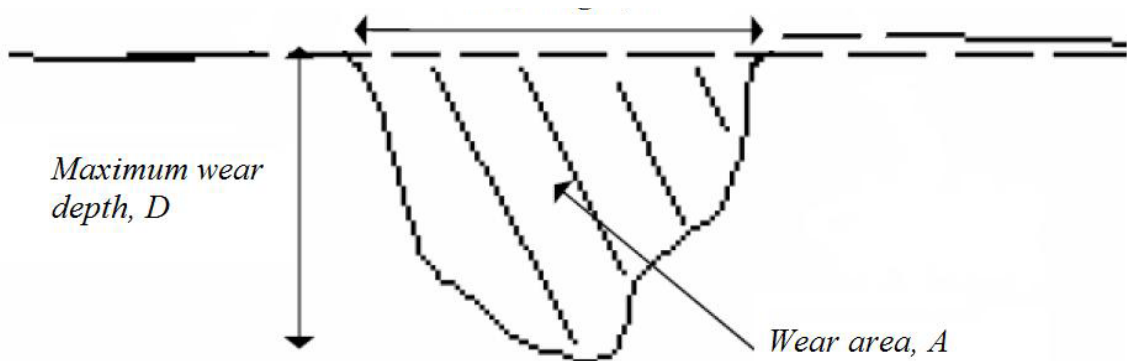


**Figure 3.18:** Representative profile of the wear track obtained by profilometer.

The wear coefficient  $k$  is calculated using the following equation:

$$k = \frac{V}{N \times l} = \frac{2 \cdot \pi \cdot r \cdot A}{N \cdot 2 \cdot \pi \cdot r \cdot n} \quad (3.11)$$

or

$$k = \frac{A}{N \times n} \quad (3.12)$$

Where;

$k$  = Wear rate ( $\text{mm}^3/\text{Nm}$ )

$A$  = Wear area ( $\text{mm}^2$ )

$V$  = Volume loss ( $\text{mm}^3$ )

$r$  = Wear track diameter (m)

$N$  = Applied load (N)

$n$  = tour number

$l$  = Sliding distance (m)

### 3.3 Résumé du Chapitre

Ce chapitre est consacré à la présentation des systèmes de pulvérisation, les matériaux cible et les substrats, les différents paramètres utilisés pour déposer les différents systèmes de couches minces ainsi qu'à la présentation détaillée des techniques de caractérisation utilisées pour élucider les propriétés des couches minces obtenues.

Dans cette étude, une cible de carbure de bore conductrice produite par pressage à chaud des poudre de carbure de bore, compatible avec la décharge courant continu, a été utilisée pour déposer les couches de carbure de bore, carbonitride de bore et les multicouches fonctionnelles. Pour comparaison, une cible de carbure de bore commerciale a été employée pour le dépôt de couches de carbure de bore par pulvérisation radiofréquence. Des aciers de type AISI M2 et AISI 430 ainsi que des « wafers » Si (100) wafers ont servi comme substrats aux couches minces.

Mono-et multicouches minces de carbure de bore et carbonitride de bore ont été déposées par différentes configurations de pulvérisation cathodique. Trois types de couches de carbure de bore bien adhérentes et homogènes ont été déposés par pulvérisation cathodique magnétron classique à courant continu (DC), pulvérisation cathodique magnétron DC assistée plasma et par pulvérisation cathodique radiofréquence (RF). Les couches minces de carbonitride de bore déposées par pulvérisation cathodique magnétron à courant continu en mode réactif avec addition d'azote dans le gaz plasmagène ont été également étudiées. Une conception multicouche fonctionnelle a été adoptée pour déposer des couches de carbure et carbonitride de bore plus épaisses et adhérentes. Les résultats sont présentés.

Les techniques de caractérisation et les raisons de leur emploi sont présentées en détail. On mentionne ici une brève liste des techniques utilisées pour caractériser les propriétés appropriées. La composition élémentaire des dépôts a été mesurée par microsonde électronique de Castaing (EPMA). La microscopie à balayage électronique à haute résolution avec un canon à émission de champ (FE-SEM) a permis l'examen de la microstructure et la topographie des couches minces obtenues. Les profils en profondeur des différents éléments constituant les dépôts ont été

obtenus par spectrométrie de masse d'ions secondaires (SIMS). Les propriétés nanomécaniques ont été évaluées par nanoindentation. Le comportement tribologique des dépôts a été étudié en utilisant un dispositif « pion-disque ». Les liaisons chimiques ont été évaluées par spectroscopie infrarouge à transformée de Fourier (FTIR). La nanostructure et la cristallinité des couches ont été caractérisées par microscopie électronique à transmission (TEM).



---

**CHAPTER 4:**  
**RESULTS AND DISCUSSION**

---



## **4. RESULTS AND DISCUSSION**

In this chapter, the results of the experimental studies obtained from various characterization techniques will be presented and discussed in separate sections for all series deposited.

### **4.1 DC Sputtered B<sub>4</sub>C Films**

In this section results obtained from the characterization studies on B<sub>4</sub>C films deposited by conventional DC magnetron sputtering and plasma-enhanced DC magnetron sputtering will be presented and discussed.

#### **4.1.1 Early studies and the optimization of deposition parameters**

Figure 4.1 shows the high-resolution cross-sectional SEM micrographs of the first boron carbide thin films deposited in this study. In Figure 4.1 (a) coarse columnar structure of boron carbide film can be seen, in (b) taken with 10° tilt angle, rough, cauliflower-like surface morphology of the deposited film is shown.

These first experiments were realized at  $3 \cdot 10^{-3}$  Pa base pressure and at 2 Pa working pressure when the chamber was back-filled with argon precursor. EPMA analyses carried out on this specimen resulted with 76 at.% B, 20 at.% C, with 3,5 at.% O and 0,5 at.% Si as impurities. The reasons of such derivation from the stoichiometry and the excess amount of oxygen incorporation for the columnar structured films deposited in this study will be explained in the following sections of this manuscript.

After the preliminary set of experiments and microstructural characterization studies, it is concluded that the main parameters influencing the coating microstructures were the base and working pressures. The mean free path of particles is decreasing while increasing the pressure in a plasma environment, as explained in Section 2.3.2.

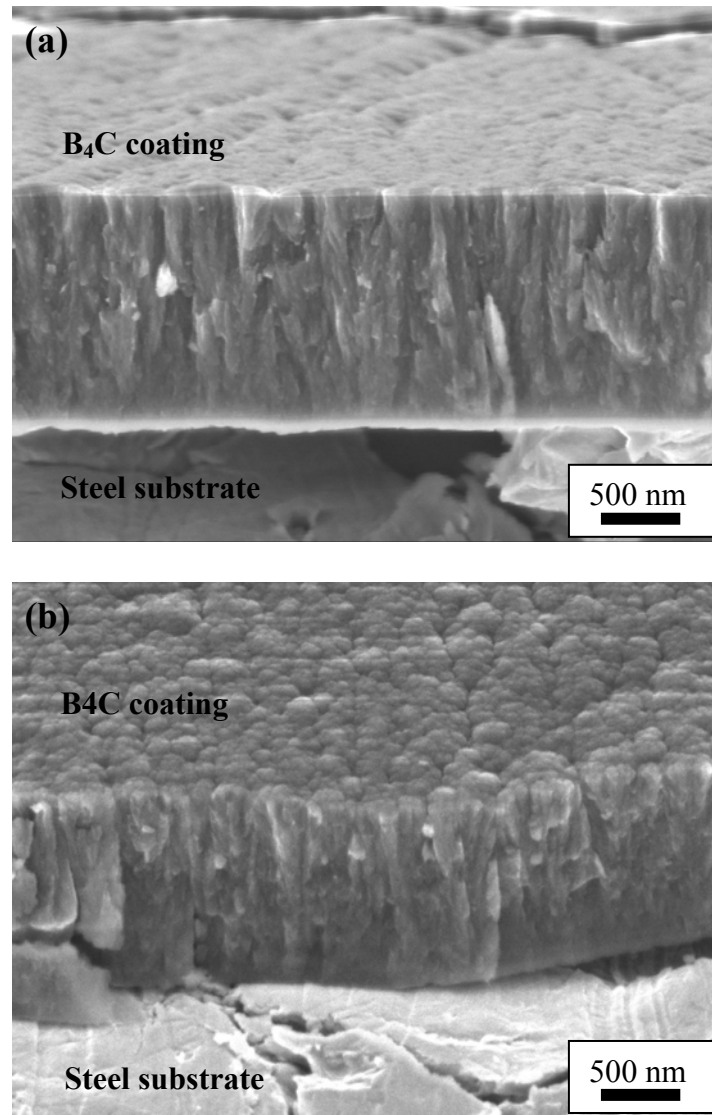


**Figure 4.1:** Cross-sectional SEM micrograph of the first boron carbide film deposited in this study showing (a) the columnar microstructure of the film (b) cauliflower-like surface morphology.

Hence, the atomic self-shadowing becomes the dominant factor while film growth due to the oblique flux because of increased scattering probability. Thus, resulting films microstructures were columnar. This was the reason to fix the base pressure below  $10^{-5}$  Pa, its minimum value that was possible to obtain by a combination of rotary and turbomolecular pumps. Furthermore, the working pressure was set to 0.3 Pa to coerce the increase the mean free path of the neutrals in the flux while decreasing the probability of the oblique flux theoretically for the rest of the coatings deposited in this study.

Second important observation was about the film thicknesses and the adhesion of the coatings. As can be seen in Figure 4.1, the thickness of the coating on AISI 430 substrate, deposited for 90 minutes was around 1  $\mu\text{m}$ . It is observed that the coating suffers from delamination a short while after its exposition to the atmospheric pressure due to the ambient moisture (no or less delamination was observed in vacuum). The adhesion problems were much important for the films deposited by auxiliary plasma configuration and in the presence of applied bias voltages. Adhesion problems are common especially for films deposited under intensive ion bombardment by applying negative bias voltages while film growth and also observed by other researchers for boron carbide and BCN thin films as explained in the Sections 2.4 and 2.5. These can be explained by the high level of internal (mostly compressive due to the ion bombardment during grown) stresses generated in these films and also the mismatch of the substrate mechanical properties with remarkably high hardness and modulus of the films deposited.

A series of experiments were carried out on three different substrates with different deposition times and resultant films were then investigated by cross-sectional SEM analyses to find out an optimum thickness below which no delamination occurs. It is concluded by direct observations coupled with SEM analyses that, for AISI 430 steel, delamination in ambient moisture starts around 500 nm and for AISI M2 steel around 900 nm. For Si substrate no delamination was observed for the thickness interval reached in this study. Figure 4.2 shows delaminated and well adherent boron carbide thin films on AISI 430 and AISI M2 substrates after the exposure to the ambient moisture.

In Figure 4.2, (a) delamination of the boron carbide coating deposited on AISI M2 substrate can be clearly seen, mirror polished steel substrate is visible especially at the extremities of the substrate. The coating thickness measured by cross-sectional SEM observation was around 1  $\mu\text{m}$ . In (b) well adherent boron carbide coating on AISI M2 substrate with 400 nm thickness is shown. Note that the bright black color of the boron carbide coating is a result of the mirror polishing of the steel substrate; otherwise, the real color of the boron carbide is dark gray. In Figure 4.2 (c) delamination of the boron carbide coating on AISI 430 steel substrate can be seen.

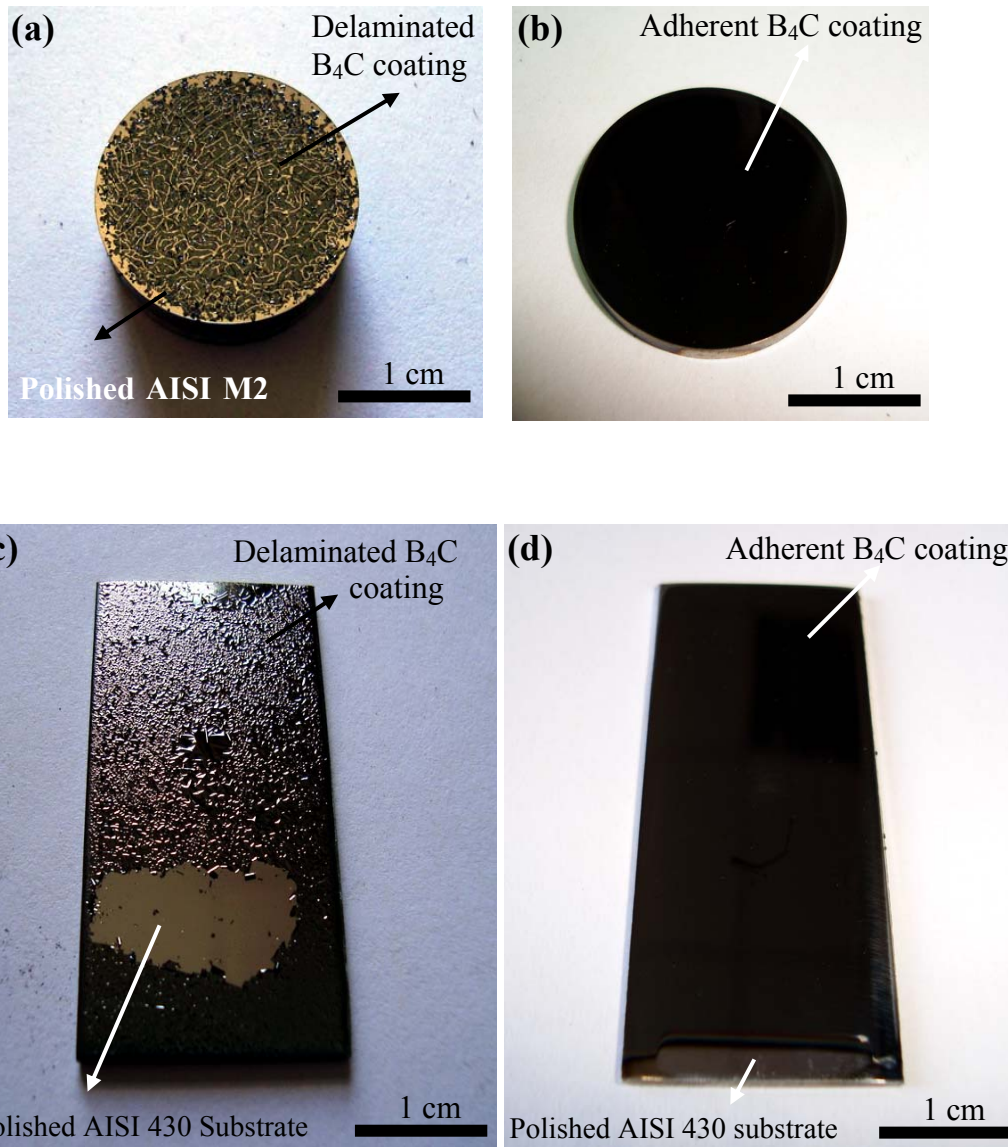


**Figure 4.2:** (a) Delaminated boron carbide coating on AISI M2 substrate (b) well adherent boron carbide coating on AISI 430 substrate (c) delaminated boron carbide coating on AISI 430 substrate (d) well adherent boron carbide coating on AISI 430 substrate.

The thickness of this coating measured by SEM was 600 nm. Mirror polished steel substrate can be seen towards the bottom of the specimen as a result of complete delamination of the coating at this zone. In (d) well adherent boron carbide coating deposited on AISI 430 substrate with 400 nm thickness is shown. It has to be noted that the zone at the bottom of this specimen, where the polished substrate is visible, is not an evidence of the coating delamination, instead it is the part, which received no flux because it was attached from this part to the special designed substrate holder.

As a result of the above observations, it is concluded that the thickness plays an important role on the generation of the internal stresses and there are different threshold thicknesses for different types of substrates used in this study, above which the delamination of the coatings occur. Thus, a thickness of about 400 nm, which was reached in 75 minutes (for boron carbide coatings), was selected for all boron carbide coatings deposited with and without auxiliary plasma configuration and on all three types of substrates, to properly compare the properties of different thin films deposited in this study.

#### **4.1.2 Conventional DC magnetron sputtered B<sub>4</sub>C films**

In order to distinguish different properties obtained from boron carbide coatings deposited by different configurations, the results will be discussed in separate sections. Followings are the results for boron carbide films deposited by conventional DC magnetron sputtering, thus without the presence of the auxiliary plasma source.

##### **4.1.2.1 Microstructural studies**

Microstructures were observed for all three coatings deposited without external plasma configuration. Figure 4.3 (a) shows cross-sectional SEM observations of the specimen BC47 deposited on Si substrate. The columnar structure can be clearly seen from the figure. Note that the micrograph is taken with a 10° tilt angle in order to observe the coating microstructure and the surface morphology together. Measured film thickness was 370 nm for this coating.

BC47 was deposited without any external hating at 44 °C which corresponds to T/T<sub>m</sub> of 0.02 and with an Ar pressure of 0.3 Pa which is equal to 3 mtorr is situated in the Zone 1 of the Thornton diagram as explained in Section 2.3.2 and is shown in the figure (b) with a circle. The same coating deposited without applying any bias voltages is also situated in the zone 1 according to Messier's SZD which replaced the Ar pressure axis with ion bombardment (bias) voltages.as can be seen in Figure 4.3 (c)

For this specimen, the formation of the columnar structure can be explained by the low adatom mobility and atomic shadowing due to the very low deposition temperature (T/T<sub>m</sub>) as explained in Section 2.3.2.

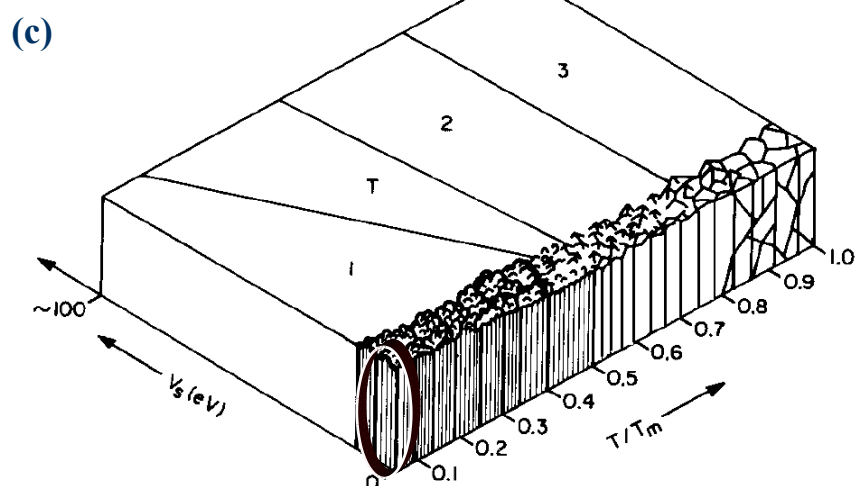
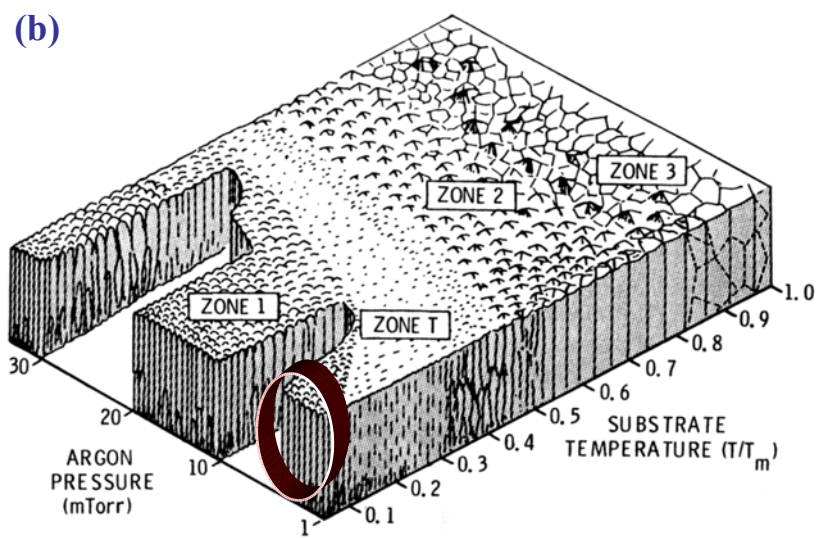
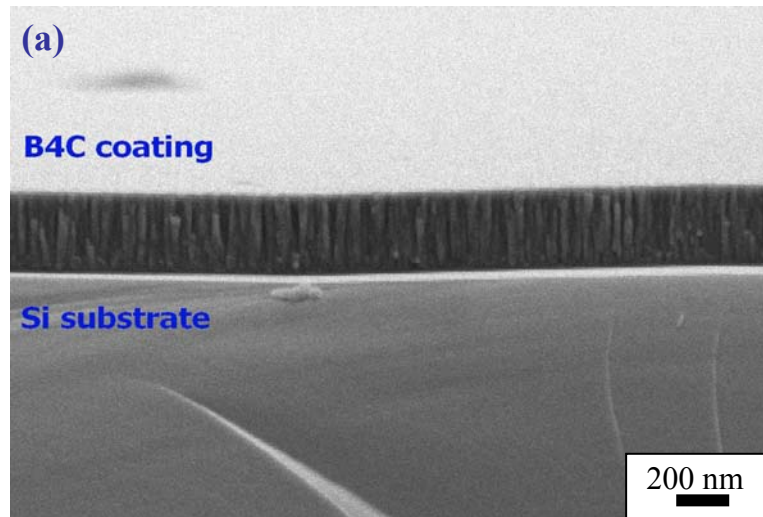


**Figure 4.3:** Cross-sectional SEM observation of the specimen BC47 (a) columnar structure of the B<sub>4</sub>C thin film (b) corresponding morphology on Thornton diagram (c) corresponding morphology on Messier's SZD.

In Figure 4.4, cross-section of the specimen BC48 is presented. This picture is taken from the coating deposited onto AISI 430 steel substrate. The sample was embrittled in liquid nitrogen and the pictures were taken from the fractured cross-section.

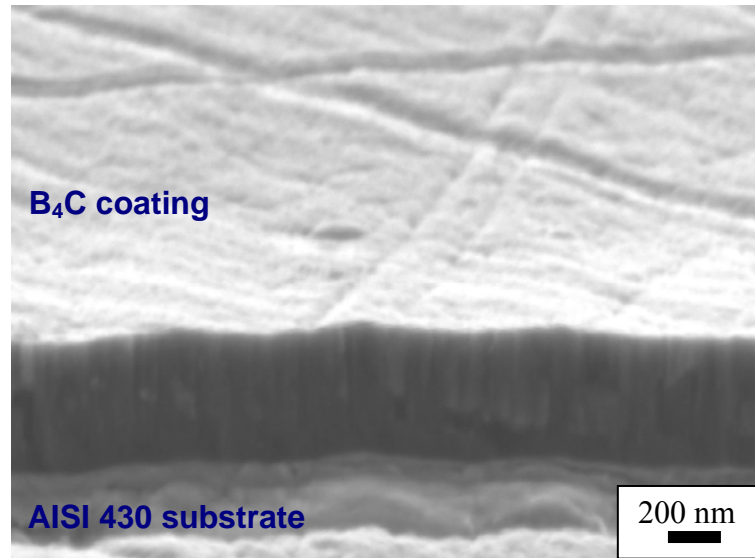


**Figure 4.4:** Cross-sectional SEM image of the specimen BC48.

As can be observed from the figure, there was no dramatic change in the microstructure of BC48, deposited with 50 V bias voltage and the coating morphology although denser was still columnar with less distinguishable voids between columns compared to the specimen deposited without applying any bias voltages. The scratches observed at the surface of the coating were originated from the scratches of the substrates due to polishing. These observations confirmed the fact that the hills receives more flux than the valleys explained in the Section 2.3.2, hence surface roughness of the substrates play a very important role on the roughness of the coating.

To explain the change in the microstructure of the specimen deposited with 50 V applied bias voltage compared to the previous one, Messier's SZD will be used as Thornton visualizes the microstructural changes in his SZD by two parameters, deposition temperature and pressure. The pressure and deposition temperature were identical for these two coatings. Thus, the main effect was the bias voltage applied to the substrates during film growth which will be more clarified by the following microstructure of the specimen deposited at 250 V bias voltage.

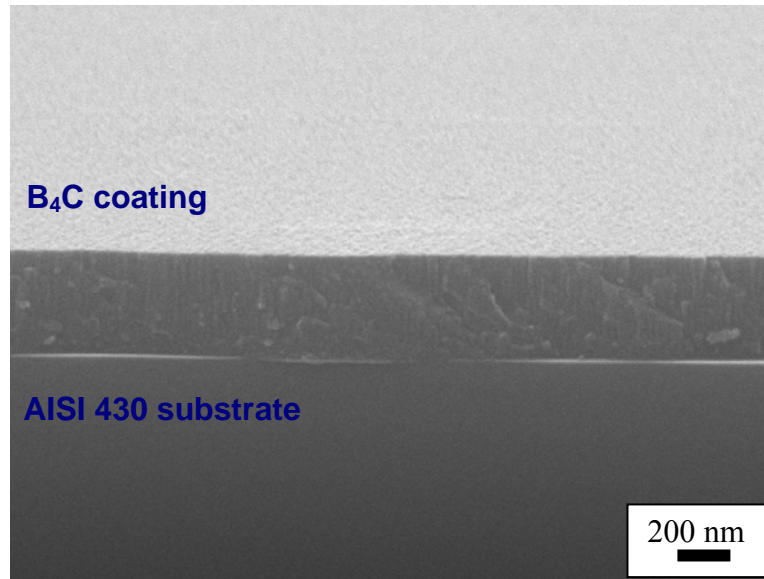


**Figure 4.5:** Cross-sectional SEM observation of the specimen BC49.

Figure 4.5 is the cross-sectional observation for BC49. From the figure, it can be seen that even for this coating deposited with 250 V bias voltage, the columnar morphology was still present. However, the columns were not clearly separate like two preceding samples deposited without applying any bias voltages and 50 V bias voltages. It can thus be concluded a transformation from zone 1 to zone T microstructure as indicating Messier's SZD, although their diagram was limited to 100 V ion-bombarding voltages. In Messier's SZD, the trend of the increase of the Transition zone with the increase in the bias voltages is remarkable between 0 V which includes almost no Transition zone even for elevated deposition temperatures and, large Transition zone at 100 V even for low deposition temperatures. Hence, it is believed that in our case, the trend continues and boron carbide coating deposited at 250 V bias voltage had zone T microstructure although it was deposited at very low temperatures. In other words, a densification occurred with the increase in the bias voltages. However, the effect was not sufficient to completely surpass the columnar structure.

#### **4.1.2.2 Chemical composition**

Electron Probe Micro analysis was used to quantify the chemical composition of B<sub>4</sub>C coatings deposited by conventional DC magnetron sputtering, without auxiliary plasma configuration, at three different bias voltages. Results are presented in Table 4.1.

**Table 4.1:** Elemental composition of the boron carbide coatings deposited without auxiliary plasma.

|      | B (at.%) | C (at.%) | O (at.%) | Si (at.%) |
|------|----------|----------|----------|-----------|
| BC47 | 77.25    | 20.87    | 1.46     | 0.42      |
| BC48 | 77.06    | 21.78    | 0.65     | 0.51      |
| BC49 | 78.05    | 21.17    | 0.32     | 0.46      |

The first observations from the elemental compositions were the difference of the oxygen concentrations between three coatings. With exactly the same deposition conditions, in the meaning of base and working pressures, sputtering power and target voltage, the coating deposited without applying bias voltage, resulted with the highest amount of oxygen incorporated with 1.46 at.%. At 50 V applied bias voltage it decreased to 0.65 at.% and at 200 V to 0.32 at.%. There was no significant change on the boron and carbon concentrations and with Si that incorporated to the composition as the target material impurity; the coatings had the hot-pressed boron carbide target material composition. As it was explained in the theoretical part of the manuscript, columnar microstructures presents voids between the columns and in our case there is a significant difference between the amounts of oxygen of different but all columnar microstructures, including the first B<sub>4</sub>C coating given in Section 4.1.1, with coarse columnar microstructure with 3.5 at.% O. Thus, it is concluded that further investigations by TEM should have been realized to analyze in details the coating microstructures and the results are presented in the next section.

#### 4.1.2.3 Nanostructural analyses

Further investigations of the columnar BC47 were carried out by means of TEM. shows the microstructure of the specimen in details. In Figure 4.6 (a), the columnar microstructure of BC47 can be seen as in the SEM observations given in Figure 4.3. However, no further investigation could be possible by SEM due to the resolution limitations. By TEM observations, in Figure 4.6 (b), columnar structure was further revealed and column boundaries were made visible. These are images obtained by defocusing the beam and forcing to obtain Fresnel fringes<sup>5</sup>.

---

<sup>5</sup> These fringes result from the electrons experiencing an abrupt change in the scattering potential parallel to the electron beam path and they are best seen when the object is slightly out of focus.

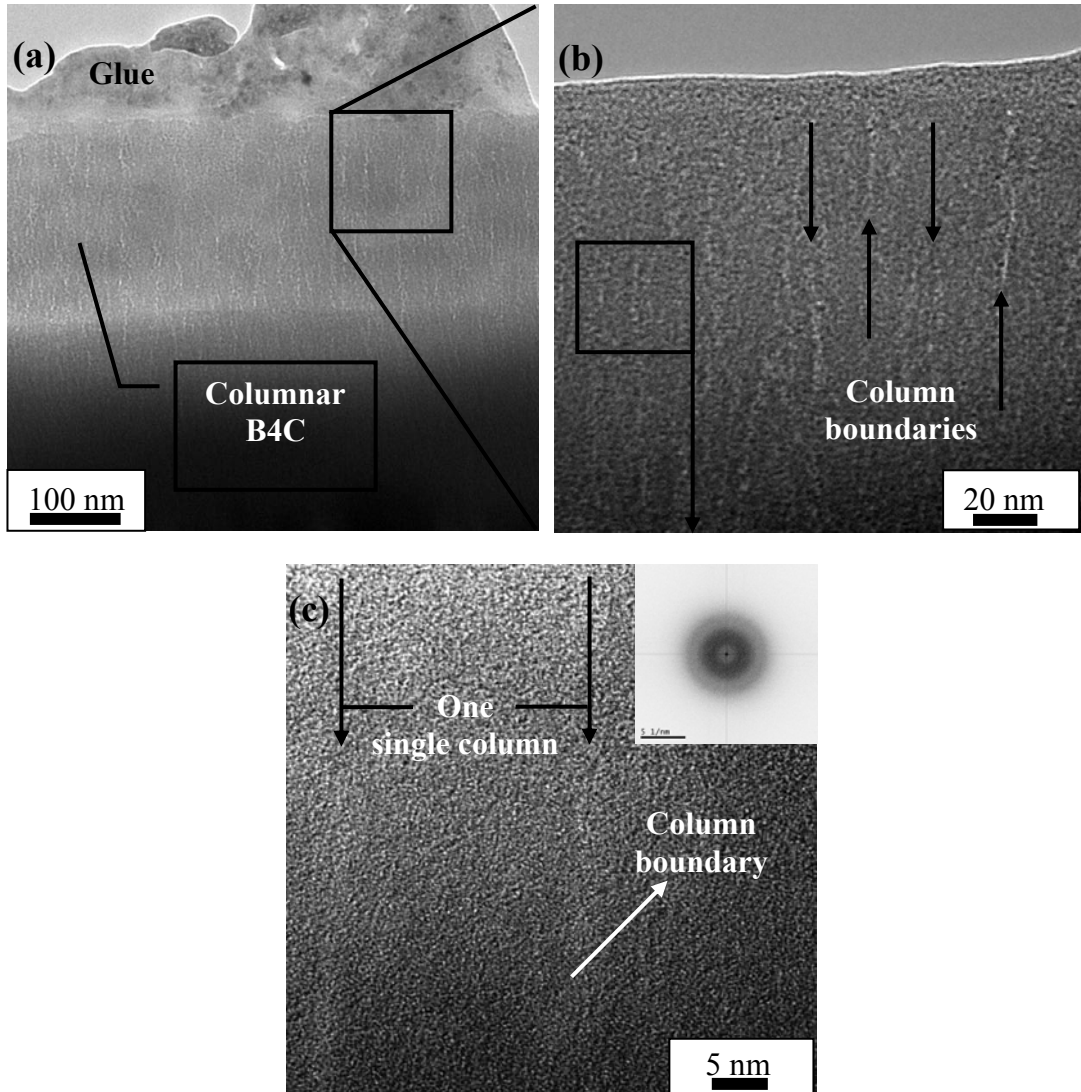


**Figure 4.6:** Cross-sectional TEM observations of the specimen BC47 (a) general view of the columnar structure (b) column boundaries in detail (c) HRTEM observation of one single column and Fast Fourier Transform (FFT) diffraction pattern.

In Figure 4.6 (c), one single column can be seen by high-resolution TEM observation, two arrows demonstrates column boundaries again obtained by Fresnel fringes. Individual columns from (b) and (c) were 20-25 nm in thickness, which is in good agreement with the findings of Messier as explained in Section 2.3.2. In Figure 4.6 (c), inset FFT pattern demonstrates the amorphous structure of boron carbide coating.

It has to be noted that, when compared the microstructural and nanostructural analyses on the same specimen realized by SEM and TEM and given in Figure 4.3 (a) and Figure 4.6 respectively, columns are better seen in SEM micrograph than in low-resolution TEM observations realized with the same magnification. It is believed that, the reason for that lies in different sample preparation used for two techniques.

For SEM observations Si substrate on which boron carbide coating was deposited, was fractured and directly observed from its cross-section. However, for TEM observations, as explained in details in Section 3.2.3.1, the specimen was prepared by sandwich technique, polished with different grain sized diamond cloths and ionically thinned to electron transparency. Hence, it is believed that while fracturing the specimen, an extra contrast was added during SEM observations. However, for TEM analyses the contrast, which should already be present, was eliminated during polishing and thinning sequences. Defocusing of the beam had to be used to create Fresnel fringes to increase the contrast and to clearly identify and observe the columnar structure.

EFTEM analyses were also carried on the same specimen. In Figure 4.7, boron EFTEM analysis is shown. Figure (a) shows the analyzed area and (b) boron mapping obtained from the same area. The distribution of boron is quite homogenous, however, a lack of boron at the column boundaries has been observed during the analyses, as can be seen in the figure.

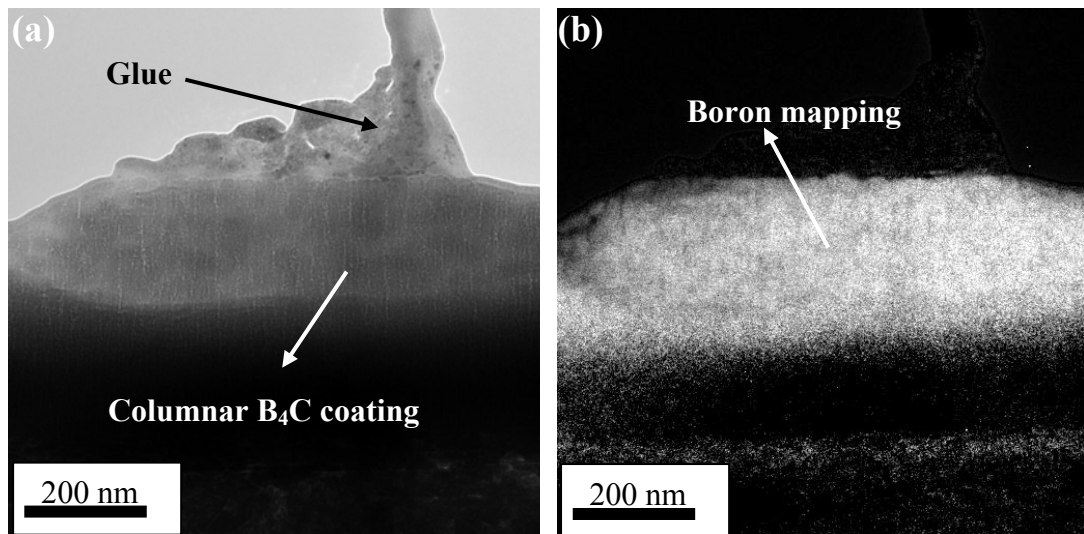


**Figure 4.7:** EFTEM analysis on the specimen BC47 (a) the area of observation (b) boron distribution in the same area.

More detailed EFTEM analyses were than conducted with higher magnifications, including boron, carbon and oxygen elemental mapping. Figure 4.8 demonstrate the results obtained, in (a) low-resolution TEM micrograph with a square indicating the analyzed area and (b) zero loss image of the analyzed area can be seen. Column boundaries are present in the figure, obtained by Fresnel fringes as precedents. Boron

distribution is shown in (c) and the same phenomenon obtained in Figure 4.7 is present in a smaller zone, which is the lack of boron at column boundaries, in other words, in nano-voids with approximately 2-3 nm thickness, which are present between the columns. It is clear from Figure 4.7 (d) that impurity oxygen present in the deposition chamber, or oxygen from the ambient atmosphere after the exposition of the specimen, is trapped at these nano-voids. Thus, the reason of the excess amount of oxygen obtained from EPMA analyses is clarified analytically by TEM observations.

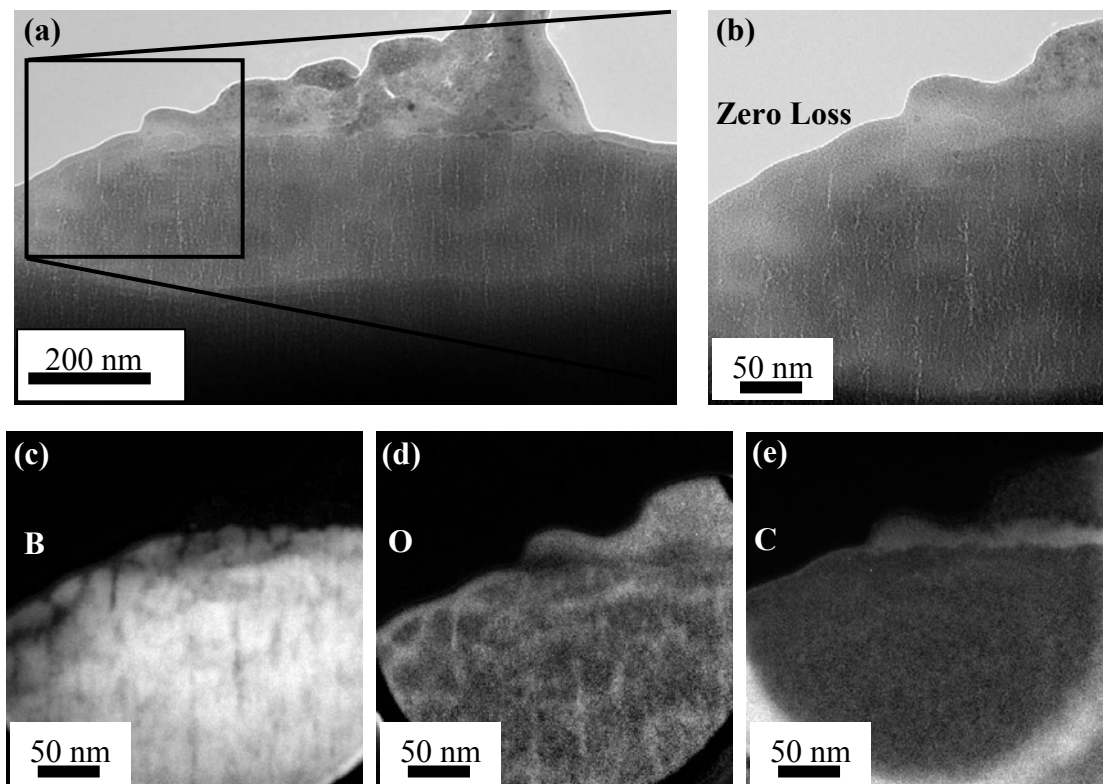


**Figure 4.8:** Elemental distribution by EFTEM analyses, (a) low-resolution TEM image of boron carbide coating indicating the observed zone (b) zero loss image of the observed zone (b) boron distribution (c) oxygen distribution (d) carbon distribution.

These results also demonstrated that boron carbide coatings deposited by conventional DC magnetron sputtering without external heating were amorphous with columnar microstructures. The columns, which can be seen in details in Figure 4.6 and Figure 4.8, were not completely continuous all along the thickness of the coating. Instead, they were randomly interrupted which was proved by the EFTEM boron and oxygen distributions.

#### 4.1.2.4 Nanomechanical properties

First, a series of nanoindentation measurements with variable maximum applied loads between 1000–8000  $\mu\text{N}$  were realized on the coatings deposited on steel and Si (100) substrates to optimize the load. Load-penetration curves for the specimen BC47 deposited on Si and AISI 430 substrates, from which the hardness and Young's modulus of the films were calculated by using the elastoplastic model proposed by Oliver and Pharr, is given in Figure 4.9. This plot was taken with an applied load of 8000  $\mu\text{N}$ . For the same coating deposited at floating potential on Si substrate, a well defined load-displacement curve for hard coatings was observed with 70% elastic recovery after unloading. However for the film deposited on AISI 430 substrate around 3000  $\mu\text{N}$  which corresponds to a penetration depth of 75 nm, a derivation occurs and the curvature of the load-displacement curve starts to decrease instead of increasing gradually like the blue curve (BC47 on Si). Since the coatings are homogeneous throughout their thickness, this derivation can be identified as the point where plastic flow starts within the AISI 430 substrate, which is softer than Si substrate and considerably softer than the coating. The same phenomenon was observed for all the coatings analyzed.

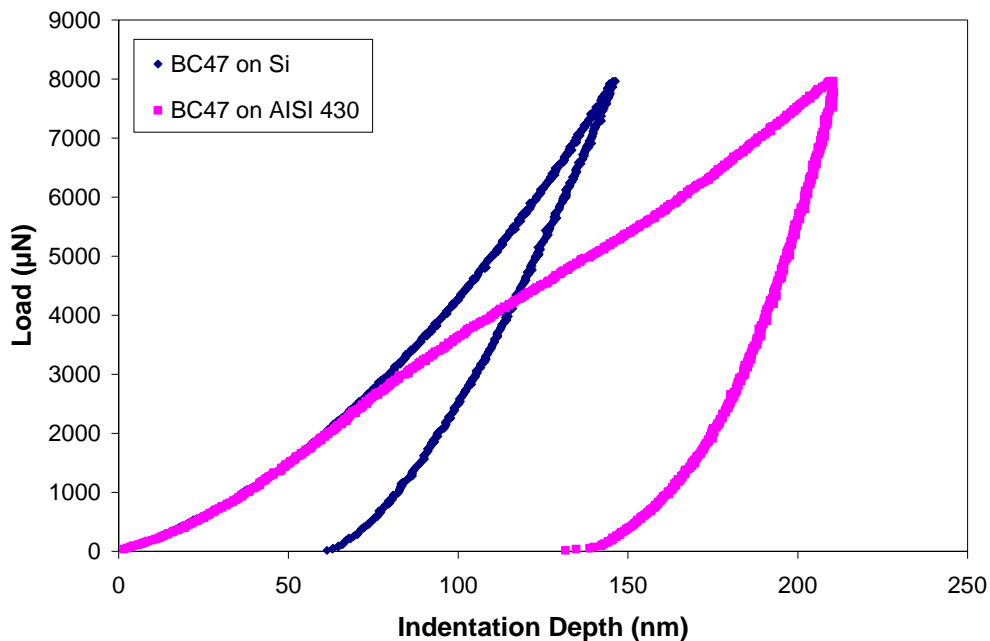


**Figure 4.9:** Load-displacement curves for BC47 on Si and AISI 430 substrates.

In Figure 4.10, the hardness and Young's modulus curves versus indentation depth obtained for the specimen BC47 for different applied loads is given.

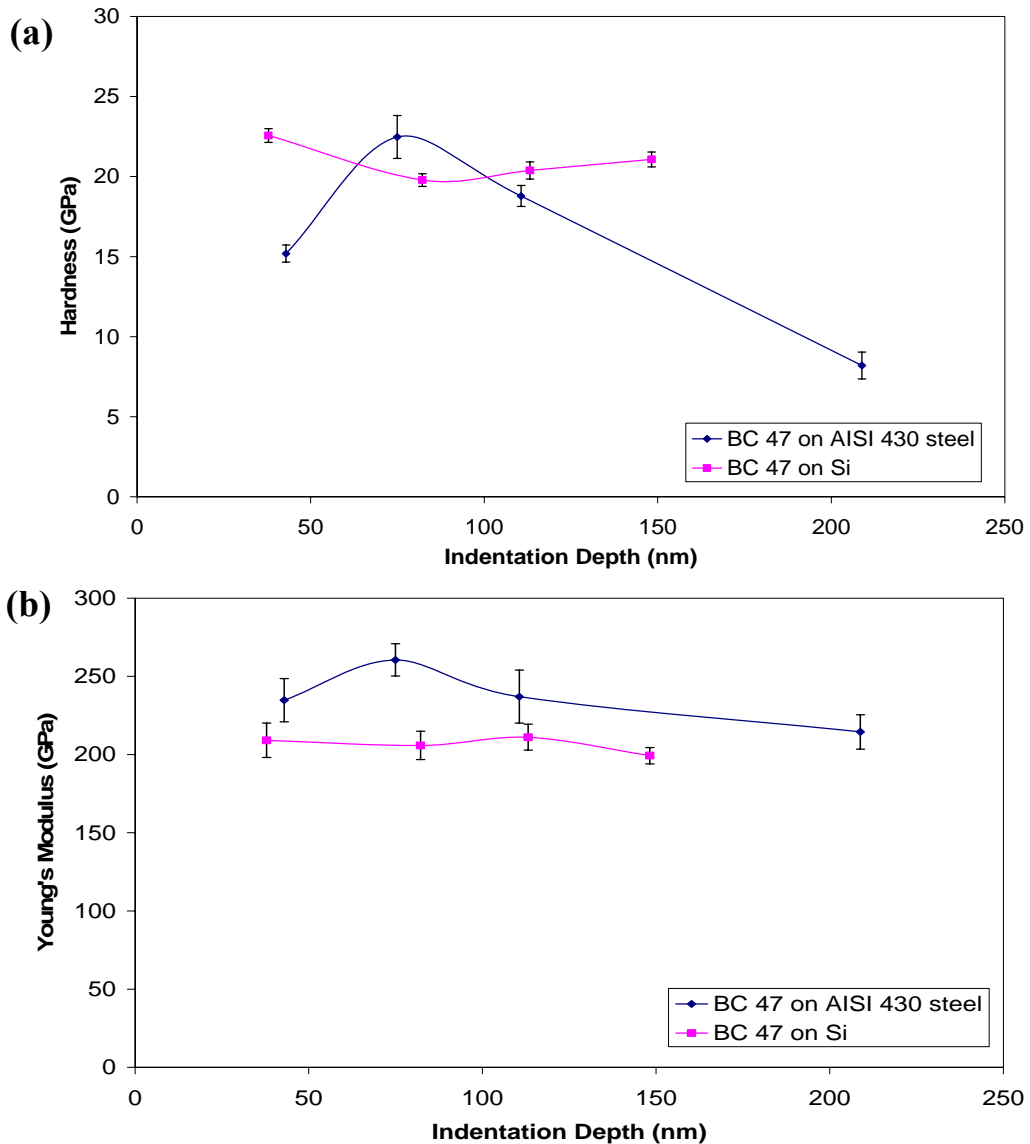


**Figure 4.10:** (a) Hardness vs. indentation depth diagram of the specimen BC 47 (b) Young's modulus vs. indentation depth diagram of the same specimen.

As can be observed from Figure 4.10 (a), for the same coating deposited on Si substrate, after 3000  $\mu\text{N}$ , the hardness values demonstrate a quite stable nature around 20 GPa, while for the film on AISI 430 substrate, a drastical decrease occurs due to the substrate effect. At 5000  $\mu\text{N}$  for 110 nm penetration depth it decreases to 18 GPa and at 8000  $\mu\text{N}$  applied load which results with a penetration depth of around 210 nm, the hardness values decreases to 7 GPa. The Young's modulus values are not much influenced from the substrate effect with increasing applied load, however, again a much stable nature is observable for the coating deposited on Si substrate in Figure 4.10 (b), while a decrease can be seen for the coating deposited on AISI 430 substrate.

In the light of above observations which were also valid for all the specimens analyzed, to study the nanomechanical properties of the coatings deposited with different process parameters solely, without the influence of the substrates, measurements were realized on the coatings deposited on Si substrates, with 3000  $\mu\text{N}$  applied force. Thus, the measurements, which demonstrated no tip rounding effect for lower loads and no substrate effect for higher loads, were taken into account while investigating the effect of deposition parameters. The results are summarized in Figure 4.11.

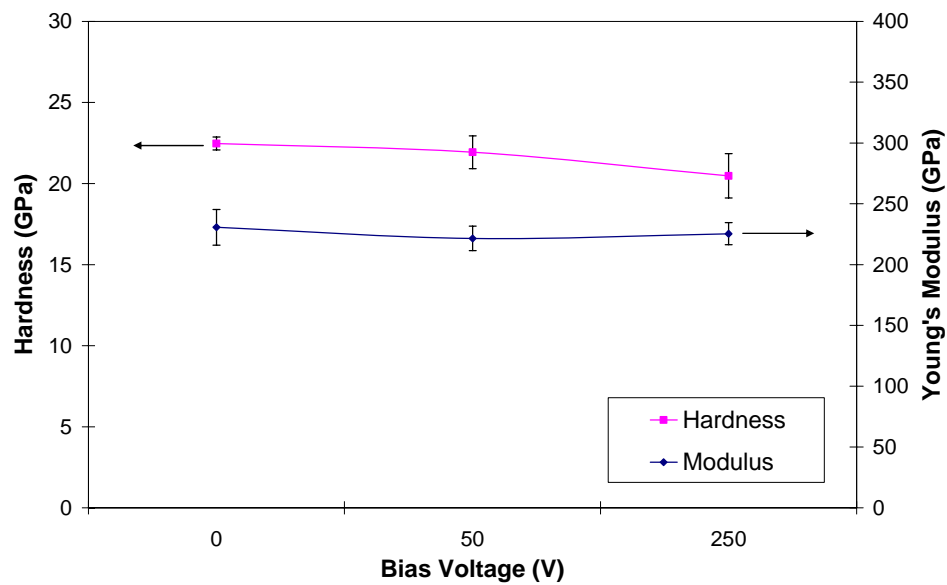


**Figure 4.11:** The effect of the bias voltage on the nanomechanical properties of  $\text{B}_4\text{C}$  films deposited without auxiliary plasma configuration.

As can be seen from Figure 4.11, the nanomechanical properties of boron carbide coatings, which were deposited without auxiliary plasma, hence with a lack of a dense plasma around the substrates, were not influenced by different applied voltages, although the microstructures have been changed from columnar for the coating deposited at floating potential to a denser structure for the coating deposited at 250 V bias voltages. It is clear from the TEM observations that the columnar structure of the film deposited at floating potential was not continuous along the coating and the voids between the columns were only a few nanometers. The densification effect for the coatings was not enough to have effect on the hardness and modulus of the coatings. In this case, the films during their growth were bombarded by insufficient amount of the ions with insufficient kinetic energy because of the absence of dense plasma around the substrates, which is the reason of this insensitiveness to the increased bias voltages.

#### 4.1.2.5 Bonding properties

The phase composition of the films was investigated by FTIR spectroscopy. Figure 4.12 shows representative FTIR spectra of boron carbide films deposited by conventional DC magnetron sputtering. There was no effect of the deposition parameters on the bonding properties of conventional magnetron sputtered boron carbide films. Infrared spectra present two broad bands, one centered at  $\sim 1100\text{ cm}^{-1}$  and the other at  $\sim 1600\text{ cm}^{-1}$ . The band at  $1100\text{ cm}^{-1}$  is attributed to B–C bonds in the icosahedra and is characteristic of  $\text{B}_4\text{C}$  thin film structure [63,97,134,136,141]. The band near  $1570\text{ cm}^{-1}$  has been attributed either to the presence of free carbon in boron carbide structure or to the vibrations of the linear C–B–B chains that interconnect the icosahedra [97,174,175].

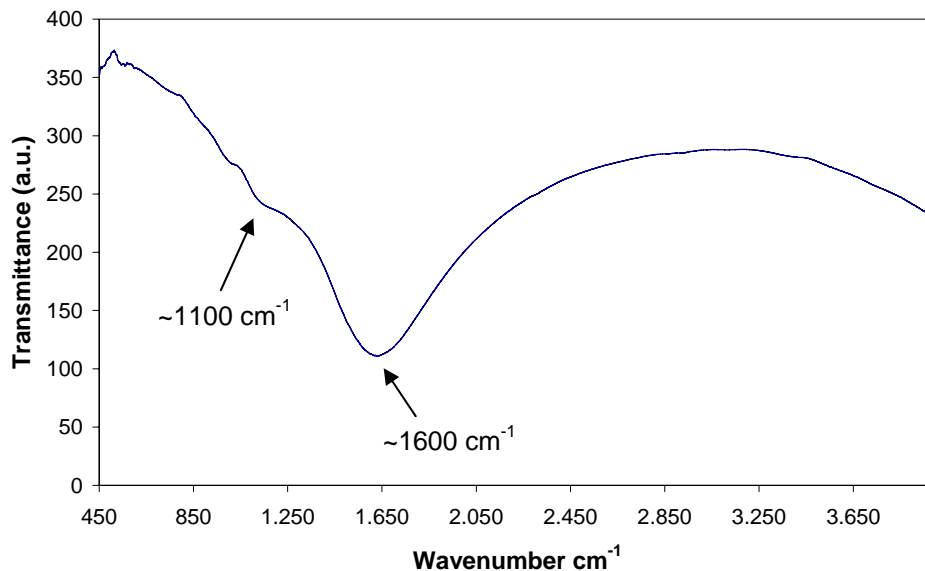


**Figure 4.12:** Representative FTIR spectra of boron carbide films deposited by conventional DC magnetron sputtering.

#### 4.1.2.6 Tribological properties

Tribological tests were performed using a “pin-on-disc” tribometer. An alumina ball of 6 mm diameter was used as the counterface. A sliding speed of 0.1 m/s was selected for all the tests. The applied force was 1 N. A radius of 8 mm was used and a total sliding distance of 300 m was chosen to see the friction coefficient behavior in details. At least 4 tests were realized with each configuration and the mean value is presented as wear rate.

Detailed optimization processes to measure tribological properties of the coatings solely, without the influence of the substrate will be described in Section 4.1.3.6. Friction coefficient evaluation of boron carbide film deposited on AISI M2 substrate against alumina ball is presented in Figure 4.13.

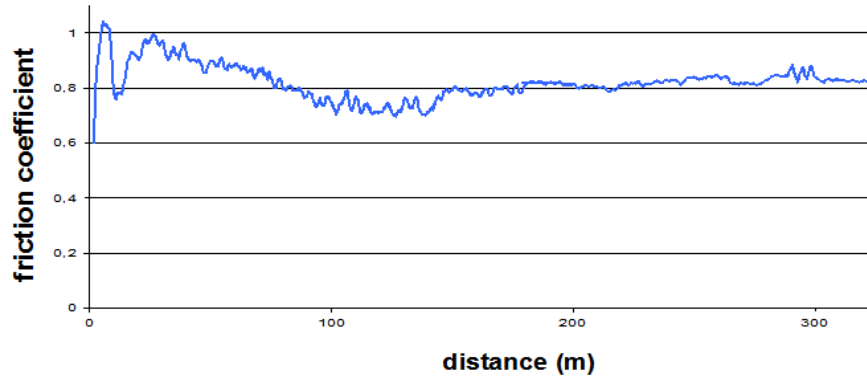


**Figure 4.13:** Representative friction coefficient vs. distance diagram of conventional DC magnetron sputtered B<sub>4</sub>C thin film against alumina ball.

As can be seen from the figure, at the beginning of the test, the friction coefficient increased drastically and reached values about 1. It decreased gradually to about 0.7, which is believed the friction coefficient of conventional DC magnetron sputtered B<sub>4</sub>C thin film against alumina ball. Then it reached a steady-state level around 0.8, which is the friction coefficient of the steel substrates against alumina ball. All three coatings deposited with three different applied bias voltages demonstrated the same friction coefficient evaluation.

According to friction coefficient evaluation, 100 m sliding distance was chosen to observe only the tribological behavior of boron carbide coatings deposited by conventional DC magnetron sputtering by applying different bias voltages. After the experiments, the wear rates were calculated by measuring the depth and width of the wear tracks by a profilometer. A representative profile of the wear track obtained at the end of 100 m sliding against alumina ball can be seen in Figure 4.14.

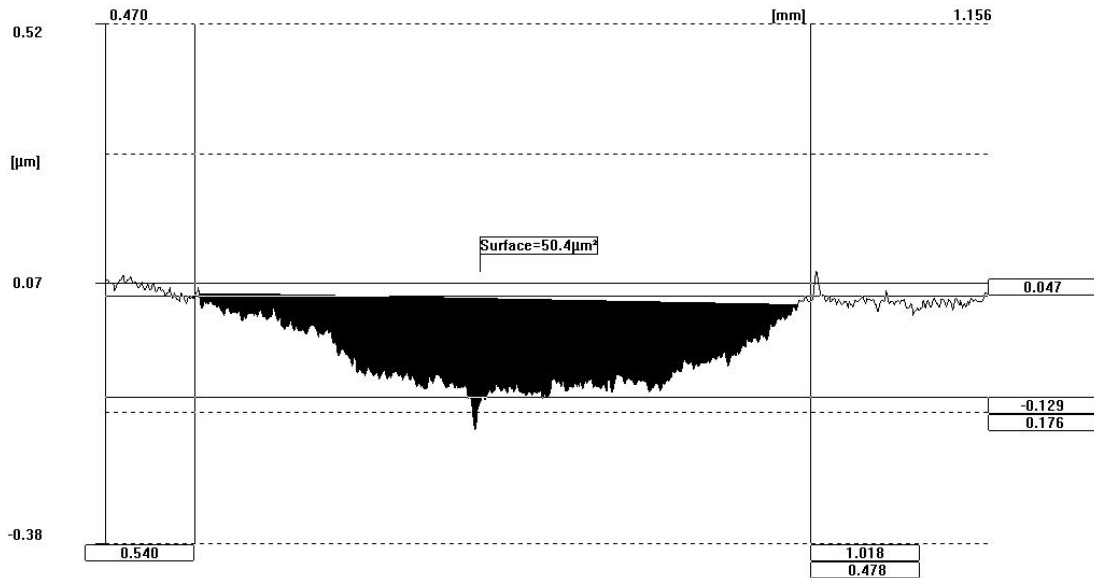


**Figure 4.14:** Representative wear track measurement of B<sub>4</sub>C coating against Al<sub>2</sub>O<sub>3</sub> pin.

All three coatings deposited with different bias voltages; floating, 50 V and 250 V demonstrated the same wear track profiles. Measured wear rates for conventional DC magnetron sputtered boron carbide films according to the equation 3.10 were about  $5 \times 10^{-8} \text{ mm}^3/\text{Nm}$ . It can thus be concluded that applied bias voltages although caused a transition from zone 1 type columnar structure to zone T type microstructure, had no significant effects on the friction and wear properties of conventional DC magnetron sputtered boron carbide coatings.

#### 4.1.2.7 SIMS elemental depth profiles

Elemental depth profiles of the coatings were obtained using a secondary ion mass spectrometer. An O<sub>2</sub><sup>+</sup> primary ion beam of 20 μm diameter was used at 15 keV acceleration voltage with 200 nA primary beam current to scan a 250 μm × 250 μm area. The data was collected from 150 μm field of analyses to prevent the edge effects while creating sputter craters.

SIMS elemental depth profile analyses were realized on the films grown on Si substrates. All the coatings deposited by conventional DC magnetron sputtering demonstrated the same profile. At least five measurements were realized on each sample. Figure 4.15 shows that the elemental film distribution was constant over the whole film depth. The intensities are qualitative and dependant to the analyses

conditions, more specifically to the secondary ion yields, depending on primary ion beams as explained in Section 3.2.4. For example, carbon intensity in the figure is lower than expected because carbon is more sensitive to negative secondary ions while  $O_2^+$  primary beam increases the yield of positive secondary ions. The same phenomena is valid for oxygen counts, however it has to be noted that oxygen counts detected could be higher than expected because of the mixing effect of the oxygen coming from the primary ion source. An example realized with an increased yield of negative secondary ions by using Cs ion source will be given in Section 4.1.3.7.

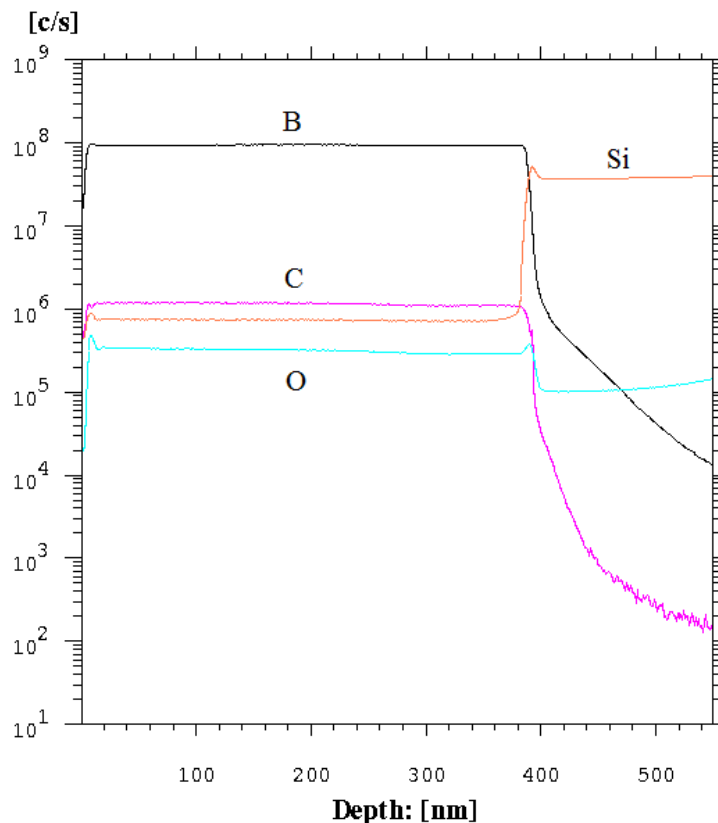


**Figure 4.15:** SIMS elemental depth profile of boron carbide coatings deposited by conventional DC magnetron sputtering.

For SIMS data given in the figure, the x-axis was converted from time to depth by measuring the crater depths obtained during analyses by a profilometer. The thicknesses were in good agreement with SEM observations with a maximum deviation of 5%.

### **4.1.3 Plasma-enhanced DC magnetron sputtered B<sub>4</sub>C films**

In this section the effect of bias voltages and different deposition on the microstructural, nanomechanical, tribological and bonding characteristics of boron carbide thin films deposited with the presence of auxiliary plasma source, hence with the presence of dense plasma around the substrates will be discussed.

#### **4.1.3.1 Microstructural studies**

Microstructural examinations of boron carbide films were realized on cross-sections and are shown in Figure 4.16. The presence of continuous and homogeneous B<sub>4</sub>C films with 350–400 nm thickness can be observed from the figure.

The coating microstructure and the surface morphology were observed in the pictures taken at a 10° tilt angle. All the coatings deposited with different bias voltages (0-250 V) and temperatures (50-250 °C) were investigated on their cross-sections. In Figure 4.16, microstructures of two coatings, BC92 deposited without external heating at floating potential (a) and BC87 deposited at 250 °C by applying 250 V bias voltage (b) are presented. As can be seen from Figure 4.16 (a), BC87 shows a quasi-featureless structure instead of columnar morphology obtained for the films deposited without auxiliary plasma configuration. The film deposited without heating, at floating potential had a relatively high surface roughness, whereas for the film deposited at 250 °C by applying 250 V bias voltage, the columnar structure completely disappeared and the coating presented a featureless non-columnar structure with a smooth surface. Thus, it can be concluded that the increase of the bias voltage and the temperature led to the surpassing of the columnar structure and therefore a decrease of the surface roughness.

These two microstructures are given as representative examples for all the coatings deposited in these series. The non-columnar structures with smooth surfaces were obtained even for an increase of 50 V in the bias voltage and with an increase of the deposition temperature to 150°C separately. The reason of this non-columnar microstructure observed, even for the films deposited without applying bias voltage, is the intensive bombardment of the coatings during film growth by highly energetic ions generated by plasma-enhanced configuration as explained in details in Section 2.3.3.

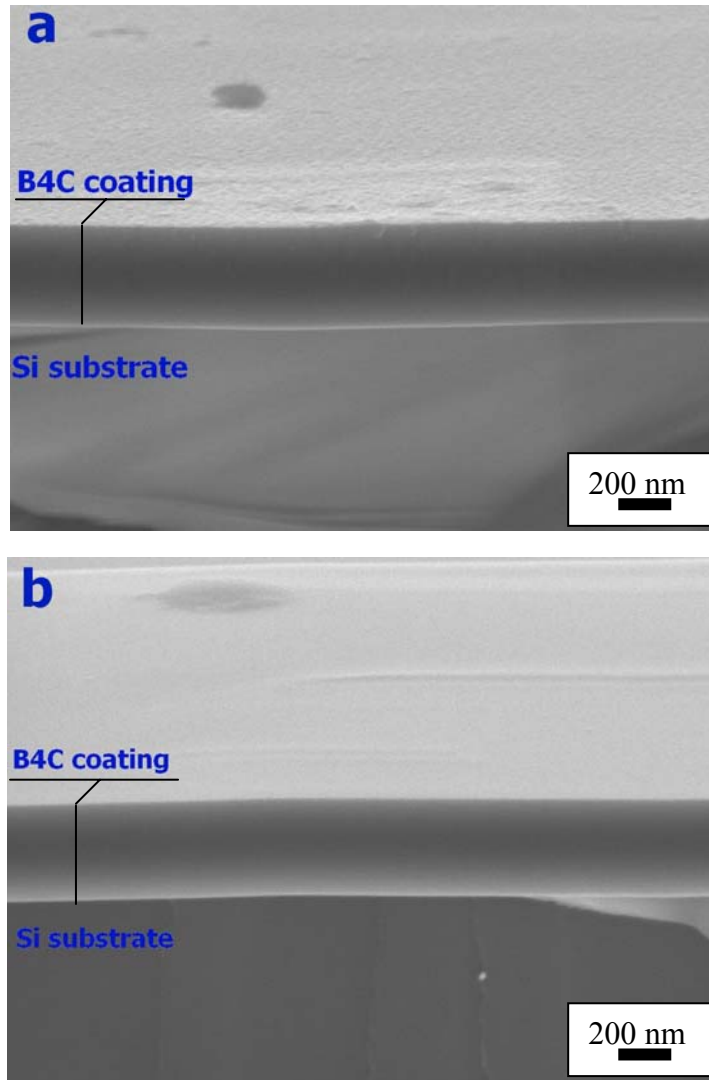


**Figure 4.16:** Cross-sectional micrograph of the specimens (a) BC92 and (b) BC87.

The effect of the different substrates on the coating growth was also investigated by cross-sectional SEM observations. To do this; BC90 which was deposited at 250 °C with 100 V applied bias voltage was selected. The coating on Si (100) substrate was directly cut by means of a scalpel while for the coatings on AISI M2 and 430 substrates, the specimens were thinned starting from the back sides of the substrates without damaging the coating, they were then embrittled in liquid nitrogen and fractured by means of a plier for fractured cross-section images. Figure 4.17 shows the cross-sectional observations of the same coating on three different substrates. From the figure, no substrates effect on the coating grown morphologies for three different substrates used in this study were observed.

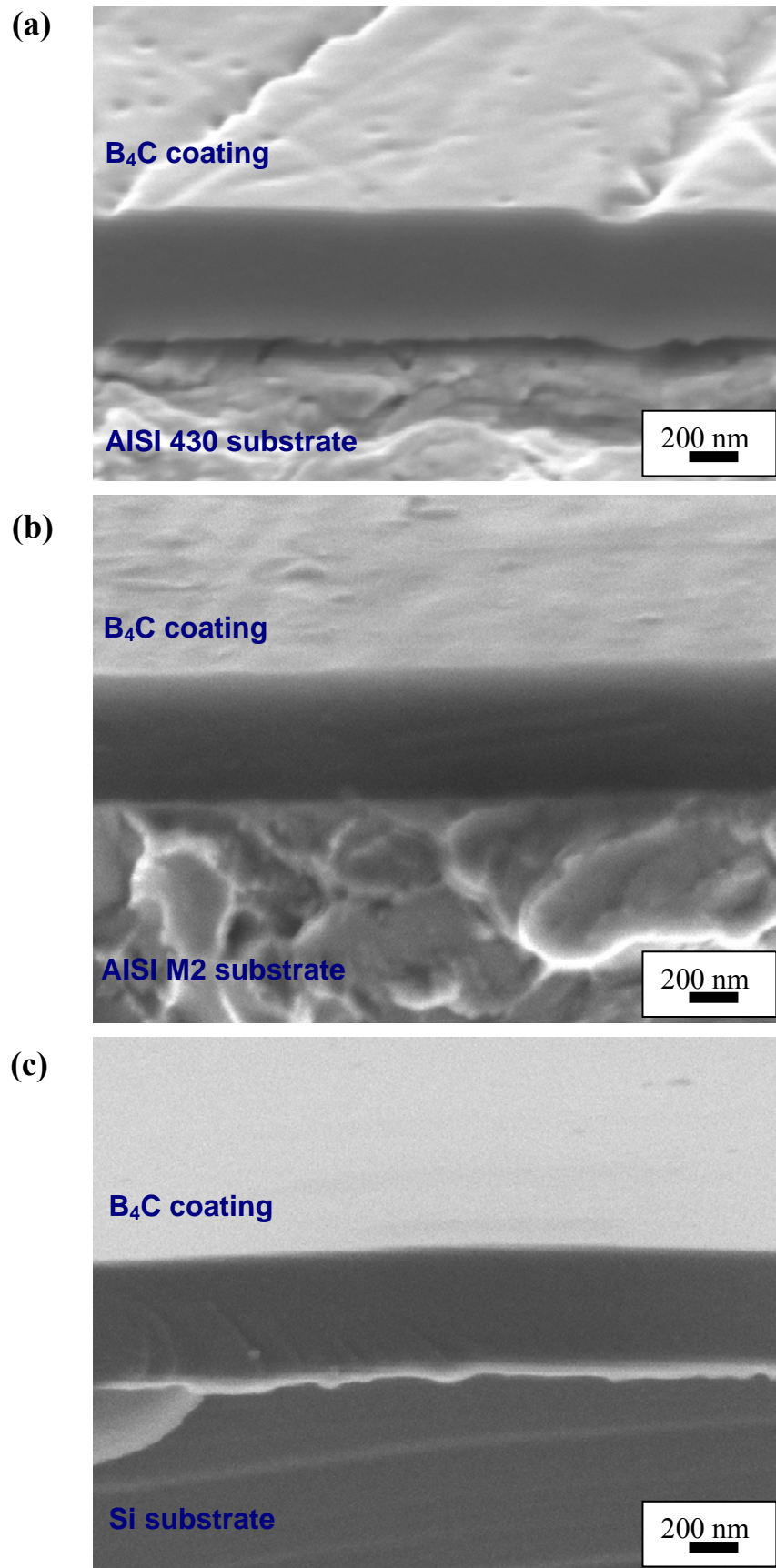


**Figure 4.17:** Cross-sectional SEM observations of the same coating BC90 on three different substrates (a) AISI 430 (b) AISI M2 (c) Si (100).

#### 4.1.3.2 Chemical compositions

Electron probe microanalysis was used to quantify the chemical composition of the B<sub>4</sub>C coating deposited by plasma enhanced DC magnetron sputtering. Results are presented in Table 4.2.

**Table 4.2:** Elemental composition of boron carbide coatings deposited by plasma enhanced DC magnetron sputtering.

|      | B (at.%) | C (at.%) | O (at.%) | Si (at.%) |
|------|----------|----------|----------|-----------|
| BC92 | 77.74    | 21.69    | 0.39     | 0.18      |
| BC83 | 78.05    | 21.51    | 0.16     | 0.28      |
| BC82 | 76.64    | 22.84    | 0.27     | 0.25      |
| BC84 | 77.23    | 22.20    | 0.32     | 0.25      |
| BC85 | 77.83    | 21.67    | 0.25     | 0.25      |
| BC96 | 77.42    | 21.88    | 0.38     | 0.32      |
| BC89 | 77.71    | 21.72    | 0.31     | 0.26      |
| BC93 | 77.96    | 21.64    | 0.23     | 0.17      |
| BC91 | 77.62    | 21.82    | 0.33     | 0.23      |
| BC86 | 76.69    | 22.86    | 0.19     | 0.26      |
| BC94 | 77.72    | 21.60    | 0.32     | 0.36      |
| BC95 | 77.75    | 21.52    | 0.27     | 0.46      |
| BC90 | 77.71    | 21.73    | 0.35     | 0.21      |
| BC88 | 77.86    | 21.46    | 0.44     | 0.24      |
| BC87 | 77.06    | 22.26    | 0.42     | 0.26      |

It can be seen from Table 4.2 that process parameters had no significant effect on the coating compositions for the films deposited by plasma-enhanced configuration. The concentrations were the same as the hot-pressed boron carbide target and thus were the same as the initial powder composition for all the coatings with negligible differences.

#### 4.1.3.3 Nanomechanical properties

For plasma-enhanced magnetron deposited B<sub>4</sub>C films like without auxiliary configuration (Sec. 4.1.2.4), first, a series of nanoindentation measurements with variable maximum applied loads between 300–9000  $\mu\text{N}$  were realized on the coatings deposited on AISI M2 steel and AISI 430 substrates to optimize the load. Load-penetration curves for the specimen BC87 deposited on AISI M2 and AISI 430 substrates, from which the hardness and Young's modulus of the films were calculated by using the elastoplastic model proposed by Oliver and Pharr, is given in Figure 4.18 as an example. This plot was taken with an applied load of 9000  $\mu\text{N}$ . For the same coating, on AISI M2 substrate a well defined force-displacement curve for

hard coatings is observed, however for the film deposited on AISI 430 substrate around 3000  $\mu\text{N}$  which corresponds to a penetration depth of 65 nm (indicated by an arrow in Figure 4.18) a derivation occurs. As the same phenomena observed in the nanoindentation of the series deposited without auxiliary plasma configuration, this is associated with the onset of plastic deformation within the substrate. The same phenomenon was observed for all the series with different bias voltages and temperatures.

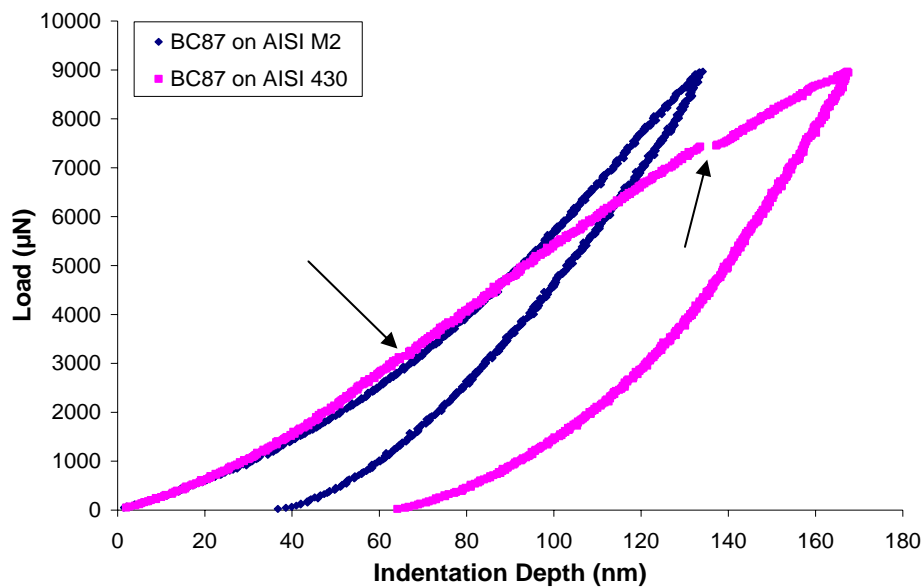


**Figure 4.18:** Load-displacement curves for BC87 on AISI M2 and AISI 430 substrates.

For all the coatings analyzed on AISI 430 substrates at higher loads (8000-9000  $\mu\text{N}$ ), another phenomena which is named pop-in in the literature and appeared by a sudden increase in indentation depth, in other words interruption in the load-displacement curves is observed. An example can be seen in Figure 4.18, for the curve, which belongs to BC87 on AISI 430, an interruption that is indicated by an arrow, occurs at  $\sim 7500$   $\mu\text{N}$  applied load which resulted with a penetration depth of  $\sim 133$  nm. The pop-in event is believed to be associated with the onset of cracking of  $\text{B}_4\text{C}$  coatings.

In Figure 4.19, the hardness and Young's modulus curves obtained from the load-displacement data, which is given in Figure 4.18 are presented.

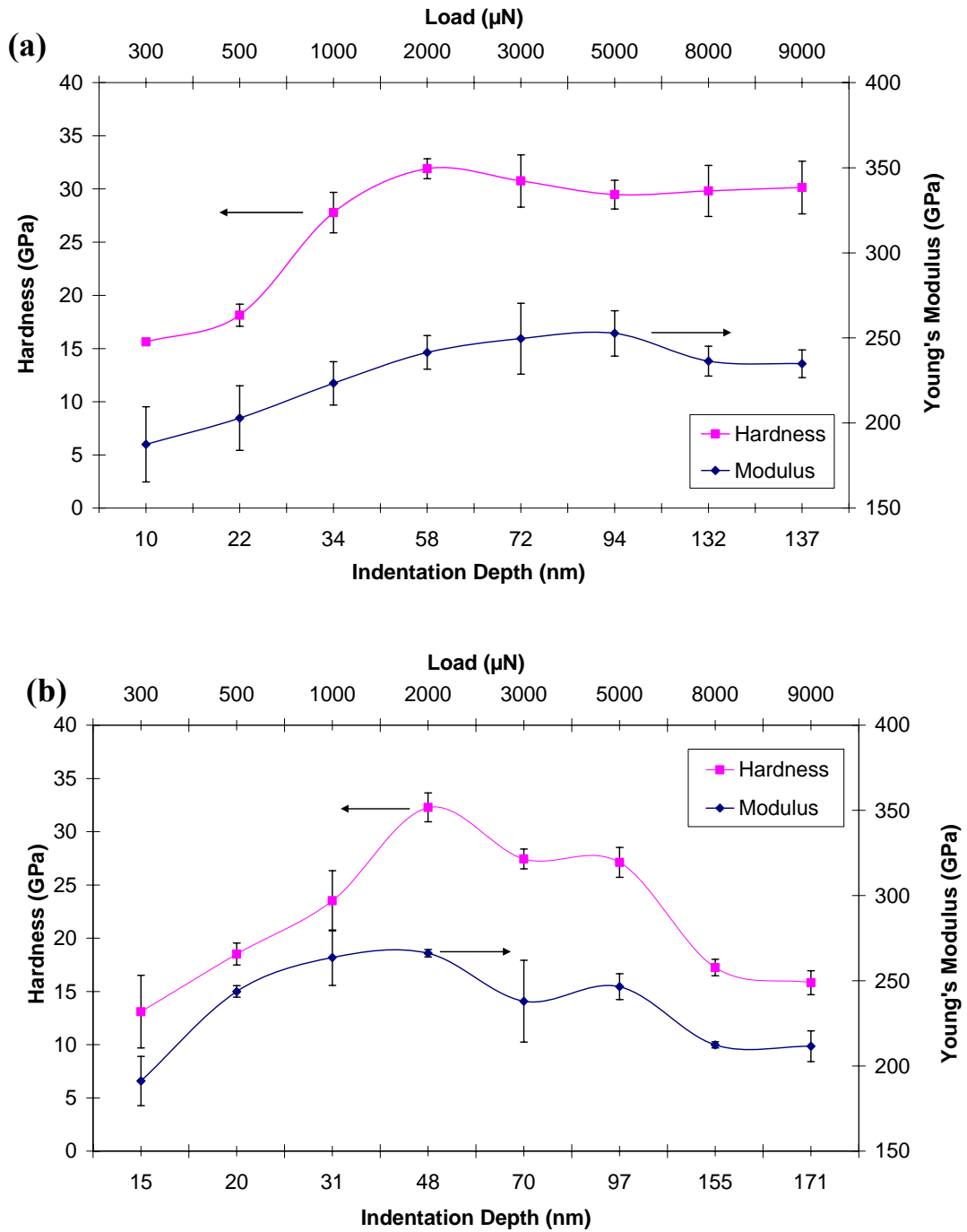


**Figure 4.19:** Hardness and Young's modulus vs. load and corresponding indentation depths curves of (a) BC87 on AISI M2 (b) BC87 on AISI 430 substrates.

From this curves, it is possible to observe the change of the hardness and modulus values for the same coating deposited on two different substrates by different applied loads and corresponding penetration depths. As can be seen from the figure, for the coating on AISI M2 (Figure 4.19 (a)), for the lower loads starting from 300  $\mu\text{N}$  to 1000  $\mu\text{N}$ , an increase of the hardness from 15 to 27 GPa was observed. With the

increase of the applied load, at 2000  $\mu\text{N}$  the hardness value reached  $\sim 30$  GPa and no important changes were observed with further increase of the load, even at 9000  $\mu\text{N}$  which was the limit load of the nanoindenter used in this study. Hence, it is concluded that below 2000  $\mu\text{N}$  applied forces, the hardness and modulus values for the same coating on both substrates were underestimated due to the tip rounding effect. The same observations were made for Young's modulus values. They were underestimated as well for the loads between 300-1000  $\mu\text{N}$  with 180-220 GPa and they demonstrated a quite stable nature with the increase of the load until 9000  $\mu\text{N}$  around 240-250 GPa. No substrate effect was observed for this specimen, which was also clear from the load-displacement curve given in Figure 4.18. For BC87 on AISI 430 substrate (Figure 4.19 (b)), the plot was quite different. For the lower loads, again an underestimate of the hardness was observed between 300-1000  $\mu\text{N}$ . The hardness values increased with applied loads from 13 to 23 GPa, it reached 32 GPa at 2000  $\mu\text{N}$ , then a drastical decrease was observed by further increase in the applied loads which results with 15 GPa at 9000  $\mu\text{N}$ . This can be explained by the effect of the substrate on boron carbide coating nanomechanical properties by combining the load-penetration depth curves and the hardness values obtained. The depth ( $\sim 65$  nm) at which the load-penetration curve derivate, corresponds the point at which the hardness values started to decrease. The indentation depth ( $\sim 130$  nm) where pop-in occurred fitted as well with the drastical decrease of the hardness values. The same tendency was observed for the Young's modulus values.

Further investigations to compare the effect of different substrates were realized on the coatings deposited on Si substrates. In the light of above observations realized with a large interval of applied loads, a series of indentation with 1000, 3000 and 5000  $\mu\text{N}$  loads only, were realized and the results are presented in Figure 4.20 for BC86 deposited on both AISI M2 and Si (100) substrates.

It is clear from the figure that two curves are completely identical. Even the corresponding penetration depths for different applied loads are the same with a few nanometers differences.

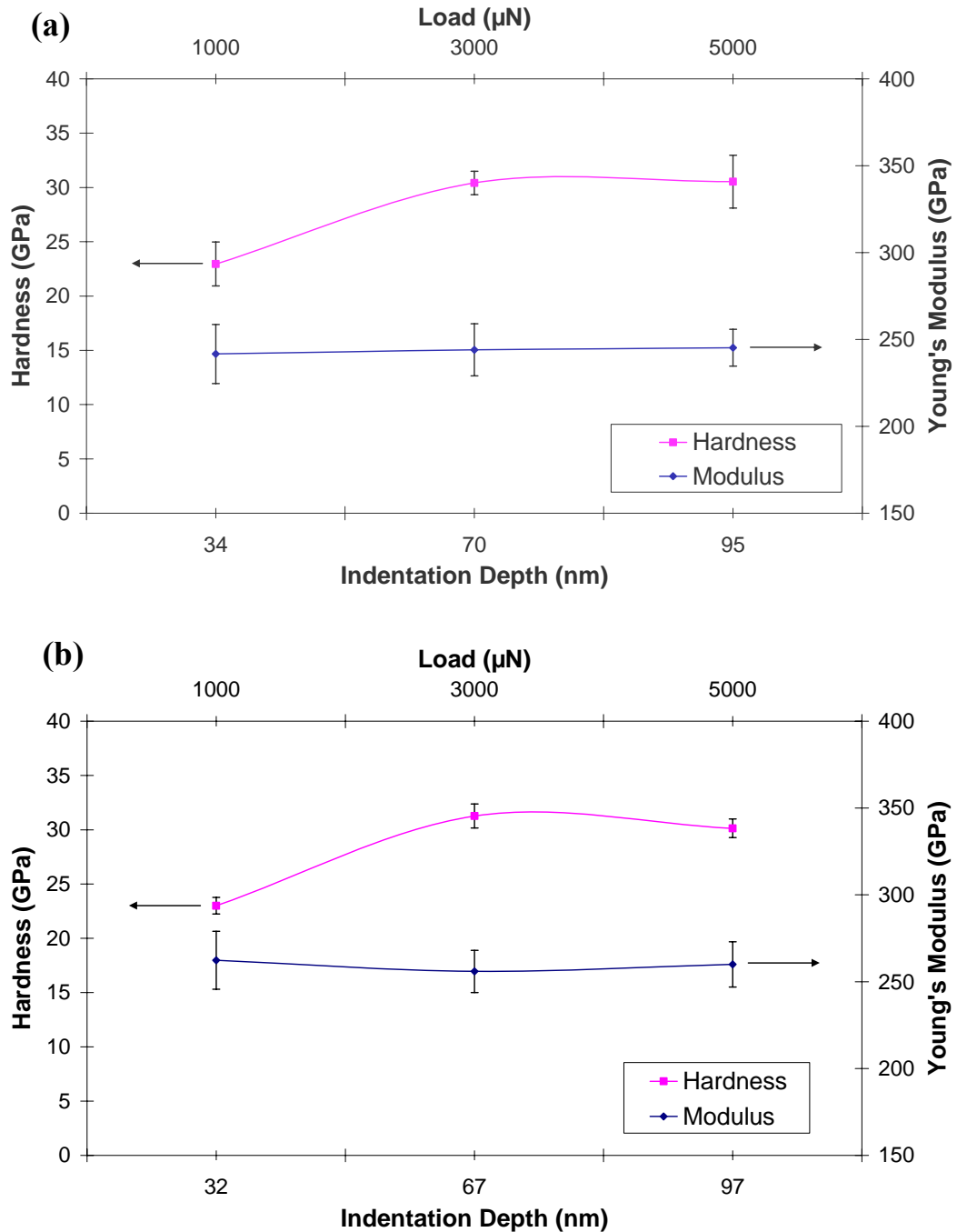


**Figure 4.20:** Hardness and Young's modulus versus load and indentation depth curves of BC86 (a) on AISI M2 (b) on Si (100).

As a result of the above observations, all the series were decided to analyze on AISI M2 substrates with 3000 and 5000  $\mu\text{N}$  applied loads. Thus, once again, only the effect of deposition parameters on the boron carbide thin film's nanomechanical properties will be discussed in the coming part. Figure 4.21 shows the effect of bias voltages and deposition temperatures on the hardness and Young's modulus of boron carbide thin films deposited by plasma-enhanced configuration.

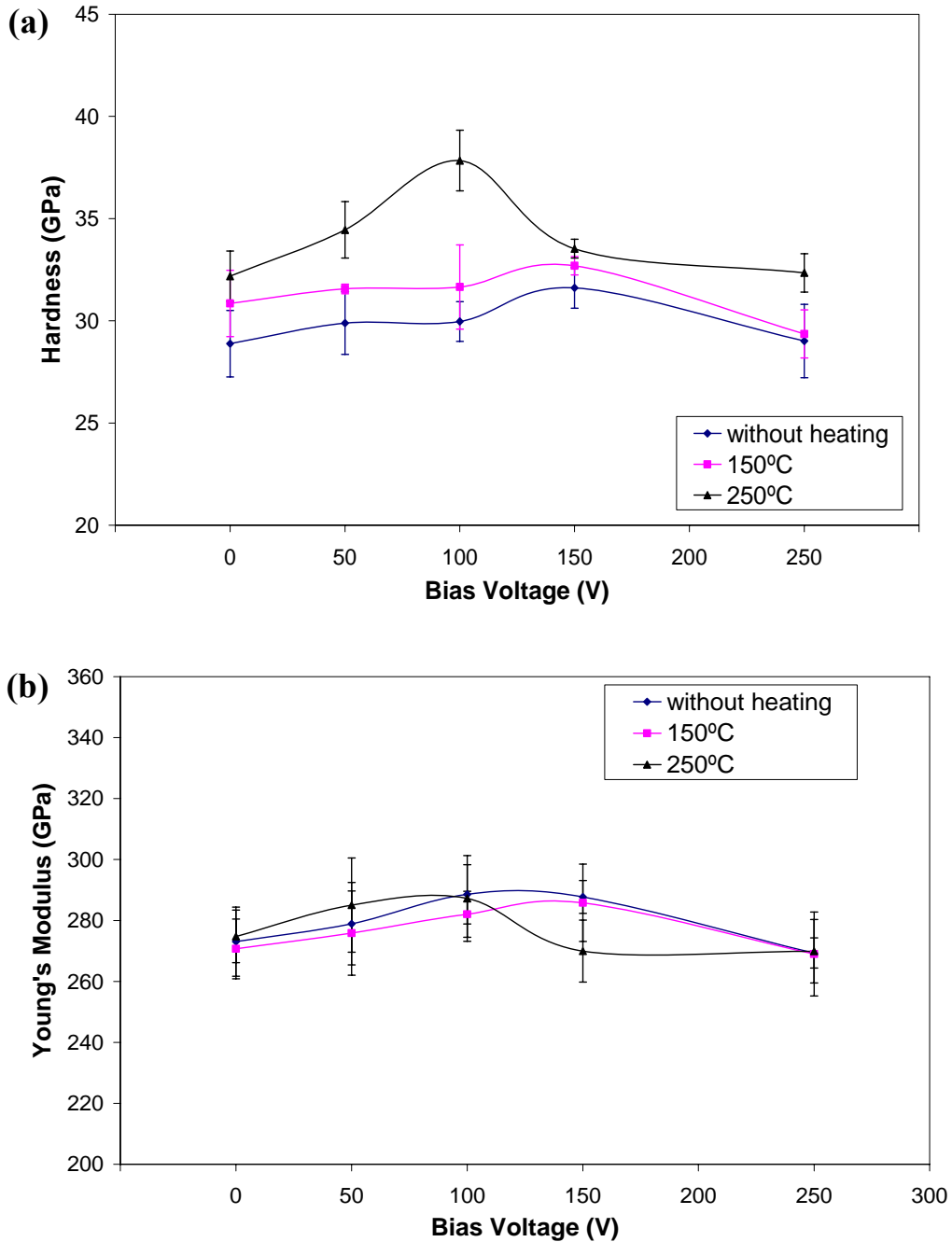


**Figure 4.21:** The effect of bias voltages and temperatures on the (a) hardness and (b) Young's modulus of the B<sub>4</sub>C thin films deposited by plasma-enhanced DC magnetron sputtering.

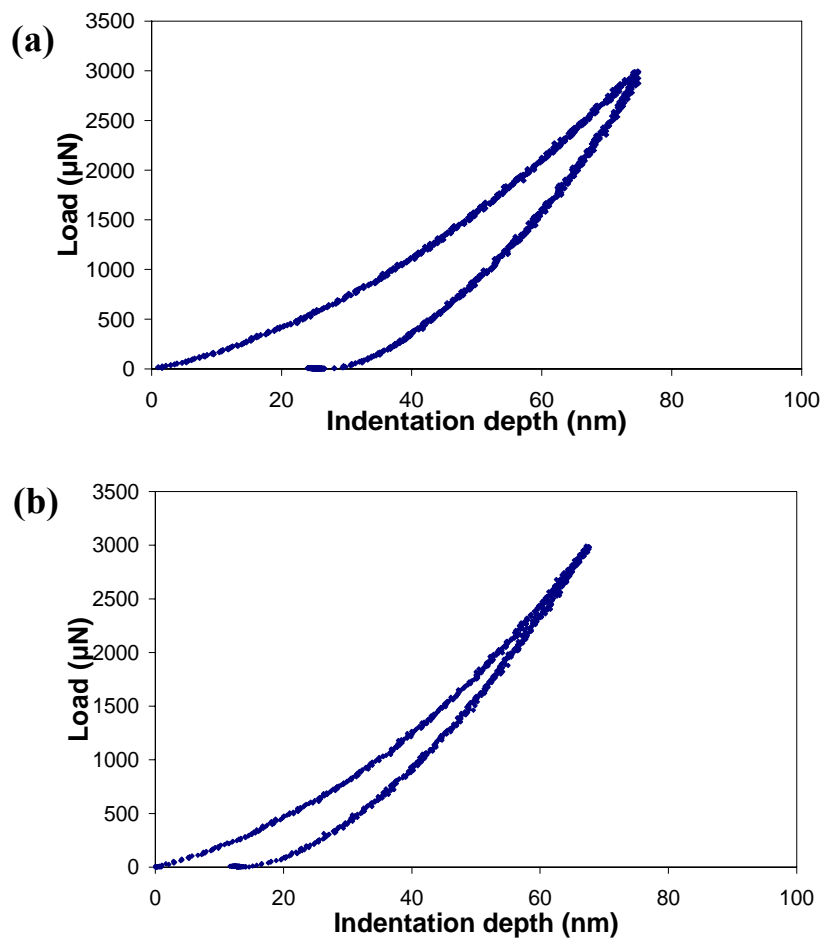
From Figure 4.21 (a), the hardness values of the three series deposited with different temperatures between 50 and 250 °C and applied bias voltages between floating potential and 250 V can be seen. For the coating deposited at floating potential without any external heating, a hardness of 28 GPa was found which was also the softest film deposited in plasma-enhanced DC magnetron sputtered series. With the increase in the temperature, at 150 °C again at floating potential, the hardness

increased to 30 GPa and at 250 °C, 32 GPa was reached for the films deposited without applying any bias voltages. This increase in the hardness with the increase of the deposition temperature can be explained by the thermally activated adatom mobility on the substrate surface as explained in Section 2.3.2. For all the series, an increase in the hardness with the increase in the applied bias voltages was observed until a critical value. This critical value is 150 V for the coatings deposited without external heating, at this voltage the hardness reached ~ 32 GPa. Then a decrease to 29 GPa was observed with further increase in the bias voltages to 250 V. For the films deposited at 150 °C the same tendency was observed; the hardness was increased to 32 GPa at 50 and 100 V applied bias voltages, reached its maximum with 33 GPa at 150 V and then decreased to 29 GPa with further increase in the bias voltages to 250 V. For the films deposited at 250 °C, the hardness was increased from 32 GPa for the boron carbide film deposited at floating potential to 35 GPa at 50 V, at 100 V the hardness reached its maximum with 38-40 GPa which is the hardest film deposited in this study, then gradually dropped to 33 at 150 V and finally to 32 at 250 V.

The increase in the hardness by ion bombardment during the growth of films can be explained by the densification effect as explained in Section 2.3.3 which first causes the suppression of the columnar structure and when coupled with thermal energy, further densification occurs until a threshold value. At 250 °C, the threshold for densification effect obtained as a result of the thermal activation of the adatoms, coupled with highly energetic ion bombardment appears at 100 V, differently from the series deposited at lower temperatures for which this threshold appeared less remarkably at 150 V bias voltages.

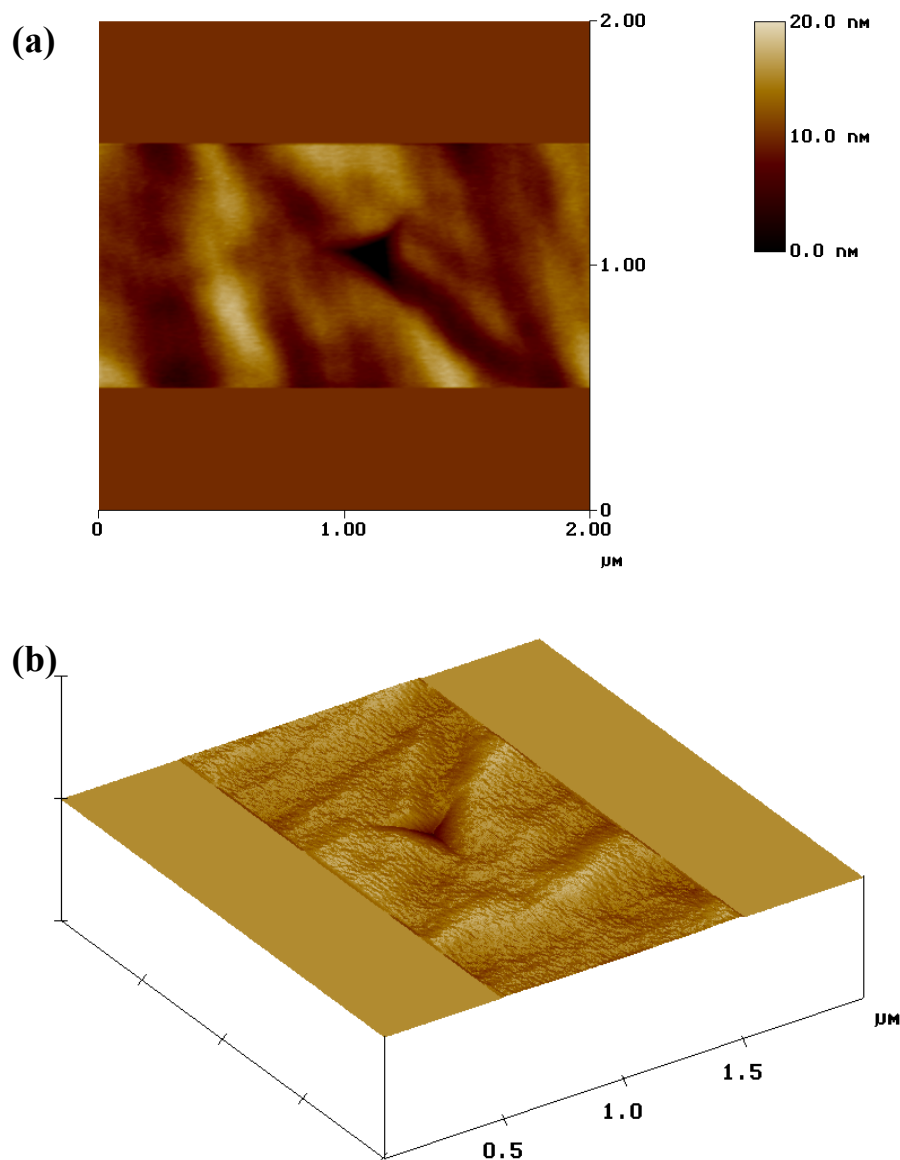
The same tendency was observed for the Young's modulus of the coatings deposited, however the effect was not as evident as the hardness results. Starting from around 270 GPa for all the coatings deposited at floating potential with different temperatures, the Young's modulus values reached their maximum at 150 V bias voltages with 280-290 GPa and decreased again to 270 GPa with further increase of the bias voltage to 250 V.

Figure 4.22 shows the load-displacement curves of two coatings, (a) BC96 deposited at 150 °C at floating potential, given as representative of the series with hardness values near 30 GPa and (b) BC90 deposited at 250 °C with 100 V applied bias voltage, which is the hardest coating obtained in this study with  $\sim 40$  GPa. As can be seen from the figure, BC96 as representative of the majority of the coatings deposited by plasma-enhanced configuration, shows approximately 70% elastic recovery after unloading in (a), whereas for BC90, more than 80% of elastic recovery is observed in (b). Thus, a high elastic recovery behavior of the boron carbide films can be deduced.



**Figure 4.22:** Load-displacement curves of (a) BC 96 (b) BC90.

Figure 4.23 shows a typical indent profile obtained by AFM on the sample BC90. The same pyramidal Berkovich indenter was used for tests and visualization before and after the indentation. In Figure 4.23 (a) 2D view of the indent can be seen with the roughness scale on the right hand side. In (b) 3D visualization of the indent and the surface of the specimen are presented.



**Figure 4.23:** Representative indent profiles obtained by AFM on the specimen BC90 (a) 2D view of the indent (b) 3D visualization of the same area.

#### 4.1.3.4 Nanostructural analyses

TEM analyses were conducted on the selected specimens from the series deposited by plasma-enhanced configuration, to further investigate the coating microstructures and to observe possible evidence of crystallization to correlate the effect of the deposition parameters on the nanomechanical properties of the coatings. Figure 4.24 shows the microstructure of the specimen BC92 with low and high-resolution TEM micrographs.

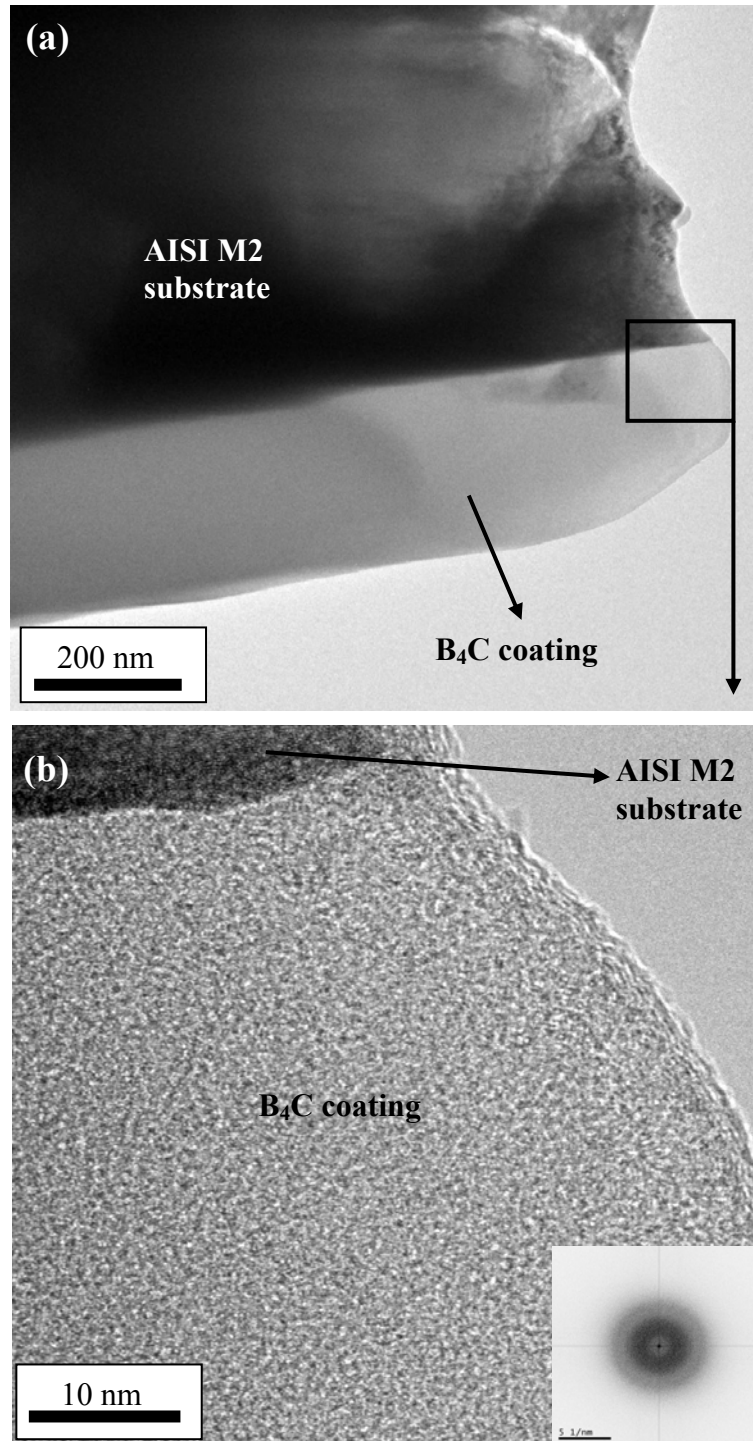


**Figure 4.24:** Cross-sectional TEM micrographs of the specimen BC92 (a) low-magnification (b) high-resolution TEM of the selected area.

The coating deposited on AISI M2 substrate was prepared by the sandwich technique and observed on its cross-section. In Figure 4.24 (a) low-magnification bright field TEM micrograph is shown. It is clear from the figure that the microstructure is not columnar neither granular, instead a featureless solid structure is observed. In Figure 4.24 (b), high-resolution observations were realized on the area indicated by the

square in (a). Amorphous structure of the coating can be clearly seen from the figure and also from the inset FFT pattern. Crystalline structure of the steel substrate can be seen and compared by the coating. Crystallographic order at the extremity of the thin foil is an artifact due to the ion milling for the final specimen preparation to electron transparency and should not be taken into consideration as an evidence of the crystallinity of boron carbide thin film. Hence, it is evident from the figure that the coating deposited by plasma-enhanced magnetron sputtering without any applied bias voltages and temperatures was amorphous in nature.

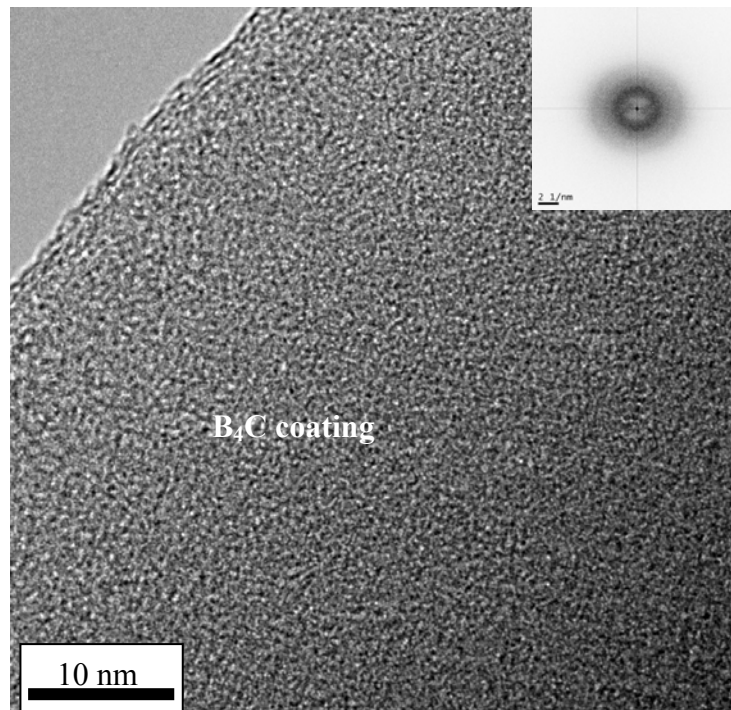


**Figure 4.25:** High-resolution TEM observation of the specimen BC94.

To observe the effect of the deposition temperature, the specimen BC94 deposited at 250 °C, at floating potential was investigated. For this sample, thin foil of the coating deposited on Si substrate was prepared for TEM in-plane observations. Figure 4.25 shows the high-resolution TEM image of the specimen BC94. The image as well as the inset FFT shows the amorphous nature of the film. Therefore, it is concluded that the temperature interval used in this study was not sufficient to crystallize boron carbide thin films. It is well known from the literature survey given in Section 2.4.1, that boron carbide films deposited by different sputtering configurations start to crystallize at temperatures above 900 °C.

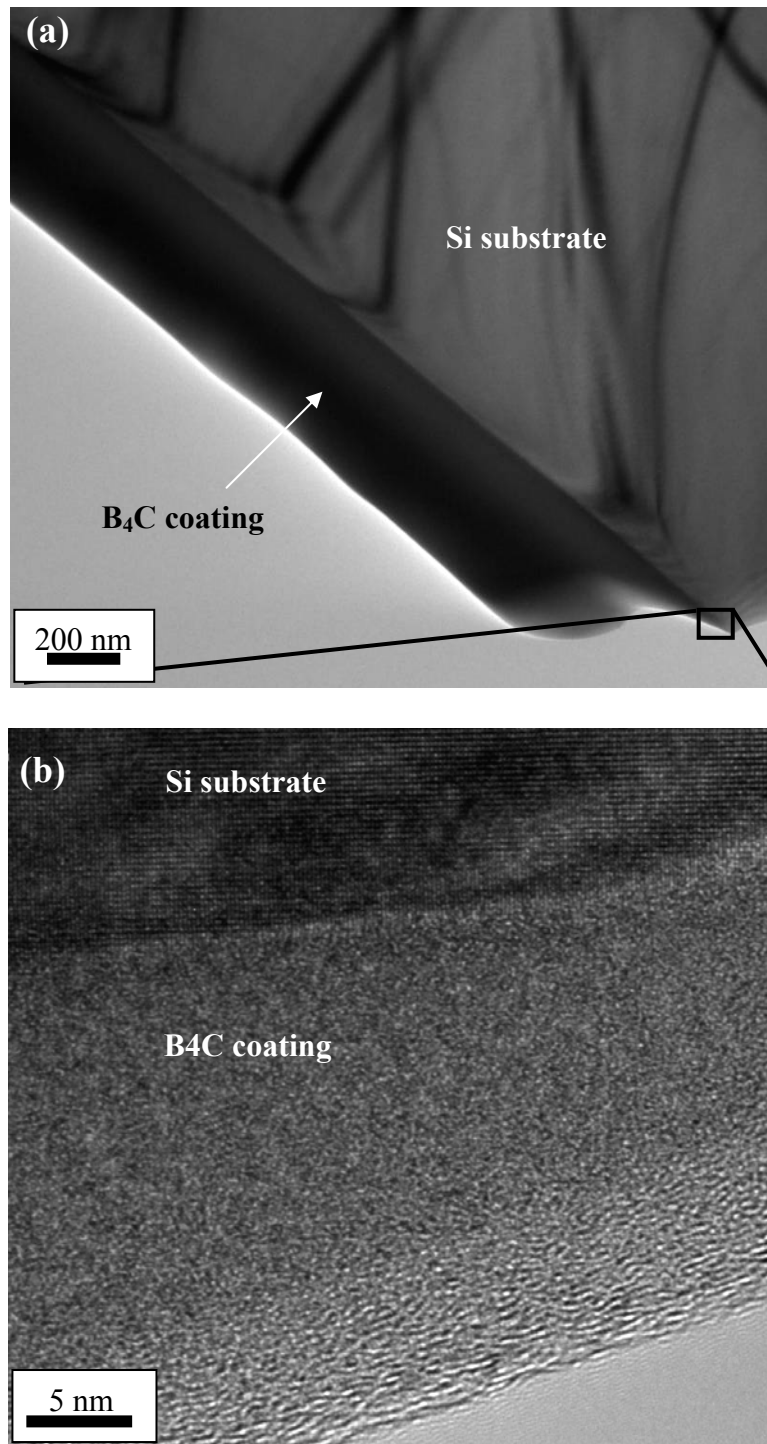


**Figure 4.26:** Cross-sectional TEM micrographs of the specimen BC90 (a) low-magnification (b) high-resolution TEM of the selected area.

To observe the effect of the deposition temperature and the bias voltages, the hardest coating of all the series deposited in this study, BC90, grown at 250 °C, with 100 V applied bias voltage was selected to investigate in details. Figure 4.26 shows low and high magnification cross-sectional TEM observations of the coating deposited on Si substrate. In the figure (a) low magnification image from cross-section of the coating

and Si substrate is shown. The area indicated by a square was investigated by high resolution TEM analyses and is shown in (b). Ordered crystal structure of Si substrate can be clearly seen in the figure, while boron carbide thin film shows a completely amorphous structure. Again the artifact of the ion milling process is present at the extremity of the coating.

In Figure 4.27 more detailed observations of the coating-substrate interface can be seen. 4-5 atomic layers, which correspond to 1-1.5 nm, were in crystallographic order just at the interface as a transition layer and then the coating becomes quickly amorphous. The crystalline structure of Si substrate and amorphous nature of B<sub>4</sub>C coating can be clearly seen from the inset FFT patterns.

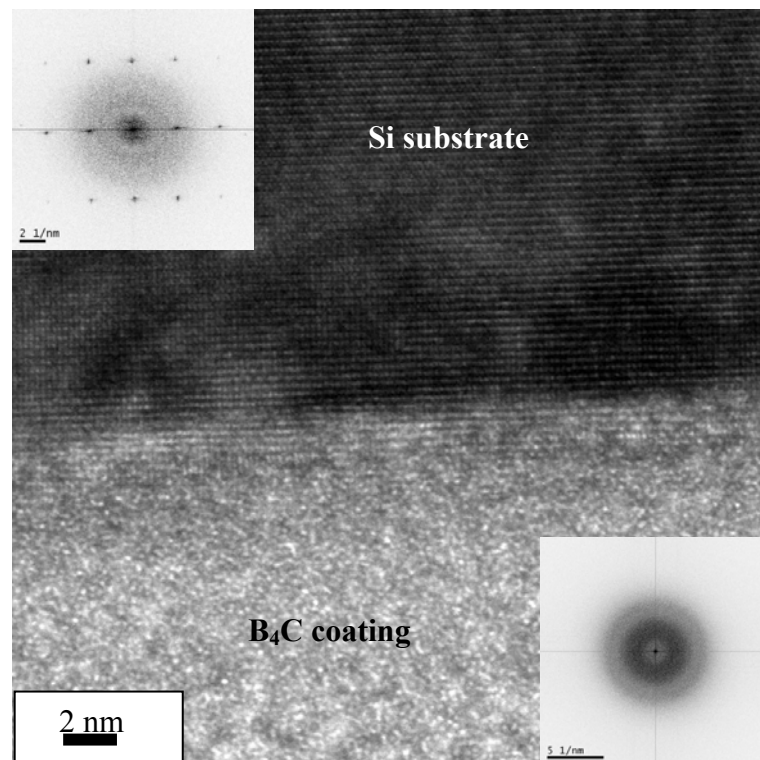


**Figure 4.27:** High resolution TEM micrograph of the specimen demonstrating the coating-substrate interface and the cristallinity of the substrate and coating with inset FFT patterns.

From the results presented, it is clear that all boron carbide coatings deposited in this study were amorphous. The difference in the hardness values between the columnar structured films deposited without auxiliary plasma and non-columnar, featurless structures deposited by the assistance of the auxiliary plasma was related to the change in the microstructures by means of a densification process. The difference in the hardness for the series deposited by enhanced-plasma configuration at different

deposition temperatures by applying different bias voltages is considered again a densification process, however, the phenomena was not observable from the change in the microstructures even with high-resolution TEM observations. It is also clear that the hardening could not be related to the degree of crystallization, because in all the high-resolution TEM observations no evidence of even the presence of nano-crystalline phase was found.

The chemical composition of the films was further investigated with an electron energy loss spectroscope (EELS) attached to the TEM. Figure 4.28 shows a typical EELS spectrum taken from boron carbide thin films deposited by plasma enhanced DC magnetron sputtering.

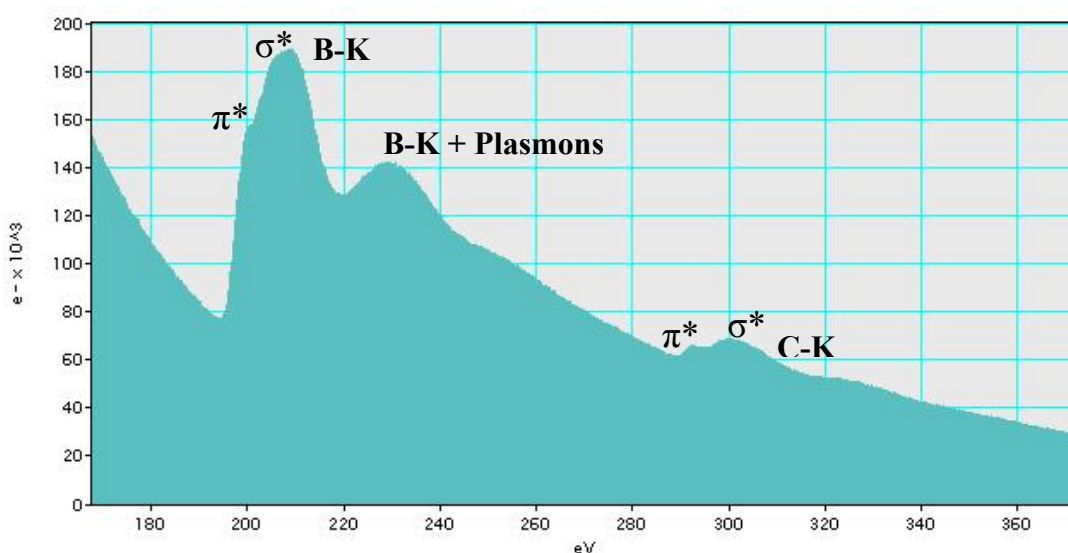


**Figure 4.28:** Typical EELS spectrum taken from boron carbide coatings.

In the EELS spectrum, ionization edges around 188 and 284 eV, corresponding to the characteristic *K*-shell ionization edges of elemental boron and carbon are present. There were no detectable traces of oxygen (532 eV) in the EELS spectrum taken from different boron carbide coatings.

The carbon and boron *K*-edges both exhibit a small  $1s \rightarrow \pi^*$  transition peak and a series of broad  $1s \rightarrow \sigma^*$  transition peaks. The  $\pi^*$  and  $\sigma^*$  features of boron *K*-edge can be usually observed from boron carbide, as in boron carbide crystals boron atoms are located either at the vertices of icosahedra ( $sp^2$  hybridization, i.e.,  $\pi^*$  feature) or the chains connecting the icosahedra ( $sp^3$  hybridization, i.e.,  $\sigma^*$  feature) as explained in Section 2.4.1.

#### 4.1.3.5 Bonding properties

The phase composition of boron carbide films deposited by plasma-enhanced DC magnetron sputtering was investigated by FTIR spectroscopy. Figure 4.29 shows FTIR spectra of boron carbide film deposited without external heating and at floating potential. Infrared spectra present two broad bands, one centered at  $\sim 1100\text{ cm}^{-1}$  and the other at  $\sim 1570\text{ cm}^{-1}$ . The band at  $1100\text{ cm}^{-1}$  is attributed to B–C bonds in the icosahedra and the band at  $1570\text{ cm}^{-1}$  has been attributed either to the presence of free carbon in boron carbide structure or to the vibrations of the linear C–B–B chains that interconnect the icosahedra as explained in Section 4.1.2.6.

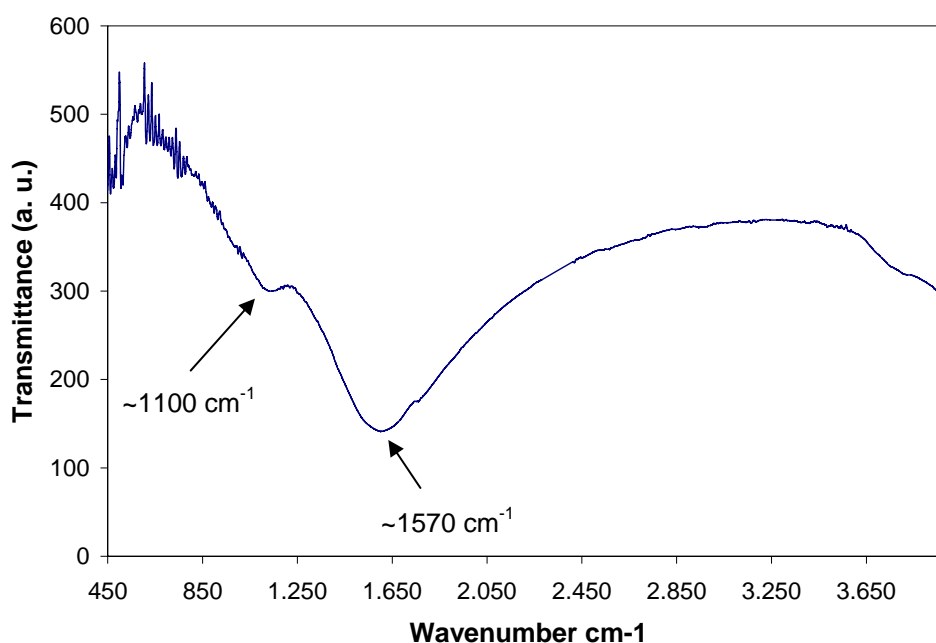


**Figure 4.29:** FTIR spectra of boron carbide film deposited without external heating and at floating potential.

The analyses were conducted on all the coatings deposited by plasma-enhanced configuration. In all the series deposited at different temperatures with applied bias voltages, a shift of the band present at  $1570\text{ cm}^{-1}$  to the higher wavenumbers was observed. A representative example for the series deposited at  $250\text{ }^{\circ}\text{C}$  with different applied bias voltages is shown in Figure 4.30. Thus, it is believed that the band near  $1570\text{ cm}^{-1}$  is an evidence of the C–B–B chains rather than the presence of free carbon and applied bias voltages resulted with a change in the vibrational properties, thus in bonding characteristics of the boron carbide films deposited.

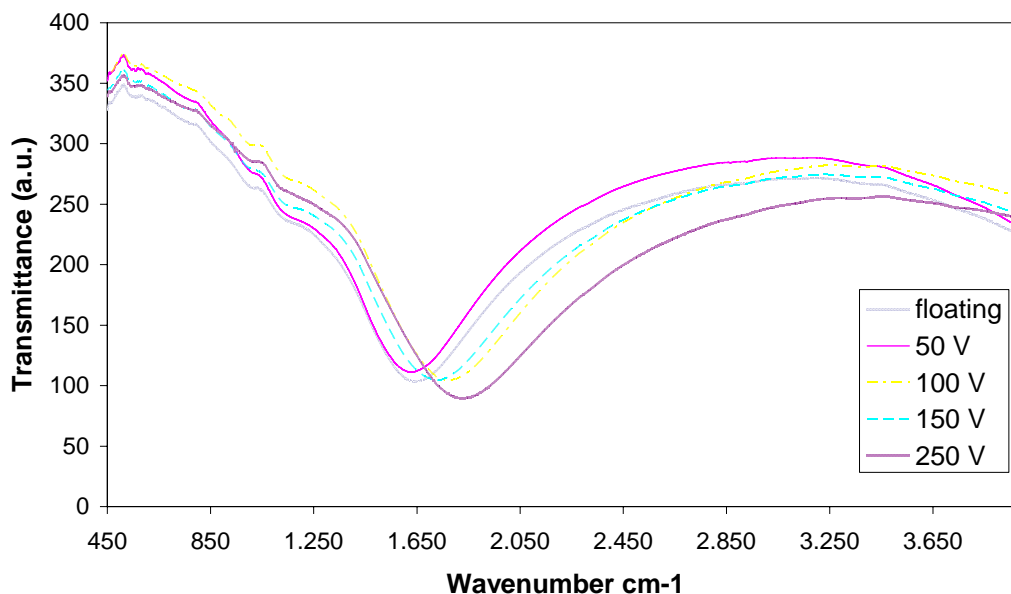


**Figure 4.30:** FTIR spectra of the boron carbide films deposited at 250 °C with different bias voltages.

#### 4.1.3.6 Tribological studies

First a series of optimization experiments were realized on B<sub>4</sub>C coatings. An alumina ball of 6 mm diameter was used as the counterface. A sliding speed of 0.1 m/s was selected for all the tests. The applied force was varied between 1–2 N. A radius of 6 mm was used during this first series of experiments and a total sliding distance of 300 m was chosen to see the friction coefficient behavior in details. After the experiments, the wear rates were measured on wear tracks by measuring the depth and width by a profilometer. At least 4 tests were realized with each configuration and the mean value is presented as wear rate. With the same configuration, using the same parameters, the friction coefficients and the wear rates of the steel (AISI M2 and AISI 430) substrates were measured against alumina ball. Friction coefficients of virgin AISI M2 steel against alumina ball and boron carbide film deposited on AISI M2 substrate against alumina ball are presented in Figure 4.31.

As a result of the adhesion problems observed during “pin-on-disc” tests realized on boron carbide coatings deposited on AISI 430 steel substrates, all the tests were realized on boron carbide films deposited on AISI M2 substrates.

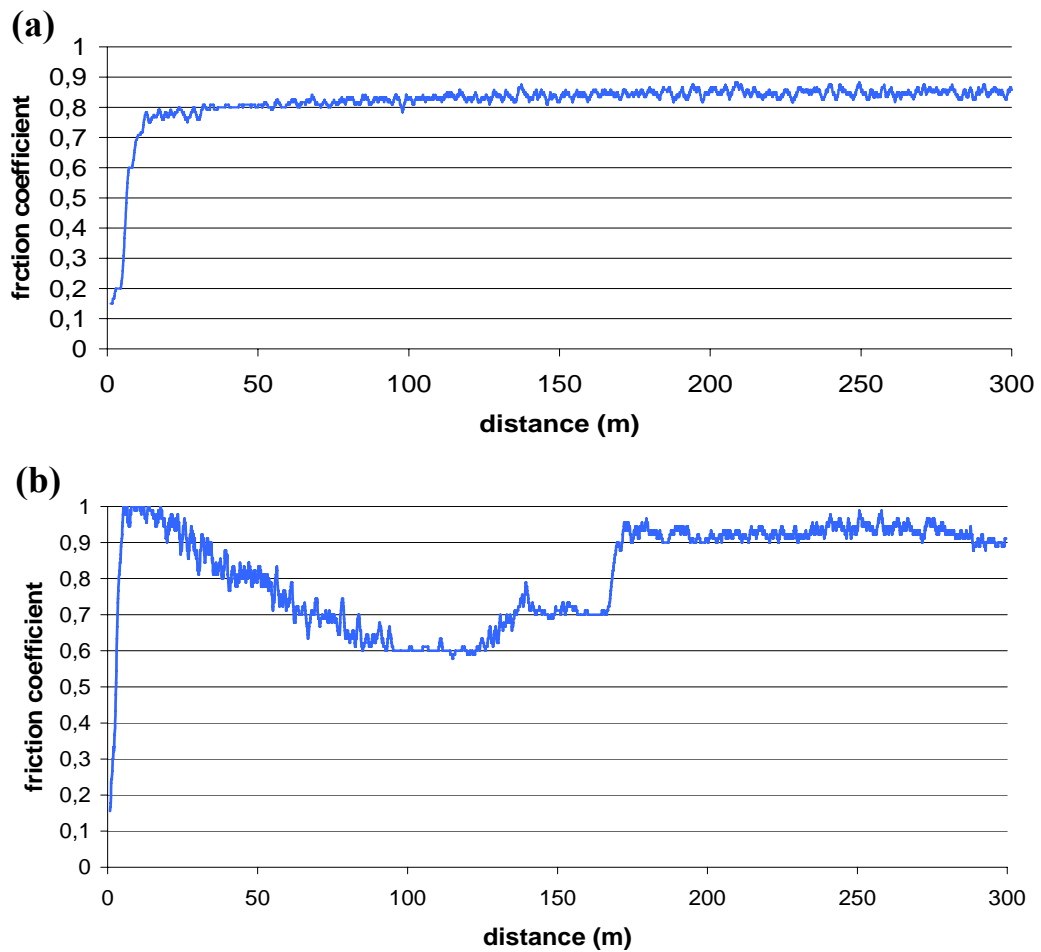


**Figure 4.31:** Representative friction coefficient vs. distance diagram of (a) AISI M2 steel without coating against alumina ball (b) B<sub>4</sub>C coated AISI M2 against alumina ball.

All the coatings investigated have been demonstrated exactly the same friction properties regardless the deposition parameters used. Tests with different sliding distances were decided to conduct in order to optimize “pin-on-disc” test conditions and to obtain information about the wear mechanism by SEM investigations of the worn surfaces. “pin-on-disc” tests with 25, 125, and 225 m were realized on the same specimen with a standard 1 N applied force. Figure 4.32 demonstrates wear tracks observed after 25 m sliding.

As can be seen from the figure, after 25 m, the wear track was hardly visible but Al<sub>2</sub>O<sub>3</sub> debris was present at both sides of the wear track. The profilometer measurements realized on this wear track are shown in Table 4.3.

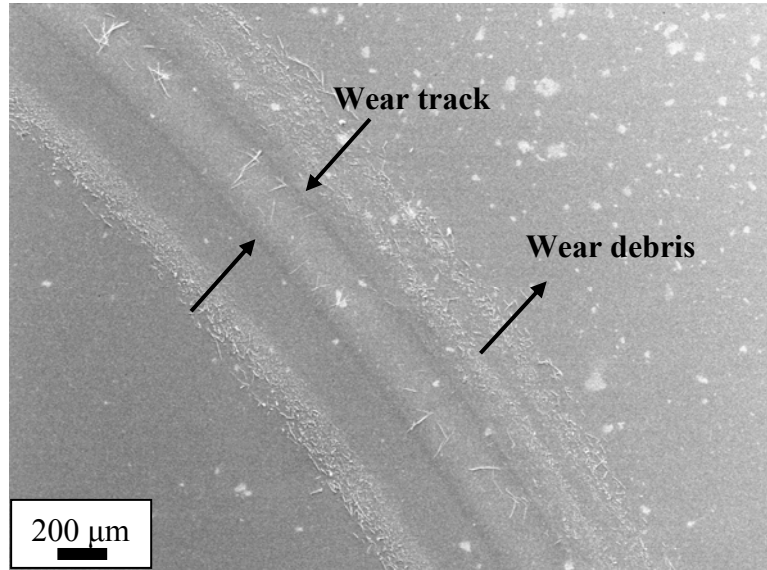


**Figure 4.32:** SEM investigation of wear track after 25 m sliding.

**Table 4.3:** Profilometer measurement of the wear track after 25 m.

| Wear track depth ( $\mu\text{m}$ ) | Wear track width ( $\mu\text{m}$ ) |
|------------------------------------|------------------------------------|
| 0.126                              | 211                                |
| 0.119                              | 246                                |
| 0.123                              | 232                                |

At this early stage of the wear test, two bodies were getting in contact, hence, an increase of the friction coefficient can be seen in Figure 4.33.

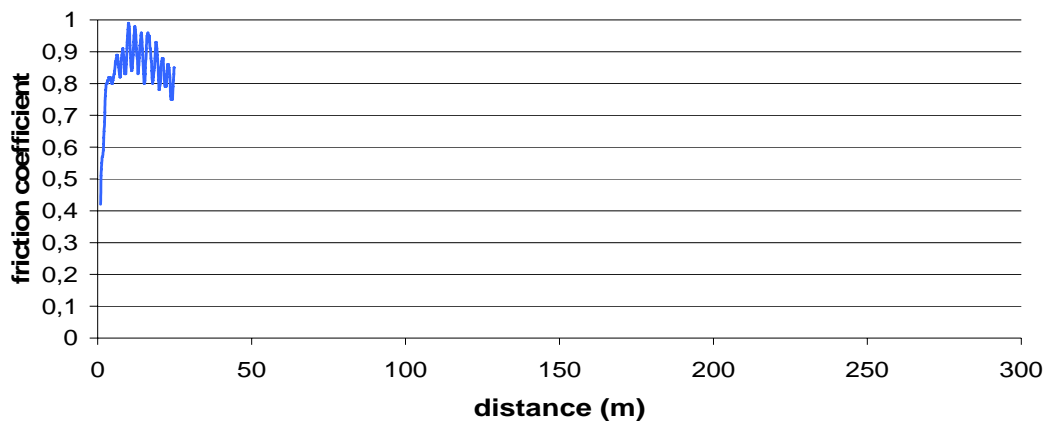


**Figure 4.33:** Friction coefficient during early stage of the wear test.

The observations were followed with 125 m sliding distance on the same specimen. SEM observation of the worn surfaces is demonstrated in Figure 4.34.

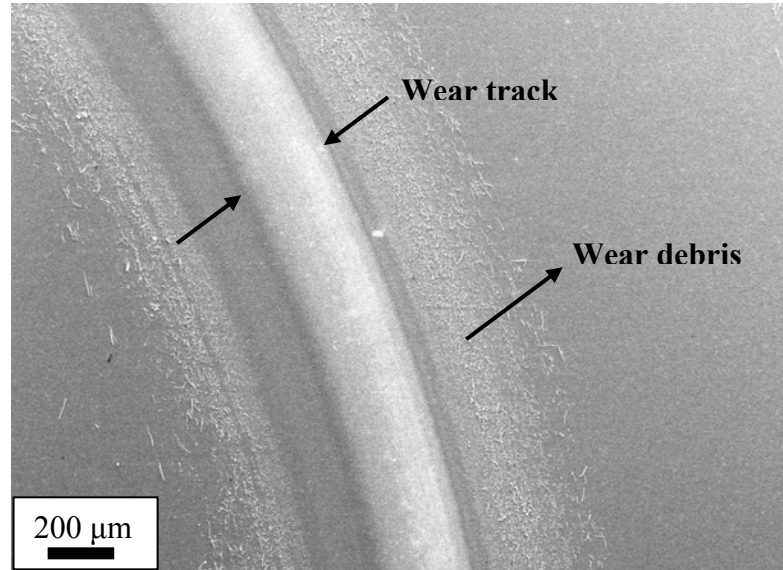


**Figure 4.34:** SEM investigation of wear track after 125 m sliding.

From Figure 4.34, it can be observed that after 125 m, the wear track became more visible. The profilometer measurements realized on the wear track obtained after 125 m are presented in Table 4.4. For further investigations, backscattered electron image of the same track was taken and presented in Figure 4.35 (a).

By EDS line scan analysis on the area shown by a square in Figure 4.35 (a) starting from the edge of the coating through the wear track, no boron was detected on the worn surface in the figure (b). The analysis was verified by EPMA and the same result was obtained, although profilometer measurements (Table 4.4) demonstrated that the “pin-on-disc” test was ended before reaching the substrate.

**Table 4.4:** Profilometer measurement of the wear track after 125 m.

| Wear track depth ( $\mu\text{m}$ ) | Wear track width ( $\mu\text{m}$ ) |
|------------------------------------|------------------------------------|
| 0.194                              | 248                                |
| 0.185                              | 230                                |
| 0.204                              | 299                                |

As a surface sensitive technique, SIMS ion imaging was used to further explore the worn surfaces as the thickness of the coating was reduced to 100 – 150 nm according to profilometer measurements. As can be seen from Figure 4.36, boron, which was not detectable with SEM-EDS and EPMA analyses, is still present on the worn surface.

Back scattered electron image does not present the exact area where the ion images were taken and is a representative one, because during the secondary ion mass spectrometry analyses, it is not possible to obtain secondary ion and electron images together.

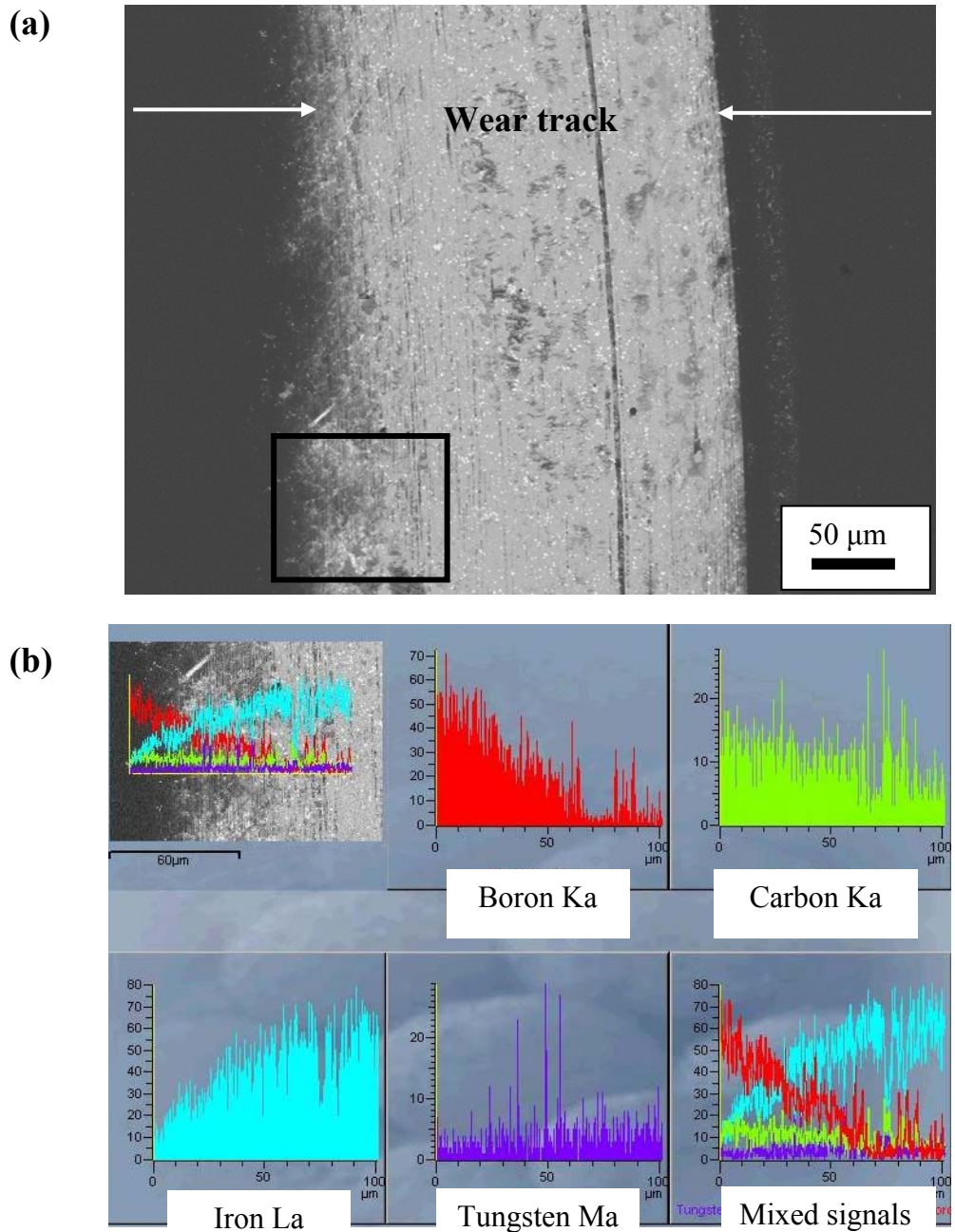


**Figure 4.35:** (a) Backscattered electron image of the worn track after 125 m (b) line scan on the zone shown by the square.

The friction coefficient versus distance diagram for 125 m sliding is given in Figure 4.37. From the figure it can be seen that between 25 and 125 m, friction coefficient stabilizes and reach a steady state level around 0,6.

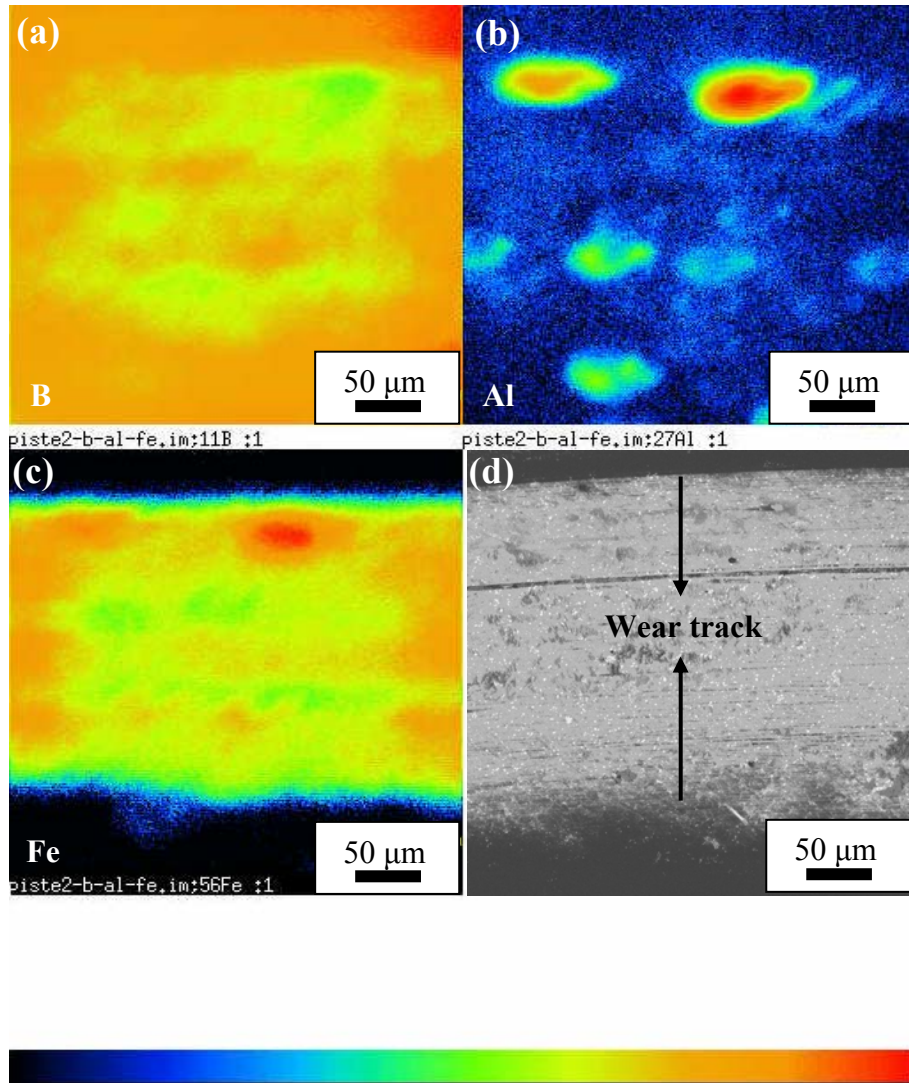


**Figure 4.36:** SIMS elemental ion imaging of the worn surfaces (a) B distribution (b) Al distribution (c) Fe distribution (d) representative SEM image of the wear track.

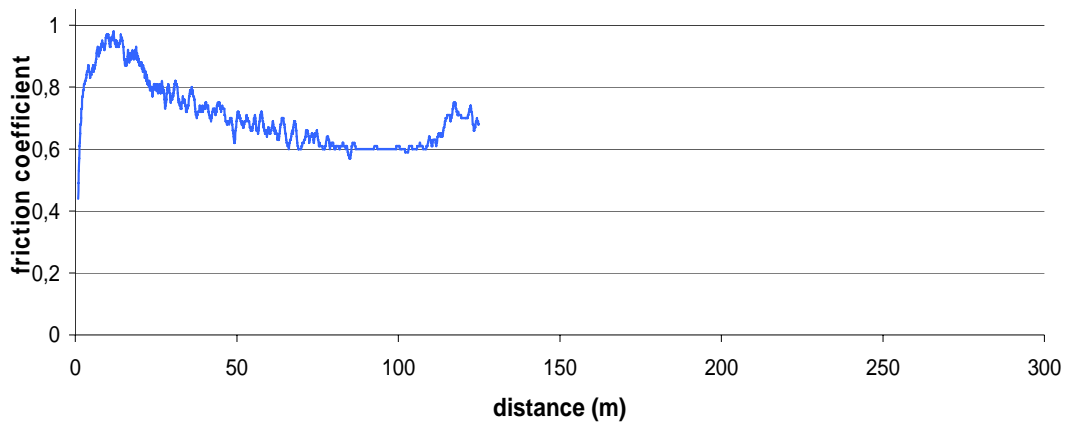


**Figure 4.37:** Friction coefficient vs. distance diagram for 125 m sliding distance.

The tests were continued with 225 m sliding distance. Figure 4.38 shows SEM observations of the wear track after 225 m.

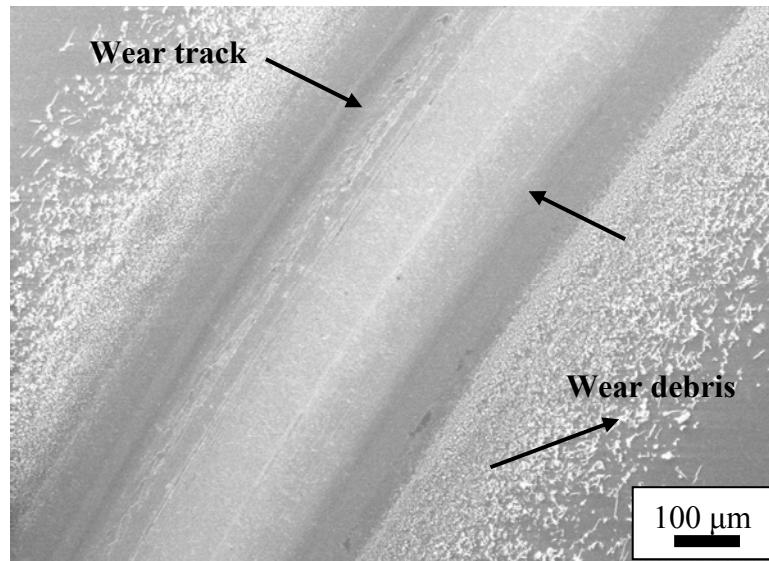


**Figure 4.38:** SEM investigations of the worn surfaces after 225 m.

Profilometer measurements realized on the wear track after 225 m sliding distance are presented in Table 4.5. In Figure 4.39, further observations by backscattered electron images of the wear tracks obtained after 225 m sliding distance are given. From the figures and complementary EPMA results from which no boron or excess amount of carbon was observed, it is evident that after 225 m, the counterface reached the substrate. Instead, some oxides were already present in the zones demonstrated in Figure 4.39 (b) indicating that the coating is completely worn and the wear of the steel substrates already started.

The increase of the friction coefficient to the values around 0.9 in Figure 4.40 coupled with the information obtained from SEM investigations and profilometer measurements, confirms that the substrate was reached.

**Table 4.5:** Profilometer measurement of the wear track after 225 m.

| Wear track depth ( $\mu\text{m}$ ) | Wear track width ( $\mu\text{m}$ ) |
|------------------------------------|------------------------------------|
| 0.482                              | 405                                |
| 0.451                              | 408                                |
| 0.494                              | 379                                |
| 0.496                              | 423                                |

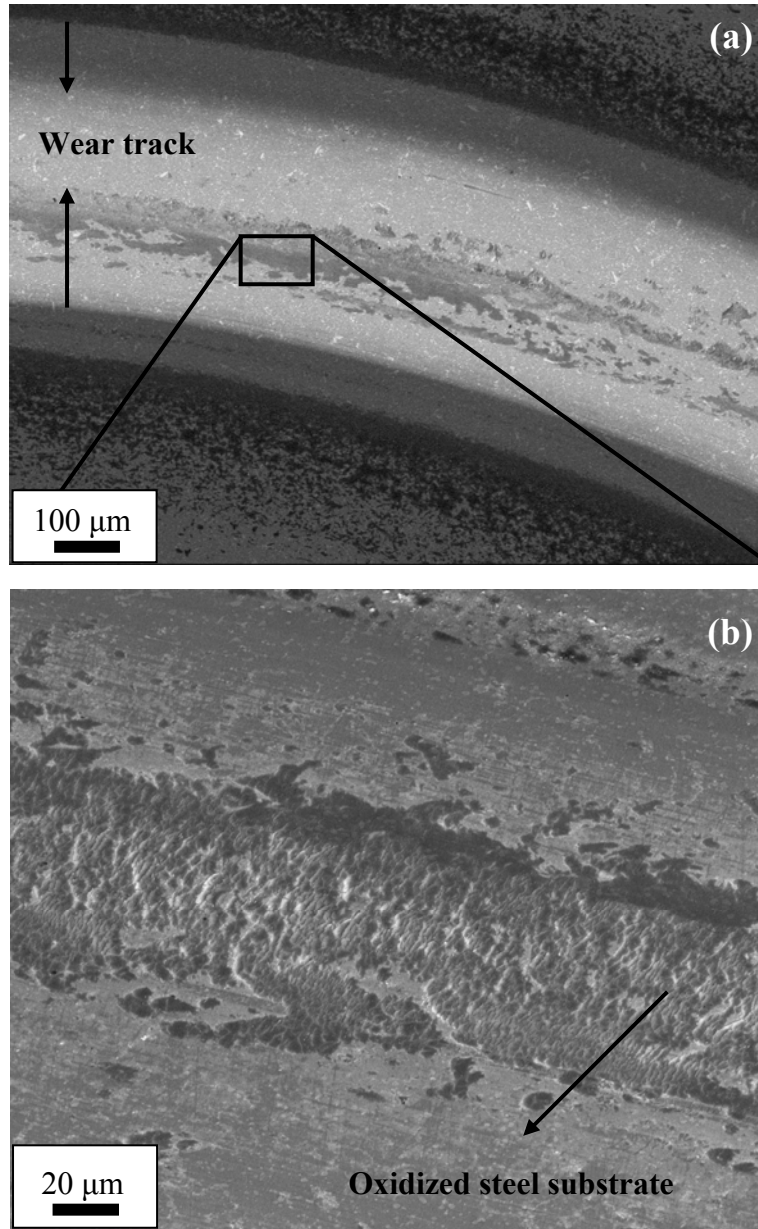


**Figure 4.39:** SEM investigations of the worn surfaces after 225 m.

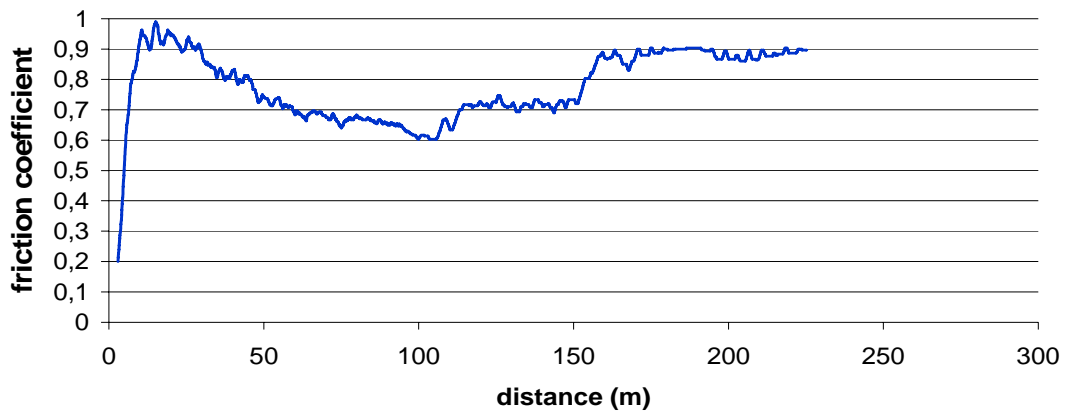


**Figure 4.40:** Friction coefficient vs. distance diagram for 225 m sliding distance.

After these first investigations, a sliding distance of 100 m was decided for all B<sub>4</sub>C thin films deposited in this study, to observe only the wear properties of the coatings. In the second stage of the wear study, a phenomenon, which occurs during wear tests by using Al<sub>2</sub>O<sub>3</sub> counterfaces, was studied. As can be seen from Figure 4.41, during wear tests, Al<sub>2</sub>O<sub>3</sub> counterface which has approximately the half of the hardness (~20 GPa) of B<sub>4</sub>C coatings, worn out and Al<sub>2</sub>O<sub>3</sub> debris was present at both sides of the wear track and on the pin itself. However, worn volumes of alumina balls were too small to detect and for that reason will not be presented here.

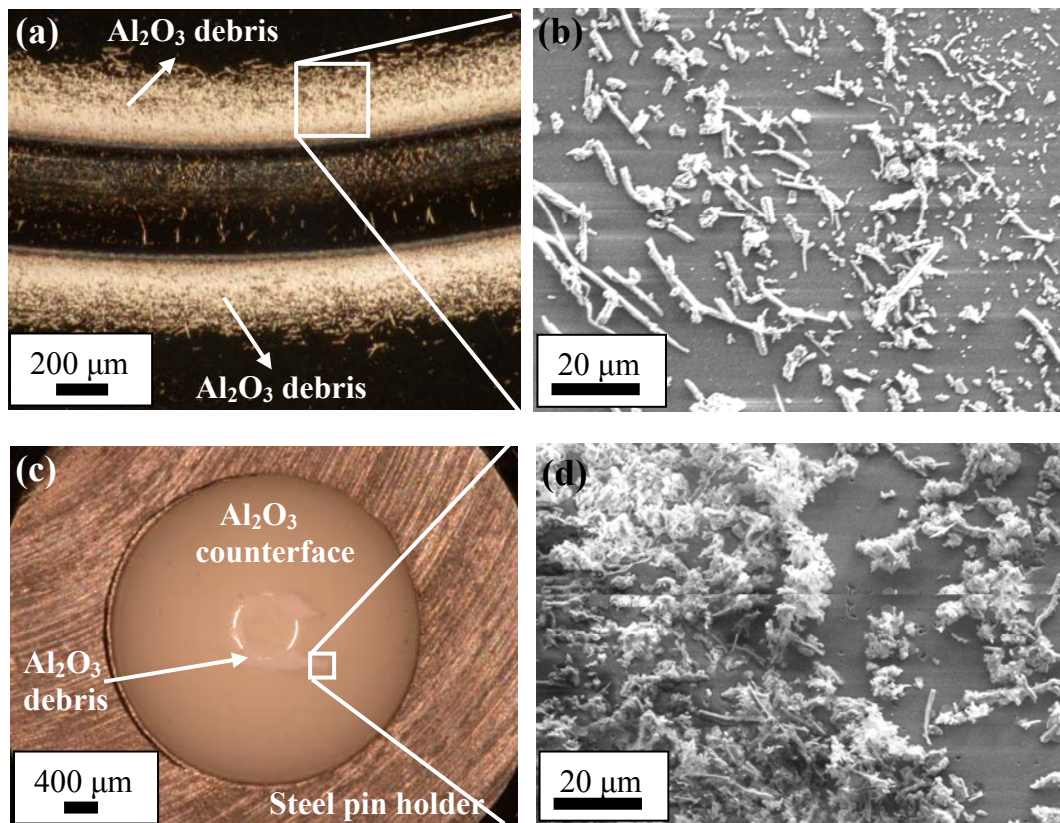


**Figure 4.41:** (a) Optical observation of the debris present at the sides of the wear track (b) SEM image of same debris (c) Optical observation of the debris on the Al<sub>2</sub>O<sub>3</sub> counterface (d) SEM image of same debris.

As a result of these observations, different counterfaces were selected to understand the wear properties of B<sub>4</sub>C coatings against different materials. Two counterfaces other than Al<sub>2</sub>O<sub>3</sub>; B<sub>4</sub>C coated steel pins and WC pins were used for wear tests with the same parameters used for Al<sub>2</sub>O<sub>3</sub>. The tests were conducted on the same specimen, the depth and width of the wear tracks were measured by means of a profilometer and wear rates were calculated for all three counterfaces. Results are presented in Figure 4.42.

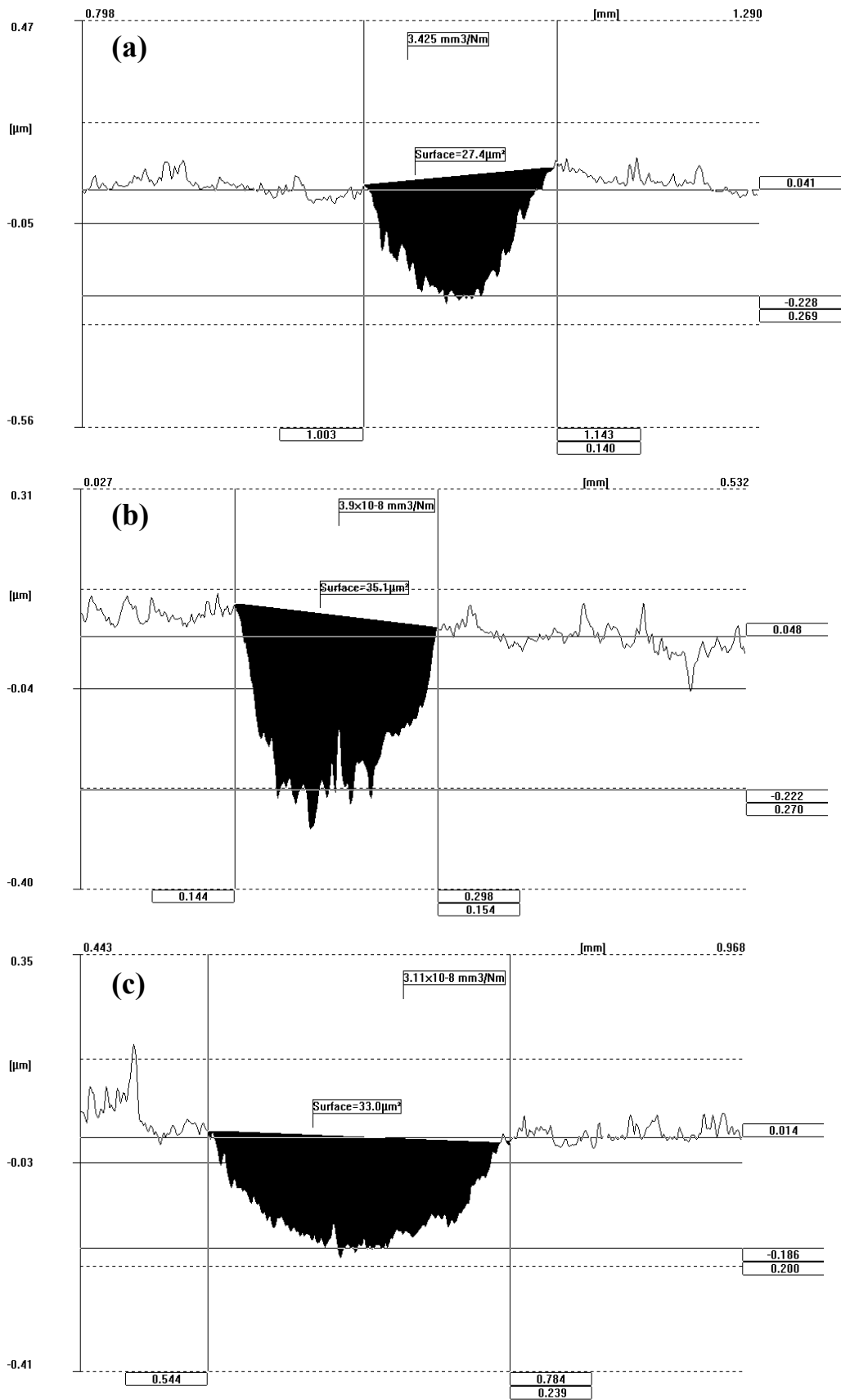


**Figure 4.42:** Wear track measurements of B<sub>4</sub>C coating against (a) WC (b) B<sub>4</sub>C (c) Al<sub>2</sub>O<sub>3</sub> pins.

The profiles of the wear tracks obtained from different counterfaces can be seen in Figure 4.42. Measured wear rates were quite similar. When compared, the profiles of three wear tracks visualized in the figure present some dissimilarities. Although there were no big differences in measured wear rates, the profiles obtained from WC and B<sub>4</sub>C coated pins presented inhomogenities at the bottom of the wear tracks. Hence, Al<sub>2</sub>O<sub>3</sub> pins were selected to measure wear rates of all the coatings deposited; using a sliding distance of 100 m. Figure 4.43 demonstrates the results obtained from these measurements.

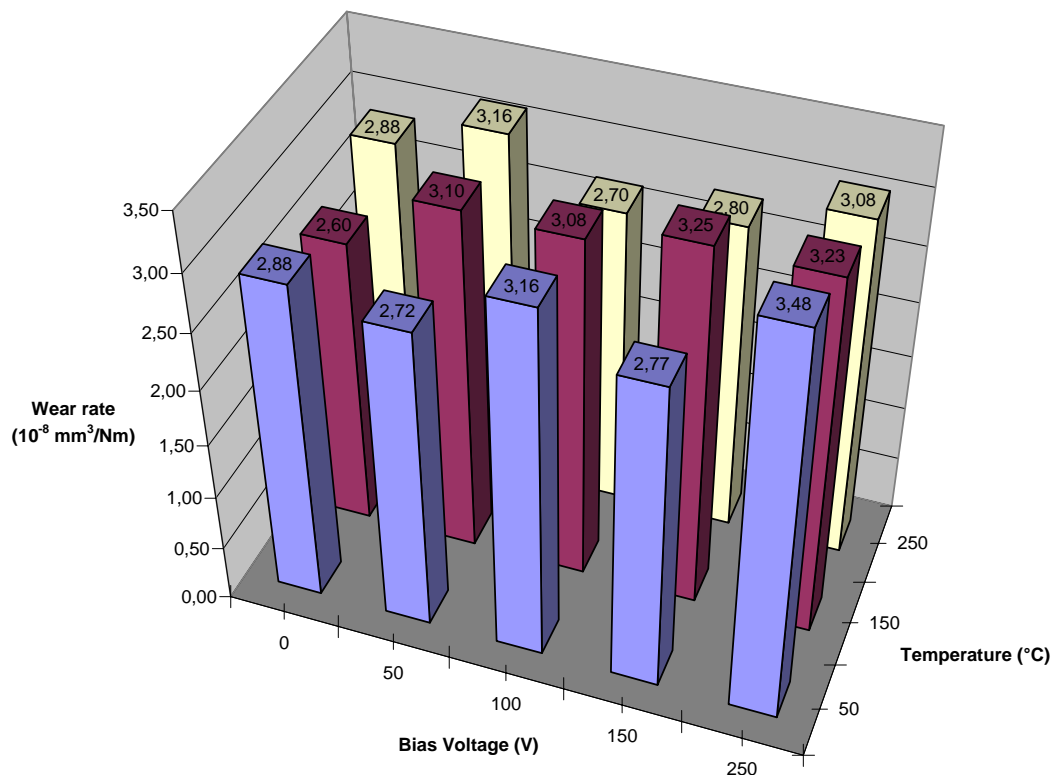


**Figure 4.43:** Wear rates of boron carbide coatings deposited with different temperatures and bias voltages by plasma-enhanced dc magnetron sputtering.

From the figure, it can be clearly seen that, the process parameters used in this study (temperature and bias voltages), had no significant effect on the wear properties of the coatings. The measured wear rates were between 2.60 and 3,48 x 10<sup>-8</sup> mm<sup>3</sup>/Nm. For the total range of process parameters, there were no drastical changes in the microstructures of the plasma-enhanced DC magnetron sputter deposited B<sub>4</sub>C films. Even the film deposited at floating potential and without external heating shows a quasi-solid structure instead of usual columnar morphology of the conventional

magnetron sputtered thin films deposited with similar conditions. It is concluded that, the microstructural stability obtained for all the films deposited in these series explains the insensitivity of the wear rates to the process parameters.

SEM investigations on the worn surfaces were also realized to define the wear mechanism of  $B_4C$  coatings against  $Al_2O_3$  counterface. Figure 4.44 shows a representative example of the wear tracks investigated.

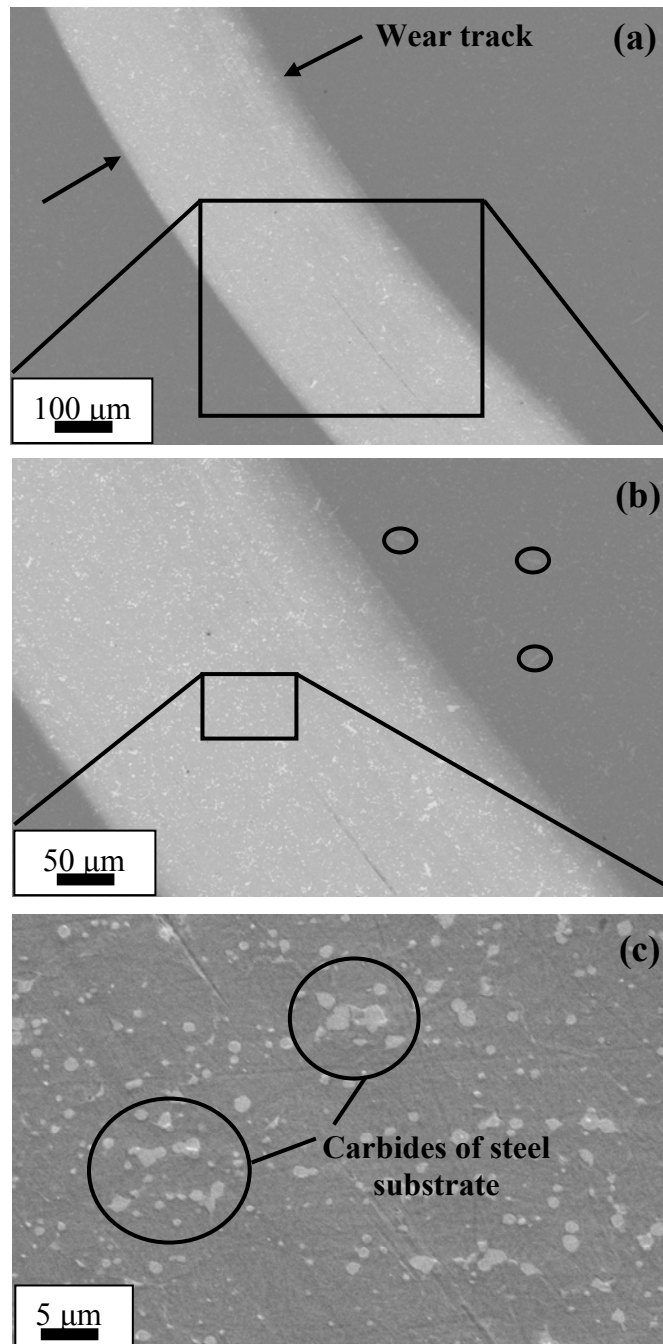


**Figure 4.44:** Representative SEM investigations of the wear track, the magnification increases from (a) to (c) for the same wear track.

It is known from the profilometer measurements that after the “pin-on-disc” test, the film thickness at the contact point was reduced to 100 – 150 nm. In Figure 4.44 (b) at low magnification, the substrate was already observed on the wear track and the white zones, which can be clearly seen at higher magnifications in Figure 4.44 (c), taken from the inside of the wear track are carbides of the AISI M2 substrate (VC, WC).

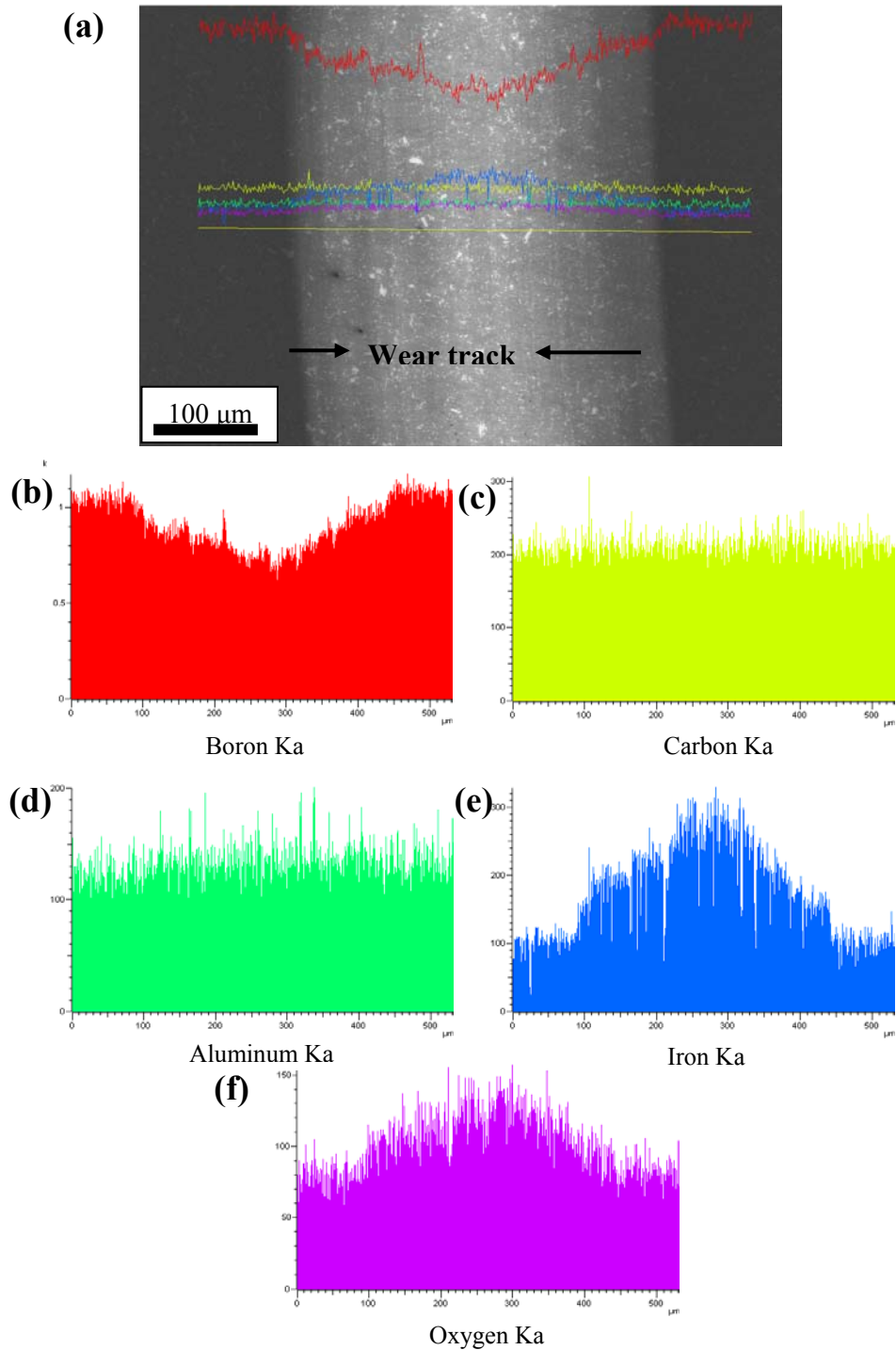


**Figure 4.45:** EDS line scan analysis of the wear track (a) BSE image of the analyzed area (b) boron (c) carbon (d) aluminum (e) iron and (f) oxygen elemental distributions.

In Figure 4.44 (b) even for the coating, which was not worn out, the carbides of the substrate, was visible. EDS line-scan analyses were carried out on the wear tracks to see the distribution of the elements which constitutes the coating structure and also Al and O, which were the pins constituent elements and the results are presented in Figure 4.45. In the figure (a) the backscattered image of the analyzed zone can be seen. In (b) boron elemental distribution is given. It is clear from the figure that boron concentration decreased in the wear track where iron and oxygen concentrations given in (e) and (f) increased respectively. The increase of the iron accounts is remarkable although there are approximately 150 nm of coatings remaining in the wear track according the profilometer measurements. The same increase was observed for the oxygen concentration. Although the decrease of the boron concentration was expected, from image analysis as well as from elemental distributions, it is concluded that electrons as well as x-rays collected were influenced from the substrate hence consequently SEM is not a convenient technique to predict the wear mechanism of thin coatings in the nanometer range.

#### **4.1.3.7 SIMS elemental depth profiles**

The elemental depth profile of plasma-enhanced DC magnetron sputtered boron carbide coatings deposited on Si substrates were analyzed with the same procedure described in Section 4.1.2.7 by using  $O_2^+$  primary ion beam. All the coatings deposited by plasma-enhanced DC magnetron sputtering demonstrated the same profile regardless the deposition conditions. Figure 4.15 shows elemental depth profiles of boron, carbon, oxygen, and silicon. It can be observed from the figure that the elemental film distribution was constant over the film thickness. The intensities are qualitative as explained in Section 4.1.2.7. To analyze particularly the oxygen and hydrogen evaluation that are sensitive to negative secondary ions, depth profiles by using  $Cs^+$  primary ion source were realized and the result is presented in Figure 4.47. As can be seen from the figure, the relative concentration of carbon that is also a secondary negative ion sensitive element is significantly increased. It is found that, hydrogen that was not detectable while using  $O_2^+$  primary ion source was present as impurity in the coatings. There was no dramatical change of oxygen concentration between analyses realized with two different ion sources according to the figure.

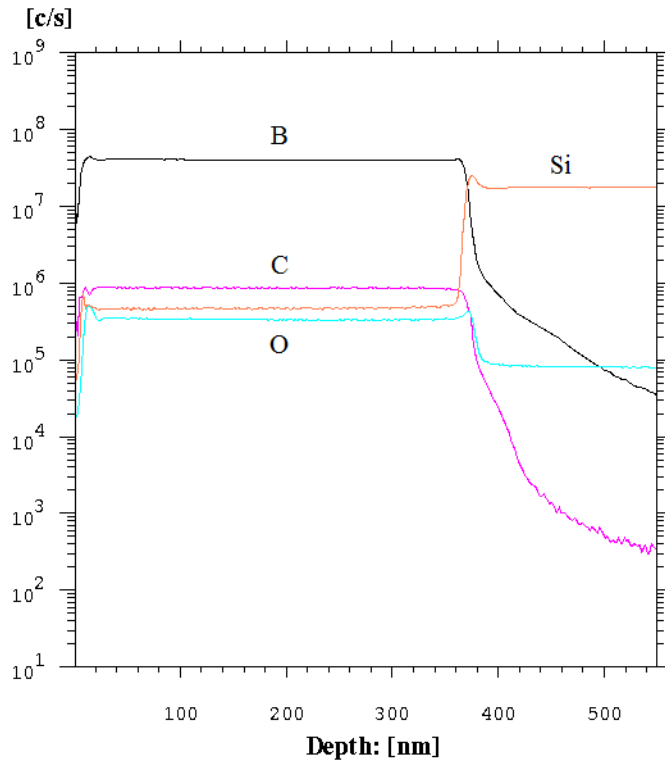


**Figure 4.46:** Representative depth profile of boron carbide films deposited by plasma-enhanced DC magnetron sputtering by using  $O_2^+$  primary ion beam.

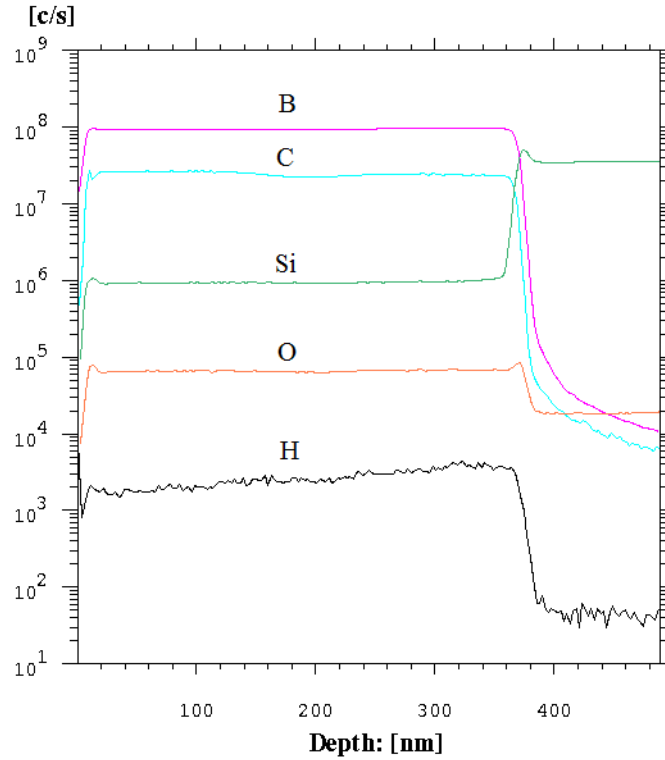


**Figure 4.47:** Representative depth profile of boron carbide films deposited by plasma-enhanced DC magnetron sputtering by using  $Cs^+$  primary ion beam.

For SIMS data given in the figure, the x-axis was converted from time to depth by measuring the crater depths obtained during analyses by a profilometer. The thicknesses were in good agreement with SEM observations with a maximum deviation of 5%.

#### **4.1.4 Conclusion**

Two types of DC magnetron sputtered boron carbide films, with and without the presence of auxiliary plasma source, were investigated in this section. Chemical compositions of deposited films were insensitive to the deposition configurations and deposition parameters investigated. Measured film compositions were the same with boron carbide target material, thus the same with source powders and were nearly stoichiometric boron carbide with 78% B, 21.4% C, 0.3% O and 0.3% Si. Boron carbide films deposited by conventional DC magnetron sputtering had columnar microstructures and a densification to zone T type structure with less pronounced columnar morphologies and less separated columns as indicated in the Thornton structural-zone diagram was observed with the increase in bias voltages. Whereas boron carbide films deposited by plasma-enhanced DC magnetron sputtering had non-columnar, featureless microstructures even for the films deposited without any applied bias voltages and external heating. All observed boron carbide thin films deposited by DC magnetron sputtering with or without auxiliary plasma configuration were amorphous according to high-resolution TEM observations and consequent FFT and/or diffraction patterns. High-resolution TEM observations and EFTEM elemental mapping on conventional DC magnetron sputtered boron carbide films revealed that, column thicknesses were about 20-25 nm and oxygen from the deposition chamber and/or ambient air, incorporated in the nanovoids of about 2-3 nm between the columns. From high-resolution TEM observations on plasma-enhanced DC magnetron sputtered boron carbide films, it is evident that there exists a transition layer of 4-5 atomic layers, which correspond to 1-1.5 nm, with a crystallographic order just at the coating-substrate interface and then the coating becomes quickly amorphous. Nanomechanical characterizations revealed that conventional DC magnetron sputtered boron carbide thin films had about 20 GPa hardness and 220 GPa modulus values and process parameters did not have an effect on the hardness and modulus values for these films. However, plasma enhanced DC magnetron sputtered boron carbide films had about 30-35 GPa hardness and 270-300

GPa modulus values. An increase in the hardness and modulus with the increase in bias voltages and temperature was observed for these films. The hardest film with about 40 GPa hardness and 300 GPa modulus values was obtained at 250 °C and 100 V applied bias voltage. Thus, there was a factor of about 1.5 to 2 times between the hardness and modulus values of boron carbide films deposited with and without auxiliary plasma configuration. Tribological studies demonstrated that DC magnetron sputtered boron carbide coatings do not give low friction coefficients against different counterfaces. Friction coefficients of about 0.7 and 0.6 were found against Al<sub>2</sub>O<sub>3</sub> for the coatings deposited without and with auxiliary plasma configuration respectively. However, good wear rate values of about  $5 \times 10^{-8}$  mm<sup>3</sup>/Nm and  $2.6 - 3.5 \times 10^{-8}$  mm<sup>3</sup>/Nm were obtained for conventional DC magnetron sputtered and plasma-enhanced DC magnetron boron carbide films respectively. It is believed that the same factor of two between the wear rates and hardness values of two types of boron carbide coatings deposited with two different configurations is an evidence of hardness and strength dominated wear resistance of these films as explained in Section 2.4.4. SIMS elemental depth profile analyses were realized on both conventional DC magnetron sputtered and plasma-enhanced DC magnetron sputtered boron carbide films. Results demonstrated that for all the films, the profiles of boron, carbon, oxygen, and silicon were the same and constant over the whole film thicknesses, regardless of deposition parameters used. Well-known primary ion beam effect on the sputtering yields during SIMS analyses was observed for elements analyzed. The concentrations are qualitative and dependant to the analyze conditions. More accurate results were obtained for boron and silicon which are more sensitive to secondary positive ions with O<sub>2</sub><sup>+</sup> primary ion beam, while for oxygen, carbon and especially trace hydrogen which was not detectable with O<sub>2</sub><sup>+</sup> better sensitivity was obtained with Cs<sup>+</sup> primary ion beam.

## **4.2 RF Sputtered B<sub>4</sub>C Thin Films**

In this section, the microstructures, nanomechanical properties, chemical bonding and tribological properties of non-magnetron radio-frequency sputtered boron carbide thin films will be discussed.

#### 4.2.1 Microstructural studies

Microstructural analyses were carried out on three specimens deposited by RF sputtering. Figure 4.48 shows the microstructures of the specimens BC27, BC28 and BC29. These micrographs were taken from the coating cross-sections. The specimens were prepared differently from previous microstructural studies; they were cut, enrobed and mirror polished before the observations. A representative back scattered image is given for the specimen BC28. As the contrast is more important for BSE images and as the coating consists of light elements, boron and carbon, the coating microstructure as well as the substrate is more distinguishable from this micrograph.

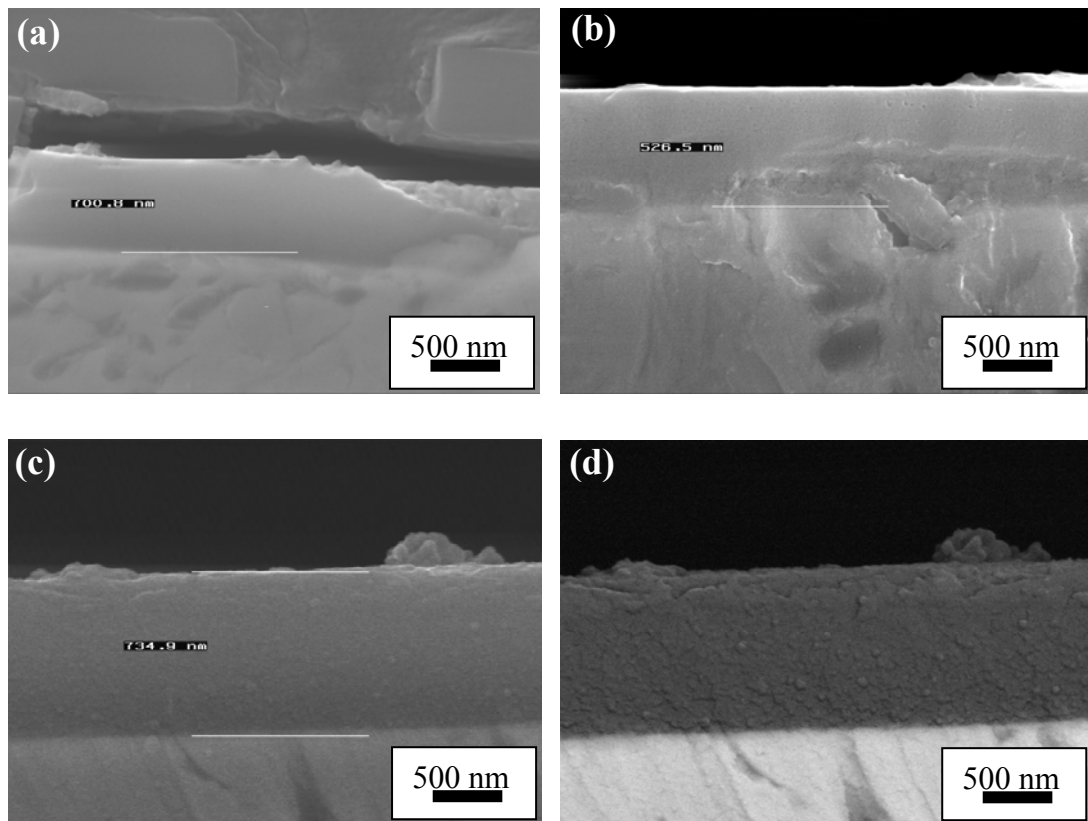


**Figure 4.48:** Cross-section SEM micrographs of (a) BC27 (b) BC28 (c) BC29 (d) BSE image of BC29.

As can be seen from the figure, all three coatings deposited had non-columnar structures. However, the surface and the coating morphologies were not as smooth as which deposited by plasma-enhanced DC magnetron sputtering. Actually, according the Thornton's SZD, the coatings should have columnar structures regarding their processing conditions; temperature and argon pressure. It is believed that this

suppressing of the columnar morphologies without applying any bias voltages, is due to the relatively high neutral bombarding of the films during their growth because of the short target-substrate distance and the increase of the deposition temperatures during long deposition times.

#### 4.2.2 Chemical compositions

Electron Probe Micro analysis was used to quantify the chemical composition of B<sub>4</sub>C coatings deposited by RF sputtering. Results are presented in Table 4.6.

**Table 4.6:** Elemental composition of boron carbide coatings deposited by RF sputtering.

|      | B (at. %) | C (at. %) | O (at. %) | Si (at. %) |
|------|-----------|-----------|-----------|------------|
| BC27 | 76.13     | 23.00     | 0.63      | 0.25       |
| BC28 | 76.20     | 23.17     | 0,51      | 0.12       |
| BC29 | 75.97     | 23.23     | 0.57      | 0.23       |

The measured chemical compositions were slightly different from the coatings deposited by DC sputtering. The target used for the deposition of RF sputtered boron carbide thin films was a commercially obtained one and there was no information about the boron carbide chemical composition. For this reason, it is hard to give a definite conclusion if the composition of the target material or the process parameters were caused this difference in the case of RF sputtered boron carbide thin films.

#### 4.2.3 Nanomechanical properties

For the nanoindentation measurements of RF deposited boron carbide films, the same procedure described in the Sections 4.1.2.4 and 4.1.3.3 were used. The coatings were deposited onto AISI 430 steel and Si (100) substrates. The substrate effect was dominant for the loads over 3000  $\mu$ N for the coatings deposited on steel substrate. Thus, 3000  $\mu$ N was used to analyze the coating properties. Figure 4.49 shows the effect of the deposition parameters, mainly sputtering power in the case of RF sputtered boron carbide thin films, on the nanomechanical properties. From the figure, it can be seen that the nanomechanical properties of boron carbide thin films were not influenced by the increase of the sputtering power hence, dependant increase of the cathode voltage.

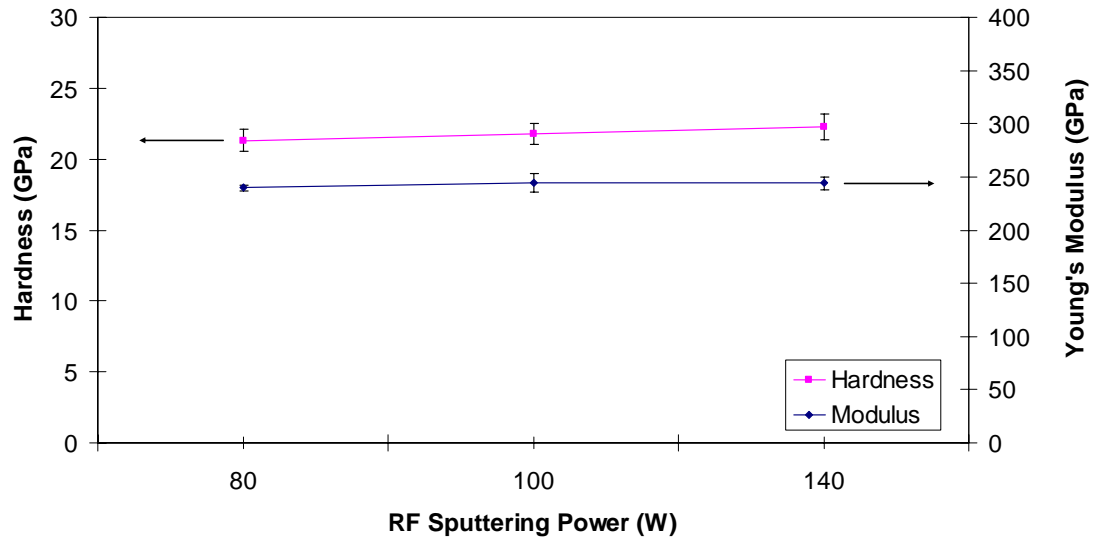


**Figure 4.49:** The effect of sputtering power on the nanomechanical properties of boron carbide films deposited by RF sputtering.

All the coatings deposited by RF sputtering had about 22 GPa hardnesses and 240 GPa Young's modulus values. Figure 4.50 shows a representative load-displacement curve of boron carbide coatings deposited by RF sputtering. As can be seen from the figure, the coating shows approximately 70% elastic recovery after unloading, the same value for the films deposited by DC magnetron sputtering without auxiliary configuration.

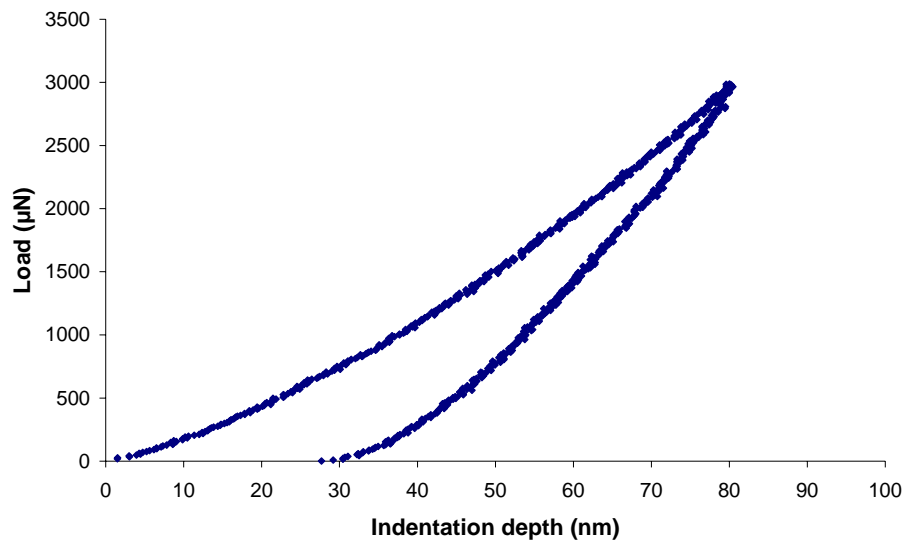


**Figure 4.50:** Representative load-displacement curve for boron carbide coatings deposited by RF sputtering.

Figure 4.51 shows the representative indent profiles obtained by AFM on the RF deposited boron carbide coatings. The same pyramidal Berkovich indenter was used for tests and visualization before and after the indentation. In Figure 4.51 (a) 2D view of the indent can be seen with the roughness scale on the right hand side. In (b) 3D visualization of the indent and the surface of the specimen are presented. If compared with the indent profile given in Figure 4.23 taken from the plasma-enhanced DC sputtered B<sub>4</sub>C film, it would be seen that, the surface presented in Figure 4.51 is rougher. The reason for that was the difficulties on the surface finishing when mirror polishing of AISI 430 substrates which was considerably softer than the AISI M2 substrates, and the dependency of the coating surface morphologies to the final substrate conditions.

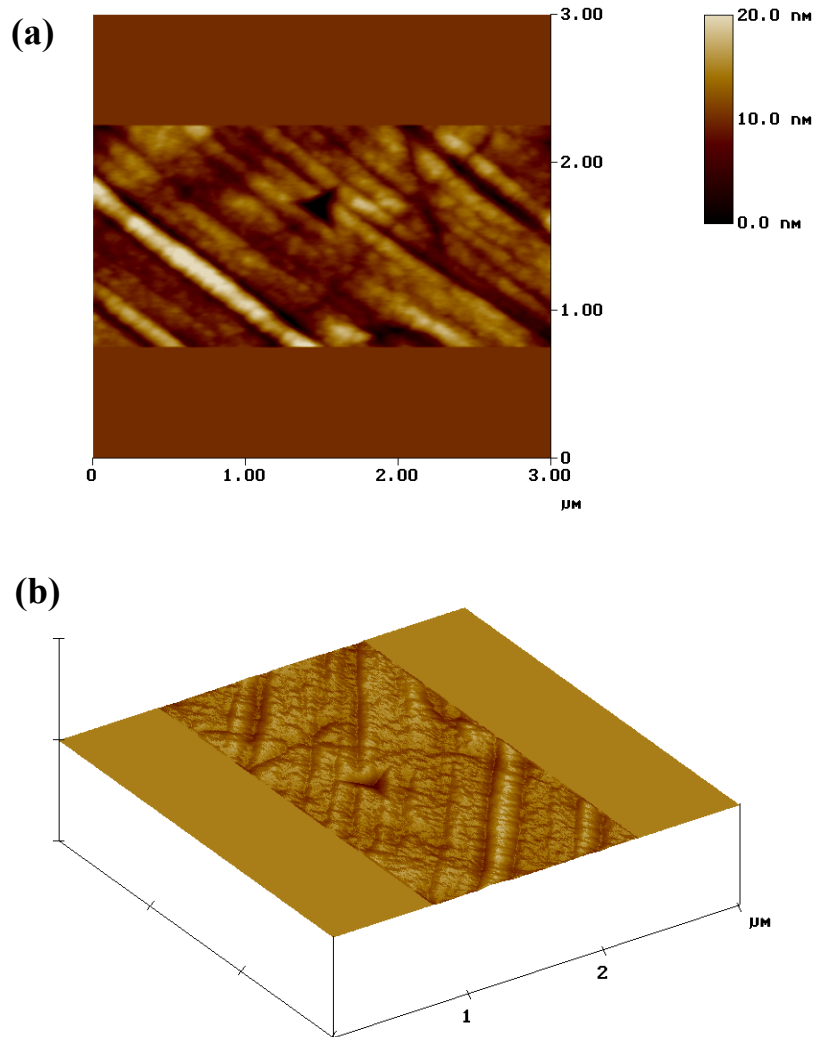


**Figure 4.51:** Representative indent profile obtained by AFM on the RF sputtered boron carbide coatings (a) 2D view of the indent (b) 3D visualization of the same area.

#### 4.2.4 Bonding properties

The phase composition of RF deposited  $B_4C$  films were also investigated by FTIR spectroscopy. Figure 4.52 shows representative FTIR spectra taken from the specimen BC27. Infrared spectra present two broad bands, one centered at  $\sim 1100\text{ cm}^{-1}$  and the other at  $\sim 1600\text{ cm}^{-1}$ . The spectrum of three specimens were identical and as can be seen from the figure were the same as DC magnetron sputtered boron carbide coatings which was presented in Figure 4.29 with a small shift.

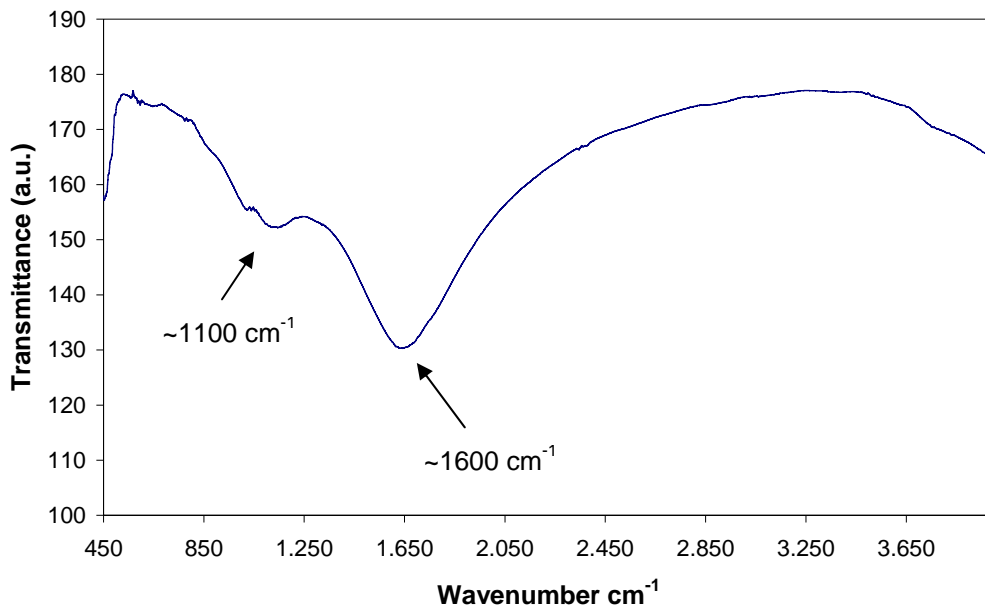


**Figure 4.52:** Representative FTIR spectra of RF sputtered boron carbide film.

#### 4.2.5 Tribological studies

The friction coefficient evolution of RF sputtered boron carbide thin films was studied by performing tribological tests until the coatings were completely worn and the substrates were exposed. Figure 4.53 shows the evaluation of friction coefficients of the coatings versus distance.

For all the three specimens the friction coefficient evolution presented three stages. During the first short time stage, the friction coefficient was unstable due to the first contact and the initial roughness of the surfaces in contact. In the second stage it stabilized at about 0.5 which is believed, the friction coefficient value of RF sputtered boron carbide coatings.

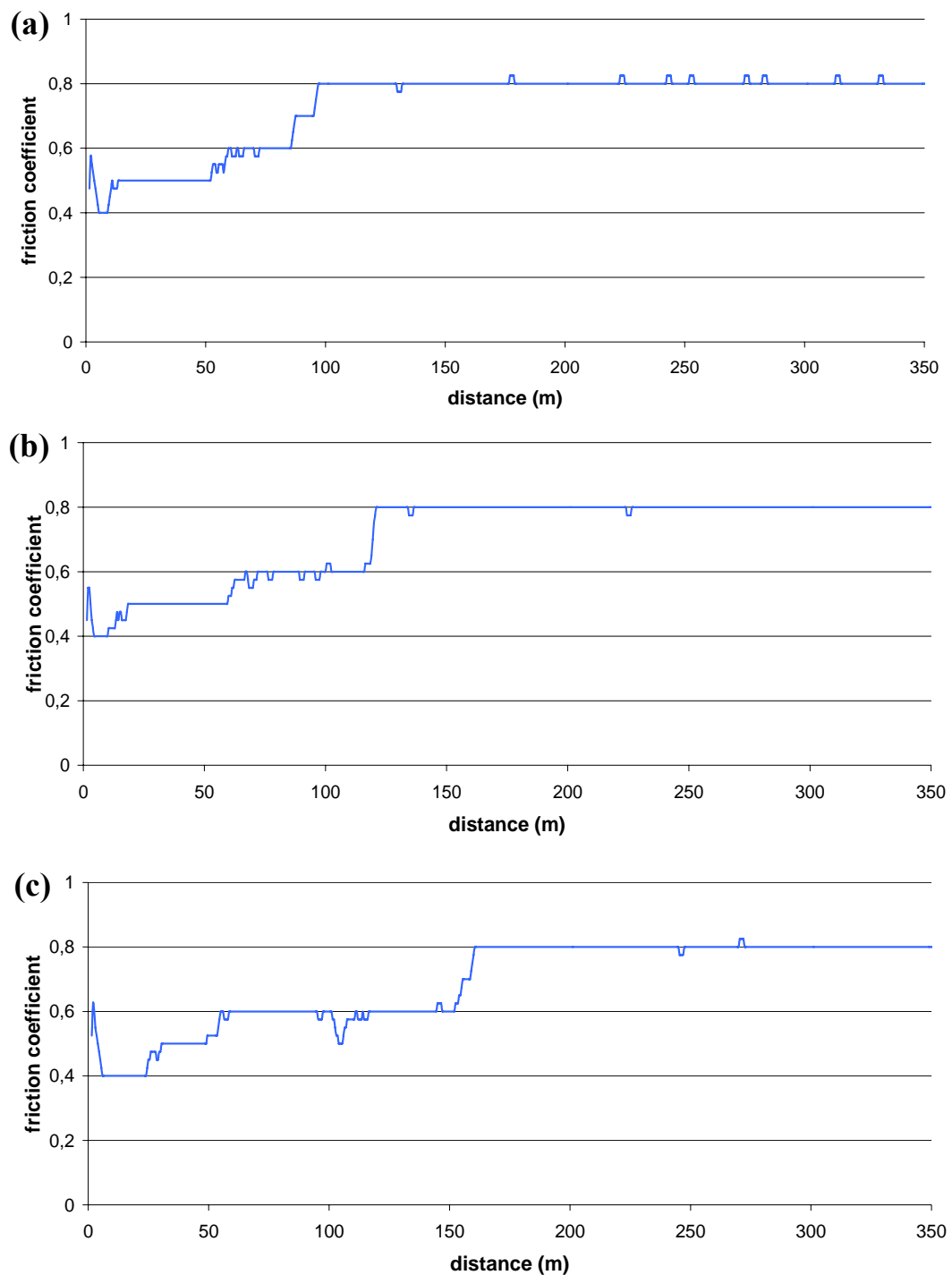


**Figure 4.53:** Friction coefficient evaluations of (a) BC27 (b) BC28 (c) BC29.

In the third stage, there was an increase to about 0.6, which is thought to be due to the propagation of the wear debris and their entrapment at the contact area between tested material and the counterface. Finally, it increased to a value of 0.8, which is the friction coefficient of the steel substrate against  $\text{Al}_2\text{O}_3$  counterface, indicating that the coating was completely worn after 120 m sliding.

As RF sputtered B<sub>4</sub>C films were deposited only on AISI 430 steel substrates, the wear rates could not be measured because of the adhesion problems observed during the tests.

#### 4.2.6 SIMS elemental depth profiles

The elemental depth profile of RF sputtered boron carbide coatings were analyzed with the same procedure described in Section 4.1.2.7. Analyses were realized on boron carbide films deposited on AISI 430 steel substrates. Representative diagram in Figure 4.15 realized with O<sub>2</sub><sup>+</sup> primary ion beam shows that, like DC magnetron sputtered boron carbide films, the elemental film distribution was constant over the whole film depth.

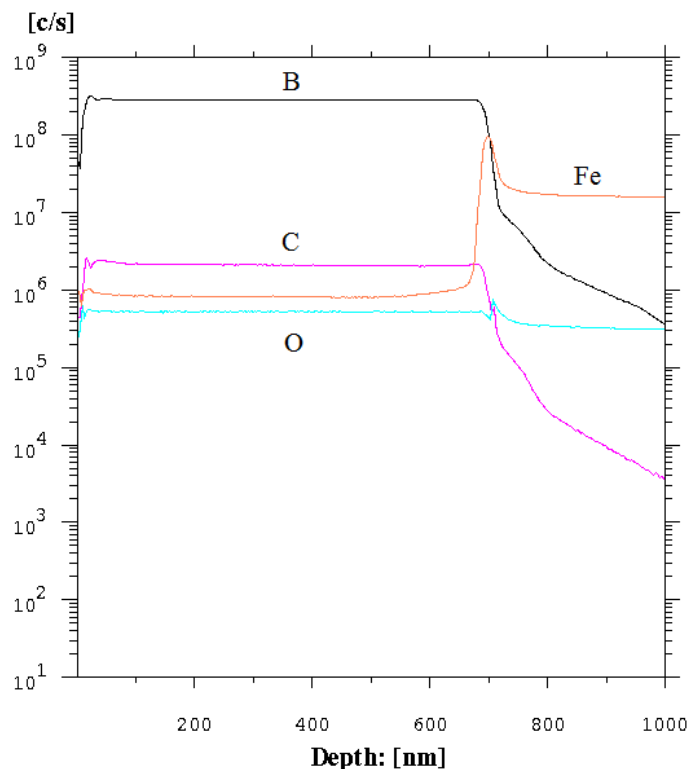


**Figure 4.54:** Representative depth profile of boron carbide films deposited by RF sputtering by using O<sub>2</sub><sup>+</sup> primary ion beam.

For SIMS data given in Figure 4.54, the x-axis was converted from time to depth by measuring the crater depths obtained during analyses by a profilometer. The thicknesses were in good agreement with SEM observations with a maximum deviation of 5%.

#### 4.2.7 Conclusion

Microstructural studies realized on RF deposited boron carbide films demonstrated the non-columnar structures of these films. It is believed that this suppressing of the columnar morphologies without applying any bias voltages, is due to the relatively high neutral bombarding of the films during their growth because of the short target-substrate distance and/or the increase of the deposition temperatures during long deposition times. Measured film compositions were about 76% B, 23.2% C, 0.5% Si, 0.3% O. Thus, slightly different from the coatings deposited by DC magnetron sputtering. However, as there was no information about the commercial boron carbide target chemical composition, it is hard to conclude whether configuration or the target itself caused this difference. The coupled effect of non-magnetron design of the deposition system and low sputtering yield of boron carbide resulted with very low deposition rates for boron carbide coatings. Films were amorphous according to grazing angle XRD results. Nanomechanical characterizations revealed that non-magnetron RF sputtered boron carbide coatings had ~22 GPa hardness and ~240 GPa Young's modulus and showed 70% of elastic recovery. Our results demonstrated that boron carbide deposition without process modifications results with hardness values about 20 GPa, and different configurations such as extensive ion bombardment or very low pressure deposition is needed to deposit ultrahard (40 GPa and above) boron carbide thin films by PVD systems. Tribological studies on RF deposited boron carbide thin films demonstrated a quite different characteristic especially for friction coefficient evolution. Lower friction coefficients compared to DC sputtered boron carbide films, about 0.4 were observed at the beginning of "pin-on-disc" tests instead high values about 1 obtained for DC sputtered films. Friction coefficients stabilized around 0.5, which is believed the friction coefficient value of RF sputtered boron carbide films. Boron, carbon, oxygen and silicon depth profiles realized by SIMS on RF sputtered boron carbide thin films demonstrated that the elemental distribution was constant over the whole film depth.

### 4.3 BCN Thin Films

In this section the effect of different  $N_2$  flow rates, hence the incorporation of different amount of nitrogen on the microstructural, nanomechanical, tribological and bonding characteristics of boron carbide thin films in other words boron carbonitride compounds deposited with the presence of auxiliary plasma source will be investigated.

#### 4.3.1 Microstructural studies

Microstructures were observed for all three coatings deposited with different  $N_2$  flow rates. Figure 4.55 demonstrates cross-sectional SEM observations of the specimen BC67 deposited on Si substrate. The columnar structure can be clearly seen from the figure. The micrograph is again taken with a  $10^\circ$  tilt angle in order to observe the coating microstructure and the surface morphology together. Measured film thickness is about 400 nm for this coating.

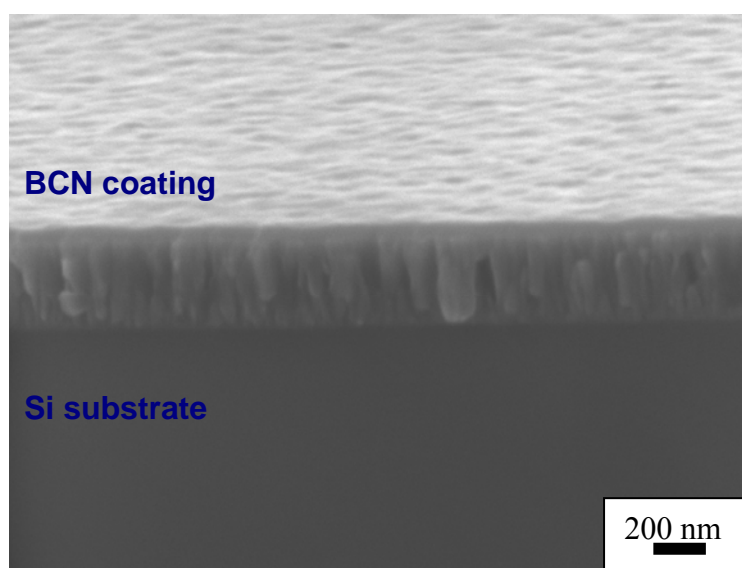


**Figure 4.55:** Cross-sectional SEM micrograph of the specimen BC67.

As can be seen from the figure, BCN film deposited with 5%  $N_2$  in the deposition gas had large columnar structure, although 250 V bias voltage and  $250^\circ C$  deposition conditions. The incorporation of the nitrogen into boron carbide structure changed the non-columnar boron carbide coating structure deposited by plasma-enhanced configuration to a coarse columnar structure for BCN films deposited in presence of 5%  $N_2$  in the process gas. Figure 4.56 shows the microstructure of BC68 from its cross-section. It can be observed from the figure that the nitrogen incorporation at

25% N<sub>2</sub> in the processing gas changed drastically the coating microstructure. For this specimen the structure was neither columnar nor a continuous solid structure without defects, instead, uniform granular structure of the coating can be seen from the figure.

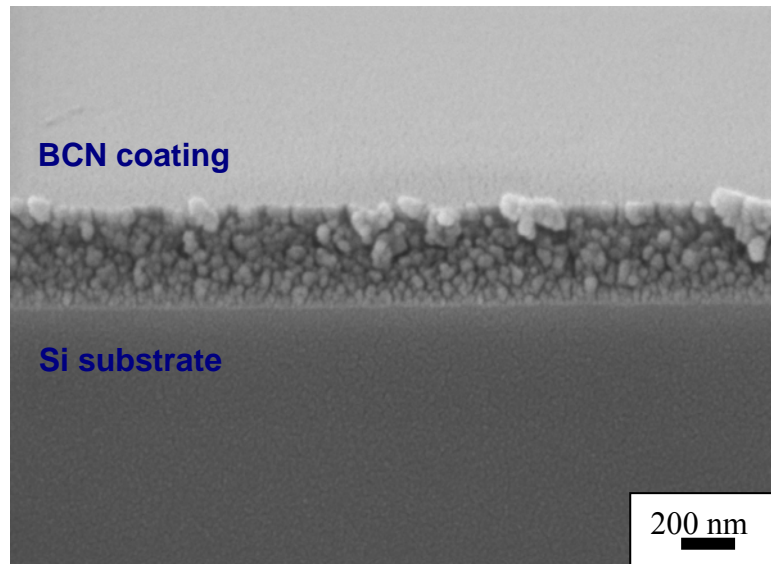


**Figure 4.56:** Cross-sectional SEM micrograph of the specimen BC68.

Figure 4.57 shows the cross-section of the specimen BC69. It can be seen from the figure that further increases of the N<sub>2</sub> to 50% in the processing gas, led to more complex microstructures. Because of this relatively high nitrogen flow, non-uniform granular structure of BCN coating can be seen from the figure.

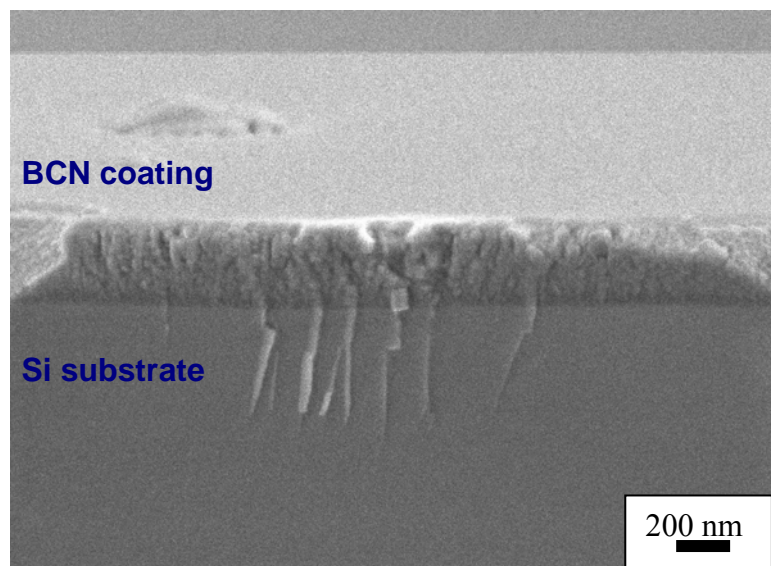


**Figure 4.57:** Cross-sectional SEM micrograph of the specimen BC69.

### 4.3.2 Chemical compositions

Electron Probe Micro analysis was used to quantify the chemical composition of BCN coatings deposited by reactive DC magnetron sputtering and results are presented in Table 4.7.

**Table 4.7:** Elemental composition of boron carbonitride coatings deposited by reactive DC magnetron sputtering.

|      | B (at. %) | C (at. %) | N (at. %) | O (at. %) | Si (at. %) |
|------|-----------|-----------|-----------|-----------|------------|
| BC67 | 51.23     | 18.18     | 30.13     | 0.21      | 0.25       |
| BC68 | 28.69     | 8.23      | 62.33     | 0.48      | 0.27       |
| BC69 | 15.68     | 6.76      | 76.23     | 1.16      | 0.17       |

From the table it can be seen that; the increase of N<sub>2</sub> in the processing gas resulted with a drastic increase of the nitrogen incorporation into the boron carbide structure. Detected N in the structure increased from 30.13 % to 76.23 %, for an increase of N<sub>2</sub> from 5 % to 50 % in the process gas. Accordingly, the amount of boron and carbon in the boron carbide structure showed a tendency of decrease with the increase of N<sub>2</sub> as a reactive gas. Boron percentage decreased from 51.23 % to 28.69 % for an increase of N<sub>2</sub> from 5% to 25 %. For 50% N<sub>2</sub> in the process gas, 15.68 % boron was detected in the coating structure. The same tendency of decrease with the increase of reactive gas flow was also observed for carbon, it decreased from 18.8 to 8.23 and to 6.76 % finally for 50% N<sub>2</sub> in the processing gas environment.

### 4.3.3 Nanomechanical properties

Nanoindentation measurements were realized with 3000  $\mu$ N applied forces for the reasons explained in the precedent sections. In Figure 4.58, hardness and Young's modulus values of three coatings plotted versus N<sub>2</sub> in the gas and N incorporated in the coatings measured by EPMA.

As can be seen from the figure, N incorporation reduced noticeably the hardness of the coatings. It is known from the results of boron carbide series deposited with auxiliary plasma configuration that the coating deposited with the same conditions without N incorporation had ~ 32 GPa hardness. The boron carbonitride coating deposited with 5% N<sub>2</sub> in the deposition gas, possessed 30% N in the composition and had 20 GPa hardness.

At 25% N<sub>2</sub> in the gas, the coating deposited had 62% N in its composition and its hardness decreased to 14 GPa. BCN film deposited at 50% N<sub>2</sub> in the processing gas resulted with 76% N in the composition with 10 GPa hardness.

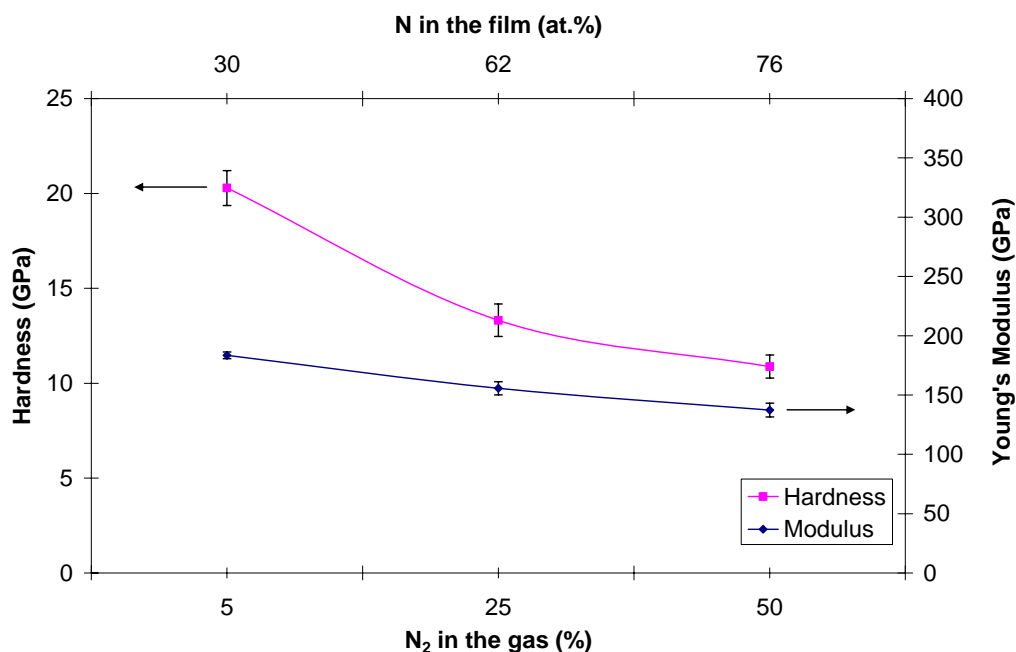


**Figure 4.58:** Hardness and modulus vs. N<sub>2</sub> in the processing gas and N incorporated in BCN films.

The Young's modulus values of the coatings showed also the same tendency to decrease with increasing N<sub>2</sub> in the processing gas, thus with the increase of incorporated nitrogen in the structure, however the influence was less considerable. It decreased from 180 GPa for 5% N<sub>2</sub> to 155 GPa at 25% N<sub>2</sub> and finally at 50% N<sub>2</sub> it reached its minimum with 135 GPa.

#### 4.3.4 Bonding properties

The phase composition of BCN films were investigated by FTIR spectroscopy. IR is a common characterization tool for BCN compounds because is very sensitive to B-N bonds and the spectra for c-BN and h-BN show distinct features. According to the majority agreement from the literature; the spectrum of h-BN is composed of two bands at 780 and 1380 cm<sup>-1</sup>, which arise from in-plane stretching B-N and bending B-N-B vibrations respectively, and the c-BN band appears around 1100 cm<sup>-1</sup> and shift to higher frequencies as the carbon content increases [133,134,135,137, 141,176,177].

However, the interpretation of the spectrum for the absorptions different from B-N bonding is delicate. There are many other infrared active bonds in the B-C-N system and the wavelength positions of these bonds found in the literature demonstrate a relatively dispersive nature. Figure 4.59 shows the spectrum of three samples deposited with varying N<sub>2</sub> content in the process gas.

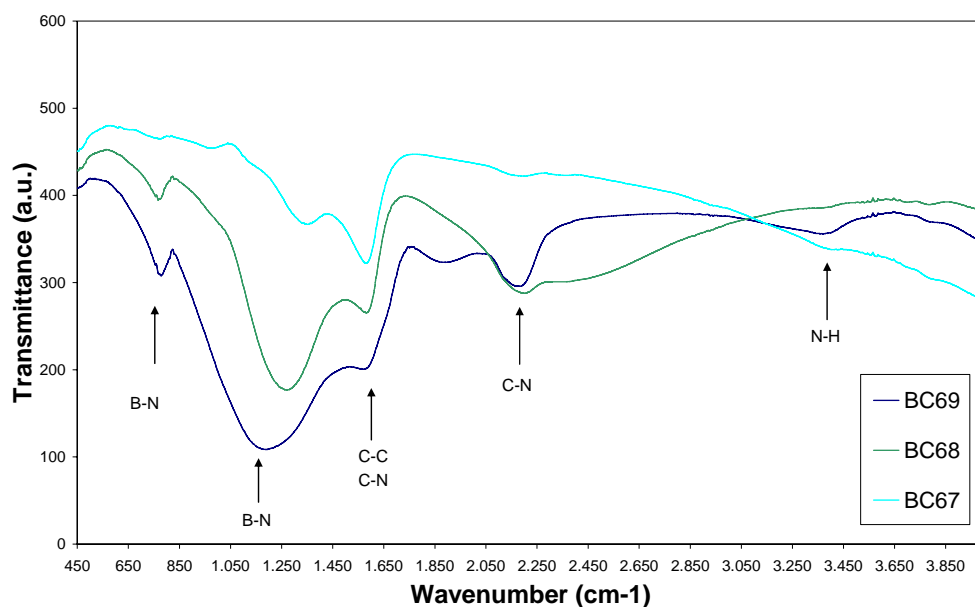


**Figure 4.59:** FTIR spectrum of BCN coatings deposited with different N<sub>2</sub> contents.

The spectrum was interpreted according to the literature in the coming way; the absorptions around 780 and 1380 cm<sup>-1</sup> are evidence of the h-BN structures that can be clearly seen from BC67 spectra. Especially the peak about 800 cm<sup>-1</sup> which was detected for all three specimens is a clear evidence of the formation of B-N bonds and in our case it becomes stronger with the increase of the N amount incorporated into the composition. Absorption peak around 1600 cm<sup>-1</sup> is attributed to C=N or C=C bonds in the literature [134,176]. According to the spectrum, as the absorption peak at this wavelength is sharper for the specimen which contains minimum nitrogen and became less sharper with increasing nitrogen and decreasing carbon content, this peak is thought to be an evidence of the C=C bonds. With the increase of the N content, a shift to the lower wavelengths for the absorption peak around 1380 cm<sup>-1</sup> was observed. From the literature it is known that there is an absorption peak at 1130 cm<sup>-1</sup> which represents wurtzite-BN (w-BN) structure [133,137]. Hence, it is believed that, the shift to the lower wavelength with the increase of the N content is an evidence of the hexagonal-wurtzite transformation for the coatings deposited with

high nitrogen content. The absorption band at  $\sim 2200\text{ cm}^{-1}$  is attributed to  $\text{C}\equiv\text{N}$  bonds and the band at  $3400\text{ cm}^{-1}$  to N-H bonds [134,141,176]. It can be seen from the figure that with the increase of N content these two peaks became sharper.

As a result, it is concluded that, there is no evidence for the presence of  $\text{sp}^2$  bonded c-BN for which the absorption band is situated at approximately  $1080\text{ cm}^{-1}$ . It is believed that the structure obtained was a mixture of h-BN and w-BN with C-C, C-N and N-H bonds for BCN coatings deposited with increasing N contents.

#### 4.3.5 Tribological studies

Tribological studies were conducted on BCN coatings deposited with different N contents to determine the friction and wear properties of the coatings.  $\text{Al}_2\text{O}_3$  counterfaces and test parameters optimized in the Section 4.1.3.6 were used for “pin-on-disc” testing of BCN coatings. At least 4 tests were realized with each configuration and the mean value is presented as wear rate. First, a wear track diameter of 6 mm was chosen for a total sliding distance of 300 m.

Figure 4.60 shows friction coefficient vs. distance diagram for the specimen BC67. The friction coefficient presents a different characteristic compared to the boron carbide coatings deposited without nitrogen incorporation. Starting from low values,  $\sim 0.2$ , while the two bodies were first in contact, the friction coefficient value increased gradually to  $\sim 0.7$  where it stabilized.

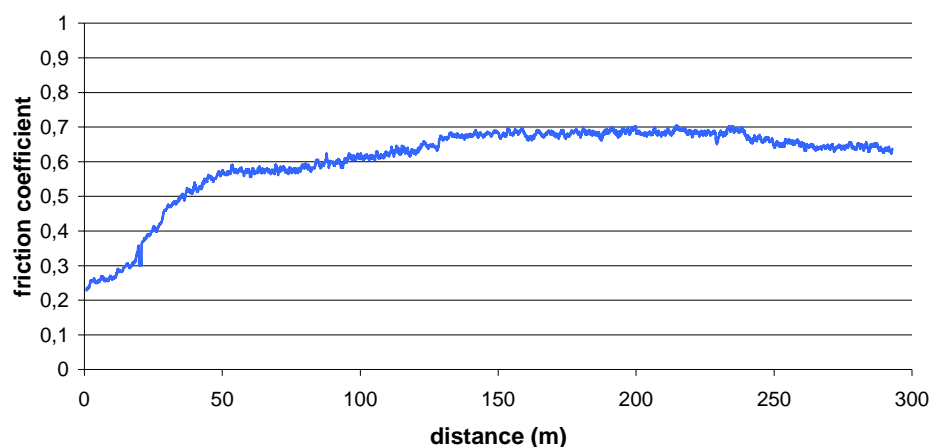


**Figure 4.60:** Friction coefficient versus distance diagram of the specimen BC67.

According to the profilometer measurements on worn surface given in Table 4.8 and wear track profile given in Figure 4.61, the substrate was not reached after 300 m sliding distance.

**Table 4.8:** Profilometer measurement of wear track on BC67 after 300 m.

| Wear track depth ( $\mu\text{m}$ ) | Wear track width ( $\mu\text{m}$ ) |
|------------------------------------|------------------------------------|
| 0.148                              | 0.117                              |
| 0.200                              | 0.112                              |
| 0.149                              | 0.116                              |

To compare the tribological properties of BCN films deposited, although the coating was not worn after 300 m sliding distance, 100 m sliding distance was selected for three BCN films with three different amount of nitrogen into their compositions. BCN films presented the same evaluation of friction coefficient during 100 m sliding. However, wear rates measured were quite different, about  $1.2 \times 10^{-9} \text{ mm}^3/\text{Nm}$  for BCN coating deposited with the presence of 5%  $\text{N}_2$  in the processing gas, about  $9 \times 10^{-10} \text{ mm}^3/\text{Nm}$  for 25%  $\text{N}_2$  and  $7.8 \times 10^{-10} \text{ mm}^3/\text{Nm}$  for 50%  $\text{N}_2$ .

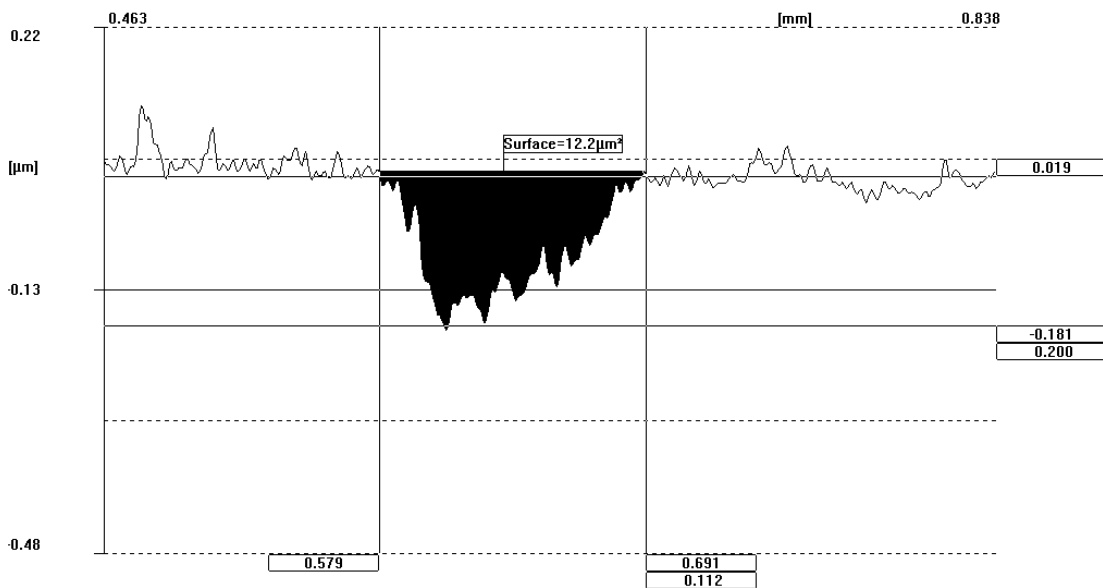


**Figure 4.61:** Wear track measurements of BCN coating after 300 m sliding.

Thus, wear rates of almost 20-40 times better than  $\text{B}_4\text{C}$  coatings deposited by plasma-enhanced configuration were found for BCN films. It is believed that, while the hardness decreased, toughness of the BCN films was increased. Also as a result of more relaxed phases obtained such as h-BN, wear rates better than boron carbide films were obtained.

### 4.3.6 SIMS elemental depth profiles

The elemental depth profiles of BCN films were analyzed with the same procedure described in Section 4.1.2.7 by using  $O_2^+$  primary ion beam. Only BCN films deposited at 5%  $N_2$  in the processing gas will be presented. It is observed that increasing N content in the film compositions increased also their electrical resistivity. Thus for films deposited at 25% and 50%  $N_2$ , charging problems occurred particularly at the beginning of the analyses during first ion-material interactions. Figure 4.62 shows elemental depth profile of BCN film deposited on steel substrate. It can be observed from the figure that the elemental film distribution was constant over the film thickness.

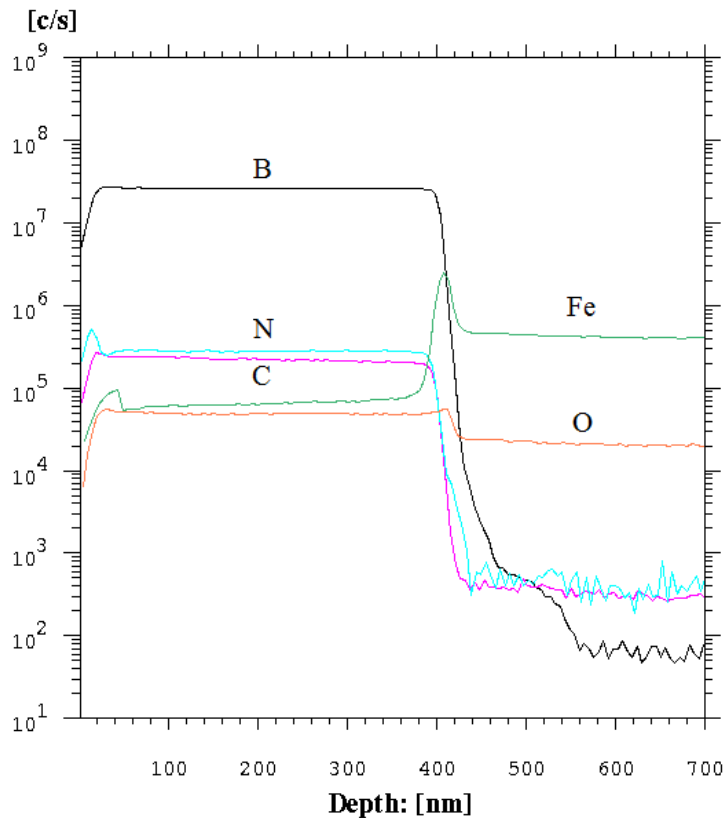


**Figure 4.62:** SIMS elemental depth profile of BCN film deposited at 5%  $N_2$  in the processing gas.

For SIMS data given in the figure, the x-axis was converted from time to depth by measuring the crater depths obtained during analyses by a profilometer. The thicknesses were in good agreement with SEM observations with a maximum deviation of 5%.

#### 4.3.7 Conclusion

Boron carbonitride films with N incorporation into boron carbide structure were also studied. Microstructural studies revealed the columnar structure of BCN film deposited in presence of 5% N<sub>2</sub> in the process gas. At 25% N<sub>2</sub>, the coating microstructure changed to a uniform granular structure and at 50% N<sub>2</sub> to a non-uniform coarse granular structure. Chemical composition of the films deposited was drastically influenced by different amount of N<sub>2</sub> in the processing gas. At 5% N<sub>2</sub>, 30.13 at.% N incorporated in the coating structure and increased to 76.23 at.%, for an increase of N<sub>2</sub> to 50 % in the processing gas. Boron percentage decreased from ~ 78 at.% to 51.23 % at 5% N<sub>2</sub> in the gas and to 28.69 % for an increase of N<sub>2</sub> from 5% to 25 %. For 50% N<sub>2</sub> in the process gas, 15.68 % B was detected in the boron carbonitride film structure. The same tendency of decrease with the increase of reactive gas flow was also observed for carbon, it decreased from ~ 21 at.% for boron carbide thin films to 6.76 % for 50% N<sub>2</sub> in the processing gas environment. Nanomechanical characterizations further revealed the effect of N incorporation. The boron carbonitride coating deposited with 5% N<sub>2</sub> in the deposition gas had 20 GPa hardness. At 25% N<sub>2</sub> it decreased to 14 GPa and at 50% N<sub>2</sub> to 10 GPa. The Young's modulus values of the coatings showed also the same tendency to decrease with increasing N<sub>2</sub> in the processing gas, from 180 GPa for 5% N<sub>2</sub> to 155 GPa at 25% N<sub>2</sub> and finally at 50% N<sub>2</sub> it reached its minimum with 135 GPa. Friction coefficients measured for BCN films were about 0.7. Thus it can not be concluded a lubricity for BCN films deposited in the test configurations used. However, wear rates measured were about  $1.5 \times 10^{-9}$  mm<sup>3</sup>/Nm for these coatings. Thus almost 20 times better than B<sub>4</sub>C coatings deposited by plasma-enhanced configuration. It is believed that, while the hardness decreased, toughness of the BCN films was increased. Also as a result of more relaxed phases obtained such as h-BN, wear rates better than boron carbide films were obtained. SIMS analyses realized on BCN films demonstrated the elemental film distribution was constant over the film thickness. Charging problems at the beginning of analyses that was observed more importantly with the increase in N content of the coatings demonstrated that the nitrogen incorporation increased the electrical resistance of BCN films deposited.

#### 4.4 Functionally Graded B<sub>4</sub>C and BCN Thin Films

Despite its good properties and potential applications, boron carbide and boron carbonitride films have found to suffer from delamination when the thickness of the coatings exceeded 500 nm as explained in the Sections 3.1.4.4 and 4.1.1. These can be explained by the high level of internal stresses generated in these films and the mismatch of the substrate mechanical properties with remarkably high hardness and modulus of the boron carbide and BCN films deposited. Functionally graded multilayered coatings, where neighboring layers share at least one common component, are one means to alleviate this problem and provide much improved adhesion as explained in the Section 3.1.4.5. Three functionally graded multilayer design; boride layers/B<sub>4</sub>C on AISI 430 substrate, Ti/TiC/B<sub>4</sub>C and Ti/TiN/BCN on AISI M2 and Si substrates are used to deposit thick and adherent boron carbide and BCN top layers and will be discussed in the following part.

##### 4.4.1 Microstructural studies

Microstructural examinations of the films deposited on Si and boronized steel substrates were observed on their cross-sections. For all the samples, secondary electron images were taken at a 10° tilt angle to observe the coating microstructure and the surface morphology together. For detailed topographical analysis of the coatings deposited, backscattered electron images were also taken. Figure 4.63 shows secondary and backscattered electron images of boron carbide thin film and boride layers on steel substrate.

As can be seen from Figure 4.63 (a) boron carbide coating on boride layer is well adherent and has approximately 1.1 μm thickness. Boride underlayer has 12 μm thicknesses. This sample was prepared by two different techniques for SEM observation; for secondary electron image the sample was embrittled in liquid nitrogen and the pictures were taken from the fractured cross-section. For back scattered electron image, the sample was cut, enrobed and mirror-polished, to observe in details the thick boride underlayer. In Figure 4.63 (b), to reveal in details the microstructure of boride underlayers, the contrast for backscattered electron image was increased, hence, the top B<sub>4</sub>C layer was not observable.

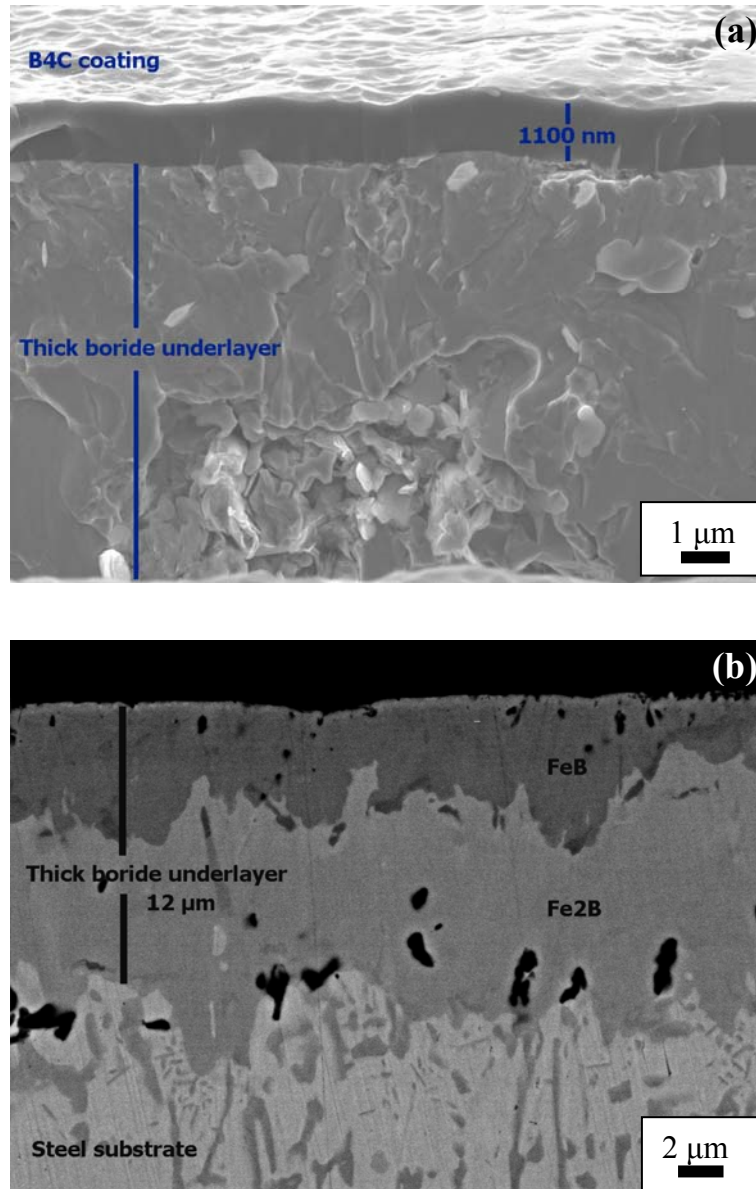


**Figure 4.63:** Cross-sectional SEM micrographs of (a) secondary electron image (b) back scattered image of boron carbide thin film on boronized steel substrate.

It can be seen from the figure that, a double phase boride layer was formed on AISI 430 substrate. The near substrate phase is  $\text{Fe}_2\text{B}$ .  $\text{FeB}$  phase which can be clearly distinguished thanks to a darker coloration stay between  $\text{Fe}_2\text{B}$  and top  $\text{B}_4\text{C}$  layer deposited by plasma-enhanced DC magnetron sputtering. Some voids were also detected at the boride layer-substrate interface. Figure 4.64 shows the microstructure of functionally graded  $\text{Ti}/\text{TiC}/\text{B}_4\text{C}$  thin film.

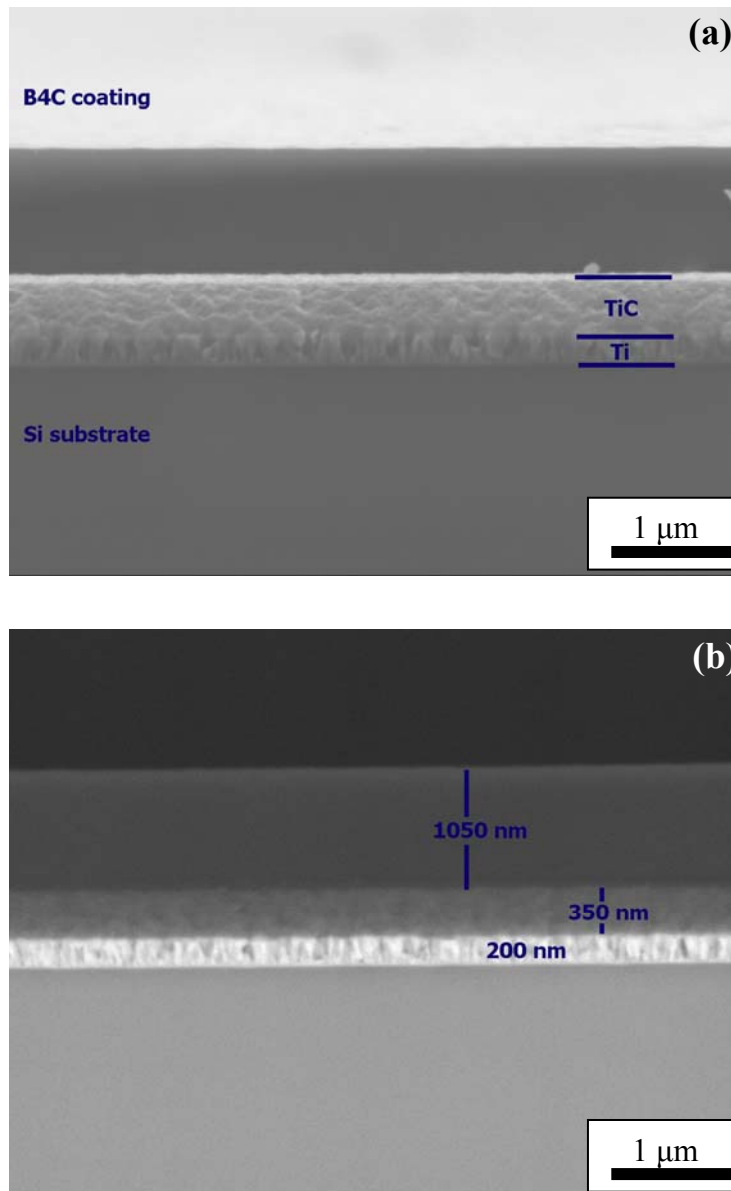


**Figure 4.64:** Cross-sectional SEM micrographs of (a) secondary electron image (b) back scattered image of Ti/TiC/B<sub>4</sub>C graded film on Si substrate.

In this design, pre-deposited Ti had columnar microstructure while TiC underlayer and 1 μm thick boron carbide top layer had non-columnar morphologies. Figure 4.65 demonstrates the graded structure of Ti/TiN/BCN thin film deposited on Si substrate observed from fractured cross-section. From the figure (a) and (b), the columnar structure of Ti and TiN underlayers with 250 and 100 nm thicknesses and well adherent columnar BCN film of 1,2 μm thick can be clearly seen.

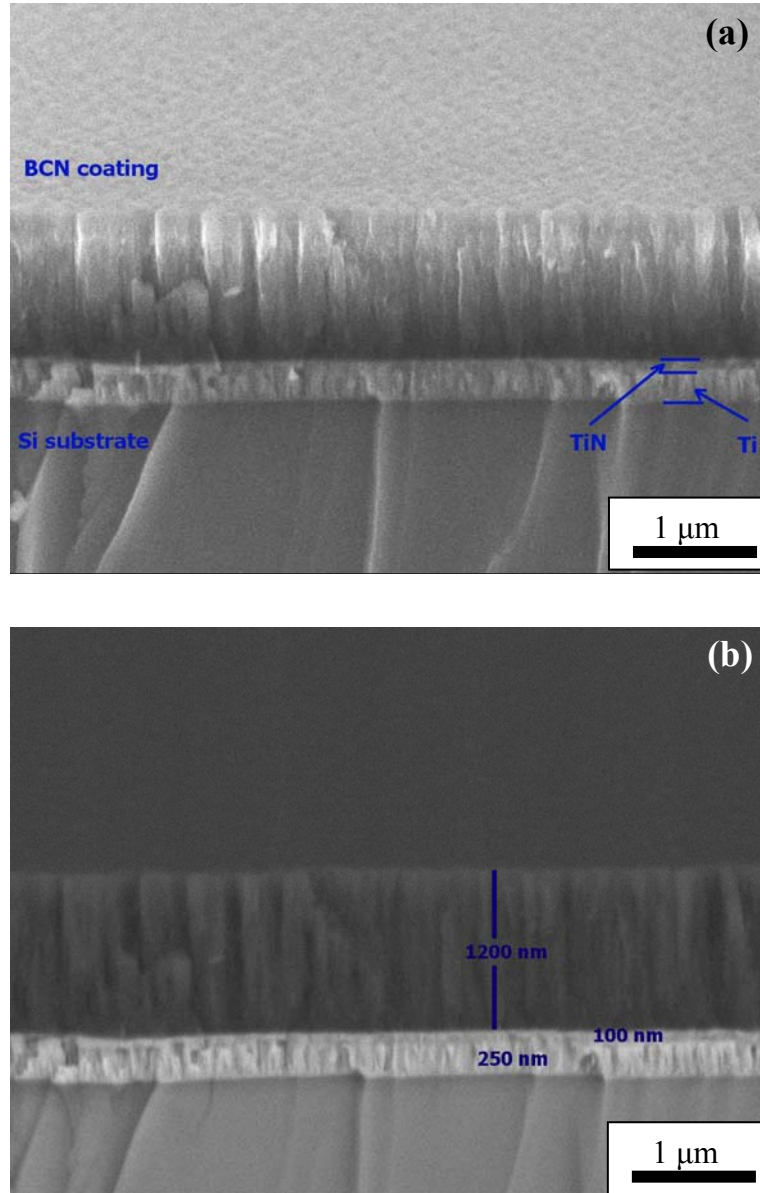


**Figure 4.65:** Cross-section SEM micrographs of (a) secondary electron image (b) back scattered image of Ti/TiN/BCN graded film on Si substrate.

#### 4.4.2 Elemental depth profile analyses

Secondary ion mass spectrometer analyses were carried out for all the samples to verify the functionally graded structures by elemental depth profiling of the major elements which constitutes the graded structure. From Figure 4.66, it can be seen that the functionally graded structure was successfully formed for all three samples.

A surface effect was observed at the beginning of the analysis for Ti/TiN/BCN structure, which is believed, due to poor conducting properties of the topmost BCN layer coupled with surface contamination. The high intensity of titanium detected in

the top B<sub>4</sub>C and BCN layers was mainly because of the high positive secondary ion yields of Ti<sup>+</sup> compared to C<sup>+</sup> while using O<sub>2</sub><sup>+</sup> as primary ion beam and secondly because of the interferences between C<sup>+</sup> and Ti<sup>+</sup> ions.

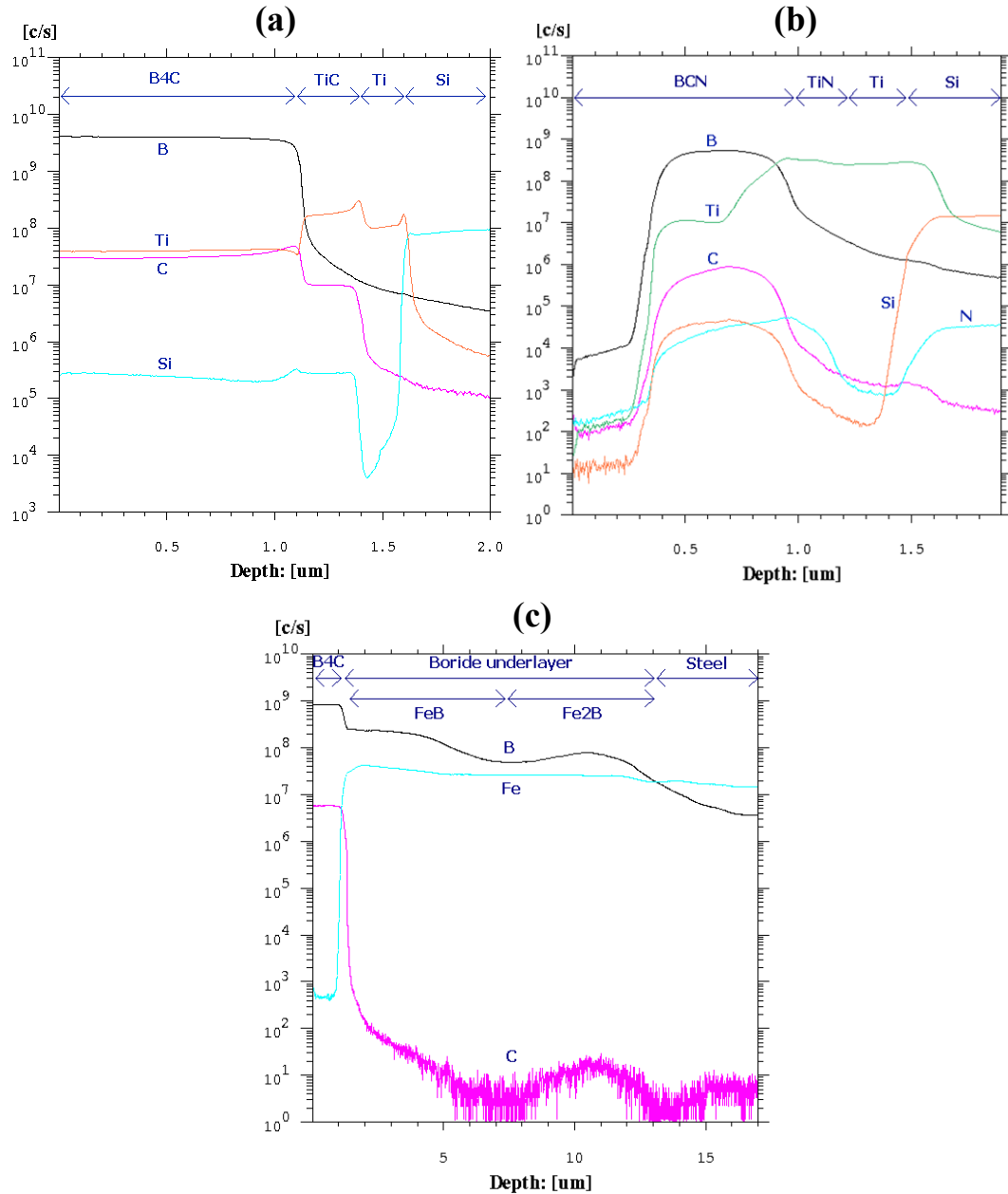


**Figure 4.66:** SIMS depth profiles of (a) Ti/TiC/B<sub>4</sub>C (b) Ti/TiN/BCN (c) Boride layer/B<sub>4</sub>C functionally graded structures.

This approach was also verified by the results of EPMA analyses which detected no Ti in the top layer elemental composition. For SIMS data, the x-axis was converted from time to depth by measuring the depth of the craters obtained during analyses by a profilometer. The layer thicknesses were in good agreement with SEM observations with a maximum deviation of 10%.

### 4.4.3 Nanomechanical properties

A series of nanoindentation measurements with variable maximum applied loads between 500–5000  $\mu\text{N}$  were realized on the coatings. This resulted with a maximum penetration depth between 20–200 nm. The results which demonstrated no tip rounding effect (for lower loads) and no substrate effects (for higher loads) were taken into consideration. Figure 4.67 demonstrates the hardness values and the Young's modulus of the substrates and layers accompanied by elemental compositions measured by EPMA.

| Material         | H (GPa) | E (GPa) | Composition (wt%)             |
|------------------|---------|---------|-------------------------------|
| B <sub>4</sub> C | 38±2    | 300±10  | 78 B-21,5 C-0,2 O-0,3 Si      |
| TiC              | 18±2    | 176±10  | 60,2 Ti-37,8 C-2 O            |
| Ti               | 8±0,6   | 163±5   | 98,8 Ti-1,2 O                 |
| AISI M2          | 7,5±0,2 | 220±17  | 0,9 C-4,1 Cr-5 Mo-1,9V-6,4W * |

| Material | H (GPa) | E (GPa) | Composition (wt%)             |
|----------|---------|---------|-------------------------------|
| BCN      | 20±2    | 193±10  | 37,2B-14,7C-47,9N-0,2O        |
| TiN      | 20±1    | 190±10  | 62,5 Ti-36,4 N-1,1 O          |
| Ti       | 8±0,6   | 163±5   | 98,8 Ti-1,2 O                 |
| AISI M2  | 7,5±0,2 | 220±17  | 0,9 C-4,1 Cr-5 Mo-1,9V-6,4W * |

| Material          | H (GPa) | E (GPa) | Composition (wt%)              |
|-------------------|---------|---------|--------------------------------|
| B <sub>4</sub> C  | 38±2    | 300±10  | 78 B-21,5 C-0,2 O-0,3 Si       |
| FeB               | 20±0,6  | 226±6   | 26,8 B-1,6 C-4 O-8 N *         |
| Fe <sub>2</sub> B | 16±0,5  | 198±10  | 13,8 B-2,2 C-2,4 O- 10,8 N *   |
| AISI 430          | 1,8±0,1 | 220±10  | 16 Cr-0,04 C-0,34 Si-0,38 Ni * |

\* Fe is the balance

**Figure 4.67:** Hardness, Young's modulus and elemental compositions of the substrates and layers.

### 4.4.4 Conclusion

FE-SEM observations and SIMS depth profile analyses revealed that Ti/TiC and Ti/TiN graded underlayers on AISI M2 and Si (100) substrates were successfully formed by plasma-enhanced DC magnetron sputtering and boride underlayer by surface boronizing on AISI 430 steel substrates. Well adherent BCN and Boron carbide top layers with thicknesses over 1  $\mu\text{m}$  were grown onto the underlayers by means of the functionally graded multilayered structures. Nanoindentation measurements revealed the graded transition of the hardness and Young's modulus values between different layers.

## 4.5 Résumé du Chapitre

Dans ce chapitre, les résultats obtenus par différentes techniques de caractérisation sont présentés et discutés dans des sous-chapitres pour chaque type de couche mince déposée.

Une série de couches de carbure de bore a été déposée par pulvérisation cathodique magnétron classique à courant continu sans chauffage externe (50 °C), sous une tension de polarisation comprise entre 0 et 200 V. Les couches déposées sans tension de polarisation présentaient des structures colonnaires. Avec l'augmentation de la tension de polarisation de 0 à 200 V, une transition de structure colonnaire à une structure plus dense bien qu'encore colonnaire avec des colonnes moins séparées a été observée. Des observations MET à haute résolution accompagnées d'analyses cartographique des éléments (EFTEM) ont montré que les épaisseurs de colonnes étaient d'environ 20-25 nm et que de l'oxygène de l'enceinte de dépôt et/ou de l'air ambiant avait été incorporé sous forme de nanovides de 2-3 nm de diamètre entre les colonnes. Toutes les couches déposées par pulvérisation cathodique magnétron classique à courant continu observées étaient amorphes comme l'ont montré l'imagerie à haute résolution par MET, les spectres FFT et/ou les diagrammes de diffraction. Des duretés de l'ordre de 20-22 GPa et des modules de 220 GPa ont été mesurés par nanoindentation pour toutes les couches minces de carbure de bore déposées par pulvérisation cathodique magnétron classique. Il n'y avait aucun effet significatif des tensions de polarisation appliquées sur la dureté des films de carbure de bore. Des coefficients de frottement, pour ces couches, de l'ordre de 0,7 et des taux d'usure de l'ordre de  $5,0 \times 10^{-8} \text{ mm}^3/\text{Nm}$  ont été déterminés avec antagoniste de alumine. Les valeurs de coefficient de frottement et les taux d'usure étaient insensibles aux paramètres de dépôt.

Une autre série de couches de carbure de bore a été déposée par pulvérisation cathodique magnétron à courant continu assisté par plasma à des températures entre 50 °C (sans chauffage) et 250 °C et sous tension de polarisation entre 0 et 250 V. On a observé des microstructures non colonnaires avec des surfaces lisses pour toutes les combinaisons de paramètres de dépôt, même pour les films déposés sans chauffage et sans polarisation. Grâce à des mesures de nanoindentation, une augmentation de la

dureté et du module des couches a été mise en évidence avec l'augmentation de la tension de polarisation et de la température de dépôt. La dureté des couches déposées avec différentes combinaisons de tensions de polarisation et de la température était environ 30-35 GPa. Une valeur de dureté de l'ordre de 40 GPa a été obtenue pour la couche déposée à 250 °C et une polarisation de 100 V, qui est la couche la plus dure déposée dans cette étude. Les modules d'Young des couches de carbure de bore déposés en configuration assisté par plasma se situaient entre 270 et 300 GPa. Les observations par MET ont prouvé que les couches de B<sub>4</sub>C déposées dans cette même configuration étaient complètement amorphes dans toute la gamme des paramètres de dépôt. Des observations à haute résolution, ont montré qu'il existait une couche de transition composées de 4-5 couches atomiques (1-1,5 nm) avec une structure cristallographique juste à l'interface couche-substrat. Au-delà, la couche devient rapidement amorphe. Les études tribologiques ont montré que les couches de carbure de bore ne donnaient pas de coefficient de frottement bas sur différents antagonistes. Des coefficients de frottement de l'ordre de 0,6 ont été trouvés pour un antagoniste Al<sub>2</sub>O<sub>3</sub>, quelle que soit la couche déposée en configuration assisté par plasma. Cependant, des faibles taux d'usure entre 2,6 – 3,5 x 10<sup>-8</sup> mm<sup>3</sup>/Nm, soit d'environ deux fois meilleurs ont été obtenus pour des couches de carbure de bore déposées par pulvérisation cathodique magnétron assisté par plasma, comparé aux couches de carbure de bore pulvérisés par pulvérisation cathodique magnétron classique. Les valeurs de coefficient de frottement et les taux d'usure étaient indépendants des paramètres de dépôt.

Les compositions chimiques des couches de carbure de bore déposées par pulvérisation cathodique magnétron avec ou sans plasma auxiliaire mesurées par la microsonde de Castaing (EPMA) étaient les mêmes avec le carbure de bore cible et étaient presque stœchiométrique avec environ 78% B, 21,4% C, 0,3% O et 0,3% Si. La composition chimique des dépôts était indépendant des paramètres de dépôt.

Des couches de carbure de bore ont été également déposées par pulvérisation cathodique radiofréquence (RF) en utilisant une cible commerciale de B<sub>4</sub>C à une puissance entre 80 et 140 W. Les études microstructurales ont montré la croissance non colonnaire de ces couches. Les compositions chimiques mesurées étaient d'environ 76% B, 23,2% C, 0,5% Si, 0,3% O. Les caractérisations nanomécaniques ont indiqué que les couches présentaient une dureté de l'ordre de 22 GPa et un

module de ~240 GPa. Des coefficients de frottement de l'ordre de 0,4 ont été obtenus au lieu de valeurs élevées de l'ordre de 1 obtenues au début des essais « pion-disque » pour des couches déposées par pulvérisation magnétron DC. Le coefficient de frottement atteignait un niveau stable autour de 0,5 jusqu'à ce que les couches fussent complètement usées.

Des couches de carbonitride de bore avec incorporation d'azote dans la structure de carbure de bore ont été également étudiées. Les études microstructurales ont mis en évidence la structure colonnaire des couches BCN déposées en présence de 5% N<sub>2</sub> dans le gaz plasmagène. La composition chimique des couches déposées a été notablement influencée par addition de différentes quantités de N<sub>2</sub> dans le gaz plasmagène. Pour 5% N<sub>2</sub> dans le gaz, 30 at.% N étaient présents dans la structure des couches. La concentration en azote incorporée augmentait jusqu'à 76 at.%, pour une augmentation de 50% N<sub>2</sub> dans le gaz. Les caractérisations nanomécaniques ont bien démontré l'effet de l'incorporation d'azote dans la composition des couches BCN. Le carbonitride de bore déposé en présence de 5% N<sub>2</sub> dans le gaz présentait une dureté de l'ordre de 20 GPa. En présence de 25% N<sub>2</sub>, la dureté des couches BCN obtenues a diminué jusqu'à 14 GPa et en présence de 50% N<sub>2</sub>, jusqu'à 10 GPa. Les valeurs de module d'Young des couches ont montré la même tendance à la diminution avec l'augmentation du pourcentage d'azote dans le gaz plasmagène. Les modules d'Young obtenues étaient de l'ordre de 180 GPa pour 5% N<sub>2</sub> dans le gaz. Ils ont diminué jusqu'à 155 GPa pour 25% N<sub>2</sub>. Finalement, en présence de 50% N<sub>2</sub>, les valeurs minimums de l'ordre de 135 GPa ont été obtenues. Des coefficients de frottement de l'ordre de 0,7 ont été trouvés pour les couches BCN déposées, avec antagoniste en alumine. Les taux d'usures mesurés pour les couches BCN déposées avec différents pourcentages d'azote dans le gaz plasmagène étaient comprises entre  $1,2 \times 10^{-9} - 7,8 \times 10^{-10} \text{ mm}^3/\text{Nm}$ . Ainsi, les taux d'usure presque 20-40 fois meilleurs pour des couches B<sub>4</sub>C déposées en configuration assisté par plasma ont été trouvés pour des couches BCN.

Des observations par microscopie électronique à balayage haute résolution (FE-SEM) et des profils en profondeur par spectrométrie de masse d'ions secondaires (SIMS) ont conclu que les sous-couches de Ti/TiC et Ti/TiN sur les substrats AISI M2 et Si (100) avaient été efficacement déposées par pulvérisation cathodique magnétron DC assisté par plasma et des sous-couches de borures obtenues sur les

substrats AISI 430 par boronisation. Des mesures de nanoindentation ont mis en évidence la transition graduelle des valeurs de dureté et de module d'Young entre les différentes couches. Des couches de BCN et de carbure de bore bien adhérentes avec des épaisseurs supérieures à 1  $\mu\text{m}$  ont été déposées sur les sous-couches.



---

**CHAPTER 5:**

**GENERAL CONCLUSIONS  
AND RECOMMENDATIONS**

---



## 5. GENERAL CONCLUSIONS AND RECOMMENDATIONS

In this thesis study, single and multilayered boron carbide and boron carbonitride thin films deposited with several sputtering configurations were investigated. Three types of well adherent and homogenous boron carbide films were deposited by conventional DC magnetron sputtering, plasma-enhanced DC magnetron sputtering and RF sputtering. Boron carbonitride thin films deposited by reactive DC magnetron sputtering in addition of nitrogen into processing gas were also studied. Functionally graded multilayered designs were used to grow thicker boron carbide and boron carbonitride films. Various characterization techniques were used in order to elucidate different growth structures and the properties of different films obtained. Following conclusions were drawn from this study;

A DC compatible conducting boron carbide target was hot-pressed from boron carbide source powders. The target chemical composition measured by EPMA was the same with the source powders and both were nearly stoichiometric boron carbide with about 78% B, 21.4% C, 0.3% O and 0.3% Si. It is believed that, the electrical conductivity of boron carbide target produced, originates from 99% of theoretical density achieved with sintering conditions used.

The chemical composition of DC magnetron sputter deposited boron carbide films with or without auxiliary plasma configuration, measured by EPMA was the same with the target material. For RF deposited boron carbide films, a composition of 76% B, 23% C, 0.6% O and 0.4% Si was obtained which is believed the composition of commercial B<sub>4</sub>C target used for RF deposition. In all the cases, there was no significant effect of deposition parameters on the elemental compositions of boron carbide films.

During preliminary DC magnetron sputtering experiments of boron carbide, coarse columnar structures with cauliflower-like surface morphologies were obtained for boron carbide films deposited at  $3 \times 10^{-3}$  Pa base pressure and 2 Pa deposition pressure. Adhesion problems with the increase in coating thickness were observed

for these films due to the generation of internal stresses. Well adherent boron carbide films were deposited on AISI 430, AISI M2, and Si (100) substrates when the thicknesses were limited to 350-400 nm, the base pressure about  $10^{-5}$  Pa and working pressure to 0.3 Pa.

When deposited by conventional DC magnetron sputtering without any external heating, and at floating potential, boron carbide coatings had columnar structures although denser with smoother surfaces morphologies compared to boron carbide coatings deposited at higher pressure. With the increase in bias voltages from floating to 200 V, a transition from columnar zone 1 type structure to denser zone T type structure with less pronounced columnar morphology and less separated columns were observed. Nanostructural observations by TEM further revealed the columnar structure of conventional magnetron sputtered boron carbide coatings. Column thicknesses were about 20-25 nm and nanovoids present at the column boundaries were about 2-3 nm according to high-resolution TEM observations and EFTEM elemental mapping results. EFTEM analyses also demonstrated that oxygen from the deposition chamber and/or from ambient air were incorporated into the nanovoids between the columns. All observed conventional DC magnetron sputtered B<sub>4</sub>C films were amorphous according to high-resolution imaging and consequent FFT and/or diffraction patterns.

Nanomechanical studies realized on boron carbide films deposited by conventional DC magnetron sputtering on three different substrates revealed the effect of the substrates on the mechanical properties. Substrate effect was observed particularly for the films deposited on AISI 430 steel, which is the softer and mechanically poorer substrate. No substrate effect was observed for coatings deposited on AISI M2 and Si substrates. When analyzed solely, without the effect of the substrates, no changes in the hardness and modulus were observed with the increase in bias voltages for boron carbide films deposited without auxiliary plasma configuration. It is concluded that the ion bombardment without intense plasma around the substrate, although demonstrated an effect of densification on the microstructures, was not sufficient to affect the hardness and modulus of the coatings obtained. About 20-22 GPa hardness and 220 GPa modulus with 70% of elastic recovery after unloading were measured for all boron carbide coatings deposited by conventional DC magnetron sputtering.

Boron carbide films deposited by plasma-enhanced DC magnetron sputtering had featureless, non-columnar structures with smooth surface morphologies for all the deposition parameters combinations, even for the films deposited at floating potential without any external heating. Ion bombardment caused the complete suppression of columnar growth and increased the density of boron carbide films by forward sputtering, atomic rearrangement and increased adatom surface diffusion by localized high temperatures. Detailed SEM investigations of the same coating deposited on three different substrates demonstrated that, the growth morphologies of boron carbide films were not influenced by the types and properties of the substrates. Especially, it is observed that surface roughness of the substrates which is an important parameter affecting the growth morphologies, had not an influence on the properties of thin films deposited, for the roughness interval used in this study.

Substrate effect was also observed during nanoindentation of plasma-enhanced DC magnetron sputtered boron carbide films deposited on AISI 430 steel and no effect was found for the films deposited on AISI M2 and Si substrates for the load intervals used in this study. When analyzed solely, an increase in the hardness and modulus of the coatings with the increase in the bias voltages and deposition temperatures were found. It is concluded that coupled effect of the bombardment and temperature was the reason for different hardness and modulus values obtained. The effect of the ion bombardment was remarkably higher than the effect the deposition temperatures. The hardness of the coatings deposited with different bias voltages and temperature combinations was about 30-35 GPa. A hardness value of  $\sim 40$  GPa was obtained for the coating deposited at 250 °C with 100 V bias voltage, which is the hardest coating deposited in this study. Thus, there was a factor of about 1.5 to 2 between the hardness values of boron carbide coatings deposited with and without auxiliary plasma configuration. Indentation moduli of boron carbide coatings followed the same trend with the hardness values and were between 270 and 300 GPa. The elastic recovery of plasma-enhanced magnetron sputter deposited boron carbide films was about 75% for the majority of the films. More than 80% of elastic recovery was observed for the hardest boron carbide film, thus, a high elastic recovery behavior of boron carbide films can be deduced from these results.

TEM observations on selected specimens showed that B<sub>4</sub>C films deposited by plasma-enhanced DC magnetron sputtering were completely amorphous in the total

range of process parameters. From high-resolution observations, it is evident that there is a transition layer of 4-5 atomic layers, which correspond to 1-1.5 nm with crystallographic order just at the coating-substrate interface and then the coating becomes quickly amorphous. According to high-resolution TEM images and diffraction patterns, no evidence of a nanocrystalline phase was found. Therefore, it is believed that, the hardening mechanism as a result of the coupled effect of deposition temperature and ion bombardment was directly related to the change in the microstructures and to the densification of the coatings.

Tribological studies demonstrated that DC magnetron sputtered boron carbide coatings do not give low friction coefficients against different counterfaces. Friction coefficients of about 0.7 and 0.6 were found against  $\text{Al}_2\text{O}_3$  for the coatings deposited without and with auxiliary plasma configuration respectively. However, good wear rate values of about  $5 \times 10^{-8} \text{ mm}^3/\text{Nm}$  and  $2.6 - 3.5 \times 10^{-8} \text{ mm}^3/\text{Nm}$  were obtained for conventional DC magnetron sputtered and plasma-enhanced DC magnetron sputtered boron carbide films respectively. It is believed that the same factor of two between the wear rates and hardness values of two types of boron carbide coatings deposited with two different configurations is an evidence of hardness and strength dominated wear resistance of these films.

Microstructural studies realized on RF deposited boron carbide films demonstrated the non-columnar growth of these films. It is believed that, this suppressing of the columnar morphology without applying any bias voltages, is due to the relatively high neutral bombardment of the films during their growth because of the short target-substrate distance and/or the increase of the deposition temperatures during long deposition times during RF sputtering of boron carbide films.

Nanomechanical characterizations revealed that non-magnetron RF sputtered boron carbide coatings had  $\sim 22 \text{ GPa}$  hardness and  $\sim 240 \text{ GPa}$  Young's modulus and showed 70% of elastic recovery. Although there is no detailed information on the properties of commercial boron carbide target used for RF sputtering, the hardness values of conventional DC magnetron sputtered and RF sputtered boron carbide films were the same. It is thus believed that boron carbide deposition without process modifications results with hardness values about 20 GPa, and different configurations such as

extensive ion bombardment and/or very low pressure deposition is needed to deposit ultrahard (40 GPa and above) boron carbide thin films by PVD systems.

Tribological studies on RF deposited boron carbide thin films demonstrated a quite different characteristic especially for friction coefficient evolution. Lower friction coefficients compared to DC sputtered boron carbide films, about 0.4 were observed at the beginning of “pin-on-disc” tests instead high values about 1 obtained for DC magnetron sputtered films. Friction coefficients stabilized around 0.5. However, to reveal the reasons of this difference and wear mechanisms lying behind, more study has to be done as a future work.

Microstructural studies revealed the columnar structure of BCN film deposited in presence of 5% N<sub>2</sub> in the process gas. At 25% N<sub>2</sub>, the coating microstructure changed to a uniform granular structure and at 50% N<sub>2</sub> to a non-uniform coarse granular structure.

Chemical composition of the films deposited was drastically influenced by different amount of N<sub>2</sub> in the processing gas. At 5% N<sub>2</sub>, 30 at.% N incorporated in the coating structure and increased to 76 %, for an increase of N<sub>2</sub> to 50 % in the processing gas. Boron percentage decreased from ~ 78 at.% to 51 at.% at 5% N<sub>2</sub> in the gas and to 28 at.% for an increase in N<sub>2</sub> from 5% to 25%. For 50% N<sub>2</sub> in the process gas, 15 % B was detected in the boron carbonitride film structure. The same tendency of decrease with the increase in reactive gas flow was also observed for carbon, it decreased from ~ 21 at.% for boron carbide thin films to 6 at.% for 50% N<sub>2</sub> in the processing gas environment.

Nanomechanical characterizations further revealed the effect of N incorporation. Boron carbonitride coating deposited with 5% N<sub>2</sub> in the deposition gas had 20 GPa hardness. At 25% N<sub>2</sub> it decreased to 14 GPa and at 50% N<sub>2</sub> to 10 GPa. The Young's modulus values of the coatings showed also the same tendency to decrease with increasing N<sub>2</sub> in the processing gas, from 180 GPa for 5% N<sub>2</sub> to 155 GPa at 25% N<sub>2</sub> and finally at 50% N<sub>2</sub> it reached its minimum value with 135 GPa.

Friction coefficients measured for BCN films were about 0.7. Thus it can not be concluded a lubricity for BCN films deposited in the test configurations used. However, wear rates measured for BCN films were between  $1.2 \times 10^{-9}$  -  $7.8 \times 10^{-10}$

mm<sup>3</sup>/Nm. Thus, wear rates of almost 20-40 times lower than B<sub>4</sub>C coatings deposited by plasma-enhanced configuration were found. It is believed that, while the hardness decreased, toughness of the BCN films was increased. Also as a result of more relaxed phases obtained such as h-BN, wear rates better than boron carbide films were obtained.

To growth thicker boron carbide and boron carbonitride thin films, functionally graded multilayered designs were also studied. FE-SEM observations and SIMS depth profile analyses revealed that Ti/TiC and Ti/TiN graded underlayers on AISI M2 and Si (100) substrates were successfully formed by plasma-enhanced DC magnetron sputtering and boride underlayer by surface boronizing on AISI 430 steel substrate. Nanoindentation measurements showed the graded transition of the hardness and Young's modulus values between different layers. Well adherent BCN and boron carbide top layers with thicknesses over 1 μm were successfully grown onto the underlayers.

SIMS depth profile analyses revealed that the elemental film distributions were constant over the whole films thicknesses for all the series deposited. Thus, it is concluded that, for all sputter configurations used, resultant films were homogenous. Measured coatings thicknesses were in good agreement with SEM observations with maximum deviations of 5-10%.

Results demonstrated that boron carbide films are promising candidates for wear resistance and hardness related applications. With a controlled change of process parameters, different microstructures, thus films with different properties were obtained. With N incorporation into boron carbide structure, optimized hard and better wear-resistant films were achieved. This showed that application ranges for these coatings may be further expanded. Additionally, it was found that functionally-graded multilayered approach is an adequate solution to prevent film delamination and intrinsic stress related problems of hard and wear-resistant films. Thicker boron carbide and boron carbonitride films for several industrial applications could therefore be deposited easily with a proper design of different underlayers.

Followings are some recommendations for further studies:

- It is believed that the hardness mechanism for the films deposited by plasma-enhanced configuration is based on the generation of internal stresses as a result of the bombardment of the films during their growth with highly energetic ions. These stresses should be quantified as a future work to better understand the hardening mechanism.
- Modelization studies should be carried out to clarify the substrate effects observed during nanoindentation measurements.
- Nanotribological studies and especially nanoscratch tests can give a different perspective to elucidate wear mechanisms of boron carbide and boron carbonitride coatings with nanometer range thicknesses.
- Electrical properties of boron carbide and boron carbonitride films deposited by different sputtering configurations should be studied as these coatings are prominent candidates for electronical applications according to the literature.

## 5.1 Résumé du Chapitre

Les résultats ont démontré que les films de carbure de bore étaient des matériaux prometteurs pour des applications tribologiques qui nécessitent des duretés élevées. Grâce à la maîtrise des paramètres de pulvérisation, différentes microstructures, associées à différentes propriétés, ont été obtenues. Grâce à l'incorporation d'azote dans la structure de carbure de bore, des couches à dureté optimale et résistance à l'usure élevée ont été développées, donnant ainsi la possibilité d'élargir les gammes d'applications pour ces dépôts. On a aussi constaté que la conception en multicouche fonctionnelle permettait d'empêcher le décollement des couches et d'éviter des problèmes liés à des contraintes résiduelles pour les dépôts durs et résistants à l'usure. Des couches plus épaisses de carbure de bore et de carbonitride de bore pour plusieurs applications industrielles, peuvent donc être efficacement déposés avec une conception appropriée de différentes sous-couches.

## REFERENCES

- [1] **Grove, W.R.**, 1852: On the electro-chemical polarity of gases, *Philosophical Transactions of the Royal Society of London*, **142**, p. 87.
- [2] **Mattox, D.M.**, 2003: *Foundations of Vacuum Technology*, p. 2-18, Noyes/William Andrew Publishing, Norwich, NY, USA.
- [3] **Url**, <[http://physics.kenyon.edu/EarlyApparatus/Static\\_Electricity/Geissler\\_Tubes/Geissler\\_Tubes.html](http://physics.kenyon.edu/EarlyApparatus/Static_Electricity/Geissler_Tubes/Geissler_Tubes.html)>, accessed at 10.02.1008.
- [4] **Plücker, J.**, 1858: Observations on the electrical discharge through rarefied gases, *The London, Edinburgh and Dublin Philosophical Magazine*, **16**, p. 409.
- [5] **Crookes, W.**, 1880: On a fourth state of matter, *Proceedings of the Royal Society of London*, **30**, p. 469.
- [6] **Crookes, W.**, 1891: On electrical evaporation, *Scientific American Supplement*, Vol. **32**, no. 811, p. 12958.
- [7] **Wright, A.W.**, 1877: On the production of transparent metallic films by electrical discharge in exhausted tubes, *Am. J. Sci. Arts*, **12**, p. 49.
- [8] **Boxman, R.L., Goldsmith, S., Ben-Shalom, A., Kaplan, L., Arbilly, D., Gidalevich, E., Zhitomirsky, V., Ishaya, A., Keidar, M., Beilis, I.**, 1995: Filtered vacuum arc deposition of semiconductor thin films, *IEEE Transactions On Plasma Science*, Vol. **23**, no. 6, p. 939.
- [9] **Boxman, R.L.**, 2001: Early history of vacuum arc deposition, *IEEE Transactions On Plasma Science*, Vol. **29**, no. 5, p. 759.
- [10] **Url**, <<http://members.chello.nl/~h.dijkstra19/page6-2.html>>, accessed at 22.02.2008.
- [11] **Url**, <<http://members.chello.nl/~h.dijkstra19/page7-3.html>>, accessed at 22.02.2008.
- [12] **Edison, T.A.**, 1894: Art of plating one material on another, *U.S. Patent*, No: 526,147.
- [13] **Edison, T.A.**, 1892: Process of duplicating phonograms, *U.S. Patent*, No: 484,582.

- [14] **Edison, T.A.**, 1902: Process of coating phonograph records, *U.S. Patent*, No: 713,863.
- [15] **Simeon, F.**, 1920: Note on the production of mirrors by cathodic bombardment, in *On the Making of Reflecting Surfaces*, p. 26, the Imperial College of Science and Technology, Fleetway Press, Ltd., London.
- [16] **Wehner, G.K., Anderson, G.S.**, 1970: The nature of physical sputtering, in *Handbook of Thin Film Technology*, ch.3, p. 1-35, Eds. Maissel L.I., Glang, R., McGraw-Hill Book Co., USA.
- [17] **Thomson, J.J.**, 1913: *Rays of Positive Electricity and Their Application to Chemical Analyses*, p. 172-175, Longmans, Gren and Co., USA.
- [18] **Penning, F.M.**, 1939: Coating by cathode disintegration, *U.S. Patent*, No: 2,146,025.
- [19] **Thornton, J.A., Greene, J.E.**, 1994: Sputter deposition processes, in *Handbook Of Deposition Technologies For Films And Coatings*, p. 275-337, Ed. Bunshah, R.F., Noyes Publications, Park Ridge, New Jersey, USA.
- [20] **Aufderheide, B.E.**, 2006: Sputtered thin film coatings, in *Coatings Technology Handbook*, ch. 30, p. 1-10, Ed. Tracton, A.A., Taylor & Francis Group, Boca Raton, FL, USA.
- [21] **ASM Handbook**, 1994: *Volume 5: Surface Engineering*, p. 1605-1625, USA.
- [22] **Rossnagel, S.**, 2002: Sputtering and sputter deposition, in *Handbook of Thin-Film Deposition Processes And Techniques 2<sup>nd</sup> Edition*, p. 319-348, Ed. Seshan, K., Noyes Publications, William Andrew Publishing, Norwich, New York, USA.
- [23] **Harsha, K.S.S.**, 2006: *Principles of Physical Vapor Deposition of Thin Films*, p.552-618, 955, Elsevier Ltd. USA.
- [24] **Mattox, D.M.**, 1998: *Handbook of Physical Vapor Deposition (PVD) Processing*, p. 343-609, Noyes Publications, Park Ridge, New Jersey, USA.
- [25] **Roth, J.R.**, 2001: *Industrial Plasma Engineering Volume 2: Applications to Nonthermal Plasma Processing*, p. 20, IOP Publishing Ltd., London, UK.
- [26] **Oechsner, H., Gerhard, W.**, 1974: Mass spectroscopy of sputtered neutrals and its application for surface analysis, *Surf. Sci.* **44**, p. 480.

- [27] **Können, G.P., Tip, A., deVries, A.E.**, 1974: On the energy distribution of sputtered dimers, *Radiat. Eff.*, **21**, p. 269.
- [28] **Können, G.P., Tip, A., deVries, A.E.**, 1975: On the energy distribution of sputtered clusters, *Radiat. Eff.*, **26**, p. 23.
- [29] **Coburn, J.W., Taglauer, E., Kay, E.**, 1974: A Study of the neutral species rf sputtered from oxide targets *Japn. J. Appl. Phys. Suppl.*, **2**, p. 501.
- [30] **Comas, J., Cooper, C.B.**, 1967: Mass-spectrometric study of sputtering of single crystals of GaAs by low-energy Ar ions, *J. Appl. Phys.*, **38**, p. 2956.
- [31] **M. Szymonski, R.S. Bhattacharyya**, 1979: The sputtering of gallium arsenide at elevated temperatures, *Appl. Phys.*, vol. **20**, no. 3, p. 207.
- [32] **Richardt, A., Durand, A.M.**, 1994: *Le vide, Les couches Minces les Couches Dures*, p. 227-252, Editions in Fine, Paris, France.
- [33] **Penfold, A.S.**, 1989: Early days of magnetron sputtering, *Thin Solid Films*, **171**, p. 99.
- [34] **Url**, <<http://www.genco.com/tech/whatplasma.html>>, accessed at 11.12.2008
- [35] **Url**, <<http://luna.sit.ac.jp/IDOLAB/english/sc97/3d.jpg>>, accessed at 11.12.2008
- [36] **Anderson, G.S., Mayer, W.N., Wehner, G.K.**, 1962: Sputtering of dielectrics by high-frequency fields, *J. Appl. Phys.*, **33**, p. 2991.
- [37] **Anderson, G.S., Moseson, R.M.**, 1966: Method and apparatus for cleansing by ionic bombardment, *U.S. Patent*, No: 3,233,137.
- [38] **Wehner, G.K.** 1955: Sputtering by ion bombardment, *Advances in Electronics and Electron Physics*, **7**, p. 239, Academic Press.
- [39] **Ohring, M.**, 1992: *The Materials Science of Thin Films*, p. 109-132, Academic Press, U.S.A.
- [40] **Mattox, D.M.**, 1994: Ion plating, in *Handbook Of Deposition Technologies For Films And Coatings*, p. 346-391, Ed. Bunshah, R.F., Noyes Publications, Park Ridge, New Jersey, USA.
- [41] **Wehner, G.K.**, 1962: Growth of solid layers on substrates which are kept under ion bombardment before and during deposition, *U.S. Patent* No: 3,021,271.

- [42] **Mattox, D.M.**, 1964: Film deposition using accelerated ions, *Electrochem. Technol.*, **2**, p. 295.
- [43] **Mattox, D.M.**, 1966: Apparatus for coating a cathodically biased substrate from plasma of ionized coating material, *U.S. Patent*, No: 3,329,601.
- [44] **Helmersson, U., Latteman, M., Bohlmark, J., Ehiasarian, A.P., Gudmundson, J.T.**, 2006: Ionized physical vapor deposition (IPVD): A review of technology and applications, *Thin Solid Films*, **513**, p. 1.
- [45] **Schneider, J.M., Rohde, S., Sproul, W.D., Matthews, A.**, 2000: Recent developments in plasma assisted physical vapour deposition, *J. Phys. D: Appl. Phys.*, **33**, p. 173.
- [46] **Overbeck, C.J.** 1933: Color in films of sputtered tin, *J. Opt. Soc. Am.*, **23**, p. 109.
- [47] **Thornton, J.A.**, 1986: The microstructure of sputter-deposited coatings, *J. Vac. Sci. Technol A*, vol. **4**, no. 6, p. 3059.
- [48] **Greene, J.E.**, 1994: Nucleation, film growth, and microstructural evolution, in *Handbook Of Deposition Technologies For Films And Coatings*, p. 707-760, ed. Bunshah, R.F., Noyes Publications, Park Ridge, New Jersey, USA.
- [49] **Greene, J.E.**, 1993: Physics of Film Growth from the Vapor Phase, in *Multicomponent and Multilayered Thin Films for Advanced Microtechnologies: Techniques, Fundamentals, and Devices*, p. 39-86, Eds. Auciello, O., Engemann, J., Kluwer Academic Publisher, Netherlands.
- [50] **Movchan, B.A., Demchishin, A.V.**, 1969: Study of the structure and properties of thick vacuum condensates of nickel, titanium, tungsten, aluminium oxide and zirconium dioxide, *Phys. Met. Metallogr.*, vol. **28**, p. 83.
- [51] **Thornton, J.A.**, 1974: Influence of apparatus geometry and deposition conditions on the structure and topography of thick sputtered coatings, *J. Vac. Sci. Technol.*, vol. **11**, no. 4, p. 666.
- [52] **Petrov, I., Barna, P.B., Hultmann, L., Grene, J.E.**, 2003: Microstructural evolution during film growth, *J. Vac. Sci. Technol. A*, vol. **21**, no. 5, p. 117.
- [53] **Messier, R., Giri, A.P., Roy, R.A.**, 1984: Revised structure zone model for thin film physical structure, *J. Vac. Sci. Technol.*, vol. **A2**, no. 2, p. 500.

- [54] **Dirks, A.G., Leamy, H.J.**, 1977: Columnar microstructure in vapor-deposited thin films, *Thin Solid Films*, vol. **47**, p. 219.
- [55] **Müller, K.H.**, 1985: Dependence of thin-film microstructure on deposition rate by means of a computer simulation, *J. Appl. Physics*, vol. **58**, no.7, p. 2573.
- [56] **Zhang, Z., Lagally, M.**, 1997: Atomistic processes in the early stages of thin-film growth, *Science*, **276**, p. 377.
- [57] **Mattox, D.M., Kominiak, G.J.**, 1972: Structure Modification by Ion Bombardment During Deposition, *J. Vac. Sci. Technol.*, vol. **9**, no. 1, p. 528.
- [58] **Müller, K.H.**, 1987: Ion-beam-induced epitaxial vapor-phase growth: A molecular-dynamics study, *Physical review B*, vol. **35**, no. 15, p. 7906.
- [59] **Müller, K.H.**, 1986: Modelling ion-assisted deposition of CeO<sub>2</sub> films, *Appl. Phys. A*, **40**, p. 209.
- [60] **Thévenot, F.**, 1990: Boron carbide—A comprehensive review, *Journal of the European Ceramic Society*, **6**, p. 205.
- [61] **Lattemann, M., Ulrich, S.**, 2007: Investigation of structure and mechanical properties of magnetron sputtered monolayer and multilayer coatings in the ternary system Si-B-C, *Surf. Coat. Tech.*, **201**, p. 5564.
- [62] **Lee, K.E., Lee, J.Y., Park, M.J., Kim, J.H., Lee, C.B., Kim, C.O.**, 2004: Preparation of boron carbide thin films for HDD protecting layer, *Journal of Magnetism and Magnetic Materials*, **272–276**, p. 2197.
- [63] **Lousa, A., Martinez, E., Esteve, J., Pascual, E.**, 1999: Effect of ion bombardment on the properties of B<sub>4</sub>C thin films deposited by RF sputtering, *Thin Solid Films*, **355-356**, p. 210.
- [64] **Chen, Y., Chung, Y.W., Li, S.Y.**, 2006: Boron carbide and boron carbonitride thin films as protective coatings in ultra-high density hard disk drives, *Surf. Coat. Tech.*, **200**, p. 4072.
- [65] **Sezer, A.O., Brand, J.I.**, 2001: Chemical vapor deposition of boron carbide, *Materials Science and Engineering B*, **79**, p. 191.
- [66] **Erdemir, A., Bindal, C., Zuiker, C., Savrun, E.**, 1996: Tribology of naturally occurring boric acid films on boron carbide, *Surf. Coat. Tech.*, **86-87**, p. 507.

- [67] **Conde, O., Silvestre, A.J., Oliveira, J.C.**, 2000: Influence of carbon content on the crystallographic structure of boron carbide films, *Surf. Coat. Tech.*, **125**, p. 141.
- [68] **Harris, S.J., Krauss, G.G., Simko, S.J., Baird, R.J., Gebremariam, S.A., Doll, G.**, 2002: Abrasion and chemical-mechanical polishing between steel and a sputtered boron carbide coating, *Wear*, **252**, p. 161.
- [69] **Eckardt, T., Bewilogua, K., Van der Kolk, G., Hurkmans, T., Trinh, T., Fleischer, W.**, 2000: Improving tribological properties of sputtered boron carbide coatings by process modifications, *Surf. Coat. Tech.*, **126**, p. 69.
- [70] **Suematsu, H., Kitajima, K., Ruiz, I., Kobayashi, K., Takeda, M., Shimbo D., Suzuki, T., Jiang, W., Yatsui, K.**, 2002: Thermoelectric properties of crystallized boron carbide thin films prepared by ion-beam evaporation, *Thin Solid Films*, **407**, p. 132.
- [71] **Ahmad, A.A., Ianno, N.J., Hwang, S.D., Dowben, P.A.**, 1998: Sputter deposition of high resistivity boron carbide, *Thin Solid Films*, **335**, p. 174.
- [72] **Aoqui, S., Miyata, H., Ohshima, T., Ikegami, T., Ebihara, K.**, 2002: Preparation of boron carbide thin film by KrF excimer laser deposition process, *Thin Solid Films*, **407**, p. 126.
- [73] **Pascual, E., Martinez, E., Esteve, J., Lousa, A.**, 1999: Boron carbide thin films deposited by tuned-substrate RF magnetron sputtering, *Diamond and Related Materials*, **8**, p. 402.
- [74] **Guruz, M.U., Dravid, V.P., Chung, Y.W.**, 2002: Synthesis and characterization of single and multilayer boron nitride and boron carbide thin films grown by magnetron sputtering of boron carbide, *Thin Solid Films*, **414**, p. 129.
- [75] **Ovshinsky, S.R., Keem, J.E., Flasck, J.D., Bergeron, R.C., Tyler, J.E.**, 1987: Coating composition and method, *U.S. Patent*, No: 4,645,715.
- [76] **Eichen, E., Flasck, J.D.**, 1984: Multilayer coating including disordered, wear resistant boron carbon external coating, *U.S. Patent*, No: 4,594,294.
- [77] **Keem, J.E., Flasck, J.D.**, 1984: Multilayer coating and method, *U.S. Patent*, No: 4,619,865.
- [78] **Eichen, E., Flasck, J.D.**, 1986: Molding tool and method, *U.S. Patent*, No: 4,590,031.

- [79] **Eichen, E., Flasck, J.D.**, 1987: Disordered coating, *U.S. Patent*, No: 4,716,083.
- [80] **Lin, S.H., Feldman, B.J., Li, D.**, 1996: Microhardness study of amorphous hydrogenated boron carbide deposited on a cathode substrate by plasma deposition, *Appl. Phys. Lett.*, **69**, p. 2373.
- [81] **Annen, A., Sab, M., Beckmann, R., Von Keudell, A., Jacob, W.**, 1998: Structure of plasma-deposited amorphous hydrogenated boron-carbon thin films, *Thin Solid Films*, **312**, p. 147.
- [82] **Kosinova, M.L., Rumyantsev, Y.M., Golubenko, A.N., Fainer, N.I., Ayupov, B.M., Dolgovesova, I.P., Kolesov, B.A., Kaichev, V.V., Kuznetsov, F.A.**, 2003: Chemical composition of boron carbonitride films grown by plasma-enhanced chemical vapor deposition from trimethylamineborane, *Inorg. Mater.*, vol. **39**, no. 4, p. 366.
- [83] **Lee, S., Mazurowski, J., Ramseyer, G., Dowben, P.A.**, 1992: Characterization of boron carbide thin films fabricated by plasma enhanced chemical vapor deposition from boranes, *J. Appl. Phys.*, Vol. **72**, no. 10, p. 4925.
- [84] **Postel, O.B., Heberlein, J.V.R.**, 1998: Deposition of boron carbide thin film by supersonic plasma jet CVD with secondary discharge, *Surf. Coat. Tech.*, **108-109**, p. 247.
- [85] **Postel, O.B., Heberlein, J.V.R.**, 1999: Boron carbide thin film deposition using supersonic plasma jet with substrate biasing, *Diamond and Related Materials*, **8**, p. 1878.
- [86] **Oliveira, J.C., Conde, O.**, 1997: Deposition of boron carbide by laser CVD: A comparison with thermodynamic predictions, *Thin Solid Films*, **307**, p. 29.
- [87] **Monteiro, O.R., Delplancke-Ogletree, M.P., Klepper, C.C.**, 2003: Boron carbide coatings prepared by cathodic arc deposition, *J. Mater. Sci.*, **38**, p. 3117.
- [88] **Suematsu, H., Kitajima, K., Suzuki, T., Jiang, W., Yatsui, K., Kurashima, K., Bando, Y.**, 2002: Preparation of polycrystalline boron carbide thin films at room temperature by pulsed ion-beam evaporation, *Applied Physics Letters*, Vol. **80**, no. 7, p. 1153.
- [89] **Ronning, C., Schwen, D., Eyhusen, S., Vetter, U., Hofsass, H.**, 2002: Ion beam synthesis of boron carbide thin films, *Surf. Coat. Tech.*, **158-159**, p. 382.

- [90] **Kokai, F., Taniwaski, M., Ishihara, M., Koga, Y.**, 2002: Effect of laser fluence on the deposition and hardness of boron carbide thin films, *Appl. Phys. A*, **74**, p. 533.
- [91] **Sun, J., Ling, H., Pan, W.J., Xu, N., Ying, Z.F., Shen, W.D., Wu, J.D.**, 2004: Chemical structure and micro-mechanical properties of ultra-thin films of boron carbide prepared by pulsed-laser deposition, *Tribology Letters*, Vol. **17**, no. 1, p. 99.
- [92] **Zeng, Y., Ding, C., Lee, S.W.**, 2001: Young's modulus and residual stress of plasma-sprayed boron carbide coatings, *Journal of the European Ceramic Society*, **21**, p. 87.
- [93] **Greuner, H., Balden, M., Boeswirth, B., Bolt, H., Gadow, R., Grigull, P., Hofmann, G., Huber, T., Kasperek, W., Kumric, H., Lindig, S., Matern, G., Mayer, M., Neu, R., Renner, H., Roth, J., Riegert-Escribano, M., Simon-Weidner, J., Wacker, R.**, 2004: Evaluation of vacuum plasma-sprayed boron carbide protection for the stainless steel first wall of WENDELSTEIN 7-X, *Journal of Nuclear Materials*, **329–333**, p. 849.
- [94] **Kitamura, J., Usuba, S., Kakudate, Y., Yokoi, H., Yamamoto, K., Tanaka, A., Fujiwara, S.**, 2003: Formation of boron carbide coating by electromagnetically accelerated plasma spraying, *Surf. Coat. Tech.*, **169–170**, p. 324.
- [95] **Zhou, M.J., Wong, S.F., Ong, C.W., Quan, L.**, 2007: Microstructure and mechanical properties of B<sub>4</sub>C films deposited by ion beam sputtering, *Thin Solid Films*, **516**, p. 336.
- [96] **Hu, T., Steihl, L., Rafaniello, W., Fawcett, T., Hawn, D.D., Mashall, J.G., Rozeveld, S.J., Putzig, C.L., Blackson, J.H., Ceramiagnani, W., Robinson, M.G.**, 1998: Structures and properties of disordered boron carbide coatings generated by magnetron sputtering, *Thin Solid Films*, **332**, p. 80.
- [97] **Jacobsohn, L.G., Nastasi, M.**, 2005: Sputter-deposited boron carbide films: Structural and mechanical characterization, *Surf. Coat. Tech.*, Vol. **200**, no. 5-6, p. 1472.
- [98] **Wu, M.L., Kiely, J.D., Klemmer, T., Hsia, Y.T., Howard, K.**, 2003: Process-property relationship of boron carbide thin films by magnetron sputtering, *Thin Solid Films*, **449**, p. 120.
- [99] **Ahn, H.S., Cuong, P.D., Shin, K.H., Lee, K.S.**, 2005: Tribological behavior of sputtered boron carbide coatings and the influence of processing gas, *Wear*, **259**, p. 807.

- [100] **Pierson, H.O.** 1996: *Handbook of Refractory Carbides and Nitrides*, p. 118-154, Noyes Publications, New Jersey, USA.
- [101] **Cho, N.**, 2006: Processing of Boron Carbide, *PhD Thesis*, p. 4, Georgia Institute of Technology, USA.
- [102] **Chiang, C.L., Holleck, H., Meyer, O.**, 1994: Properties of RF sputtered B<sub>4</sub>C thin films, *Nucl. Instrum. Meth. Phys. Res. B*, vol. **91**, no. 1-4, p. 692.
- [103] **Han, Z., Li, G., Tian, J., Gu, M.**, 2002: Microstructure and mechanical properties of boron carbide thin films, *Materials Letters*, **57**, p. 899.
- [104] **Kulikovsky, V., Vorlicek, V., Bohac, P., Ctvrtlik, R., Strayanek, M., Dejneka, A., Jastrabik, L.**, 2009: Mechanical properties and structure of amorphous and crystalline B<sub>4</sub>C films, *Diamond and Related Materials*, **18**, p. 27.
- [105] **Chen, H.Y., Wang, J., Yang, H., Li, W.Z., Li, H.D.**, 2000: Synthesis of boron carbide films by ion beam sputtering, *Surf. Coat. Tech.*, **128-129**, p. 329.
- [106] **Lee, K.E., Kim, C.O., Park, M.J., Kim, J.H.**, 2004: Preparation of boron carbide thin films from reactive sputtering of boron, *Phys. Stat. Sol. (b)*, Vol. **241**, no. 7, p. 1637.
- [107] **Ono, T., Kawamura, T., Ishii, K., Yamamura, Y.**, 1996: Sputtering yield formula for B<sub>4</sub>C irradiated with monoenergetic ions at normal incidence, *Journal of Nuclear Materials*, vol. **232**, no. 1, p. 52.
- [108] **Riiwekamp, M., Goehlich, A., Diible, H.F.**, 1992: Diagnostics of sputtering processes of carbon and carbides by laser-induced fluorescence spectroscopy in the VUV at 166 nm, *Appl. Phys. A*, vol. **54**, no. 1, p. 61.
- [109] **Cohen, M.L.**, 1985: Calculation of bulk moduli of diamond and zinc-blende solids, *Phys. Rev. B*, vol. **32**, no. 12, p. 7988.
- [110] **Cohen, M.L.**, 1994: Predicting properties and new materials, *Solid State Comm.*, **92**, p. 45.
- [111] **Liu, A.Y., Cohen, M.L.**, 1990: Structural properties and electronic structure of low-compressibility materials:  $\beta$ -Si<sub>3</sub>N<sub>4</sub> and hypothetical  $\beta$ -C<sub>3</sub>N<sub>4</sub>, *Phys. Rev. B*, vol. **41**, no. 15, p. 10727.

- [112] **Linss, V., Barzola-Quiquia, J., Haussler, P., Richter, F.,** 2004: Structural properties of DC magnetron sputtered B–C–N thin films and correlation to their mechanical properties: A new empirical formula, *Thin Solid Films*, vol. **467**, no. 1-2, p. 66.
- [113] **Ulrich, S., Theel, T., Schwan, J., Ehrhardt, H.,** 1997: Magnetron-sputtered superhard materials, *Surf. Coat. Tech.*, **97**, p. 45.
- [114] **Ulrich, S., Ehrhardt, H., Schwan, J., Samlenski, R., Bren, R.,** 1998: Subplantation effect in magnetron sputtered superhard boron carbide thin films, *Diamond and Related Materials*, **7**, p. 835.
- [115] **Cuong, P.D., Ahn, H.S., Yoon, E.S., Shin, K.H.,** 2006: Effects of relative humidity on tribological properties of boron carbide coating against steel, *Surf. Coat. Tech.* **201**, p. 4230.
- [116] **Knotek, O., Lugscheider, E., Siry, C.W.,** 1999: Superhard PVD coatings in the B-N-C triangle, *International Journal of Refractory Metals & Hard Materials*, **17**, p. 157.
- [117] **Knotek, O., Lugscheider, E., Siry, C.W.,** 1997: Tribological properties of B-C thin films deposited by magnetron-sputter ion plating method, *Surf. Coat. Tech.*, **91**, p. 167.
- [118] **Jacobsohn, L.G., Averitt, R.D., Nastasi, M.,** 2003: The role of trapped Ar atoms in the mechanical properties of boron carbide films deposited by dc-magnetron sputtering, *J. Vac. Sci. Technol. A*, Vol. **21**, no. 5, p. 1639.
- [119] **Erdemir, A., Eryilmaz, O.L., Fenske, G.R.,** 1999: Self-replenishing solid lubricant films on boron carbide, *Surface Engineering*, **15**, p. 291.
- [120] **Larsson, P., Axén, N., Hogmark, S.,** 1999: Tribofilm formation on boron carbide in sliding wear, *Wear*, **236**, p. 73.
- [121] **Martinez, E., Lousa, A., Esteve, J.,** 2001: Micromechanical and microtribological properties of BCN thin films near the B<sub>4</sub>C composition deposited by r.f. magnetron sputtering, *Diamond and Related Materials*, **10**, p. 1892.
- [122] **Reigada, D.C., Prioli, R., Jacobsohn, L.G., Freire Jr. F.L.,** 2000: Boron carbide films deposited by a magnetron sputter-ion plating process: Film composition and tribological properties, *Diamond and Related Materials*, **9**, p. 489.
- [123] **Kustas, F., Mishra, B., Zhou, J.,** 2001: Wear behavior of B<sub>4</sub>C-Mo co-sputtered wear coatings, *Surf. Coat. Tech.*, **141**, p. 48.

- [124] **Erdemir, A.**, 1992: Rolling-contact fatigue and wear resistance of hard coatings on bearing-steel substrates, *Surf. Coat. Technol.*, **54-55**, p. 482.
- [125] **Harris, S.J., Krauss, G., Siniawski, M.T., Wang, Q., Liu, S., Ao, Y.**, 2002: Surface feature variations observed in 52100 steel sliding against a thin boron carbide coating, *Wear*, **249**, p. 1004.
- [126] **Siniawski, M.T., Harris, S.J., Wang, Q.**, 2005: Effects of contact on the abrasiveness of a thin boron carbide coating, *Tribology Letters*, Vol. **20**, no. 1, p. 21.
- [127] **Jacobson, L.G., Schulze, R.K., Maia da Costa, M.E.H., Nastasi, M.**, 2004: X-ray photoelectron spectroscopy investigation of boron carbide films deposited by sputtering, *Surface Science*, **572**, p. 418.
- [128] **Sasaki, S., Takeda, M., Yokoyama, K., Miura, T., Suzuki, T., Suematsu, H., Jiang, W., Yatsui, K.**, 2005: Thermoelectric properties of boron-carbide thin film and thin film based thermoelectric device fabricated by intense-pulsed ion beam evaporation, *Science and Technology of Advanced Materials*, **6**, p. 181.
- [129] **Ahmad, A.A., Ianno, N.J., Hwang, S.D., Dowben, P.A.**, 1998: Sputter deposition of high resistivity boron carbide, *Thin Solid Films*, vol. **335**, no. 1-2, p. 174.
- [130] **Ahmad, A.A., Ianno, N.J., Synder, P.G., Welipitiya, D., Byun, D., Dowben P.A.**, 1996: Optical properties of boron carbide ( $B_5C$ ) thin films fabricated by plasma-enhanced chemical-vapor deposition, *J. Appl. Phys.* Vol. **79**, no. 11, p. 8643.
- [131] **Reigada, D.C., Freire Jr., F.L.**, 2001: Nitrogen incorporation into boron carbide thin films deposited by DC-magnetron sputtering: Film microstructure and tribological properties, *Surf. Coat. Technol.*, **142-144**, p. 889.
- [132] **Freire, F.L., Reigada, D.C., Prioli, R.**, 2001: Boron carbide and boron-carbon nitride films deposited by DC-magnetron sputtering: Structural characterization and nanotribological properties, *Phys. Stat. Sol. (a)*, Vol. **187**, no. 1, p. 1.
- [133] **Tsai, T.H., Yang, T.S., Cheng, C.L., Wong, M.S.**, 2001: Synthesis and properties of boron carbon nitride (BN:C) films by pulsed-DC magnetron sputtering, *Materials Chemistry and Physics*, **72**, p. 264.

- [134] **Linss, V., Hermann, I., Scharzer, N., Kreissig, U., Richter, F.,** 2003: Mechanical properties of thin films in the ternary triangle B-C-N, *Surf. Coat. Tech.*, **163-164**, p. 220.
- [135] **Lousa, A. Esteve, J., Muhl, S., Martinez, E.,** 2000: BCN thin films near the B<sub>4</sub>C composition deposited by radio frequency magnetron sputtering, *Diamond and Related Materials*, **9**, p. 502.
- [136] **Kouptsidis, S., Lüthje, H., Bewilogua, K., Schütze, A., Zhang, P.,** 1998: Deposition of c-BN films by DC magnetron sputtering, *Diamond and Related Materials*, **7**, p. 26.
- [137] **Yang, T.S., Tsai, T.H., Lee, C.H., Cheng, C.L., Wong, M.S.,** 2001: Deposition of carbon-containing cubic boron nitride films by pulsed-DC magnetron sputtering, *Thin Solid Films*, **398-399**, p. 285.
- [138] **Sell K., Ulrich S., Nold E., Ye J., Leiste H., Stüber M., Holleck H.,** 2003: The constitution and properties of cubic boron nitride thin films: A comparative study on the influence of bombarding ion energy, *Surf. Coat. Tech.*, **174-175**, p. 1121.
- [139] **Kratzsch, A., Ulrich, S., Leiste, H., Stüber, M., Holleck, H.,** 1999: Stress reduction in boron carbonitride films by ion energy-modulated multilayers, *Surf. Coat. Tech.*, **116-119**, p. 253.
- [140] **Yamamoto, K., Keuncke, M., Bewilogua, K., Czigany, Zs., Hultman, L.,** 2001: Structural features of thick c-boron nitride coatings deposited via a graded B-C-N interlayer, *Surf. Coat. Tech.*, **142-144**, p. 881.
- [141] **Linss, V., Rodil, S.E., Reinke, P., Garnier, M.G., Oelhafen, P., Kreissig, U., Richter, F.,** 2004: Bonding characteristics of DC magnetron sputtered B-C-N thin films investigated by Fourier-transformed infrared spectroscopy and X-ray photoelectron spectroscopy, *Thin Solid Films*, **467**, p. 76.
- [142] **Miyamoto, Y., Niino, M., Koizumi, M.,** 1997: FGM research programs in Japan – from structural to functional uses, in *Functionally Graded Materials 1996, Proceedings of the 4<sup>th</sup> International Symposium on Functionally Graded Materials, AIST Tsukuba Research Center, Tsukuba, Japan, October 21-24, 1996*, p. 1-9, Eds. Shiota, I., Miyamoto, Y., Elsevier Science B.V., Netherlands.
- [143] **Miyamoto, Y., Kayser, W.A., Rabin, B.H., Kawasaki, A., Ford, R.G.,** 1997: *Functionally Graded Materials: Design Processing and Applications*, p. 1-29, Kluwer Academic Publishers, Massachusetts, USA.

- [144] **Choy, K.L., Felix, E.**, 2000: Functionally graded diamond-like carbon coatings on metallic substrates *Materials Science and Engineering A*, vol. **278**, no. 1-2, p. 162.
- [145] **Schulz, U., Peters, M., Bach, F.W., Tegeder, G.**, 2003: Graded coatings for thermal, wear and corrosion barriers, *Materials Science and Engineering A*, **362**, p. 61.
- [146] **Krishna, B.V., Xue, W., Bose, S., Bandyopadhyay, A.**, 2008: Functionally graded Co–Cr–Mo coating on Ti–6Al–4V alloy structures, *Acta Biomaterialia*, **4**, p. 697.
- [147] **Xu, M., Cai, X., Liu, Y., Pu, S., Chu, P.K.**, 2008: Tribological properties of graded diamond-like carbon films on Ti ion-implanted aluminum substrate, *Diamond and Related Materials*, **17**, p. 1844.
- [148] **Fernandez-Ramos, C., Sanchez-Lopez, J.C., Justo, A., Rojas, T.C., Papst, I., Hofer, F., Fernandez, A.**, 2004: Microstructural characterization of Ti–TiN/CN<sub>x</sub> gradient-multilayered coatings, *Surf. Coat. Tech.*, **180–181**, p. 526.
- [149] **Url**, <<http://htna.bodycote.com/resources/BoronCarbide.zip>>, accessed at 11.12.2008.
- [150] **Hèau, C., Terrat, J.P.**, 2004: Device for Amplifying the Current of an Abnormal Electrical Discharge and System for Using an Abnormal Electrical Discharge Comprising one Such Device, *U.S. Patent Application Publication*, No: US2004/0026241 A1.
- [151] **DIN51056**, 1959: *Bestimmung des offenens Porenranines*, Germany.
- [152] **McGuire, G.E.**, 1994: Characterization of thin films and coatings, in *Handbook Of Deposition Technologies For Films And Coatings*, p. 789-845, Ed. Bunshah, R.F., Noyes Publications, Park Ridge, New Jersey, USA.
- [153] **Bindell, J.B.**, 1992: Scanning electron microscopy, in *Encyclopedia of Materials Characterization*, p. 70-84, Eds. Brundle, C.R., Evans Jr., C.A., Wilson, E.S., Butterworth-Heinemann Inc. , USA.
- [154] **Geiss, R.H.**, 1992: Energy-dispersive X-ray spectroscopy, in *Encyclopedia of Materials Characterization*, p. 120-134, Eds. Brundle, C.R., Evans Jr., C.A., Wilson, E.S., Butterworth-Heinemann Inc. , USA.
- [155] **Newbury, D.E.**, 1992: Electron probe X-ray microanalysis, in *Encyclopedia of Materials Characterization*, p. 175-191, Eds. Brundle, C.R., Evans Jr., C.A., Wilson, E.S., Butterworth-Heinemann Inc. , USA.

- [156] **Sickafus, K.E.**, 1992: Transmission electron microscopy, in *Encyclopedia of Materials Characterization*, p. 99-115, Eds. Brundle, C.R., Evans Jr., C.A., Wilson, E.S., Butterworth-Heinemann Inc. , USA.
- [157] **Url**, <[http://www.thaindian.com/newsportal/tech-news/new-record-in-tem-resolution\\_1005436.html](http://www.thaindian.com/newsportal/tech-news/new-record-in-tem-resolution_1005436.html)>, accessed at 17.03.2008.
- [158] **Url**, <<http://www.smt.zeiss.com>>, accessed at 17.03.2008.
- [159] **Benninghoven, A., Rüdener, F.G., Werner, H.W.**, 1987: *Secondary Ion Mass Spectrometry, Basic Concepts, Instrumental Aspects, Applications and Trends*, p. 1-6, John Wiley & Sons, USA.
- [160] **Chu, P.K.**, 1992: Dynamic secondary ion mass spectrometry, in *Encyclopedia of Materials Characterization*, p. 532-548, Eds. Brundle, C.R., Evans Jr., C.A., Wilson, E.S., Butterworth-Heinemann Inc., USA.
- [161] **Katz, B.**, 1992: Static secondary ion mass spectrometry, in *Encyclopedia of Materials Characterization*, p. 549-558, Eds. Brundle, C.R., Evans Jr., C.A., Wilson, E.S., Butterworth-Heinemann Inc., USA.
- [162] **Hutter, H.**, 2002: Dynamic secondary ion mass spectrometry, in *Surface and Thin Film Analysis: Principles, Instrumentation, Application*, p. 106-121, Eds. Hubert, H., Jenett, H., Wiley-VCH Verlag GmbH, Weinheim, Germany.
- [163] **Chudoba, T.**, 2006: Measurement of hardness and Young's modulus by nanoindentation, in *Nanostructured Coating*, p. 216-260, Eds. Cavaleiro, A., De Hosson, J.T.M., Springer Science, New York, USA.
- [164] **Bhushan, B.**, 1999: Nanomechanical properties of solid surface and thin films, in *Handbook of Micro/Nano Tribology*, ch. 10, p. 1-91, Ed. Bhushan, B., CRC Pres, USA.
- [165] **Loubet, J.L., Georges, J.M., Marchesini, O., Meille, G.**, 1984: Vickers indentation curves of magnesium oxide (MgO), *J. Tribology*, **106**, p. 43.
- [166] **Doerner, M.F., Nix, W.D.**, 1986: A method for interpreting the data from depth-sensing indentation instruments, *J. Mater. Res.*, vol. **1**, no. 4, p. 601.
- [167] **Oliver, W.C., Pharr, G.M.**, 1992: An improved technique for determining hardness and elastic modulus using load and displacement sensing indentation experiments, *J. Mater. Res.*, Vol. **7**, no. 6, p. 1564.

- [168] **Pharr, G.M., Oliver, W.C., Brotzen, F.R.**, 1992: On the generality of the relationship among contact stiffness, contact area, and elastic modulus during indentation, *J. Mater. Res.*, vol. **7**, no. 3, p. 613.
- [169] **Bhushan, B.**, 1999: Introduction-Measurement techniques and applications, in *Handbook of Micro/Nano Tribology*, ch. 1, p. 1-77, Ed. Bhushan, B., CRC Pres, USA.
- [170] **Stachowiak, G.W., Batchelor, A.W.**, 2005: *Engineering Tribology 3rd Edition*, p. 1-9, Elsevier Inc. USA
- [171] **Axén, N., Hogmark, S., Jacobson, S.**, 2001: Friction and wear measurement techniques, in *Modern Tribology Handbook*, p. 493 Ed. Bharat Bhushan, CRC Press, Florida, USA.
- [172] **Delqué, M.**, 2007: Influence de la Microstructure sur le Comportement Tribologique de Dépôts Composites Projétés Plasma, p. 37-57, *PhD Thesis*, Ecole des Mines de Paris, France.
- [173] **ASM Handbook**, 1992 : *Volume 18: Friction, Lubrication and Wear Technology*, p. 1, USA.
- [174] **Domnich, V., Gogotsi, Y., Trenary, M., Tanaka, T.**, 2002: Nanoindentation and raman spectroscopy studies of boron carbide single crystals, *App. Phys. Letters*, Vol. **81**, no. 20, p. 3783.
- [175] **Kuhlmann, U., Werheit, H.**, 1994: Raman effect of boron carbide ( $B_{4.3}C$  to  $B_{10.37}C$ ), *J. Alloys Compd.*, **205**, p. 87.
- [176] **Gago, R., Jimenez, I., Agullo-Rueda, F., Albella, J.M., Czigan, Zs., Hultman, L.**, 2002: Transition from amorphous boron carbide to hexagonal boron carbon nitride films induced by nitrogen ion assistance, *Journal of Applied Physics*, Vol. **92**, no. 9, p. 5177.
- [177] **Kim, H.S., Choi, I.H., Baik, Y.J.**, 2000: Characteristics of carbon incorporated BN films deposited by radio frequency PACVD, *Surf. Coat. Tech.*, **133-134**, p. 473.



## CURRICULUM VITAE



**Full Name:** Tolga TAVŞANOĞLU  
**Place and Date of Birth:** Trabzon/Turkey, 05/04/1974  
**Permanent Address:** Sevgi Sitesi Gül Sok. Polat Çamlık Apt. No:25/1  
Tarabya 34457 Sarıyer, İstanbul/Turkey

### Universities and Colleges Attended:

- 2005-2009** Ecole des Mines de Paris, Centre des Matériaux P.M. Fourt, Science et Génie des Matériaux, PhD
- 2001-2009** Istanbul Technical University, Institute of Science and Technology, Metallurgical and Materials Engineering Department, Materials Programme, PhD
- 1998-2001** Istanbul Technical University, Institute of Science and Technology, Metallurgical and Materials Engineering Department, Materials Programme, MSc
- 1993-1998** Istanbul Technical University, Metallurgical and Materials Engineering Department, BSc
- 1984-1992** Lycée Galatasaray

### Publications:

1. **T. Tavsanoğlu**, M.H. Berger, M. Jeandin, O Addemir, “Effect of pressure and controlled ion bombardment on the micro/nanostructural and nanomechanical properties of boron carbide thin films grown by a DC magnetron sputter/ion plating process” (Article in preparation, to be submitted to Thin Solid Films), 2009.
2. **T. Tavsanoğlu**, S. Labdi, M.H. Berger, M. Jeandin, O Addemir, “Synthesis and characterization of boron carbide thin films by DC magnetron sputter/ion plating method: Effect of bias voltage and temperature on the structural and mechanical properties” (Article in preparation, to be submitted to Surf. Coat. Tech.), 2009.

3. **T. Tavsanoglu**, O. Addemir, M. Jeandin, "Synthesis and characterization of boron carbonitride thin films by reactive DC magnetron sputtering", 11<sup>th</sup> International Conference and Exhibition of the European Ceramic Society (ECERS 2009), June 21–25, 2009, Krakow, Poland.
4. **T. Tavsanoglu**, S. Labdi, M. Jeandin, "Synthesis and Characterization of Boron Carbide Thin Films Grown by RF Sputtering", TMS 2009 138<sup>th</sup> Annual Meeting and Exhibition, 15–19 February, 2009, San Francisco, California, USA. Supplemental Proceedings Vol. I: Fabrication, Materials Processing and Properties, pp. 573–580.
5. **T. Tavsanoglu**, O. Yucel, O. Addemir, M. Jeandin, "A functionally graded design study for boron carbide and boron carbonitride thin films deposited by plasma-enhanced DC magnetron sputtering", TMS 2008 137<sup>th</sup> Annual Meeting and Exhibition, 9–13 March, 2008, New Orleans, Louisiana, USA. Supplemental Proceedings Vol. I: Materials Processing and Properties, 279–285.
6. **T. Tavsanoglu**, S. Labdi, M. Jeandin, O. Addemir, "The effect of controlled ion bombardment on the properties of boron carbide thin films deposited by plasma-enhanced dc magnetron sputtering", Innovations on Thin Films Processing and Characterisation–ITFPC 07, 20–23 Novembre 2007, Nancy, France (Abstract published).
7. **T. Tavsanoglu**, S. Labdi, M. Jeandin, O. Addemir, "Characterization of Boron Carbide Thin Films Grown by DC Magnetron Sputtering of a Hot-Pressed Boron Carbide Target", 10<sup>th</sup> International Conference and Exhibition of the European Ceramic Society, June 17–21, 2007, Berlin, Germany. Proceedings CD-Rom, 265–270.
8. **T. Tavşanoğlu**, B. Alparslan, M.E. Cura, O. Addemir, "Effect of Oxygen Flow Rate and Substrate Temperature on ZnO Thin Film Properties Deposited By Reactive DC Magnetron Sputtering", XIII. International Materials Research Congress, Cancun / Mexico, 22–26 August 2004 (Abstract published).
9. M.E. Cura, **T. Tavşanoğlu**, "Deposition of AlN Thin Films by Reactive DC Magnetron Sputtering: Effect of Bias Voltage and N<sub>2</sub> Rate on Optical and Microstructural Properties", XIII. International Materials Research Congress, Cancun / Mexico, 22–26 August 2004 (Abstract published).
10. **T. Tavşanoğlu**, O. Addemir, E. Başaran, S. Alkoy "Processing and Characterization of Functionally Graded Ti/Ti<sub>x</sub>Cy/DLC Thin Film Coatings", Key Engineering Materials Vols. 264–268 (2004) pp. 593–596, presented at 8<sup>th</sup> Conference and Exhibition of the European Ceramic Society (ECerS), 29 June–3 July 2003, Istanbul, Turkey.

11. T. Boyraz, A. Kılıç, B. Ertuğ, **T. Tavşanoğlu**, Y. Karakaş, O. Addemir “The Characterization of Metal-Ceramic Interfaces in Porcelain Teeth”, Key Engineering Materials Vols. 264–268 (2004) pp. 683–686, presented at 8<sup>th</sup> Conference and Exhibition of the European Ceramic Society (ECerS), 29 June–3 July 2003, Istanbul, Turkey.
12. **T. Tavşanoğlu**, O. Addemir, E. Başaran, S. Alkoy, “Investigation of Production Parameters and Characterization of Functionally Graded Ti/Ti<sub>x</sub>Cy/DLC Thin Film Coatings Deposited Using Reactive Magnetron Sputtering/PECVD Hybrid Technique”, 11<sup>th</sup> International Metallurgy and Materials Congress, 05–08 June 2002, Istanbul, Turkey.
13. B. Alpaslan, **T. Tavşanoğlu**, A. Yeşilçubuk, O. Addemir “Deposition of ZnO Thin Films on Glass Substrates by Using DC Reactive Magnetron Sputtering”, 11<sup>th</sup> International Metallurgy and Materials Congress, 05–08 June 2002, Istanbul, Turkey.